Interner Bericht
DESY-Zeuthen 94-04
Dezember 1994

Neutral Current Physics with τ Leptons using the L3 Detector at LEP

Thesis

Stefan Kirsch

Neutral Current Physics with τ Leptons using the L3 Detector at LEP

Thesis

Stefan Kirsch

Abstract

In this thesis the analysis of the neutral current process $e^+e^- \to \tau^+\tau^-$ has been discussed. Results on measurements of the total cross section, the forward-backward asymmetry, the polarization asymmetry and the forward-backward polarization asymmetry have been presented using the data which were collected with the L3 detector from 1990 to 1992. Special emphasis was given to the measurement of the polarization asymmetry and forward-backward polarization asymmetry. Combining these two measurements $\mathcal{A}_e$ and $\mathcal{A}_\tau$ can be extracted. The results are:

$$\begin{aligned} \mathcal{A}_e &= 0.125 \pm 0.022(stat.) \pm 0.013(sys.), \\ \mathcal{A}_\tau &= 0.171 \pm 0.016(stat.) \pm 0.014(sys.). \end{aligned}$$

In addition to these results also the measurements of the total cross section and the forward-backward asymmetry in the channels $e^+e^- \to e^+e^-$, $e^+e^- \to \mu^+\mu^-$, $e^+e^- \to \tau^+\tau^-$ and of the total cross section in the channel $e^+e^- \to q\bar{q}$ are used to determine the properties of the Z boson. The data are interpreted in the frame work of the Standard Model and of the following model independent ansatzes: the S-matrix, effective couplings and partial width approach. Using exclusively results from the channel $e^+e^- \to \tau^+\tau^-$, the mass and width of the Z boson are measured to be:

$$\begin{aligned} m_Z &= 91.189 \pm 0.036 \text{ GeV}, \\ \Gamma_Z &= 2.502 \pm 0.061 \text{ GeV}. \end{aligned}$$

The effective couplings of τ to the Z boson are determined to be:

$$\begin{aligned} \hat{g}_V^\tau &= -0.0454 \pm 0.0053, \\ \hat{g}_A^\tau &= -0.4993 \pm 0.0042. \end{aligned}$$

The effective weak mixing angle is derived:

$$\sin^2 \hat{\theta}_W = 0.2273 \pm 0.0027.$$

The partial decay width of the Z boson into $\tau^+\tau^-$ pairs is measured to be:

$$\Gamma_\tau = 83.97 \pm 0.99 \text{ MeV}.$$

All measurements are in good agreement with the predictions of the Standard Model. The hypothesis of lepton universality is confirmed.

Neutral Current Physics with τ Leptons using the L3 Detector at LEP

DISSERTATION

zur Erlangung des akademischen Grades

doctor rerum naturalium
(Dr. rer. nat.)

eingereicht am

Institut für Physik der Humbold-Universität zu Berlin

von

Diplom-Physiker Stefan Kirsch,
geboren am 26. Februar 1964 in Berlin

Präsidentin der Humboldt-Universität zu Berlin
Professor M. Dürkop

Dekan der Mathematisch-Naturwissenschaftlichen Fakultät I
Professor M. von Ortenberg

Gutachter: Professor Dr. T. Hebbeker
Professor Dr. P. Söding
Privatdozent Dr. M. Pohl

Tag der mündlichen Prüfung: 14.November 1994

L3 is a huge collaboration operating a complex detector. This thesis was only possible due to the combined effort of many people. In the following I would like to mention some of them in particular.

First of all I thank my advisors T. Hebbeker and especially W. Lohmann for support and fruitful discussions, which helped to solve many problems.

Special thanks to Ian Brock for his patience in explaining to me how one has to present and discuss physical problems. Especially I acknowledge his very careful work correcting this manuscript.

I have to thank M. Pohl for his constant interest in my work and many encouraging hints and suggestions.

I enjoyed the collaboration with S. Riemann, who also introduced me to the problems of fitting electroweak parameters.

I am glad that T. Riemann gave me the possibility to participate in the development of the SMATASY package. I always appreciate his successful attempts to answer my questions in a way which is understandable for an experimentalist.

H. Vogt introduced me to the complicated world of L3 offline programming. Only with his help was it possible to use the z-detector in my analysis.

I benefit from the collaboration with M. W. Grünewald. His permanent pressure forced me to finalize apparently endless tasks.

Together with C. Paus I explored the "last" secrets of our fitting codes, which increased my confidence in the fit results.

Furthermore I would like to thank A. Kunin, A. Böhm, S. Ganguli, A. Gurtu, G. Rahal, J. Mnich and M. Merk, who always had time for discussions and enlightening clarifications.

Many other people contributed to my work, who I do not mention explicitly; I apologize for that and thank them all.
Last but not least, I would like to thank Antje for her patience and her understanding during the last years.

– *Stefan*

Contents

List of Figures

List of Tables

Chapter 1

Introduction

The theory of electroweak interactions, the Standard Model [1], describes a wide variety of experimental observations. The forces between the three different lepton types: electrons, muons and τ's, are mediated by the photon and the W and Z bosons. The couplings of the leptons to the photon, which are proportional to their electromagnetic charges, are well measured at low energies. The couplings to the W boson are determined by investigating the decay properties of the muon and the τ. With the present experimental precision these couplings appear the same for all leptons. This fact is referred as *lepton universality*.

The couplings of the leptons to the Z boson are currently under study at the Large Electron Positron Collider (LEP) at CERN. LEP operates at center-of-mass energies in the vicinity of the mass of the Z, and the Z boson is produced in high rates in the neutral current process of electron-positron annihilation into fermion-pairs, $e^+e^- \to f\bar{f}$. The clean environment of e^+e^- collisions allows the properties of the Z boson and its couplings to various final states to be determined very precisely. Therefore, a sensitive test of lepton universality at LEP energies can be performed.

The couplings to the Z boson are determined from the measurements of the total cross section and the forward-backward asymmetry for each leptonic final state. Among the leptonic final states of the Z, the decay into two τ leptons is of special interest. In addition to the total cross section and the forward-backward asymmetry, for $e^+e^- \to \tau^+\tau^-$ the polarization and forward-backward polarization asymmetry can be measured, which are very sensitive to the couplings of the electron and τ to the Z boson. Assuming helicity conservation, only the channel $e^+e^- \to \tau^+\tau^-$ provides the full set of independent observables of the neutral current process, $e^+e^- \to f\bar{f}$.

Interpreting the experimental measurements within the framework of different model independent ansatzes, such as the S-matrix, the effective coupling and partial width approaches, and comparing the results to the expectations of the Standard Model constitute stringent tests of the theory.

This thesis is organized as follows:

In Chapter 2, the framework of the Standard Model is introduced. The basic formulas for the observable quantities, total cross section, forward-backward asymmetry, polarization asymmetry and forward-backward polarization asymmetry are given. The incorporation of higher order effects in the theory are discussed. The properties of the τ lepton are summarized.

In Chapter 3, three *model independent* approaches to describe the process $e^+e^- \rightarrow f\bar{f}$ in the vicinity of the Z resonance are discussed. These ansatzes are: the S-matrix approach, the effective coupling approach and the partial width approach.

Chapter 4 describes the main features of the LEP collider. An overview of the construction and performance of one of four experiments at LEP, the L3 experiment, is given.

In Chapter 5 one subdetector of the L3 experiment, the z-detector, is described in detail. The z-detector is essential for the measurement of the τ polarization using the acollinearity between the τ-decay products, which is described in the next chapter.

In Chapter 6 the experimental methods to measure the total cross section and the three asymmetries are discussed. Special emphasis is given to the ways of measuring the polarization asymmetries. Results are presented using the data sample recorded by the L3 collaboration in 1991-1992 and compared to the measurements of the other LEP experiments.

In Chapter 7 the experimental results of Chapter 6 are interpreted in terms of different model independent ansatzes and compared to the predictions of the Standard Model. Combined LEP results are presented.

The work is summarized in Chapter 8 and remarks about future prospects are given.

In this thesis all quantities are expressed in natural units: $\hbar = 1$ and $c = 1$.

Chapter 2

The Standard Model

In the Standard Model of electroweak and strong interactions the building blocks of matter are fermions (particles with half integer spin). Each fermion is associated with an antifermion of exactly the same mass but with opposite sign for the quantum numbers characterizing the fermion. The fermions are grouped in three generations of increasing fermion masses. A generation is formed by a lepton, its neutrino and a quark pair. Apart of their masses the physical properties of the corresponding fermions in each generation are the same. The forces between the fermions are mediated by the exchange of bosons (particles with integer spin). These bosons are the photon, the W and Z bosons and eight different gluons. Gluons are exchanged only between quarks and impose the strong interaction. The remaining bosons are related to the electroweak interactions.

The Standard Model is a gauge theory and the symmetry properties of its Lagrangian restrict the dynamics of interactions. In general one distinguishes internal and external symmetries. Only internal symmetries are considered by gauge theories. External symmetries describe the invariance of the system under certain coordinate transformations in space and time, while internal symmetries are related to the properties of the particles. Furthermore, one has global and local symmetries. For global symmetries, the symmetry transformation is independent of space and time. Noethers Theorem states that each global symmetry leads to a conserved quantity, i.e. to a quantity which is independent of time. An example of a global external symmetry is the translation invariance in space, resulting in momentum conservation. The invariance of a system under a global phase transformation of the wave function is a global internal symmetry, which leads to charge conservation. If the symmetry transformation depends on the position of the system in space and time the symmetry is local. The invariance of the Lagrangian under local symmetries requires the existence of an interaction between particles. Using local internal symmetries, the electromagnetic and weak forces can be described in a unifying way. The unified theory of electromagnetic and weak interaction, the electroweak Standard Model, was developed by Glashow, Salam and Weinberg [1]. The framework of the electroweak Standard Model is discussed in this chapter.

2.1 The Lagrangian of the Electroweak Standard Model

The dynamics of electroweak interactions are described by a non-Abelian, local gauge theory. The underlying gauge group is $SU(2)_L \times U(1)_Y$. The conserved quantities related to the symmetries of the gauge group, are the weak isospin vector, T, and the hypercharge, Y. T_3 is the third component of T. The electromagnetic charge, Q, is given by $Q = T_3 + Y$. The particle content of the model is listed in Table 2.1. All left-handed fermions are grouped in isospin doublets with isospin components $T_3 = \pm\frac{1}{2}$. The right-handed fermions form isospin singlets (T=0). Interactions are introduced by the symmetry properties of

Generation:	1	2	3	T_3	Y	Q
Leptons	$\begin{pmatrix} \nu_e \\ e \end{pmatrix}_L$	$\begin{pmatrix} \nu_\mu \\ \mu \end{pmatrix}_L$	$\begin{pmatrix} \nu_\tau \\ \tau \end{pmatrix}_L$	$1/2$ $-1/2$	$-1/2$ $-1/2$	0 -1
	e_R	μ_R	τ_R	0	-1	-1
Quarks	$\begin{pmatrix} u \\ d' \end{pmatrix}_L$	$\begin{pmatrix} c \\ s' \end{pmatrix}_L$	$\begin{pmatrix} t \\ b' \end{pmatrix}_L$	$1/2$ $-1/2$	$1/6$ $1/6$	$2/3$ $-1/3$
	u_R	c_R	t_R	0	$2/3$	$2/3$
	d_R	s_R	b_R	0	$-1/3$	$-1/3$
Gauge Bosons	γ			0	0	0
	Z			0	0	0
	W^+			1	0	1
	W^-			-1	0	-1
Higgs	$\Phi = \begin{pmatrix} \phi^+ \\ \phi^0 \end{pmatrix}$			$1/2$ $-1/2$	$1/2$ $1/2$	1 0

Table 2.1: Particles and fields in the electroweak Standard Model. The quantum numbers for weak isospin T_3, hypercharge Y and charge Q are given; they are related by $Q = T_3 + Y$.

$SU(2)_L \times U(1)_Y$. Quantum Electrodynamics (QED) follows from the invariance of the Lagrangian under local phase transformation of the wave function. The weak interaction is imposed by invariance of internal rotations in the left-handed doublet fields.

The Lagrangian of the electroweak Standard Model, $\mathcal{L}_{SM}$, is a sum of four terms [2]:

$$\mathcal{L}_{SM} = \mathcal{L}_{Fermion} + \mathcal{L}_{Gauge} + \mathcal{L}_{Higgs} + \mathcal{L}_{Yukawa}. \tag{2.1}$$

The fermion Lagrangian, $\mathcal{L}_{Fermion}$, describes massless fermion fields, ψ, and their interaction with gauge boson fields:

$$\mathcal{L}_{Fermion} = \bar{\psi} i \gamma^\mu D_\mu \psi. \tag{2.2}$$

The covariant derivative D_μ contains the gauge fields and ensures the required symmetry of the Lagrangian under local symmetry transformations:

$$D_\mu = \partial_\mu + ig_1 B_\mu Y + ig_2 W_\mu^a T_a. \qquad (2.3)$$

B_μ, W_μ^a(a=1,2,3) are the four gauge fields and g_1, g_2 the coupling constants for the $U(1)_Y$ and $SU(2)_L$ group, respectively. These gauge fields form the gauge field Lagrangian, $\mathcal{L}_{Gauge}$, which also describes the self-interaction of the W_μ^a fields. The self-interaction is a feature of the non-Abelian gauge group $SU(2)_L$.

The gauge fields are massless, because explicit mass terms in the Lagrangian destroy the symmetry. On the other hand the weak force is only a short distance interaction, which requires massive carriers for the force. Spontaneous symmetry breaking is the mechanism for generating gauge boson masses, without destroying the symmetry of the Lagrangian. Therefore, an isospin doublet of complex scalar fields is introduced [3]:

$$\Phi(x) = \begin{pmatrix} \phi^+(x) \\ \phi^0(x) \end{pmatrix}, \qquad (2.4)$$

which adds a further contribution to the Lagrangian:

$$\mathcal{L}_{Higgs} = D_\mu \Phi^+ D^\mu \Phi - V(\Phi). \qquad (2.5)$$

The potential $V(\Phi)$ is given by:

$$V(\Phi) = -\mu^2 \Phi^+ \Phi + \lambda(\Phi^+\Phi)^2, \quad \lambda > 0. \qquad (2.6)$$

The vacuum, defined as a state with minimal energy, is reached when the field $\Phi(x) = \Phi_0$ is constant and the potential $V(\Phi)$ is minimal. For $-\mu^2 < 0$ this is satisfied by:

$$\Phi_{min} = \frac{1}{\sqrt{2}} \begin{pmatrix} 0 \\ v \end{pmatrix}, \text{with } v = \sqrt{\mu^2 / \lambda}. \qquad (2.7)$$

The vacuum expectation value for $V(\Phi)$ is not zero and there exists a whole set of possible solutions for the vacuum state. The choice of the specific vacuum state above breaks the $SU(2)_L$ symmetry. If one considers excitations of the field Φ around the minima, Φ_{min}, and takes advantage of the SU(2) gauge symmetry, a new field Φ' can be written as:

$$\Phi'(x) = \frac{1}{\sqrt{2}} \begin{pmatrix} 0 \\ v + \eta(x) \end{pmatrix}. \qquad (2.8)$$

Using $\Phi'(x)$ instead of $\Phi(x)$ in the Lagrangian, $\mathcal{L}_{Higgs}$, one ends up with mass terms. The combination of fields associated with the same mass are interpreted as the observed gauge bosons, W^+, W^-, Z and γ:

$$\begin{aligned} W_\mu^+ &= \frac{1}{\sqrt{2}}\left(W_\mu^1 - iW_\mu^2\right), \\ W_\mu^- &= \frac{1}{\sqrt{2}}\left(W_\mu^1 + iW_\mu^2\right), \\ Z_\mu &= \cos\theta_W W_\mu^3 - \sin\theta_W B_\mu, \\ A_\mu &= \sin\theta_W W_\mu^3 + \cos\theta_W B_\mu. \end{aligned} \qquad (2.9)$$

The electroweak mixing angle θ_W is defined by:

$$\cos\theta_W = \frac{m_W}{m_Z} = \frac{g_2}{\sqrt{g_1^2 + g_2^2}}. \tag{2.10}$$

The masses of the bosons are given by:

$$\begin{aligned} m_W &= \frac{1}{2} v g_2, \\ m_Z &= \frac{1}{2} v \sqrt{g_1^2 + g_2^2}, \\ m_\gamma &= 0. \end{aligned} \tag{2.11}$$

The field η is interpreted as a particle (Higgs) with mass given by the vacuum expectation value, v:

$$m_H = \sqrt{2\mu^2}. \tag{2.12}$$

Fermion masses are generated in a similar manner to boson masses. The fermion fields are coupled in a gauge invariant way to the Higgs field, Φ. After symmetry breaking the fermions acquire mass due to the non-vanishing vacuum expectation value of the Higgs field. This additional interaction does not follow from a gauge principle, as was the case for the fermion-boson interaction. Hence, all coupling constants are free parameters, i.e. of Yukawa type. The GSW model does not predict the fermion masses, but it requires proportionality between the Higgs-fermion couplings and the fermion mass. The additional term in the Lagrangian related to the fermion mass generation is denoted with $\mathcal{L}_{Yukawa}$.

The interactions between fermions and bosons can be described by currents. The interaction part of the Lagrangian, $\mathcal{L}_{int}$, is expressed as follows:

$$\begin{aligned} \mathcal{L}_{int} &= -e A_\mu J^\mu_{EC} \\ &\quad - \frac{e}{\sin\theta_W \cos\theta_W} Z_\mu J^\mu_{NC} \\ &\quad - \frac{e}{\sqrt{2}\sin\theta_W}(W^+_\mu J^{+\mu}_{CC} + W^-_\mu J^{-\mu}_{CC}), \end{aligned} \tag{2.13}$$

where the electromagnetic(EC), neutral(NC) and charged(CC) currents are defined by:

$$\begin{aligned} J^\mu_{EC} &= \bar{\psi}\gamma^\mu Q \psi, \\ J^\mu_{NC} &= \bar{\psi}\gamma^\mu (T_3 - Q\sin^2\theta_W)\psi, \\ J^{\pm\mu}_{CC} &= \bar{\psi}\gamma^\mu (T_1 \pm i T_2)\psi. \end{aligned} \tag{2.14}$$

e denotes the electromagnetic coupling constant:

$$e = \frac{g_1 g_2}{\sqrt{g_1^2 + g_2^2}}. \tag{2.15}$$

The neutral weak current, J^{μ}_{NC}, can be expressed for a certain fermion, f, in the following form:

$$J^{\mu}_{NC} = \frac{1}{2}\bar{\psi}\gamma^{\mu}(g^f_V - g^f_A\gamma_5)\psi, \tag{2.16}$$

where the vector and axial-vector current couplings of the neutral current, g^f_V and g^f_A respectively, are defined by:

$$\begin{aligned} g^f_V &= T^f_3 - 2Q_f \sin^2\theta_W, \\ g^f_A &= T^f_3. \end{aligned} \tag{2.17}$$

The neutral weak current interaction is a unique feature of the electroweak Standard Model. Its discovery [4] therefore strongly supported the model.

The free parameters of the GSW model are the coupling constants for the group $SU(2)_L \times U(1)_Y$, g_1 and g_2, the vacuum expectation value of the Higgs potential, v, the mass of the Higgs, m_H, the fermion masses, m_f, and the linear independent elements of the CKM matrix [1]. The first three parameters are usually replaced by experimentally measurable quantities:

$$g_1,\ g_2,\ v \rightarrow \alpha,\ m_W,\ m_Z, \tag{2.18}$$

using Equations 2.11 and 2.15. The fine structure constant $\alpha = e^2 / 4\pi$ is precisely known from the Thomson limit of Compton scattering. Another very accurately measured quantity is the Fermi Constant, G_μ, from the muon decay lifetime. This can be related to m_W, because in the low energy limit the GSW model must be equivalent with the Fermi four point interaction [5]:

$$G_\mu = \frac{\pi\alpha}{\sqrt{2}}\frac{1}{m^2_W \sin^2\theta_W} = \frac{\pi\alpha}{\sqrt{2}}\frac{1}{m^2_Z\cos^2\theta_W \sin^2\theta_W}. \tag{2.19}$$

Since the numerical precision of G_μ is higher than that of m_W, it is often used instead of the latter. The masses of all fermions, apart from the t quark [2], are known. In the boson sector the Higgs boson has not been discovered.

It is the aim of LEP to determine precisely the properties of the Z boson. Therefore, a possible choice for the remaining unknown parameters of the electroweak Standard Model for physics in the vicinity of the Z pole are:

$$m_Z,\ m_H,\ m_t, \tag{2.20}$$

where the latter denotes the mass of the t quark [3].

---

[1] The isospin eigenstates of the d', s', b' quarks are not identical with their mass eigenstates d, s, b. The transformation between the symmetry and the mass eigenstates is described by the Cabibbo-Kobayashi-Maskawa (CKM) mixing matrix.

[2] The CDF collaboration reported recently experimental evidence for t-quark production in $p\bar{p}$ collisions at $\sqrt{s} = 1.8$ TeV [6].

[3] An additional free parameter is the strong coupling constant, α_s, which is related to the strong quark-gluon interactions. The theory of these interactions, Quantum Chromodynamics (QCD), is not further discussed.

2.2 The Process $e^+e^- \rightarrow f\bar{f}$ in the Electroweak Standard Model

The annihilation of an electron-positron pair and its transition to a pair of fermions is described in the Standard Model by the exchange of a photon or Z boson and their interference (see Figure 2.1). In addition to the s-channel process one has to consider

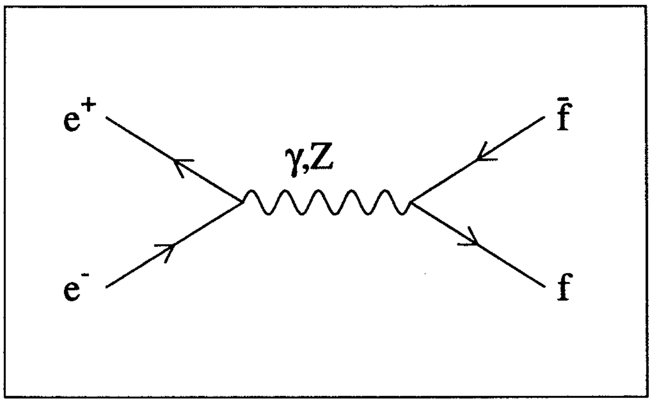

Figure 2.1: S-channel electron-positron scattering.

t-channel scattering if an electron-positron pair is formed in the final state. Since this work concentrates on the process $e^+e^- \rightarrow \tau^+\tau^-$, the t-channel process is not discussed in the following.

For unpolarized electron and positron beams the differential cross section in lowest order of perturbation theory (Born approximation) for the creation of a fermion-antifermion pair, $f\bar{f}$, with helicity $h_f = \pm 1$ reads [7]:

$$\begin{aligned}\frac{d\sigma^0(\cos\theta, s, h_f)}{d\cos\theta} &= \frac{4}{3}\pi\alpha^2 \frac{3c_f}{16s}\Big[A(1+\cos^2\theta) + 2B\cos\theta - \\ &\quad h_f\{C(1+\cos^2\theta) + 2D\cos\theta\}\Big],\end{aligned} \tag{2.21}$$

where c_f denotes the QCD color factor (1 for leptons and 3 for quarks). Fermion masses are neglected for simplicity [4]. θ is the scattering angle between the initial state electron and the final-state fermion f (see Figure 2.2). The coefficients A to D are given by:

[4]For the correct treatment of fermion masses see for example [8]. However, the effect of finite fermion masses, m_f, is of the order m_f^2 / m_Z^2 at LEP. For the heaviest lepton, τ, this amounts to $m_\tau^2 / m_Z^2 \approx 0.0004$.

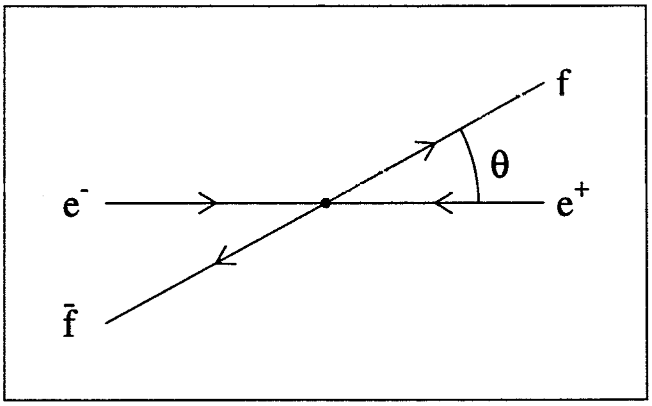

Figure 2.2: Definition of the scattering angle θ.

$$
\begin{aligned}
A(s) &= Q_e^2 Q_f^2 + \left[(g_V^e)^2 + (g_A^e)^2\right]\left[(g_V^f)^2 + (g_A^f)^2\right]|\chi(s)|^2 + 2Q_eQ_f\, g_V^e g_V^f\, \Re e(\chi(s)),\\
B(s) &= 4 g_V^e g_A^e g_V^f g_A^f |\chi(s)|^2 + 2Q_eQ_f\, g_A^e g_A^f\, \Re e(\chi(s)),\\
C(s) &= 2\left[(g_V^e)^2 + (g_A^e)^2\right] g_V^f g_A^f |\chi(s)|^2 + 2Q_eQ_f\, g_V^e g_A^f\, \Re e(\chi(s)),\\
D(s) &= 2 g_V^e g_A^e \left[(g_V^f)^2 + (g_A^f)^2\right]|\chi(s)|^2 + 2Q_eQ_f\, g_A^e g_V^f\, \Re e(\chi(s)),
\end{aligned}
\tag{2.22}
$$

where $\chi(s)$ is:

$$\chi(s) = \frac{1}{4\sin^2\theta_W \cos^2\theta_W}\,\frac{s}{s - m_Z^2 + i m_Z \Gamma_Z}. \tag{2.23}$$

The contribution $Q_e^2 Q_f^2$ to the coefficient A originates from the γ-exchange. The Z-exchange is described by the terms proportional to $|\chi(s)|^2$, while the γZ-interference is given by the terms proportional to $\Re e(\chi(s))$. The width of the Z boson, Γ_Z, is given by the sum of the partial decay widths, Γ_f, over all open fermion flavours:

$$\Gamma_Z = \sum \Gamma_f; \quad f = e, \nu_e, \mu, \nu_\mu, \tau, \nu_\tau, u, d, s, c, b, \tag{2.24}$$

with

$$\Gamma_f = c_f \frac{G_\mu m_Z^3}{6\sqrt{2}\pi}\left[(g_V^f)^2 + (g_A^f)^2\right]. \tag{2.25}$$

The total cross section for a certain helicity state, h_f, in the fiducial volume $c_1 \le \cos\theta \le c_2$ is defined by the integral (for the following discussion see also [9]):

$$
\begin{aligned}
\sigma_{\text{tot}}^0(c_1, c_2, s, h_f) &= \int_{c_1}^{c_2} \frac{d\sigma^0(\cos\theta, s, h_f)}{d\cos\theta} d\cos\theta\\
&= \int_0^{c_2} \frac{d\sigma^0(\cos\theta, s, h_f)}{d\cos\theta} d\cos\theta - \int_0^{c_1} \frac{d\sigma^0(\cos\theta, s, h_f)}{d\cos\theta} d\cos\theta.
\end{aligned}
\tag{2.26}
$$

The forward-backward cross section is defined as the difference between the cross section for particles scattered in forward direction $\cos\theta \geq 0$ and these in backward direction $\cos\theta < 0$:

$$\begin{aligned} \sigma^0_{\text{fb}}(c_1, c_2, s, h_f) &= \int_0^{c_2} \frac{d\sigma^0(\cos\theta, s, h_f)}{d\cos\theta} d\cos\theta - \int_{c_1}^{0} \frac{d\sigma^0(\cos\theta, s, h_f)}{d\cos\theta} d\cos\theta \\ &= \int_0^{c_2} \frac{d\sigma^0(\cos\theta, s, h_f)}{d\cos\theta} d\cos\theta + \int_0^{c_1} \frac{d\sigma^0(\cos\theta, s, h_f)}{d\cos\theta} d\cos\theta. \end{aligned} \tag{2.27}$$

Hence, σ_{tot} and σ_{fb} contain only integrals of the following form:

$$\sigma^0(0, c, s, h_f) = \int_0^{c} \frac{d\sigma^0(\cos\theta, s, h_f)}{d\cos\theta} d\cos\theta, \tag{2.28}$$

which can be written as:

$$\sigma^0(0, c, s, h_f) = \frac{1}{2}\left[\sigma^0_{\text{tot}}(c, s, h_f) + \sigma^0_{\text{fb}}(c, s, h_f)\right]. \tag{2.29}$$

$\sigma_{\text{tot}}(c, s, h_f)$ and $\sigma_{\text{fb}}(c, s, h_f)$ are the cross sections defined in Equations 2.26 and 2.27, respectively, but with symmetric integration limits $c_1 = -c$ and $c_2 = c$. Since the $\cos\theta$ integration is symmetric for the total cross section and asymmetric for the forward-backward cross section, only terms even and odd in $\cos\theta$ respectively, contribute to the final result. Therefore, the $\cos\theta$ integration can be treated independently:

$$\begin{aligned} \sigma^0_{\text{tot}}(c, s, h_f) &= \sigma^0_{\text{tot}}(s, h_f)\, \mathrm{C}_{\text{tot}}(c), \\ \sigma^0_{\text{fb}}(c, s, h_f) &= \sigma^0_{\text{fb}}(s, h_f)\, \mathrm{C}_{\text{fb}}(c), \end{aligned} \tag{2.30}$$

where $\sigma^0_{\text{tot}}(s, h_f)$ and $\sigma^0_{\text{fb}}(s, h_f)$ are the cross sections for the total volume ($c = 1$):

$$\begin{aligned} \sigma^0_{\text{tot}}(s, h_f) &= \frac{4}{3}\pi\alpha^2 \frac{c_f}{2s}(A - h_f C), \\ \sigma^0_{\text{fb}}(s, h_f) &= \frac{4}{3}\pi\alpha^2 \frac{c_f}{2s}(B - h_f D). \end{aligned} \tag{2.31}$$

The functions $\mathrm{C}_{\text{tot}}(c)$ and $\mathrm{C}_{\text{fb}}(c)$ contain the result of the $\cos\theta$ integration and the normalization factor 3/4:

$$\begin{aligned} \mathrm{C}_{\text{tot}}(c) &= \frac{\int_{-c}^{c}(1+\cos^2\theta)\, d\cos\theta}{\int_{-1}^{1}(1+\cos^2\theta)\, d\cos\theta} &&= \frac{3}{4}(c + \frac{c^3}{3}), \\ \mathrm{C}_{\text{fb}}(c) &= \frac{\int_0^{c}\cos\theta\, d\cos\theta - \int_{-c}^{0}\cos\theta\, d\cos\theta}{\int_0^{1}\cos\theta\, d\cos\theta - \int_{-1}^{0}\cos\theta\, d\cos\theta} &&= \frac{3}{4}c^2. \end{aligned} \tag{2.32}$$

Using the notations above, the total cross section and the forward-backward cross section are determined by summing over $h_f = \pm 1$:

$$\begin{aligned}
&\sigma^0_{\mathrm{tot,fb}}(c_1,c_2,s)\\
&= \sigma^0_{\mathrm{tot,fb}}(c_1,c_2,s,h_f=+1)+\sigma^0_{\mathrm{tot,fb}}(c_1,c_2,s,h_f=-1)\\
&= \frac{1}{2}\left[\sigma^0_{\mathrm{tot}}(s,h_f=+1)+\sigma^0_{\mathrm{tot}}(s,h_f=-1)\right]\left[\mathrm{C_{tot}}(c_2)\mp \mathrm{C_{tot}}(c_1)\right]+ \\
&\quad \frac{1}{2}\left[\sigma^0_{\mathrm{fb}}(s,h_f=+1)+\sigma^0_{\mathrm{fb}}(s,h_f=-1)\right]\left[\mathrm{C_{fb}}(c_2)\mp \mathrm{C_{fb}}(c_1)\right]\\
&= \frac{4}{3}\pi\alpha^2\,\frac{c_f}{2s}\left\{A\left[\mathrm{C_{tot}}(c_2)\mp \mathrm{C_{tot}}(c_1)\right]+\frac{3}{8}B\left[\mathrm{C_{fb}}(c_2)\mp \mathrm{C_{fb}}(c_1)\right]\right\}.
\end{aligned} \tag{2.33}$$

The polarization cross section and forward-backward-polarization cross section are defined by:

$$\begin{aligned}
&\sigma^0_{\mathrm{pol,fb-pol}}(c_1,c_2,s)\\
&= \sigma^0_{\mathrm{tot,fb}}(c_1,c_2,s,h_f=+1)-\sigma^0_{\mathrm{tot,fb}}(c_1,c_2,s,h_f=-1)\\
&= \frac{1}{2}\left[\sigma^0_{\mathrm{tot}}(s,h_f=+1)-\sigma^0_{\mathrm{tot}}(s,h_f=-1)\right]\left[\mathrm{C_{tot}}(c_2)\mp \mathrm{C_{tot}}(c_1)\right]+ \\
&\quad \frac{1}{2}\left[\sigma^0_{\mathrm{fb}}(s,h_f=+1)-\sigma^0_{\mathrm{fb}}(s,h_f=-1)\right]\left[\mathrm{C_{fb}}(c_2)\mp \mathrm{C_{fb}}(c_1)\right]\\
&= -\frac{4}{3}\pi\alpha^2\,\frac{c_f}{2s}\left\{C\left[\mathrm{C_{tot}}(c_2)\mp \mathrm{C_{tot}}(c_1)\right]+\frac{3}{8}D\left[\mathrm{C_{fb}}(c_2)\mp \mathrm{C_{fb}}(c_1)\right]\right\}.
\end{aligned} \tag{2.34}$$

Usually the cross sections σ_{fb}, σ_{pol} and $\sigma_{\mathrm{fb-pol}}$ are not measured experimentally, rather the corresponding asymmetries:

$$\mathcal{A}_A = \frac{\sigma_A}{\sigma_{\mathrm{tot}}};\; A = \mathrm{fb,pol,fb-pol}. \tag{2.35}$$

The main dependence of the total cross section and the three asymmetries from the vector and axial-vector couplings at the Z resonance is given by:

$$\begin{aligned}
\sigma_{\mathrm{tot}} &\propto \left[(g^{\mathrm{e}}_{\mathrm{A}})^2+(g^{\mathrm{e}}_{\mathrm{V}})^2\right]\left[(g^{f}_{\mathrm{A}})^2+(g^{f}_{\mathrm{V}})^2\right],\\
\mathcal{A}_{\mathrm{fb}} &\propto \frac{g^{\mathrm{e}}_{\mathrm{A}}g^{\mathrm{e}}_{\mathrm{V}}g^{f}_{\mathrm{A}}g^{f}_{\mathrm{V}}}{\left[(g^{\mathrm{e}}_{\mathrm{A}})^2+(g^{\mathrm{e}}_{\mathrm{V}})^2\right]\left[(g^{f}_{\mathrm{A}})^2+(g^{f}_{\mathrm{V}})^2\right]},\\
\mathcal{A}_{\mathrm{pol}} &\propto \frac{g^{f}_{\mathrm{A}}g^{f}_{\mathrm{V}}}{\left[(g^{f}_{\mathrm{A}})^2+(g^{f}_{\mathrm{V}})^2\right]},\\
\mathcal{A}_{\mathrm{fb-pol}} &\propto \frac{g^{\mathrm{e}}_{\mathrm{A}}g^{\mathrm{e}}_{\mathrm{V}}}{\left[(g^{\mathrm{e}}_{\mathrm{A}})^2+(g^{\mathrm{e}}_{\mathrm{V}})^2\right]}.
\end{aligned} \tag{2.36}$$

Thus, the total cross section and the forward-backward asymmetry depend on the couplings of the initial state and the final state fermions, while the polarization asymmetries depend only on the couplings of one fermion flavor. Therefore, it is possible to test lepton universality by measuring both polarization asymmetries in one final state only.

Furthermore, since $\mathcal{A}_{\text{pol}}$ and $\mathcal{A}_{\text{fb-pol}}$ are linear in the couplings one can determine the relative sign of g_V^e, g_A^e and g_V^f, g_A^f. However, if one chooses the sign of one coupling constant, i.e. $g_A^e < 0$, then the sign of g_V^e is fixed by the measurement of $\mathcal{A}_{\text{fb-pol}}$. Now one can determine also with $\mathcal{A}_{\text{fb}}$ the relative sign of g_A^f and g_V^f, but it is not possible to get the absolute signs for g_A^f and g_V^f by measuring σ_{tot}, $\mathcal{A}_{\text{fb}}$, $\mathcal{A}_{\text{pol}}$ and $\mathcal{A}_{\text{fb-pol}}$ only at the Z pole. In fact, it is not possible to distinguish vector and axial-vector couplings, since the Equations 2.36 are symmetric for an exchange between vector and axial-vector couplings. Therefore, measurements at off peak-energies are required. The center-of-mass energy, $\sqrt{s}$, dependence of the asymmetries is mainly given by the γZ-interference terms, j_A^f. Their dependence on the couplings reads:

$$\begin{aligned} j_{\text{tot}}^f &\propto g_V^e g_V^f, \\ j_{\text{fb}}^f &\propto g_A^e g_A^f, \\ j_{\text{pol}}^f &\propto g_V^e g_A^f, \\ j_{\text{fb-pol}}^f &\propto g_A^e g_V^f. \end{aligned} \tag{2.37}$$

These relations are not symmetric for vector and axial-vector couplings and the ambiguity between $g_A$and g_V can be resolved. Furthermore, the unknown sign of g_V^f and g_A^f can be determined by the sign of j_A^f, since g_V^e and g_A^e are already fixed. The sign of the interference terms is related to the slope of the $\sqrt{s}$ dependence of the asymmetries, $j_A^f \Re e(\chi(s)) \approx j_A^f(s - m_Z^2)$.

According to Equation 2.34, in order to measure polarization asymmetries one has to determine the helicity state of the final-state fermion. This is possible if the fermion decays inside the detector. Then the helicity of the mother fermion can be extracted by analyzing its decay particles. The only lepton with such a lifetime that it decays inside the detector is the τ. Thus, the leptonic decay mode where the full potential of the neutral current process $e^+e^- \to f\bar{f}$ can be exploited is $e^+e^- \to \tau^+\tau^-$.

The total cross section and the asymmetries also depend on the coupling of the photon to fermions, $\alpha(s)$. The decay of the τ is accompanied by a W boson. The photon and W-boson couplings have been studied at lower energies and found to be in agreement with the Standard Model. Since this thesis is devoted to the measurement of the Z boson couplings, the predictions of the Standard Model are always used for the photon and W-boson couplings

2.3 Radiative corrections

To compare the experimental measurements of cross sections and asymmetries with the theoretical predictions the precision of the Born approximation is not sufficient. Therefore, one has to include higher order corrections. The most important corrections are (see Figure 2.3):

- real photon Bremsstrahlung;
- photon and Z boson vacuum polarization;

- vertex corrections.

Feynman diagrams containing closed loops lead to divergences in observable quantities. These divergences can be removed by renormalizing the basic parameters of the Lagrangian. The remaining finite corrections to the Born level predictions can be split into two categories:

- QED corrections. This set includes diagrams with real photon emissions, i.e. Bremsstrahlung. The corrections are large in the vicinity of the Z resonance and precisely known.

- Electroweak corrections. This set contains one-loop corrections to the photon and Z boson propagator and vertex corrections. The corrections are small. Some of them are sensitive to the mass of the Higgs and the t quark.

Theoretically the QED corrections can be treated independently, because the corresponding diagrams form a gauge invariant subset in $O(\alpha)$. Another justification for the splitting is that the inclusion of QED corrections can give more than two final-state particles. It depends on the acceptance of the detector, whether these radiated photons are detected or not. Therefore, one has to consider additional photons and the acceptance and resolution of the detector in the calculation of cross sections. This causes significant differences from the Born level results. QED corrections are treated by convoluting the Born cross section, σ_A^0, with a radiator function R:

$$\sigma_A(s) = \int_{4m_f/s}^{1} dz \sigma_A^0(z) R_A(z,s), \tag{2.38}$$

where z is the remaining center-of-mass energy after the photon is radiated. At energies near the Z resonance initial state radiation gives the largest effect on the cross section, while the contribution from final state radiation is much smaller.

Electroweak corrections contain only loop diagrams. Thus, the number of final state particles remains two and the cross section after applying electroweak corrections still has a Born-like form. These corrections are almost independent of the experimental setup. Self-energy insertions to the photon propagator yield a center-of-mass energy, $\sqrt{s}$, dependent electromagnetic fine-structure constant:

$$\alpha \rightarrow \alpha(s) = \frac{\alpha}{1-\Delta\alpha(s)}. \tag{2.39}$$

Self-energy insertions to the Z boson propagator are taken into account by a $\sqrt{s}$ dependent Z width:

$$\Gamma_Z \quad \rightarrow \quad \Gamma_Z(s) = \frac{s}{m_Z^2}\Gamma_Z, \tag{2.40}$$

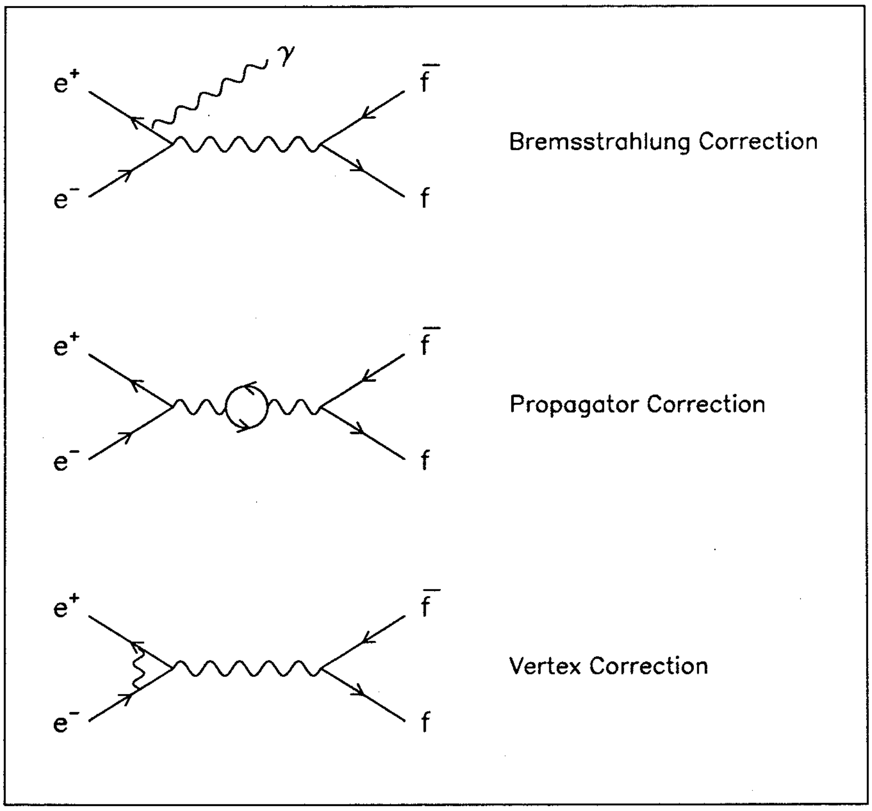

Figure 2.3: Examples for the most important Feynman diagrams containing radiative corrections.

These corrections are independent of the fermion flavor. Vertex corrections are incorporated by $\sqrt{s}$ dependent vector and axial-vector coupling constants:

$$\begin{aligned} g_A^f &\rightarrow g_A^f(s) = \sqrt{\rho^f(s)}\,T_3^f, \\ g_V^f &\rightarrow g_V^f(s) = \sqrt{\rho^f(s)}\,\left[T_3^f - 2\kappa_f(s)Q_f \sin^2\theta_W\right]. \end{aligned} \tag{2.41}$$

In summary, the electroweak corrections are taken into account by replacing the constant quantities α, Γ_Z g_A^f and g_V^f by the $\sqrt{s}$ dependent quantities in the Born formula of Equation 2.21. This replacement leaves the functional form of the Born cross section unchanged and the result is therefore called the *improved Born approximation*. Another source of electroweak corrections are box diagrams with double vector boson exchange. Since these diagrams are not resonant, their contributions at center-of-mass energies near the Z mass are small. The effect of radiative corrections on the total cross section and the three asymmetries, defined in Equation 2.35, can be seen in Figure 2.4.

The relation between G_μ and m_W (see Equation 2.19) is also affected by radiative corrections:

$$G_\mu = \frac{\pi\alpha}{\sqrt{2}} \frac{1}{m_Z^2 \cos^2\theta_W \sin^2\theta_W} \frac{1}{1-\Delta r}. \tag{2.42}$$

Δr contains QED and electroweak corrections:

$$\Delta r = \Delta\alpha - \left(\frac{\cos^2\theta_W}{\sin^2\theta_W}\Delta\rho\right) + \ldots\ . \tag{2.43}$$

The leading term of $\Delta\rho$ depends on the mass of the t quark, m_t:

$$\Delta\rho = \frac{3G_\mu m_t^2}{8\sqrt{2}\pi^2}. \tag{2.44}$$

At LEP it is therefore possible to constrain the value of the t-quark mass by measuring cross sections and asymmetries with a precision that electroweak corrections become significant.

2.4 The τ Lepton

The τ lepton was discovered 1975 by Perl *et al.* [10] as an enhancement of lepton production in the reaction $e^+e^- \rightarrow \ell^+\ell^-$ at the SLAC colliding beams facility, SPEAR. The authors found events of the form $e^+e^- \rightarrow e^\pm\mu^\pm$ + missing energy. Most of these events are detected at center-of-mass energies at or above 4 GeV. A possible explanation for these events was the pair production of a heavy lepton, ℓ, or a charged boson, B, which further decays into

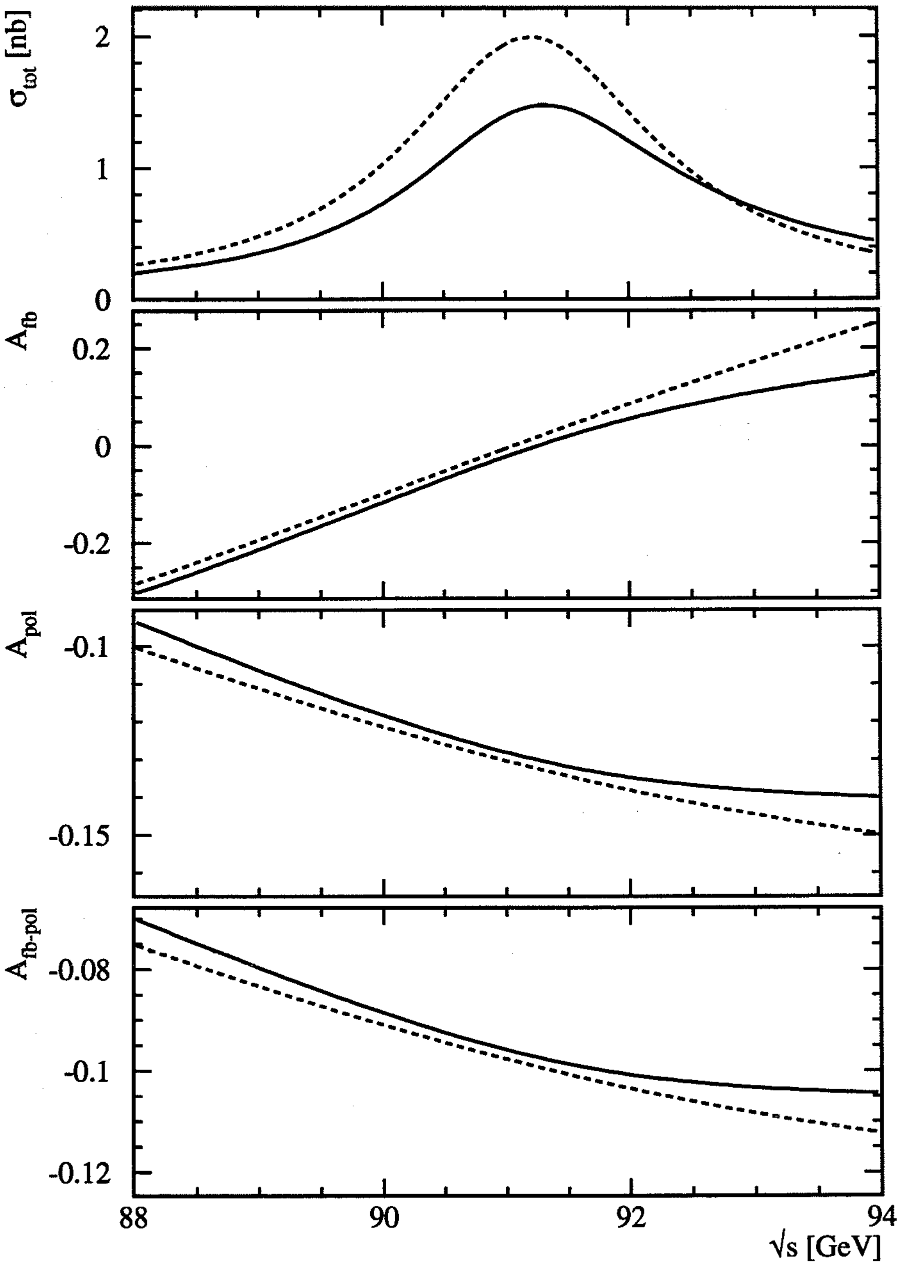

Figure 2.4: The total cross section and the asymmetries in the vicinity of the Z pole with (solid line) and without (dashed line) radiative corrections for the process $e^+e^- \to \ell^+\ell^-$.

lighter leptons, the electron and muon:

$$\begin{aligned} \ell &\rightarrow e\nu_e\nu_\ell, \\ \ell &\rightarrow \mu\nu_e\nu_\mu, \\ B &\rightarrow e\nu_e, \\ B &\rightarrow \mu\nu_\mu. \end{aligned}$$

The discovery was confirmed by the DASP collaboration at the DORIS e^+e^- storage ring [11]. Their measurement of the $e^+e^- \rightarrow \ell^+\ell^-$ cross section near threshold suggested that the new particle, the τ, is a fermion and not a boson. The τ, as the heaviest known lepton, belongs therefore to the third fermion generation (see Table 2.1). The best value for the mass of the τ,

$$m_\tau = 1776.9^{+0.4}_{-0.5} \pm 0.2\,\text{MeV}, \tag{2.45}$$

was obtained by the BES collaboration [12]. Since the τ is heavy, its lifetime is very short ($\tau_\tau \propto m_\tau^{-5}$). The mean value for the lifetime measured by the four LEP collaborations is [13]:

$$\tau_\tau = 292.2 \pm 2.4\,\text{fs}. \tag{2.46}$$

The τ lepton decays by the charged current process into the corresponding τ neutrino, ν_τ, and a W boson. The W boson further decays into two particles belonging to a weak isospin doublet (see Figure 2.5). Since the τ has a high mass, possible doublets are (e, ν_e),

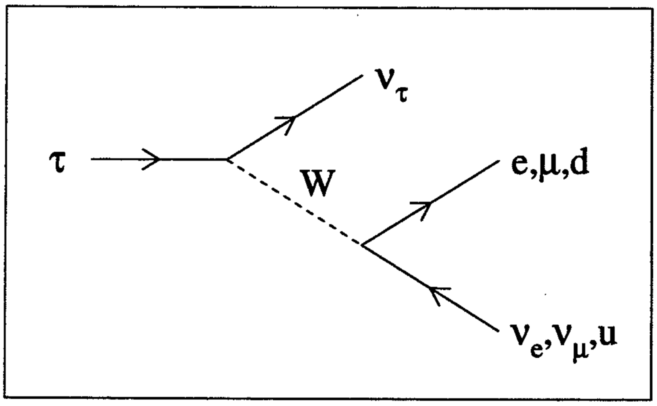

Figure 2.5: The decay of the τ lepton.

(μ, ν_μ) and (u, d'). d' is a mixture of the d and s-quark mass eigenstates. Therefore, the τ decays also into strange mesons (kaons). The selection of τ-decay modes, described in this thesis, will not distinguish between pions and kaons and these decay modes are treated in common. The current world averages of branching ratios for important τ-decay modes [5] are listed in Table 2.2 [14].

Decay Mode	Branching Ratio [%]
$\tau \rightarrow e\nu\nu$	17.93±0.26
$\tau \rightarrow \mu\nu\nu$	17.58±0.27
$\tau \rightarrow \pi\nu$	11.6 ±0.4
$\tau \rightarrow \rho\nu \rightarrow \pi\pi^0\nu$	24.0 ±0.6
$\tau \rightarrow a_1\nu \rightarrow \pi\pi^0\pi^0\nu$	10.3 ±0.9
$\tau \rightarrow a_1\nu \rightarrow \pi\pi\pi\nu$	8.4 ±0.4

Table 2.2: Branching ratios of the τ lepton.

The τ is the only lepton, which decays inside the detector. The electron is stable and the lifetime of the muon is such that it normally leaves the detector before it decays. Therefore, the τ decay offers the unique possibility to analyze its polarization by measuring the distribution of its decay particles.

[5] Only these decay modes are listed where a polarization measurement is performed which is described in Section 6.6. .

Chapter 3

Model Independent Approaches to the Process $e^+e^- \to f\bar{f}$

In this chapter three "model independent" ansatzes are introduced: the S-matrix, effective coupling and partial width approaches. The term "model independent" in this context means that no special assumptions about the weak part of the process, i.e. the Z-exchange and the γZ-interference, are made. QED is assumed to be known. Therefore, the electromagnetic coupling constant, $\alpha(s)$, is not considered as a free parameter. Initial and final state radiation can be taken into account by convolution, as described in the previous chapter. Weak corrections are not applied. Hence, the free parameters of the model independent approaches are effective ones. Since the integration of a differential cross section in $\cos\theta$ can be treated independently from the matrix element related part (see Equation 2.30), only Born cross sections in 4π are given.

Two different definitions of the mass, m_Z, and the total width, Γ_Z, of the Z boson are used in this chapter. In the improved Born approximation the total width of the Z boson is defined as $\sqrt{s}$ dependent in the propagator function:

$$\mathcal{K}(s) = \frac{s}{s - m_Z^2 + i\, m_Z \Gamma_Z(s)}, \tag{3.1}$$

with $\Gamma_Z(s)$ from Equation 2.40. The $\sqrt{s}$ dependence of Γ_Z is a result of self-energy corrections in the Z propagator. This definition is used, following the literature (i.e. [15]), for the effective coupling and partial width approaches. Γ_Z is assumed to be constant in the S-matrix approach [16], where the position of the pole of an unstable particle in the complex energy plane is defined by two constants, its mass and width:

$$\overline{\mathcal{K}}(s) = \frac{s}{s - \overline{m}_Z^2 + i\, \overline{m}_Z \overline{\Gamma}_Z}. \tag{3.2}$$

This leads to a shift of the parameter values between these two definitions of:

$$\begin{aligned} \overline{m}_Z &= [1 + (\Gamma_Z / m_Z)^2]^{-\frac{1}{2}} m_Z \approx m_Z - 34\ \text{MeV}, \\ \overline{\Gamma}_Z &= [1 + (\Gamma_Z / m_Z)^2]^{-\frac{1}{2}} \Gamma_Z \approx \Gamma_Z - 1\ \text{MeV}. \end{aligned} \tag{3.3}$$

For more details refer to the discussions in [17, 18].

3.1 The S-Matrix Approach

In [16, 19] a model independent approach is proposed to describe cross sections and asymmetries in e^+e^-annihilation. It relies only on basic quantum mechanical assumptions such as the unitarity and analyticity of the S-matrix. No assumptions are made about the dynamics of the scattering process.

The matrix element for the exchange of a massless and a massive vector boson, the photon and Z boson respectively, in the annihilation of a massless e^+e^- pair into massless fermions, f, can be written as:

$$\mathcal{M}^{fi}(s) = \frac{\mathrm{R}^f_\gamma}{s} + \frac{\mathrm{R}^{fi}_\mathrm{Z}}{s - s_Z} + \sum_{n=0}^{\infty} \mathrm{F}^{fi}_n (s - s_Z)^n; \quad i = 0, 3; \tag{3.4}$$

with

$$s_Z = \overline{m}_Z^2 + i\,\overline{m}_Z\overline{\Gamma}_Z.$$

R^f_γ and $\mathrm{R}^{fi}_\mathrm{Z}$ are the residuals of the photon and the Z boson respectively. The position of the pole is given by s_Z. R^f_γ is defined by:

$$\mathrm{R}^f_\gamma = \frac{\alpha(s)}{\alpha} Q_e Q_f. \tag{3.5}$$

Q_f is the charge of the corresponding fermion and $\alpha(s)$ the running QED coupling constant. The residuals $\mathrm{R}^{fi}_\mathrm{Z}$ describe the four complex helicity amplitudes for the Z-exchange, which are defined by the spins of all fermions taking into account helicity conservation:

$$\begin{aligned}
\mathrm{R}^{f0}_\mathrm{Z} &= \mathrm{R}_\mathrm{Z}(e^-_L e^+_R \to f^-_L f^+_R), \\
\mathrm{R}^{f1}_\mathrm{Z} &= \mathrm{R}_\mathrm{Z}(e^-_L e^+_R \to f^-_R f^+_L), \\
\mathrm{R}^{f2}_\mathrm{Z} &= \mathrm{R}_\mathrm{Z}(e^-_R e^+_L \to f^-_R f^+_L), \\
\mathrm{R}^{f3}_\mathrm{Z} &= \mathrm{R}_\mathrm{Z}(e^-_R e^+_L \to f^-_L f^+_R).
\end{aligned} \tag{3.6}$$

The coefficients, F^{fi}_n, of the Taylor expansion in Equation (3.4) describe non-resonant contributions to the scattering process. As shown in reference [16] these are numerically small around the Z resonance and neglected in the following. The cross sections, σ_i, derived from $\mathcal{M}^{fi}$ are combined to four linearly independent cross sections, which are observable at LEP:

$$\begin{aligned}
\sigma^0_\mathrm{tot}(s) &= +\,\sigma_0(s) + \sigma_1(s) + \sigma_2(s) + \sigma_3(s) = \sigma^0_\mathrm{tot}(s, h_f = +1) + \sigma^0_\mathrm{tot}(s, h_f = -1), \\
\sigma^0_\mathrm{fb}(s) &= +\,\sigma_0(s) - \sigma_1(s) + \sigma_2(s) - \sigma_3(s) = \sigma^0_\mathrm{fb}(s, h_f = +1) + \sigma^0_\mathrm{fb}(s, h_f = -1), \\
\sigma^0_\mathrm{pol}(s) &= -\,\sigma_0(s) + \sigma_1(s) + \sigma_2(s) - \sigma_3(s) = \sigma^0_\mathrm{tot}(s, h_f = +1) - \sigma^0_\mathrm{tot}(s, h_f = -1), \\
\sigma^0_\mathrm{fb-pol}(s) &= -\,\sigma_0(s) - \sigma_1(s) + \sigma_2(s) + \sigma_3(s) = \sigma^0_\mathrm{fb}(s, h_f = +1) - \sigma^0_\mathrm{fb}(s, h_f = -1).
\end{aligned} \tag{3.7}$$

For comparison, the dependence of the cross sections $\sigma^0_\mathrm{tot}(s, h_f)$ and $\sigma^0_\mathrm{fb}(s, h_f)$ introduced in Equation 2.31 is given as well. The cross sections, σ_A, can be parameterized as follows:

$$\sigma^0_A(s) = \frac{4}{3}\pi\alpha^2 \left[\frac{r^{\gamma f}_A}{s} + \frac{s r^f_A + (s - \overline{m}_Z^2) j^f_A}{(s - \overline{m}_Z^2)^2 + \overline{m}_Z^2 \overline{\Gamma}_Z^2} \right]; \quad A = \mathrm{tot}, \mathrm{fb}, \mathrm{pol}, \mathrm{fb-pol}, \tag{3.8}$$

where $r_A^{\gamma,f}$ is the γ-exchange term:

$$r_A^{\gamma,f} = \begin{cases} c_f \left|R_\gamma^f\right|^2 & \text{if } A = \text{tot} \\ 0 & \text{if } A \neq \text{tot}. \end{cases} \tag{3.9}$$

$r_A^{\gamma,f}$ is equal to zero for all asymmetric cross sections as a consequence of Equation 3.4, because R_γ^f has the same value and sign for all four helicity amplitudes. The Z-exchange term, r_A^f, and the γZ-interference term, j_A^f, are given by:

$$\begin{aligned} r_A^f &= c_f \left\{ \frac{1}{4} \sum_{i=0}^{3} \{\pm 1\} \left|R_Z^{fi}\right|^2 + 2\frac{\overline{\Gamma}_Z}{\overline{m}_Z} \Im\mathrm{m} C_A^f \right\}, \\ j_A^f &= c_f \left\{ 2\Re\mathrm{e} C_A^f - 2\frac{\overline{\Gamma}_Z}{\overline{m}_Z} \Im\mathrm{m} C_A^f \right\}, \\ C_A^f &= (R_\gamma^f)^* \left(\frac{1}{4} \sum_{i=0}^{3} \{\pm 1\} R_Z^{fi} \right), \end{aligned} \tag{3.10}$$

where $\{\pm 1\}$ indicates that the sign of $\left|R_Z^{fi}\right|^2$ and R_Z^{fi} corresponds to the sign of σ_i in Equation (3.7).
Asymmetries are defined according to Equation 2.35.

It follows from the formalism, that there are in general two alternative sets of free parameters to derive cross sections and asymmetries in the S-matrix approach:

1. $\overline{m}_Z$, $\overline{\Gamma}_Z$ and R_Z^{fi},
2. $\overline{m}_Z$, $\overline{\Gamma}_Z$, r_A^f and j_A^f.

Since each cross section, σ_A, depends on all four helicity amplitudes, it is not possible to determine a subset of helicity amplitudes. Therefore, one has to measure the total cross section and all asymmetries, if one wants to determine the R_Z^{fi}. Thus, the maximum number of free parameters of the first set is eight. The r_A^f and j_A^f parameters of the second set belong only to one specific cross section, σ_A, and it is possible to determine r_A^f and j_A^f by only measuring σ_A or $\mathcal{A}_A$ as a function of $\sqrt{s}$. Nevertheless, by measuring the total cross section and all asymmetries, the number of free parameters is the same as for the first parameter set. Without further assumptions the S-matrix parameters for a given final state, f, are completely independent from other final states.

3.2 The Effective Coupling Approach

In the effective coupling approach it is assumed that the Z boson has only vector and axial-vector couplings to fermions. The couplings of the Standard Model (see Equation

2.41) are replaced by constant effective couplings $\hat{g}^f_V$ and $\hat{g}^f_A$:

$$\begin{aligned} \hat{g}^f_A &= \sqrt{\hat{\rho}^f}\, T^f_3, \\ \hat{g}^f_V &= \sqrt{\hat{\rho}^f}\left[T^f_3 - 2Q_f \sin^2\hat{\theta}^f_W\right]. \end{aligned} \tag{3.11}$$

Higher order weak corrections are approximated by:

$$\begin{aligned} \hat{\rho}^f &= \rho^f(s = m^2_Z), \\ \hat{\kappa}^f &= \kappa^f(s = m^2_Z). \end{aligned} \tag{3.12}$$

Therefore, the effective weak mixing angle, $\sin^2\hat{\theta}_W$, also becomes flavor dependent:

$$\sin^2\hat{\theta}^f_W = \hat{\kappa}^f \sin\theta_W. \tag{3.13}$$

However, the weak form factors, $\hat{\rho}^f$ and $\hat{\kappa}^f$, are equal for all fermions to a good approximation, except for b quarks.

The helicity amplitudes of Equation 3.6 can then be expressed as function of the effective couplings:

$$\begin{aligned} R^{f0}_Z &= \kappa(\hat{g}^e_V + \hat{g}^e_A)(\hat{g}^f_V + \hat{g}^f_A), \\ R^{f1}_Z &= \kappa(\hat{g}^e_V + \hat{g}^e_A)(\hat{g}^f_V - \hat{g}^f_A), \\ R^{f2}_Z &= \kappa(\hat{g}^e_V - \hat{g}^e_A)(\hat{g}^f_V - \hat{g}^f_A), \\ R^{f3}_Z &= \kappa(\hat{g}^e_V - \hat{g}^e_A)(\hat{g}^f_V + \hat{g}^f_A), \end{aligned} \tag{3.14}$$

with

$$\kappa = \frac{G_\mu m^2_Z}{2\sqrt{2}\pi\alpha}. \tag{3.15}$$

The parameters r^f_A and j^f_A of Equation (3.8) are given by:

$$\begin{aligned} r^f_{tot} &= \kappa^2\left[(\hat{g}^e_A)^2 + (\hat{g}^e_V)^2\right]\left[(\hat{g}^f_A)^2 + (\hat{g}^f_V)^2\right] - 2\kappa\hat{g}^e_V\hat{g}^f_V C_{Im}, \\ r^f_{fb} &= 4\kappa^2\hat{g}^e_A\hat{g}^e_V\hat{g}^f_A\hat{g}^f_V - 2\kappa\hat{g}^e_A\hat{g}^f_A C_{Im}, \\ r^f_{pol} &= -\ 2\kappa^2\left[(\hat{g}^e_A)^2 + (\hat{g}^e_V)^2\right]\hat{g}^f_A\hat{g}^f_V + 2\kappa\hat{g}^e_V\hat{g}^f_A C_{Im}, \\ r^f_{fb-pol} &= -\ 2\kappa^2\hat{g}^e_A\hat{g}^e_V\left[(\hat{g}^f_A)^2 + (\hat{g}^f_V)^2\right] + 2\kappa\hat{g}^e_A\hat{g}^f_V C_{Im}, \end{aligned} \tag{3.16}$$

$$\begin{aligned} j^f_{tot} &= 2\kappa\hat{g}^e_V\hat{g}^f_V(C_{Re} + C_{Im}), \\ j^f_{fb} &= 2\kappa\hat{g}^e_A\hat{g}^f_A(C_{Re} + C_{Im}), \\ j^f_{pol} &= -\ 2\kappa\hat{g}^e_V\hat{g}^f_A(C_{Re} + C_{Im}), \\ j^f_{fb-pol} &= -\ 2\kappa\hat{g}^e_A\hat{g}^f_V(C_{Re} + C_{Im}), \end{aligned} \tag{3.17}$$

with

$$
\begin{aligned}
C_{Im} &= |Q_e Q_f| \frac{\Gamma_Z}{m_Z} \Im\mathrm{m} \frac{\alpha(s)}{\alpha}, \\
C_{Re} &= |Q_e Q_f| \Re\mathrm{e} \frac{\alpha(s)}{\alpha}.
\end{aligned}
\tag{3.18}
$$

Using Equations 2.35, 3.8, 3.16, 3.17, neglecting the γ-exchange and taking the correct normalization given in Equation 2.32 the asymmetries on the Z peak read:

$$
\begin{aligned}
\mathcal{A}_{\mathrm{fb}} &= \frac{3\hat{g}_A^e \hat{g}_V^e \hat{g}_A^f \hat{g}_V^f}{\left[(\hat{g}_A^e)^2 + (\hat{g}_V^e)^2\right]\left[(\hat{g}_A^f)^2 + (\hat{g}_V^f)^2\right]} &&= \frac{3}{4}\mathcal{A}_e \mathcal{A}_f, \\
\mathcal{A}_{\mathrm{pol}} &= -\frac{2\hat{g}_A^f \hat{g}_V^f}{\left[(\hat{g}_A^f)^2 + (\hat{g}_V^f)^2\right]} &&= -\mathcal{A}_f, \\
\mathcal{A}_{\mathrm{fb-pol}} &= -\frac{3}{2}\frac{\hat{g}_A^e \hat{g}_V^e}{\left[(\hat{g}_A^e)^2 + (\hat{g}_V^e)^2\right]} &&= -\frac{3}{4}\mathcal{A}_e,
\end{aligned}
\tag{3.19}
$$

with

$$
\mathcal{A}_\ell = 2\frac{\hat{g}_A^\ell \hat{g}_V^\ell}{\left[(\hat{g}_A^\ell)^2 + (\hat{g}_V^\ell)^2\right]}. \tag{3.20}
$$

Note that in this approximation $\mathcal{A}_{\mathrm{fb}} = \mathcal{A}_{\mathrm{pol}} \cdot \mathcal{A}_{\mathrm{fb-pol}}$.

The effective coupling approach has six parameters to describe the process $e^+e^- \rightarrow f\bar{f}$, m_Z, Γ_Z, $\hat{g}_V^e$, $\hat{g}_A^e$, $\hat{g}_V^f$, $\hat{g}_A^f$. Since the effective coupling ansatz originates from a Feynman graph formulation in contrast to the S-matrix approach, the initial state parameters $\hat{g}_V^e$ and $\hat{g}_A^e$ are the same for all decay modes. Hence, they can be determined also in other Z decay processes.

3.3 The Partial Width Approach

The partial width approach describes the scattering process by the creation and the decay of a resonance. The Z-exchange term, r_{tot}^f, reads:

$$
r_{\mathrm{tot}}^f = 9\,\frac{\Gamma_e \Gamma_f}{\alpha^2 m_Z^2}. \tag{3.21}
$$

Γ_e and Γ_f are the partial decay widths of the Z boson into an e^+e^- and an $f\bar{f}$ pair and are given by:

$$
\Gamma_f = \frac{G_\mu m_Z^3}{6\sqrt{2}\pi}\left[(\hat{g}_V^f)^2 + (\hat{g}_A^f)^2\right] = \kappa \frac{m_Z}{3}\alpha\left[(\hat{g}_V^f)^2 + (\hat{g}_A^f)^2\right]. \tag{3.22}
$$

The γZ-interference term, $j^f_{\rm tot}$, cannot be expressed as a function of Γ_e and Γ_f. Possibilities to handle $j^f_{\rm tot}$ in this approach are (see [9]):

- leave $j^f_{\rm tot}$ as a free parameter,
- assuming $j^f_{\rm tot}$ is zero,
- fixing $j^f_{\rm tot}$ to the Standard Model expectation value, given by:

$$j^f_{\rm tot} = 2\kappa g^{\rm e}_{\rm V}(s) g^f_{\rm V}(s)(C_{Re} + C_{Im}). \tag{3.23}$$

The first method is preferred, because it allows to take into account possible correlations of $j^f_{\rm tot}$ with the other parameters of the ansatz.

The partial width approach has four free parameters, $m_{\rm Z}$, $\Gamma_{\rm Z}$, Γ_e, Γ_f and $j^f_{\rm tot}$, which describe the total cross section for $e^+e^- \to f\bar{f}$. Γ_e can be also determined by analyzing other decay channels.

Chapter 4

The L3 Experiment at LEP

4.1 The LEP Collider

The Large Electron Positron collider, LEP [20] at CERN, is located between the Jura mountains and the Geneva airport on both sides of the border between France and Switzerland (see Figure 4.1). LEP is the last part of a chain of accelerators (see Figure 4.2).

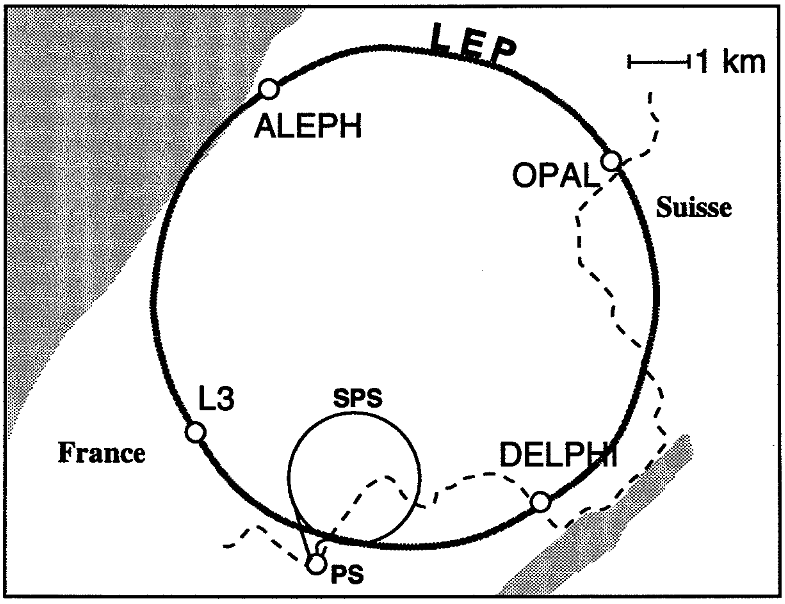

Figure 4.1: The LEP collider at CERN.

Before the electron and positron bunches are injected in LEP, they have to be accumulated and accelerated to 20 GeV. This is done by the following system of accelerators:

- The LEP Injector Linacs (LIL) create electrons and positrons and accelerates them to 600 MeV.

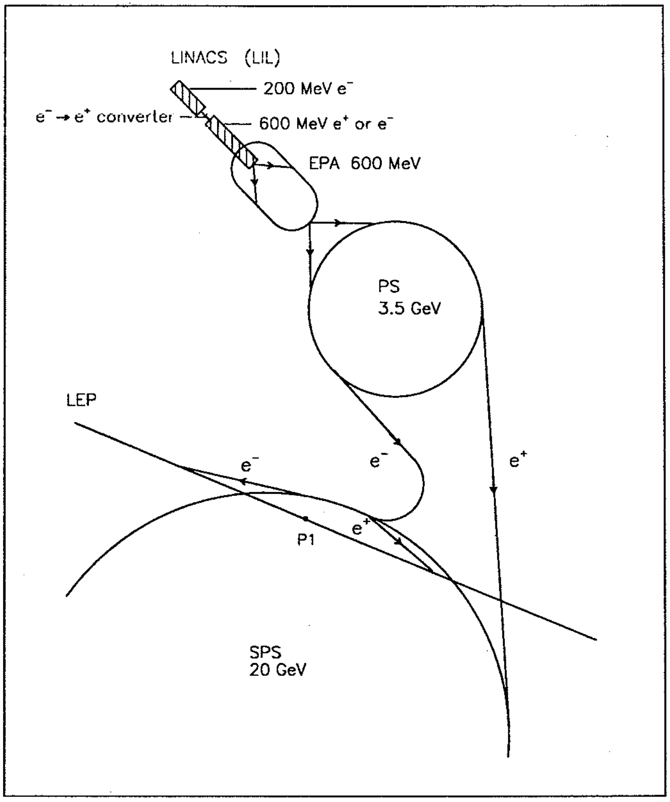

Figure 4.2: The LEP injection setup.

- The Electron Positron Accumulator (EPA) accumulates these particles into bunches.
- The Proton Synchrotron (PS) accelerates the bunches up to 3.5 GeV.
- The Super Proton Synchrotron (SPS) accelerates these bunches to 20 GeVand injects them into the LEP ring.

The LEP collider is in the form of an octagon with rounded corners and a circumference of about 27 km. The circumference is defined by the design energy at which LEP operates and the requirement of a minimal energy loss due to synchrotron radiation. The nominal LEP parameters are listed in Table 4.1 [20]. The main components of the LEP collider are:

- Eight bending sections of 2840 m length each, with a total of 3304 dipole magnets,
- Eight straight sections, four equipped with the experiments ALEPH [21], DELPHI [22], L3 [23] and OPAL [24]. To increase the luminosity the beam is compressed using superconducting quadrupole magnets on each side of an experiment.

Circumference	26658.883 m
RF frequency	352.20904 MHz
RF gradient	1.474 MV/m
Total RF power	16 MW
Number of RF cavities	128
Harmonic Number	31320
Revolution time	88.92446 μs
Number of bunches per beam	4 (8 since August 1992)
Number of interaction points	4
Number of experimental areas	4
Average beam current	3 mA
Horizontal beam radius	300 μm
Vertical beam radius	12 μm
Bunch length	16 mm
Dipole field	0.05 T
Maximum luminosity	1.6×10^{31} cm$^{-2}s^{-1}$
Injection energy	20 GeV

Table 4.1: Nominal LEP parameters

- Two of the straight sections contain the radiofrequency (RF) cavities to accelerate the injected beam to the required collision energy and replace the energy lost by synchrotron radiation.

LEP is currently running at a center-of-mass energy around the Z pole of 91 GeV. In 1990 and up to August 1991 (1991a) LEP ran at 7 different center-of-mass energies in the vicinity of the Z resonance. Since then, until the middle of 1993, LEP has run exclusively on the Z pole. The history of the integrated luminosity delivered to a single LEP experiment is shown in Figure 4.3. Up to the end of 1992 an integrated luminosity of 40.8 pb^{-1} was collected by the L3 experiment. This corresponds in total to 1.2×10^6 Z boson decays.

4.2 The Energy Calibration of LEP

4.2.1 Methods

The mass, m_Z, and the width, Γ_Z, of the Z boson can be measured at LEP with outstanding precision. In order to benefit from the high statistics of the accumulated data sample and the accuracy of the cross section measurements, a precise calibration of the LEP energy is required [25, 26]. Four different methods are used, which also allow for cross-checks between them:

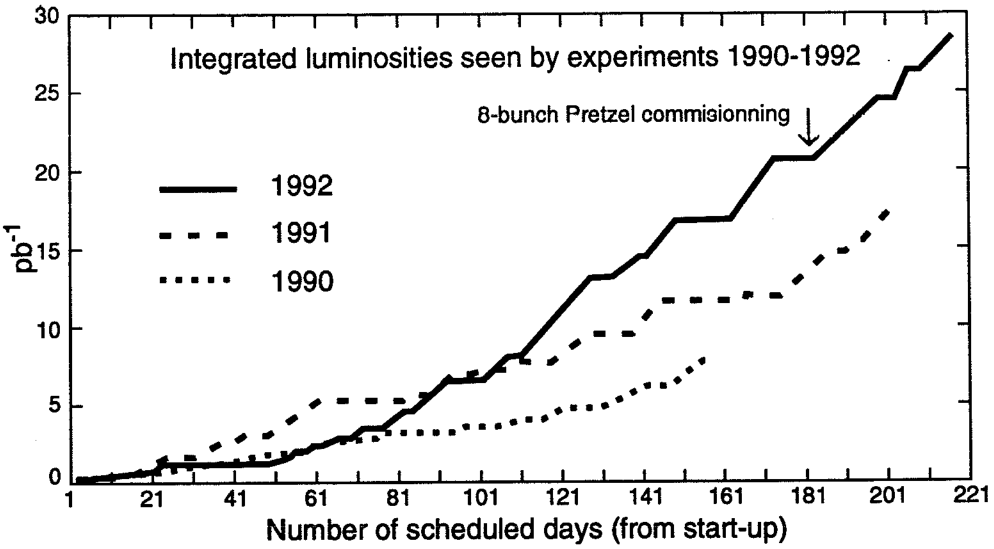

Figure 4.3: Integrated luminosity delivered to a single LEP experiment.

1. The magnetic field in the bending magnets is monitored continuously by measuring the field in a reference magnet. This magnet is connected in series with the LEP ring magnets, but is kept in a well controlled environment with temperature stabilization. The magnetic field strength is determined by measuring the induced current in a flipping coil. The reproducibility of the *field display* measurements is about 2.5×10^{-5}. The results of this method are used as reference and all corrections are performed with respect to them.

2. Each dipole is equipped with a closed loop of copper wire. Altering the dipole current, the induced voltage in the *flux loops* is a direct measurement of the magnetic field with an absolute precision of about 10^{-4}, which corresponds to 6 MeV on the beam energy. However, this method is not sensitive to constant fields and additional bending of the quadrupoles and sextupoles for particles circulating on non-central orbits.

3. The momentum of the circulating particles can be determined from their velocity, if they are not ultra-relativistic. Therefore, *protons* of 20 GeV are injected in LEP with the same magnetic settings as for positrons. The momentum of the protons can be measured by the frequency of the RF cavities. The precision of this measurement is high, but decreases due to the extrapolation to 45 GeV.

4. *Resonant depolarization* uses the fact that the LEP beams can be transversely polarized to a level of more then 30%. The spin precession frequency is measured by superimposing an additional oscillating magnetic field. If the oscillating field has the same or a multiple frequency as the spin precession, beam depolarization occurs. This

frequency is related to the beam energy and allows its most precise measurement close to data taking conditions.

The energy measurements have to be corrected for several systematic effects:

- The dipole cores are filled with cement mortar. Due to dehydration the cores shrink which changes the *flux-loop* response.
- The correlation between the *flux-loop* measurements and the temperature was demonstrated with controlled experiments and the results are used for the temperature correction.
- The *flux-loop* measurements are not sensitive to constant fields. Therefore, they have to be corrected for the earth's magnetic field.
- The electrons and positrons lose about 120 MeV of energy per turn due to synchrotron radiation. This loss is compensated by the RF units at only two points and causes a variation of the mean beam energy around the ring. Furthermore, the distribution of the mean energy of the beams around the ring depends on the actual hardware status of the collider. A fill-to-fill correction, different for each experiment, is applied.
- The tidal forces from the moon and the sun distort the spheroidal shape of the earth. The local change of the earth's radius induces an expansion of the earth crust. The 26.7 km circumference of LEP is changed by about 1 mm. This causes an beam energy change of about 15 MeV from low to high tide. This effect was observed with the *resonant depolarization* measurements (see Figure 4.4 from [27]).

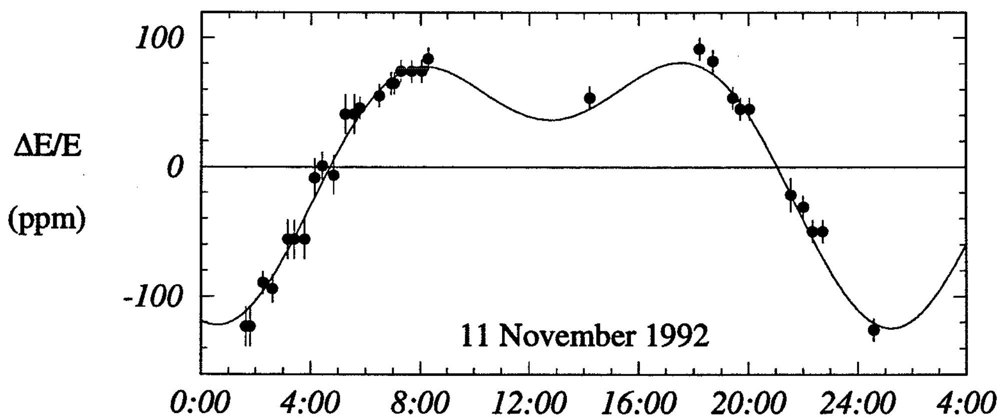

Figure 4.4: Change in energy of the LEP beams measured by resonant depolarization over time. The solid curve is the expected change of energy caused by tidal effects.

4.2.2 Treatment of energy errors

For a precise measurement of the Z resonance one has to know the errors on the corrected LEP energies. To do so, the errors on the energy measurements and the calibrations are combined into four uncorrelated numbers:

- The absolute energy scale, $(\frac{\Delta E}{E})_{abs}$, which is defined by *resonant depolarization* at the energy E_{cal}.
- The local energy-scale error, $\Delta\alpha$, accounts for the uncertainty of the local energy, E_{loc}, which is measured with *flux loop*. This error is proportional to the difference between E_{loc} and E_{cal}.
- The energy-point-to-energy-point error, $(\frac{\Delta E}{E})^{set}_{p-t-p}$, takes into account higher order effects in the relation of the *field display* and the magnetic field in the dipoles.
- The non-reproducibility error, $(\frac{\Delta E}{E})_{rep}$, accounts for uncertainties in the temperature measurements and tidal corrections and the unknown status of the RF and corrector settings.
- The last two errors can be combined into an energy-point-to-energy-point error, $(\frac{\Delta E}{E})^{i}_{p-t-p}$, for each energy point i:

$$\left(\frac{\Delta E}{E}\right)^{i}_{p-t-p} = \sqrt{\left[\left(\frac{\Delta E}{E}\right)^{set}_{p-t-p}\right]^2 + \frac{1}{\bar{N}^{i}_{fills}}\left[\left(\frac{\Delta E}{E}\right)_{rep}\right]^2}, \tag{4.1}$$

where $\bar{N}^{i}_{fills}$ is the luminosity weighted number of fills:

$$\bar{N}^{i}_{fills} = \frac{(\sum_{j=1}^{fills(i)} \mathcal{L}_j)^2}{\sum_{j=1}^{fills(i)} \mathcal{L}_j^2}. \tag{4.2}$$

One can define a Gaussian distributed random variable, X, with zero mean and unit variance. The fluctuation of each energy point around the luminosity weighted mean of its various fills is then described by:

$$\frac{\Delta E^i}{E^i} = \left(\frac{\Delta E}{E}\right)_{abs} \times X_{abs} \oplus \frac{(E^i - E_{cal})}{E^i}\Delta\alpha \times X_\alpha \oplus \left(\frac{\Delta E}{E}\right)^{i}_{p-t-p} \times X^{i}_{p-t-p}. \tag{4.3}$$

The energy errors for 1990-1992 are summarized in Table 4.2.

4.2.3 LEP beam spread

The distribution of energies of single particles in the electron and positron bunches is finite. The width of this distribution scales linearly with energy and amounts to 51 MeV at 45 GeV beam energy.

Energy Error	1990, 1991a	1991b	1992
E_{cal} [GeV]	91.2	93.0	93.0
$\Delta\alpha$	1.5×10^{-3}	1.5×10^{-3}	1.5×10^{-3}
$(\frac{\Delta E}{E})_{abs}$	2.9×10^{-4}	5.7×10^{-5}	2.0×10^{-4}
$(\frac{\Delta E}{E})^{set}_{p-t-p}$	3.0×10^{-3}	3.0×10^{-3}	3.0×10^{-3}
$(\frac{\Delta E}{E})_{rep}$	1.0×10^{-4}	1.0×10^{-4}	1.0×10^{-4}

Table 4.2: Summary of the LEP energy errors for 1990 - 1992.

4.3 The L3 Detector

The L3 Detector [23,28] shown in Figure 4.5 is one of the four general purpose detectors installed in the LEP ring. It is designed to measure e^+e^- collisions up to an energy

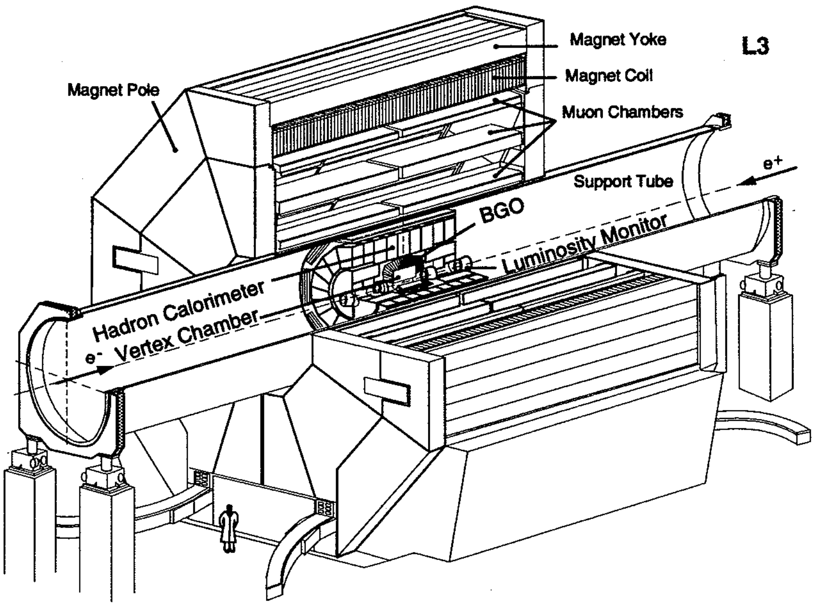

Figure 4.5: The L3 detector

of 200 GeV, with emphasis on the precise energy measurement of leptons, photons and hadron jets. The whole detector is installed within a 7800 ton magnet with a field of 0.5 Tesla. The detector consists of the following subdetectors, which are described in subsequent sections:

- the muon detector,

- the hadron calorimeter (HCAL),
- the scintillation counters,
- the electromagnetic calorimeter (BGO),
- the central track detector, subdivided into the Time Expansion Chamber (TEC) and the z-detector,
- the luminosity monitor.

The subdetectors are supported by a 32m long, 4.45 m diameter steel tube. The axis of the tube is aligned to the beam axis. The muon detector is mounted on the outside of the tube, while all other detectors are placed inside in its central section. This design allows the momentum of a track in the muon chambers to be measured accurately. The inner part of the L3 detector is divided into a barrel and a forward-backward section.

4.3.1 The L3 coordinate system

The origin of the right-handed coordinate system (see Figure 4.6) coincides with the geometric center of the detector, which defines also the nominal interaction point of the e^+e^- beams. The z direction corresponds to the direction of the electron beam. The y direction points vertically upwards and the x direction points to the center of the LEP ring. The distance in the (x, y) plane to the geometric center is denoted with the radius, r. The polar angle, θ, is the angle in the (s, z) plane with respect to the z axis, while the azimuthal angle, ϕ, is the angle in the (x, y) plane with respect to the x axis. For details of the definition of track parameters for particles traversing the detector see Section 6.6.3.

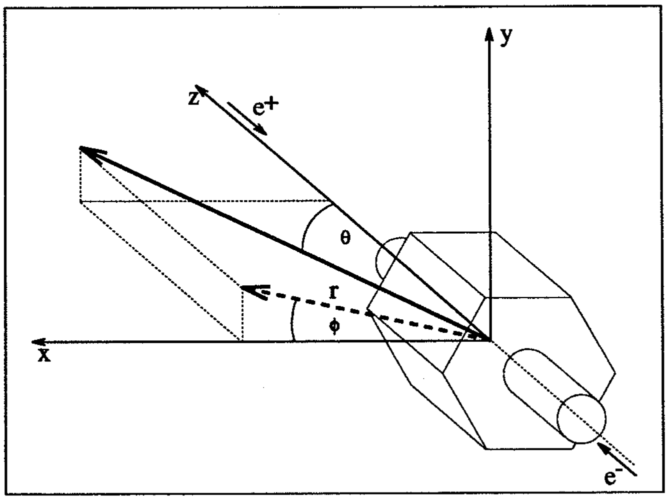

Figure 4.6: The coordinate system of L3.

4.3.2 The muon detector

The design goal of the muon detector is to determine the momentum of muons at 50 GeV with an accuracy of $\Delta p/p \approx 2\%$. This is achieved by measuring the curvature of the muon tracks in a solenoidal magnetic field of 0.5 Tesla. The muon detector consists of two ferris wheels subdivided into octants. One octant contains five chambers in three layers. Figure 4.7 shows a schematic view of a muon detector octant. The inner layer is supplied with

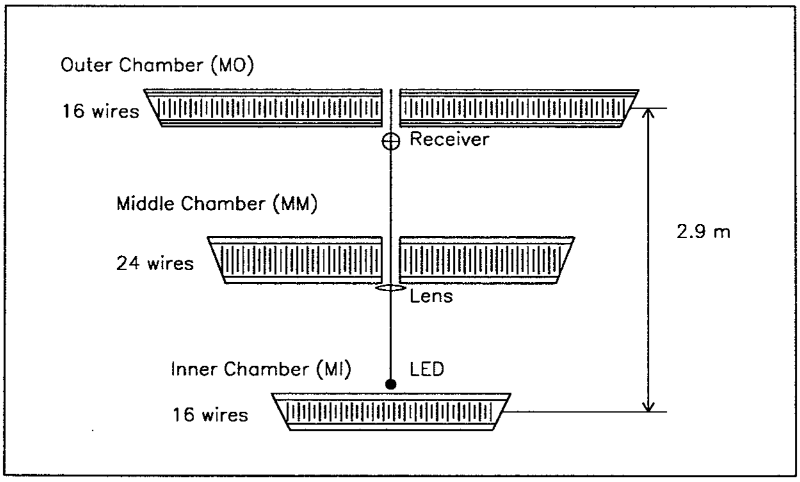

Figure 4.7: An octant of the muon chambers

one chamber and the middle and outer layer with two chambers each. The main part of the muon detector is formed by the precision chambers (P-chambers), which measure the projection of the track in the (r, ϕ) plane. The chambers are equipped with 16, 24 and 16 wires for the inner, middle and outer layers respectively. The single wire resolution is 200 μm. The polar angle of a track is measured with the z-chambers with a resolution of 500 μm. The z-chambers are installed at the top and bottom of the inner and outer layers. The relative position of the layers is monitored with an LED alignment system. The curvature of the muon track is determined with the sagitta method. The lever arm of the chambers is 2.9 m and a sagitta of 3.4 mm is expected for a particle momentum of 45 GeV. The sagitta has to be measured with an accuracy of $\Delta s = 70\mu$m to reach the design goal for the momentum resolution. The following sources contribute to the error of the sagitta measurement [29]:

- the uncertainty of the single wire resolution, which is 54 μm,
- the multiple Coloumb scattering of the muon traversing the muon chambers, estimated to 31 μm,
- the uncertainty of the internal alignment of the three layers of an octant, with 33 μm.

Experimentally Δs is measured to be very close to the required value of 70 μm. The resolution for muons with 45 GeV is 2.5% (see Figure 4.8).

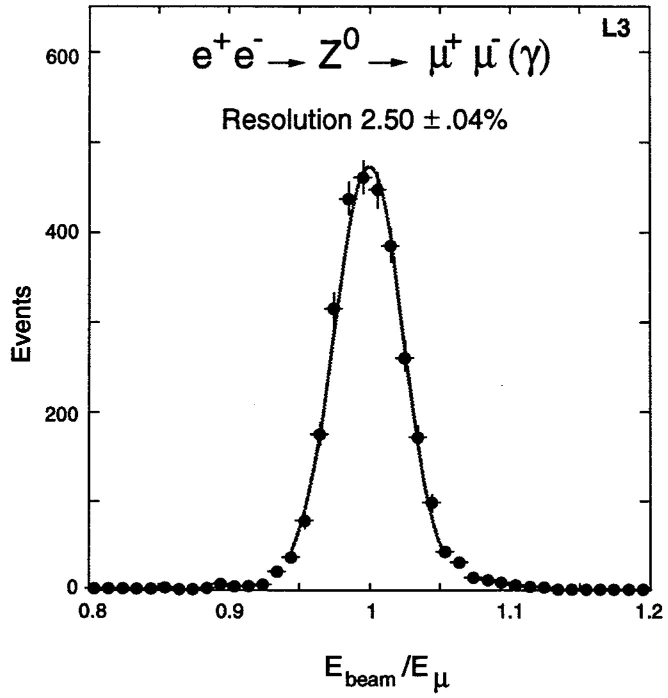

Figure 4.8: The momentum resolution of the muon detector for 45 GeV muons.

4.3.3 The hadron calorimeter

The energy of hadrons coming from e^+e^-collisions is measured by the total absorption technique using an electromagnetic and a hadron calorimeter. The hadron calorimeter (see Figure 4.9) consists of three parts:

- the hadron calorimeter barrel with an angular coverage of $35° \leq \theta \leq 145°$,
- the forward-backward hadron calorimeter with an angular coverage of $5.5° \leq \theta \leq 35°$ and $145° \leq \theta \leq 174.5°$,
- the muon filter, mounted on the inside wall of the support tube.

The combined coverage of the hadron calorimeter is 99.5% of 4π. It is made of depleted uranium absorber plates interspersed with proportional wire chambers. The wire chamber signal is proportional to the number of charged tracks in the shower, which is linearly related to the energy of the incoming particle. The barrel has a modular structure consisting of 9 rings of 16 modules each. The endcaps consist of three rings, splitted vertically into

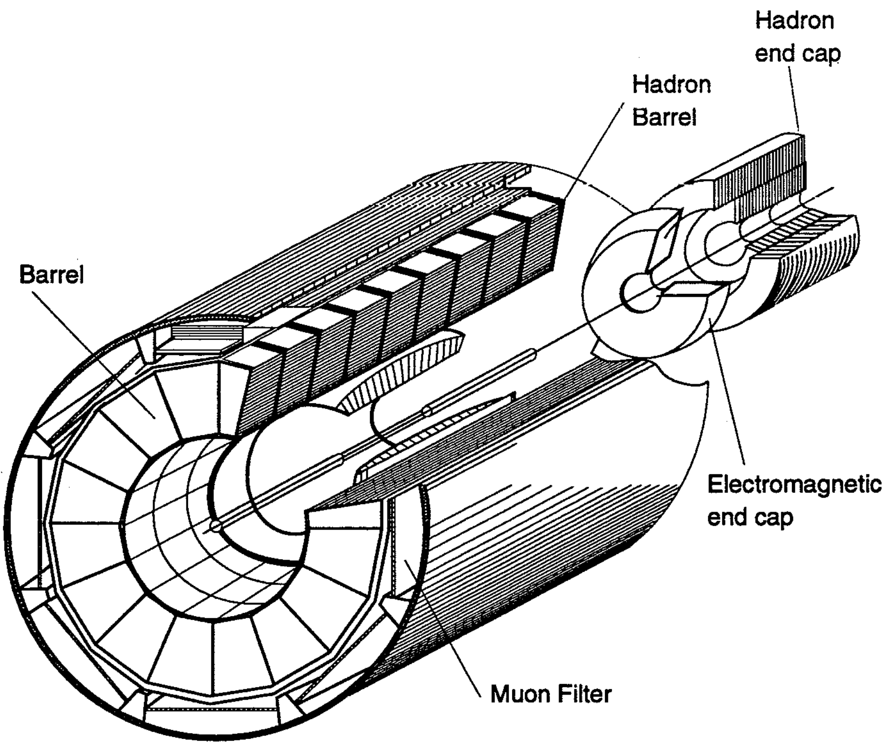

Figure 4.9: The hadron calorimeter

half-rings. The wires of each module are grouped in towers, which cover $\Delta\theta = 2°$ and $\Delta\phi = 2°$. The material of the electromagnetic calorimeter, the hadron calorimeter and the support structure corresponds to 6 nuclear absorption lengths at normal incidence. An additional absorption length is introduced by the muon filter to make sure that only minimum ionizing particles reach the muon detector.

The hadron jet energy resolution of the calorimeter was measured to be $(55/\sqrt{E}+8)\%$ [23]. The direction of the jet axis can be measured with a resolution of about 2.5°.

4.3.4 The scintillation counters

The scintillation counters are located between the hadron and electromagnetic calorimeters and consist of 30 single plastic counters. Their main goal is to distinguish cosmic muons passing the detector center from $e^+e^- \to \mu^+\mu^-$ events, coming from a Z decay. Therefore, a good time resolution is required. The time difference between opposite scintillator hits for a cosmic muon traversing the detector is about 6 ns, while it is 0 ns for muons from the detector center. The distribution of the measured time, corrected for the expected time-of-flight is shown in Figure 4.10 for $e^+e^- \to \mu^+\mu^-$ events. A resolution of 460 ps is achieved. Furthermore, the scintillator hit multiplicity is used to trigger hadron events.

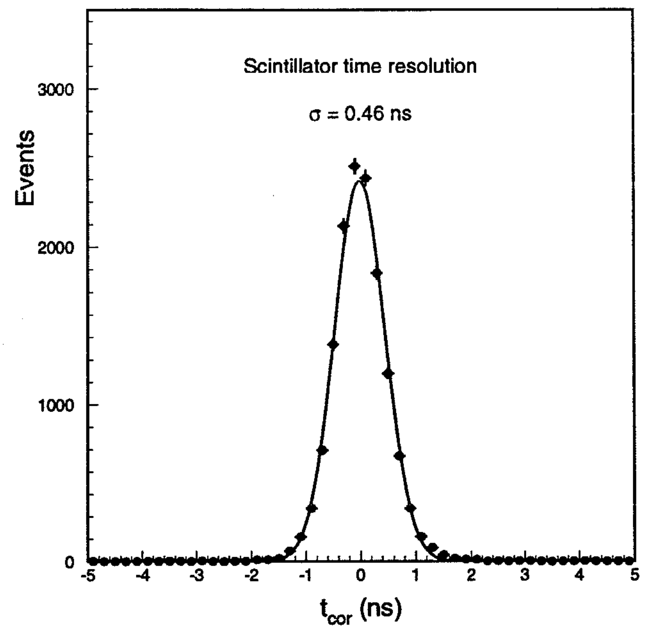

Figure 4.10: Scintillator time corrected for the expected time-of-flight.

4.3.5 The electromagnetic calorimeter

The electromagnetic calorimeter is designed to measure the energy and position of electrons and photons with excellent resolution for energies between 100 MeV and 100 GeV. It consists of about 11000 bismuth germanate (BGO) crystals pointing to the interaction region. The $Bi_4Ge_3O_{12}$ crystals are used as absorption and detection medium, to ensure that the complete shower is measured. The detector is subdivided into (see Figure 4.11):

- two half barrels with a total of 7680 crystals; the polar angle coverage is $42° < \theta < 138°$,
- two endcaps, each made of 1527 crystals ; the polar angle coverage is $11.6° < \theta < 38°$ and $142° < \theta < 168.4°$.

The BGO crystals in the barrel are in the form of truncated pyramids with a front face of 2×2 cm^2 and a rear face of 3×3 cm^2. Their length of 24 cm corresponds to 22 radiation lengths. All crystals point to the interaction region, but with a small tilt in the azimuthal direction, to reduce the probability that particles traverse the calorimeter in the support structure between the crystals, without showering. The support structure and clearances, to ensure that a structural deformation does not affect the crystals, represent 1.75% of the solid angle covered by the barrel. Each crystal is equipped with two photodiodes glued to its rear face. Due to the wide energy range measured with the electromagnetic calorimeter, ADC's with a dynamic range equivalent to 21 bits and 10 bits resolution are used.

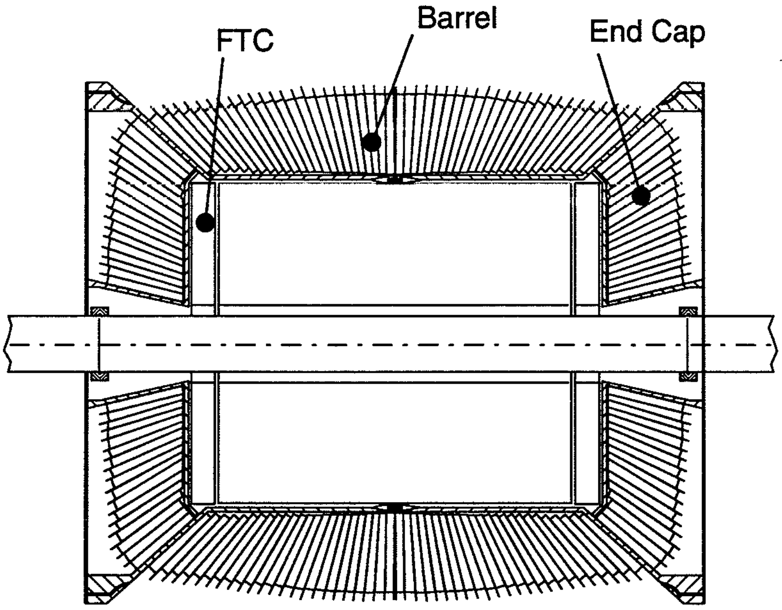

Figure 4.11: The BGO electromagnetic calorimeter.

The barrel part of the calorimeter was calibrated in a test beam with electrons of various momenta from 180 MeV to 50 GeV. An energy resolution of 4% at 100 MeV and better than 1% at high energies was measured (see Figure 4.12). Apart from the test beam calibration a continuous calibration and monitoring of the calorimeter is required. A Xenon flasher monitoring system measures the transparency of the crystals by shining light pulses on each crystal and detecting the response of the photo diode. A global energy calibration at two energy points is possible. Using $e^+e^- \rightarrow e^+e^-$ events the detector response is calibrated to the beam energy. In addition the minimum ionizing signal of cosmic muons provides a intercalibration point at low energies [30].

4.3.6 The central track detector

The central track detector [31] is designed to measure tracks from charged particles with high spatial resolution in the limited space available within the electromagnetic calorimeter. The main purposes of the detector are:

- measurement of the position and direction of charged tracks,
- determination of the transverse momentum and the charge of particles up to 50 GeV,
- prediction of the impact point of a charged particle in the electromagnetic calorimeter,
- reconstruction of the interaction point and possible secondary vertices.

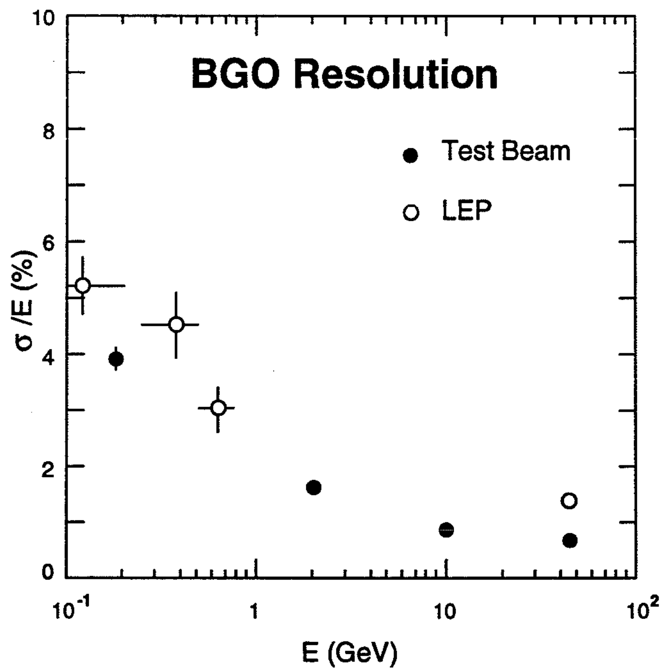

Figure 4.12: Energy resolution of the barrel electromagnetic calorimeter.

The central track detector consists of the following parts (see Figure 4.13):

- two concentric gas drift chambers operating in the *time expansion* mode (TEC), to measure the (r, ϕ) coordinates of a track,
- two concentric proportional wire chambers with cathode strip readout mounted on the outside of the TEC, the z-detector [32], to measure the z coordinate,
- a plastic scintillating fiber ribbon (PSF) used as reference to calibrate the drift velocity in the time expansion chambers.

The volume of the TEC is subdivided into sectors consisting of a large drift region with low electric field and a small amplification region with high electric field. In the latter region gas amplification occurs and the electron avalanche is detected by the anodes. The two regions are separated by a grid plane, to obtain a homogeneous drift field in the drift region. The TEC operates with a gas mixture of 80% CO_2 and 20% isobutane. The drift velocity is typically $6\mu m$ / *ns*. The low drift velocity (about 10% of conventional drift chambers) permits a time "center-of-gravity" measurement of the anode pulse, which is therefore sampled with a 100 MHz flash analog-to-digital converter (FADC).

In the TEC chambers all wires are strung in the axial direction, parallel to the beam pipe. The inner TEC is subdivided into 12 sectors, measuring 8 coordinate points in the (r, ϕ) plane and the outer TEC is subdivided in 24 sectors with 54 coordinate points. The

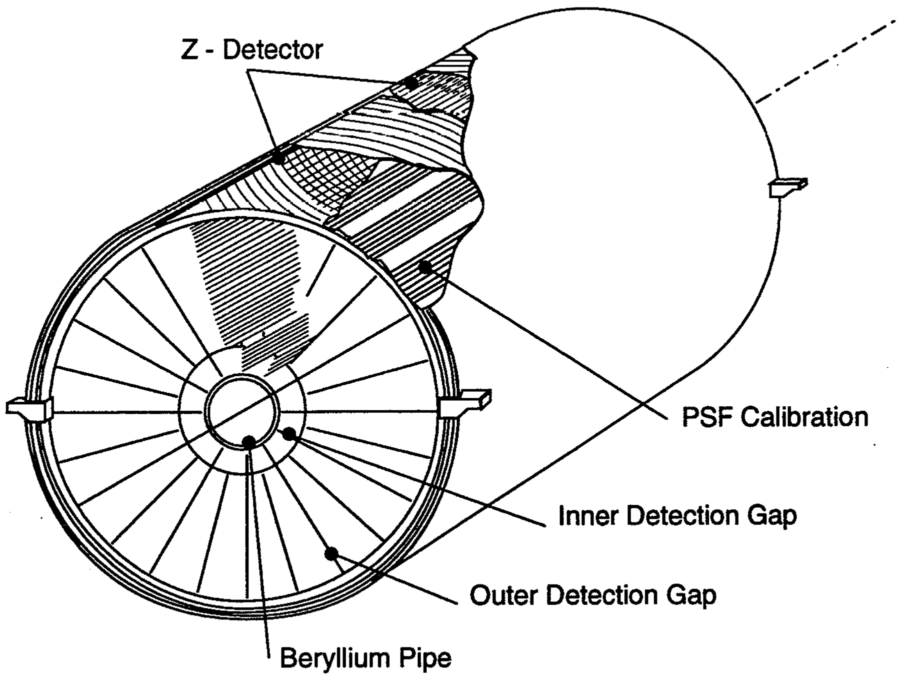

Figure 4.13: The central track detector.

lever arm is 31.7 cm in the (r, ϕ) plane. Since the TEC sectors are symmetric with respect to the anode plane, it is impossible to decide by only measuring the drift time on which side of the anode plane the track passed. To resolve this ambiguity the signal of pick-up wires in grid planes is read out and the tracks measured in inner and outer TEC are matched. The wire layout of the TEC is displayed in Figure 4.14. To support the drift velocity calibration of the TEC each outer sector is equipped with a plastic scintillating fiber (PSF) ribbon. Each fiber yields an azimuthal resolution of $700 / \sqrt{12}$ μm. The drift velocity can be determined by analyzing the relationship between the drift time and PSF position for each anode. Since the anode wires are strung in the z direction, the drift time does not contain information on the z coordinate of the track. Therefore, some anodes are read out on both ends. Since the resistance of the wires is finite, a comparison of the integrated charge signal of both sides determines the z position (charge division principle). A resolution of several cm has been measured. To complete the position measurement of the track with a precise determination of the z coordinate, the TEC is surrounded by two proportional wire chambers with cathode strip readout, the z-detector, which measure the z position with a resolution of about 300 μm for tracks crossing the chambers perpendicularly. The design and operation of these chambers will be described in more detail in Chapter 5.

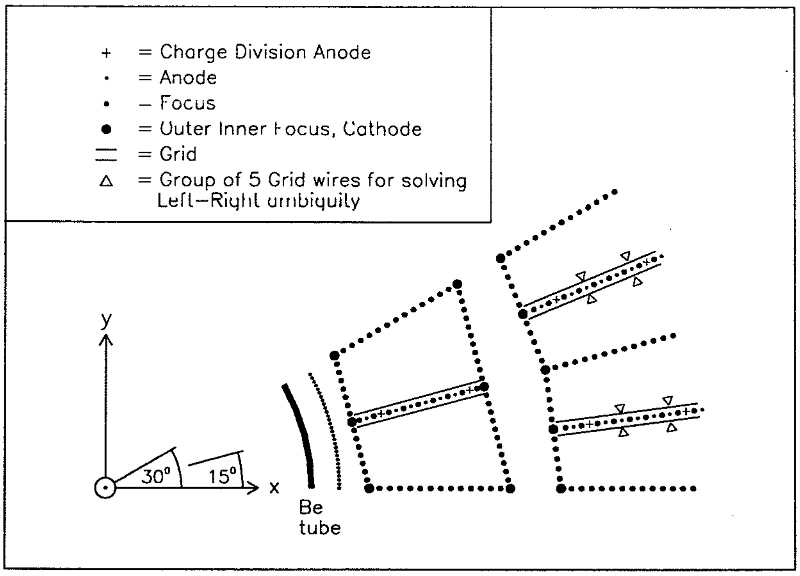

Figure 4.14: The wire layout of the TEC.

4.3.7 The luminosity monitor

The luminosity monitor measures the LEP luminosity at the position of the L3 detector using small angle Bhabha scattering. The monitor consists of two half-detectors, positioned in front of the calorimeter endcaps on either side of the interaction region in a distance of $z = \pm 2.65$m. Each half detector consists of:

- an array of 304 BGO crystals (see Figure 4.15), with an angular coverage of 24.93 mrad $< \theta < 69.94$ mrad,
- a tracking chamber mounted in front of the BGO crystals, to measure the polar angle of the tracks.

Every crystal is mounted with a photodiode and an LED to monitor the transparency. The calorimeters have an energy resolution for electromagnetic showers of 2%. The angular resolution is 0.4 mrad in θ and 9 mrad in ϕ.

4.3.8 The trigger system

The goal of the trigger system is to record only the detector signals from those beam crossings in which particles came from the e^+e^- interaction point. This task is performed by a chain of three trigger levels with intermediate event buffering. The complexity of the decisions increases with each level, while the trigger rate decreases from beam crossing rate down to a few Hz written onto tape. The function of the level-1 trigger is to select interesting events with loose criteria, while level-2 and level-3 have to reject the background which was selected by level-1.

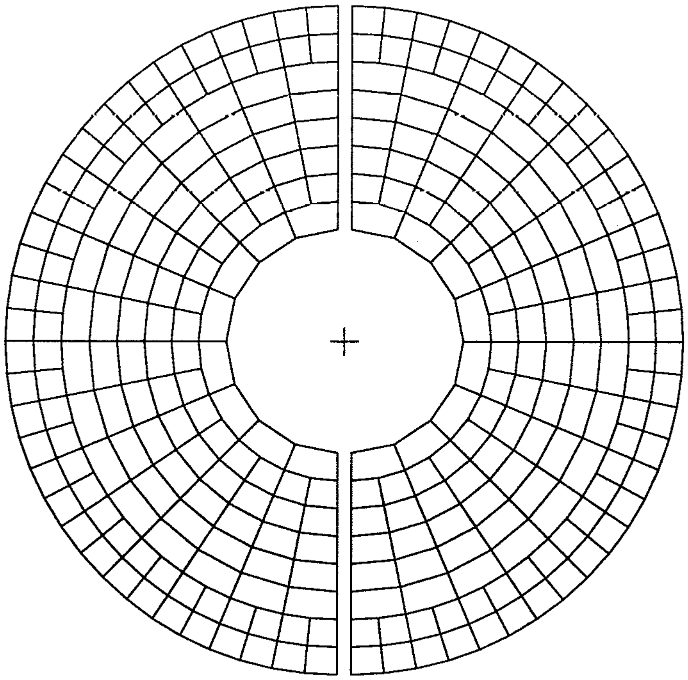

Figure 4.15: Crystal arrangement in the luminosity monitor. The detector is split into two vertical planes.

Level-1 trigger

The level-1 trigger is based on five single triggers from different subdetectors. Each trigger starts operation at beam crossing. If one of the triggers gives a positive result the whole detector is read out and the information is buffered, waiting for the level-2 decision. The level-1 trigger rate is typically less than 8 Hz with a dead time of less than 5%. The trigger components of level-1 are:

1. the *energy trigger*, which selects events which deposit energy in the hadronic or electromagnetic calorimeters, including e^+e^-, $\tau^+\tau^-$, hadronic and $\nu\bar{\nu}\gamma$ final states,

2. the *scintillator trigger* is used to select high multiplicity events,

3. the *muon trigger* is designed to select events, where at least one particle traverses the muon chambers,

4. the *TEC trigger* detects events with charged tracks,

5. the *luminosity trigger* selects Bhabha events in the luminosity monitor.

Level-2 trigger

The level-2 trigger uses the coarse data from level-1, the level-1 results and a more detailed TEC information for analysis. At level-2 one has more time to spent on one event, which allows more complicated decisions and one can combine information from different subdetectors. The level-2 trigger removes calorimeter triggers induced by electronic noise, beam-gas events, beam-wall interactions triggered by TEC and synchrotron radiation. Events with more than one positive decision of the single triggers at level-1 are not rejected. The output rate of level-2 is less than 6 Hz.

Level-3 trigger

The level-3 decision relies on the full detector information for the event. The calculation here is based on the final digitization of the signals. Thresholds are defined more precisely. Therefore, a further background suppression can be achieved. The quality of the correlation of subdetector signals is also improved. Events with more than one trigger on level-1 are not rejected by level-3. Luminosity triggers from level-1 are also all kept. The output rate is reduced to 2-3 Hz and is delivered to a memory buffer, from where the events are written to tape.

Chapter 5

The Z-Detector of L3

5.1 Design and Operation Principles

The z-detector supplements the measurement of the azimuthal angle, ϕ, from the TEC with two precise determinations of the z-coordinate. Furthermore, a rough measurement of ϕ is performed in order to match the measurements of the z-detector to the track measured by the TEC. This allows a complete measurement of the direction of a charged particle within the vertex chamber and its entry point into the BGO.

The z-detector consists of two cylindrical proportional wire chambers with cathode readout, mounted on the outside of the TEC. The mean radius of the detector is 0.48 m and the effective length 1 m. Figure 5.1 shows the position of the z-detector within the central track detector. Three self supporting cylinders form the mechanical frame of the detector. These cylinders are constructed as a sandwich of glass fiber reinforced Kapton foils and foam. The cathodes are glued onto the Kapton foils.

The measurement of the image charges of the avalanche, induced on the cathodes, allows a localization of the avalanche position along the wire, which is much more precise than expected from the cathode strip width. For a description of the z-detector and its performance see also [32].

5.2 Cathode Readout

The position measurement capability of a proportional wire chamber is much improved by measuring the induced charge distribution on the cathode strips (see for example [33]). Generally, the distribution of the image charges, induced by the electron avalanche at the anode wires, is represented by the solution of the electrostatic problem. There are several approximate solutions described in the literature:

(a) In reference [34] the image charge on the cathode is obtained neglecting the effects of the anode wires and the opposite cathode;

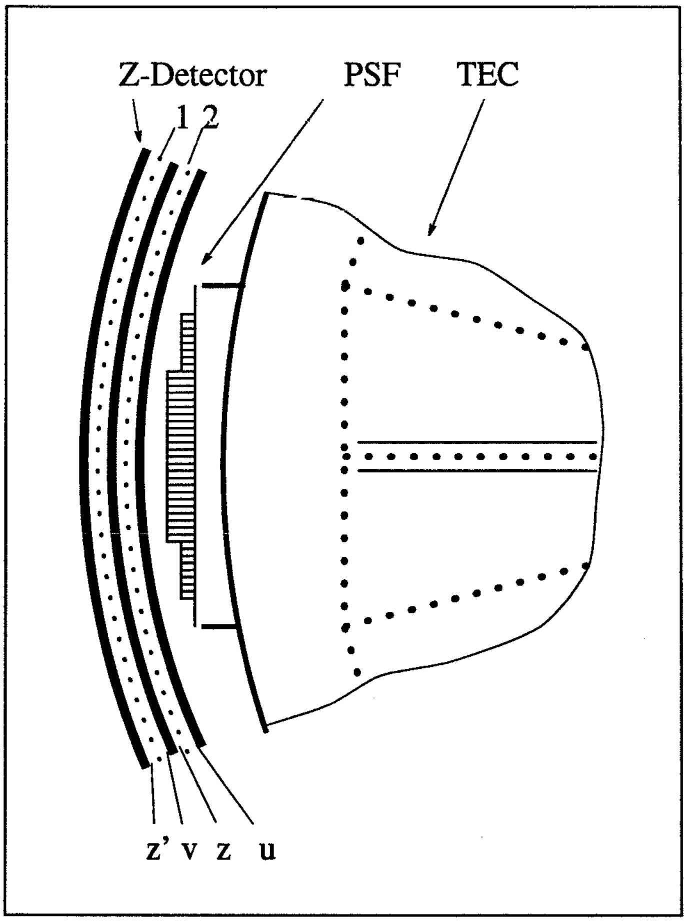

Figure 5.1: A cutaway view of the central track detector perpendicular to the chamber axis. Labels 1 and 2 denote the anode wire planes, labels u, z, v, z' the cathode layers of the z-detector.

(b) In reference [35] the charge distribution is calculated assuming a continuous anode plane instead of single wires, but the effect of the opposite cathode is also neglected;

(c) In reference [36] the effect of the image charges induced by a charge cloud sitting at an anode wire on both cathode planes is taken into account.

There is experimental evidence that the first two models, (a) and (b) do not describe the real charge distribution [37], but the third one, (c), does [36]. Model (c) is used for the z-detector to describe the charge deposition and its coordinate.

For the electrostatic case, the induced charge density $\sigma(z - z_a, y)$ on both cathode planes by the charge, Q, of the avalanche sitting on the anode wire at z_a is described by:

$$\sigma(z - z_a, y) = \frac{-Q}{2\pi} \sum_{n=0}^{\infty} (-1)^n \frac{(2n+1)L}{\{(2n+1)^2L^2 + (z - z_a)^2 + y^2\}^{3/2}}, \tag{5.1}$$

where $L = 3.5$ mm is the anode-cathode distance. The coordinate system is shown in Figure 5.2. To obtain the charge distribution projected onto the z axis, $\sigma(z - z_a)$, one has

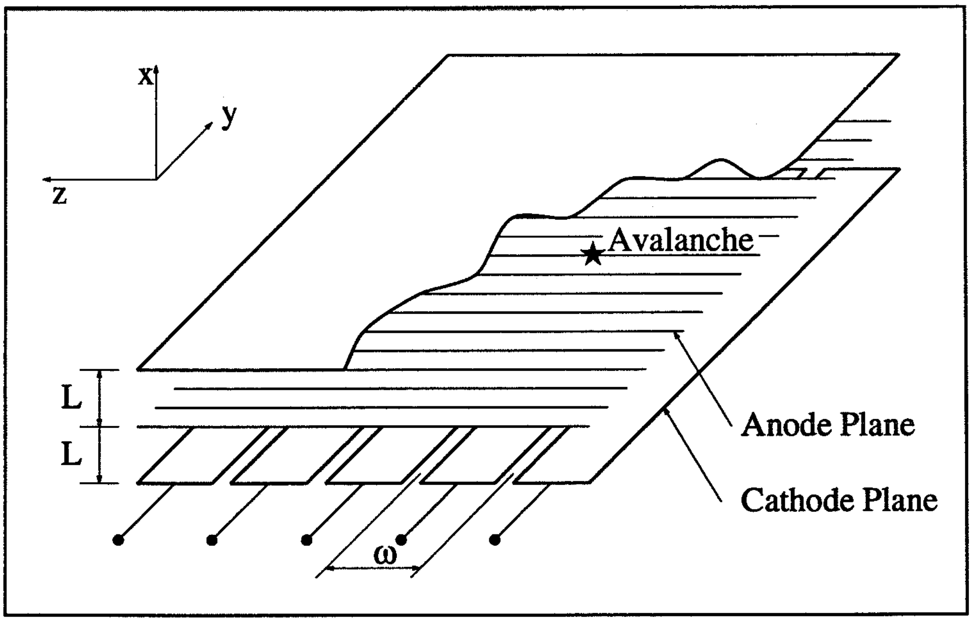

Figure 5.2: The coordinate system for the cathode read out used in model (c).

to integrate over the y axis:

$$\begin{aligned}\sigma(z - z_a) &= \int_{-\infty}^{\infty} \sigma(z - z_a, y)dy \\ &= \frac{-Q}{\pi}\sum_{n=0}^{\infty}(-1)^n \frac{(2n+1)L}{(2n+1)^2L^2 + (z - z_a)^2} \\ &= \frac{-Q}{4L} sech \frac{\pi(z - z_a)}{2L}.\end{aligned} \tag{5.2}$$

If the cathode plane is subdivided into strips of infinite length along the y axis, one integrates over the width of one strip, $\omega = 4.45$ mm, and gets the induced image charge, Q_i, on the i'th cathode strip at the position, $b < z < b + \omega$:

$$\begin{aligned}Q_i &= \frac{-Q}{4L}\int_b^{b+\omega} sech \frac{\pi(z - z_a)}{2L} dz \\ &= \frac{-Q}{4L}\left[arctan(e^{\pi(z-z_a)/2L})\right]_b^{b+\omega} ; \; for\ b \geq 0.\end{aligned} \tag{5.3}$$

The coordinate of a cluster in the z-detector is calculated by a charge ratio method, proposed in [38]. This method considers only the strip with maximum charge, Q_i, in the cluster and the charge of the adjacent strips, Q_{i-1} and Q_{i+1}. The charge ratios,

$$\begin{aligned}R_- &= Q_{i-1} \,/\, Q_i, \\ R_+ &= Q_{i+1} \,/\, Q_i,\end{aligned} \tag{5.4}$$

are related to the position of the avalanche, z_a, via Equation 5.3. The advantage of the coordinate determination by charge ratios is, that it is independent of cross-talk, if the latter is symmetric about the central strip. In order to obtain an optimal coordinate resolution for the cathode readout the ratio $r = \omega / L$ has to be of the order of 1 to 2. The resolution is then estimated to be $0.07 - 0.008 \times L$. For the z-detector r is 1.3. The resolution in this model is thus expected to be 280 μm.

5.3 Construction of the Z-Detector

The z-detector has to fit into the radial space of 22 mm between the TEC and the BGO. The necessary stability of the mechanical frame to hold the force of 2048 anode wires, ca. 2 kN, is achieved using a sandwich construction of the cylinders. Each cylinder consists of two glass fiber reinforced Kapton foils. The space between them is filled with polyurethane foam. The outermost and middle cylinder form one *z-chamber* and the innermost and the middle cylinder the other one. The sandwich structure is illustrated in Figure 5.3. The active length of the detector is 1068 mm, the inner radius is 467.5 mm and

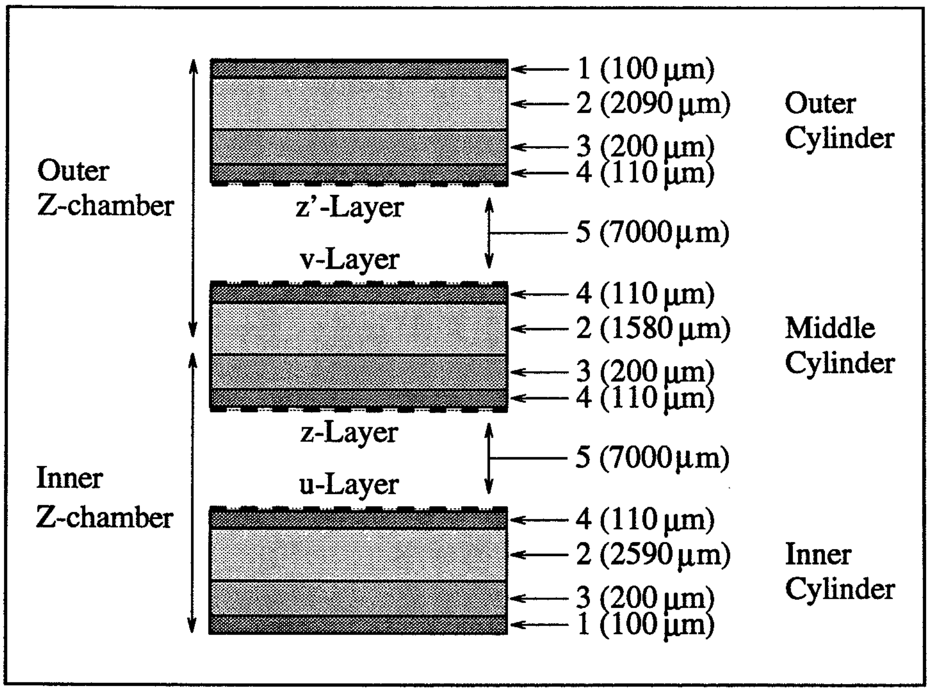

Figure 5.3: The sandwich structure of the z-chamber cylinders. The labels indicate the different layers with their thickness: 1 - Copper plated Kapton foil, 2 - Polyurethane foam, 3 - Glass fiber epoxy, 4 - Kapton foil with copper strips, 5 - Gas volume .

the radial thickness amounts to 21.5 mm. The mechanical tolerance of the construction is 200 μm. The material of the detector corresponds to 2% of a radiation length for a particle traversing the detector perpendicularly. Within one chamber 2×512 anode and field shaping wires are strung alternating in the axial direction. The Kapton foils are plated with 35 μm copper and form the cathode layers. The four cathode layers consist of 240 strips each, with a width of $\omega = 4.45$ mm. Two of the layers (z and z') have ring like strips perpendicular to the chamber axis to measure the z-coordinate. For the remaining two layers (u and v) the cathodes form a helix with an angle to the chamber axis of $\pm$ 69°. The u and v layers allow the azimuthal angle to be measured in order to match the measurement of the z-detector with the track measured in the TEC. The z-measuring cathode layers, z and z', are displaced with respect to each other in axial direction by half a pitch. For a detailed definition of all relevant z-detector geometry constants and variables see Appendix A.

5.4 Readout Electronics

The electronic chain to read out the cathode strips consists of a preamplifier, line driver, and charge to digital converter (QTC) (see Figure 5.4). The capacity of a cathode strip

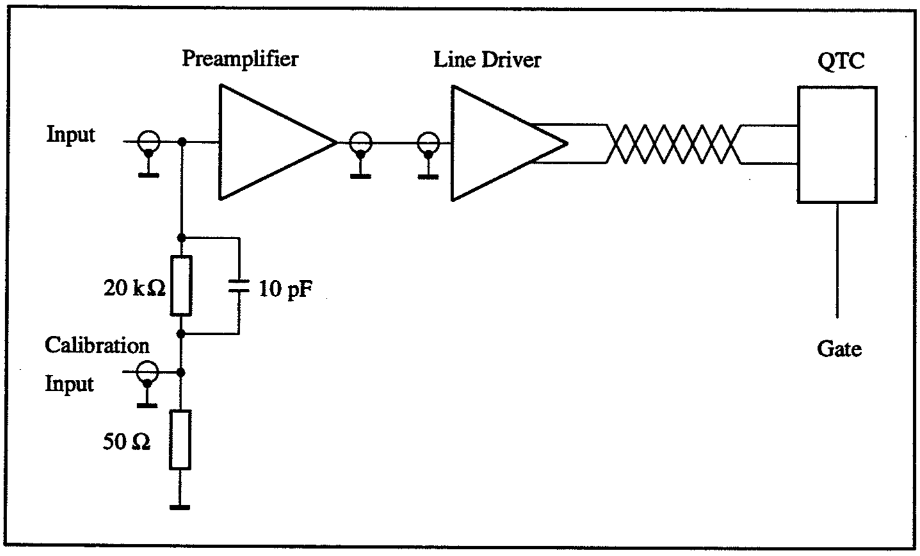

Figure 5.4: Principal scheme of the readout electronics of the z-detector.

is on average 500 pF. This results in a noise level of 15000 electron charges, Q_e, at the preamplifier input. The preamplifiers are thick film hybrids and are mounted in shielded boxes on the end support rings of the detector. The preamplifier signals are fed to the line drivers via 45 m long coaxial cable. The line drivers generate a differential signal, which is sent via 80 m of twisted pair cables to the QTC. The QTC integrates the incoming signal over a time gate of 300 ns and produces a digital output proportional to the induced charge on the strip. Since the z-coordinate measurement relies on the determination of charge ratios of adjacent strips, the amplification of each electronic channel is measured. This is done by feeding a test charge into a single preamplifier input and calibrating the response of the QTC. Furthermore, the cross talk to the adjacent channels can be measured.

5.5 Test Run Results

The performance of the z-detector was studied using hadrons with a momentum of 13 GeV. The trajectory of the particles was measured using four silicon microstrip detectors with a pitch of 50 μm up and downstream of the z-detector.

The chambers are operated typically at 1600 Volts. A gas amplification of 5×10^4 was measured with a gas mixture of 80% argon and 20% CO_2. Before analyzing the data, the QTC signals are normalized to each other and common noise and pedestals are subtracted.

The spatial resolution of the chambers is determined by calculating the difference between the silicon microstrip detector prediction, z_{MSD}, and a single z-chamber measurement, z_{CH}, where z_{CH} can be z or z', the coordinates of the cathode layers z and z'. The width of a Gaussian fit to the distribution $\delta z = z_{CH} - z_{MSD}$ gives the z-chamber resolution. The single track resolution without corrections for the amplification and cross-talk was measured to be:

$$\sigma_{CH} = 350\mu m, \tag{5.5}$$

for an angle of the beam to the chamber axis of 87° and

$$\sigma_{CH} = 470\mu m, \tag{5.6}$$

for an angle of 66°. The contribution of the silicon microstrip detectors to the resolution can be neglected. If the amplification of the channels is normalized, the resolution improves by 10% (see Figure 5.5). A cross-talk correction does not improve the result.

In order to determine the efficiency, only events were considered, where at least three of the silicon microstrip detectors detected a signal. Then a z-chamber hit was counted if one found a signal within $\pm\, 3\sigma_{CH}$. The efficiency of each chambers was determined to be 97%.

5.6 Performance during Data Taking

The performance of the detector in situ is studied using clean samples of $e^+e^- \to \mu^+\mu^-$ and $e^+e^- \to e^+e^-$ events taken in 1991 and 1992, which are selected using information from the muon chambers and the BGO. Figure 5.6 shows an example of such an event, detected in the z-detector.

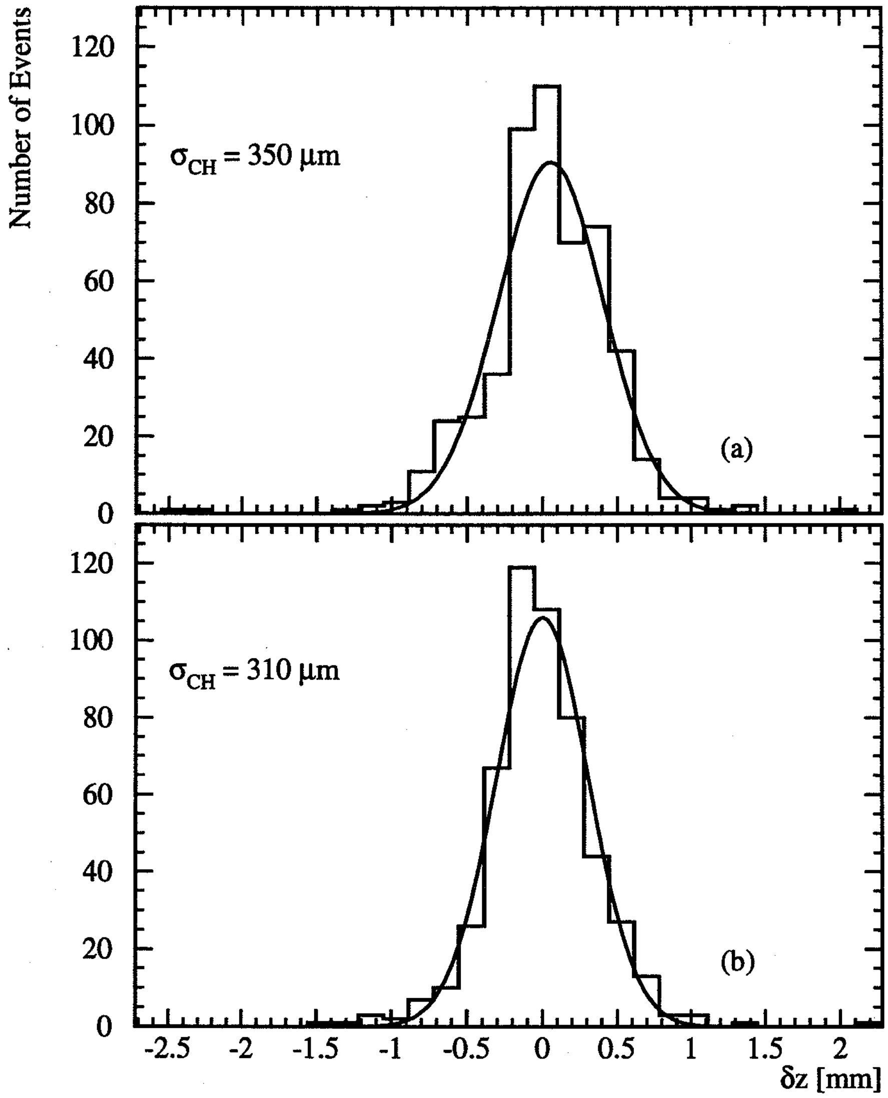

Figure 5.5: (a) Resolution of one z-chamber in test run for an angle of the beam to the chamber axis of 87°; (b) resolution for the same condition as in (a), but the amplification of the channels is normalized. σ_{CH} is the result of a Gaussian fit to δz.

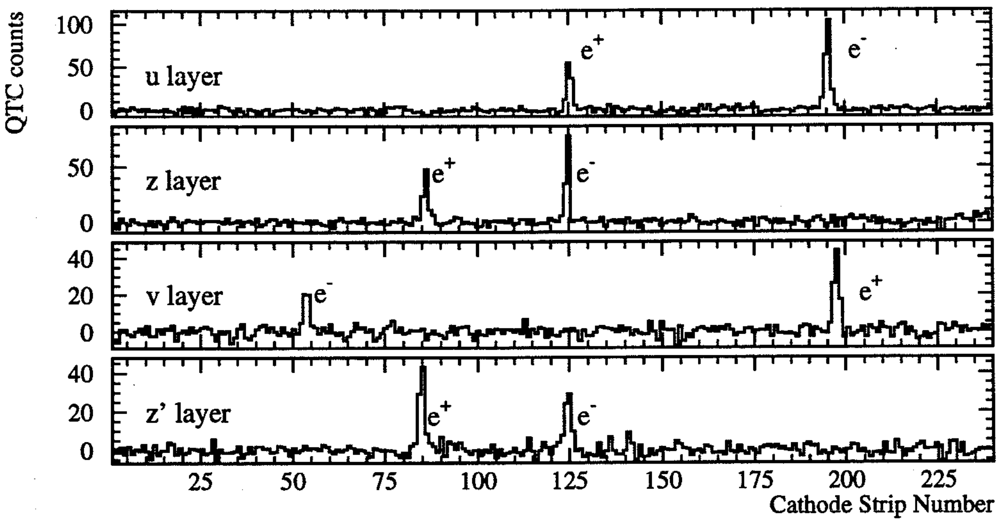

Figure 5.6: An $e^+e^- \rightarrow e^+e^-$ event detected in the z-detector.

5.6.1 Signal-to-noise ratio and cathode charge correlations

Figure 5.7 shows the charge sum of all hits belonging to one cluster for one cathode layer. Its shape reflects well the expected Landau distribution. An important characteristic of the chamber is the signal-to-noise ratio S/N:

$$\mathrm{S}\,/\,\mathrm{N} = \frac{\sum Q_i}{\sqrt{\sum \sigma^2_{\mathrm{ped},i}}}. \tag{5.7}$$

Q_i is the charge of each of the three adjacent strips around the maximum of the cluster and the $\sigma_{\mathrm{ped},i}$ are the pedestals widths of each of these channels. Figure 5.8 shows the distribution of S/N superimposed with a noise peak. The noise peak is calculated with three channels not belonging to a cluster. This peak around S/N=0 is clearly separated from the signal.

The charge avalanche at the anode wire induces equal image charges on both cathodes layers. Therefore, the clusters of the layers assigned to the same track should carry the same charges. Figure 5.9(a) shows the scatter plot of the charges, Q_{u} and Q_{z}. The expected linear correlation between Q_{u} and Q_{z} is confirmed. Q_{v} and $Q_{\mathrm{z'}}$ show the same effect. In Figure 5.9(b) the asymmetry

$$\frac{\delta Q}{Q} = \frac{Q_{\mathrm{z}} - Q_{\mathrm{u}}}{Q_{\mathrm{z}} + Q_{\mathrm{u}}} \tag{5.8}$$

is plotted. The width of $\delta Q\,/\,Q$ is 8%. Since the amplification calibration of the readout is done channel by channel for each layer separately, the slope in Figure 5.9(a) is not equal to one and the mean value of $\delta Q\,/\,Q$ in Figure 5.9(b) is not necessarily zero.

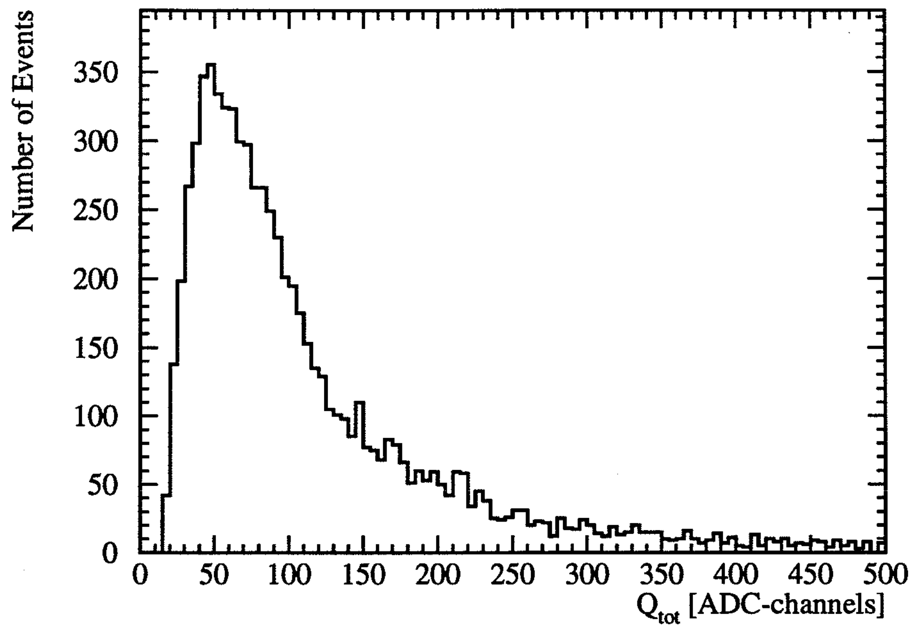

Figure 5.7: Landau distribution of the charge sum for the hits in the z layer.

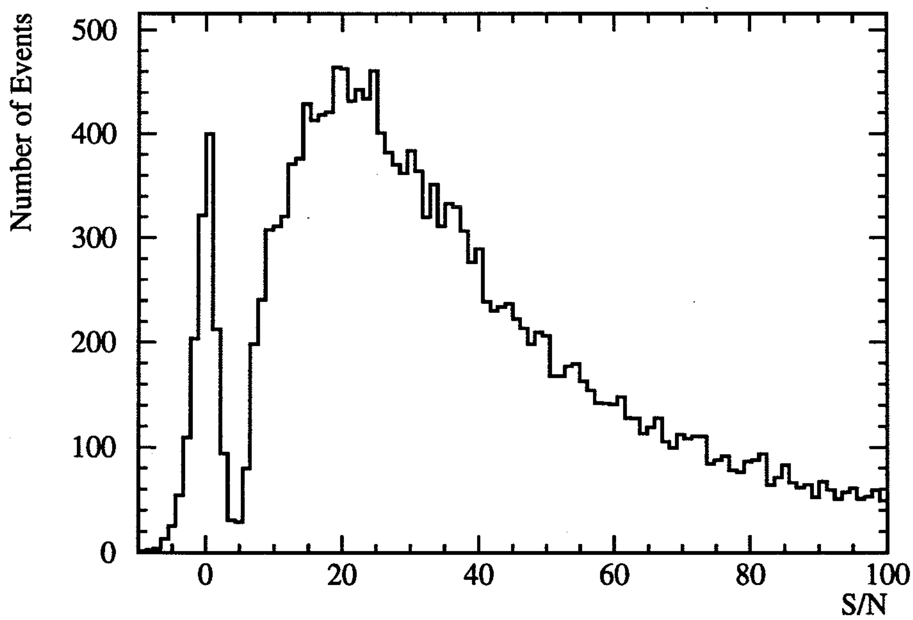

Figure 5.8: S/N ratio for charge clusters superimposed with a noise peak around S/N = 0.

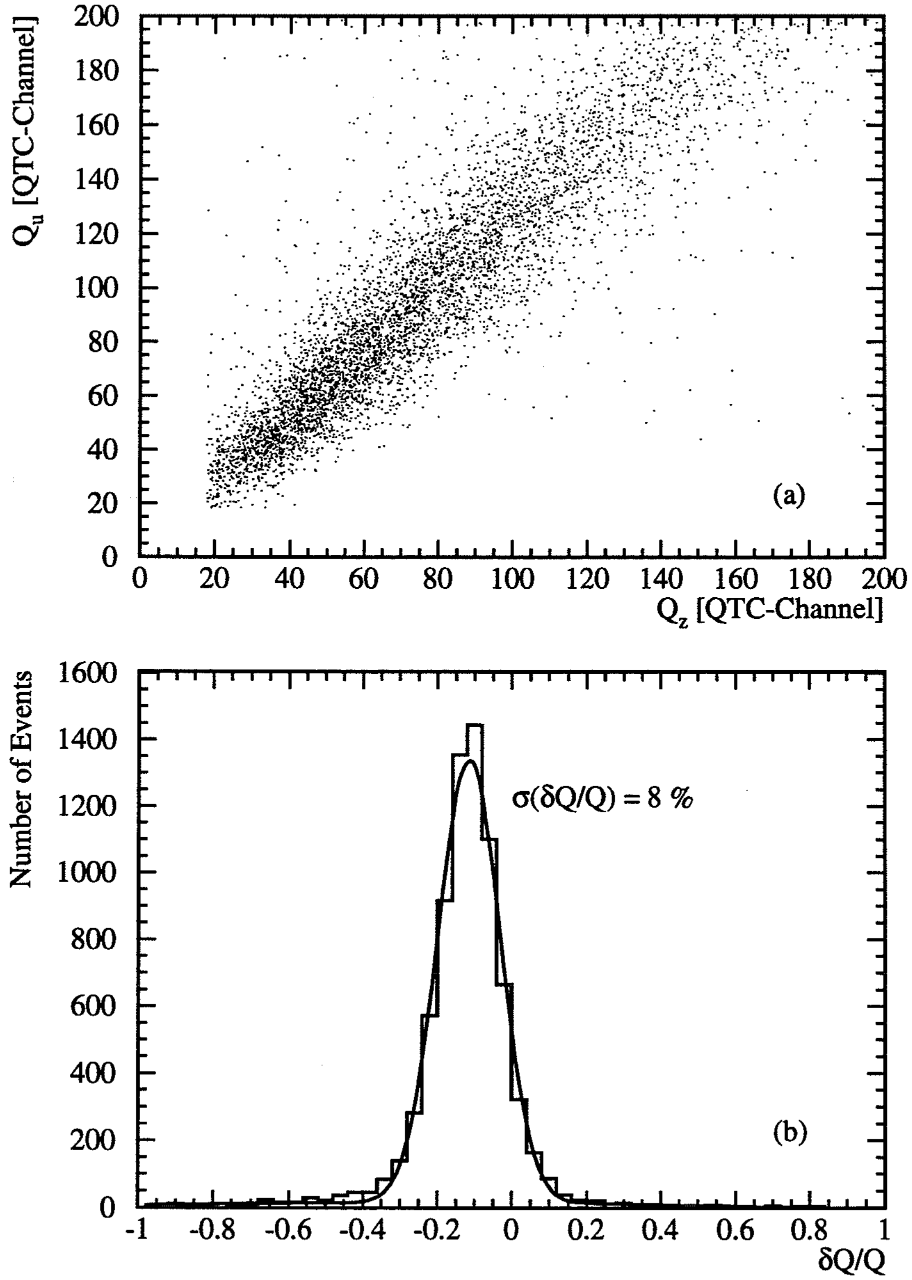

Figure 5.9: (a) Scatter plot of charges Q_u and Q_z measured at opposite cathode layers. (b) The asymmetry $\delta Q\,/\,Q$ for Q_u and Q_z.

5.6.2 Z-vertex measurement

In order to determine the resolution of the detector, one of the chambers serves as reference for the other, because one has no outside reference frame which measures the z-coordinate with a comparable resolution to the z-detector. Therefore, the measurement of the inner z-chamber, z, is then extrapolated to the outer one, z_{ex}, assuming the position of the interaction point in the z direction of the event, the z-vertex, V_z^{ev}, is known,

$$z_{ex} = V_z^{ev} + \frac{R_O}{R_I}(z - V_z^{ev}). \tag{5.9}$$

$R_I = 474.5$ mm and $R_O = 483.5$ mm are the radii of the inner and outer anode wire plane respectively. V_z^{ev} can also be measured with the z-detector for e^+e^- and $\mu^+\mu^-$ events under the assumption that there is no additional photon in the final state. Then both tracks are strictly back-to-back and one can connect all four z-coordinates by a straight line. The crossing point of this line with a line in z direction through the point $V_{x,y}^{fill}$ [1] gives the vertex position of the event in z direction, V_z^{ev}, (see Figure 5.10) with a resolution of

$$\sigma_{V_z^{ev}} = \frac{\sigma_{\mathrm{CH}}}{2}. \tag{5.10}$$

From the test beam results (see Equations 5.5, 5.6) one expects $\sigma_{V_z^{ev}} < 0.5$ mm. In the more general case of a final-state photon or the tracks originate from a secondary vertex, i.e. the decay of the τ lepton, one has to introduce an additional degree of freedom in the vertex determination to account for an acollinearity between the tracks. In this case the resolution of the z-vertex, $\sigma_{V_z^{ev}}$, is of the order of 25 mm, which is larger then the bunch length (see Table 4.1). Thus, the z-chamber provides a meaningful z-vertex measurement only for event classes, where the acollinearity between the tracks can be neglected. Nevertheless, using $e^+e^- \rightarrow e^+e^-$ and $e^+e^- \rightarrow \mu^+\mu^-$ events one can determine an average position, $\langle V_z^{ev}\rangle$, and width, σ_z^{int} of the interaction region. $\langle V_z^{ev}\rangle$ and σ_z^{int} are then used to constrain the z-vertex position in a fit to determine the polar angle of a track. Since the width of the interaction region, σ_z^{int}, is mainly determined by the length of the positron and electron bunches, the contribution due to the finite z-detector resolution can be safely neglected. $\langle V_z^{ev}\rangle$ is not constant over a certain data taking period at LEP. The variation is related to changes in the hardware status and the operating conditions of LEP. However, one can assume that during one fill of LEP the status does not change considerably, because this would cause a loss of the beam. Therefore, the interaction position can be considered as constant during one fill. A time dependent determination of $\langle V_z^{ev}\rangle$ is performed by averaging the $e^+e^- \rightarrow \mu^+\mu^-$ and $e^+e^- \rightarrow e^+e^-$ events fill by fill. Figure 5.11 shows these fill vertices, $V_z^{fill} = \langle V_z^{ev}\rangle^{fill}$ for 1991 and 1992. Figure 5.12 shows the results of a Gaussian fit to the V_z^{ev} distribution for the 1991 and 1992 data sample. For 1991 and 1992 one finds a

[1] The point $V_{x,y}^{fill}$ is the average position of the interaction point in x and y direction for one LEP fill. Thus, its definition corresponds to the definition of V_z^{fill}, which will be given later on in this chapter. This point is determined using the TEC [39].

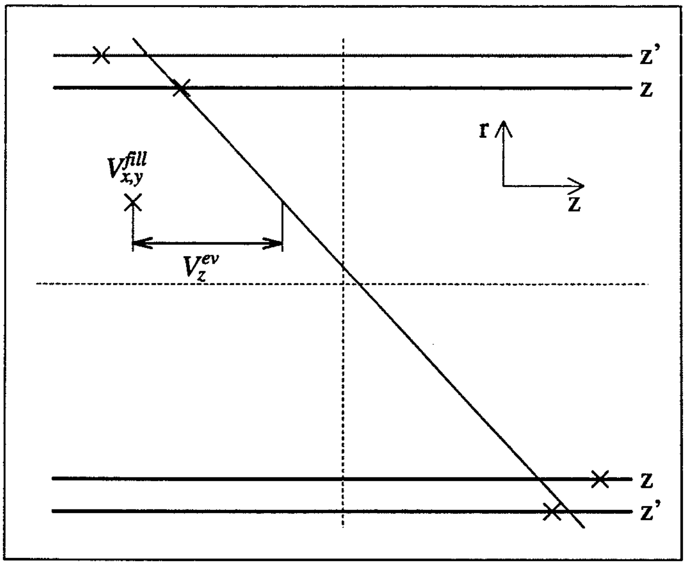

Figure 5.10: Z-vertex determination using the z-detector.

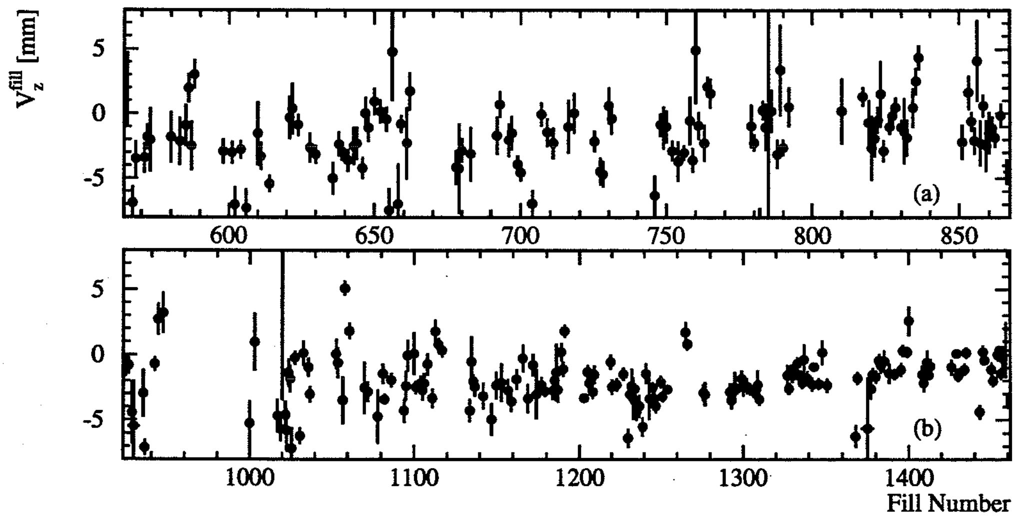

Figure 5.11: The fill vertices, V_z^{fill}, for (a) 1991 and (b) 1992.

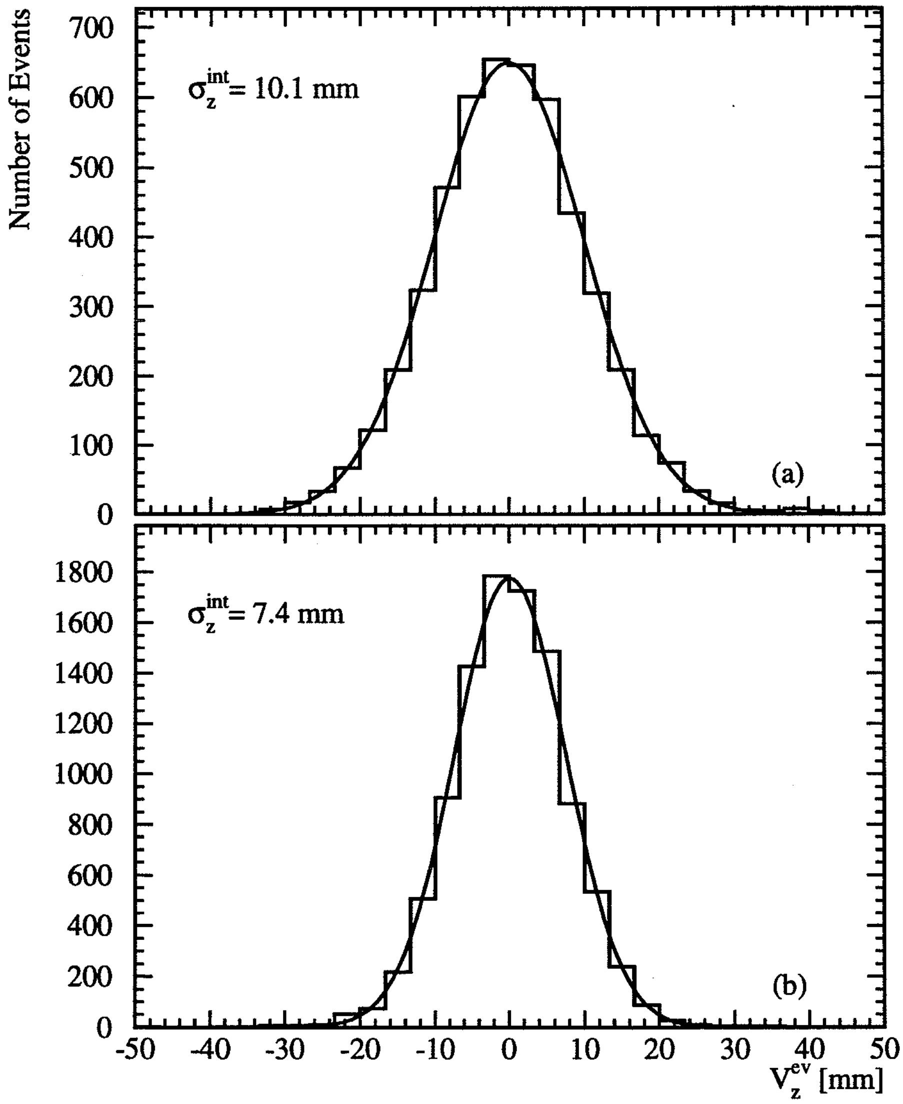

Figure 5.12: Width of the interaction region in z direction measured with $e^+e^- \rightarrow \mu^+\mu^-$ and $e^+e^- \rightarrow e^+e^-$ events taken in (a) 1991 (b) 1992.

width of the interaction region of:

$$\begin{aligned} \sigma_z^{int}(1991) &= 10.1 \pm 0.1 \text{ mm}, \\ \sigma_z^{int}(1992) &= 7.40 \pm 0.06 \text{ mm}. \end{aligned} \tag{5.11}$$

5.6.3 Single hit resolution

As shown in the previous section, in general, a precise determination of the z-vertex for one event is not possible. Therefore, one has to use V_z^{fill} in Equation 5.9:

$$z_{ex} = V_z^{fill} + \frac{R_O}{R_I}(z - V_z^{fill}). \tag{5.12}$$

The width, σ_{raw}, of the distribution of the difference between the coordinate measured in the outer chamber and the projection of the coordinate from the inner chamber, $\sigma(z' - z_{ex})$, is a function of the resolution of inner and outer z-chamber, σ_{ZI} and σ_{ZO}, and the finite size of the interaction region, σ_z^{int}:

$$\sigma_{raw}(z) = \sigma(z' - z_{ex}) = \sqrt{\frac{R_O^2}{R_I^2}\sigma_{ZI}(z)^2 + \sigma_{ZO}(z')^2 + \hat{\sigma}_z^{int}(z)^2}, \tag{5.13}$$

where $\hat{\sigma}_z^{int}(z)$ is the width of the interaction region projected onto the outer z-chamber. It can be expressed as follows:

$$\hat{\sigma}_z^{int}(z) = \frac{R_O - R_I}{R_O} \sin\theta(z)\sigma_z^{int}, \tag{5.14}$$

where θ is given by the inner z-coordinate, z. $\hat{\sigma}_z^{int}(z)$ has its maximum at $z = 0$, which amounts to 20 μm. Therefore, the contribution of $\hat{\sigma}_z^{int}(z)$ to the z-chamber resolution can be safely neglected, since the theoretically expected resolution is 280 μm (see Section 5.2). If one assumes that the resolution for both chambers, σ_{CH}, is the same, Equation 5.13 simplifies to:

$$\sigma_{raw}(z) = \sqrt{(\frac{R_O^2}{R_I^2} + 1)}\ \sigma_{CH}(z). \tag{5.15}$$

Since $R_O / R_I = 1.019 \approx 1$, σ_{CH} can be finally written as:

$$\sigma_{CH}(z) = \frac{\sigma_{raw}(z)}{\sqrt{2}}. \tag{5.16}$$

If one calculates z_{ex} according to Equation 5.12 one gets a resolution for one z-chamber for particles traversing the detector perpendicular to the beam axis of:

$$\sigma_{CH}(\theta \sim 90^\circ) = 320\ \mu\text{m}, \tag{5.17}$$

as shown in Figure 5.13(a). This number is only 40 μm higher than the theoretically expected resolution in Section 5.2. In Figure 5.13(b) the z dependence of σ_{CH} is plotted.

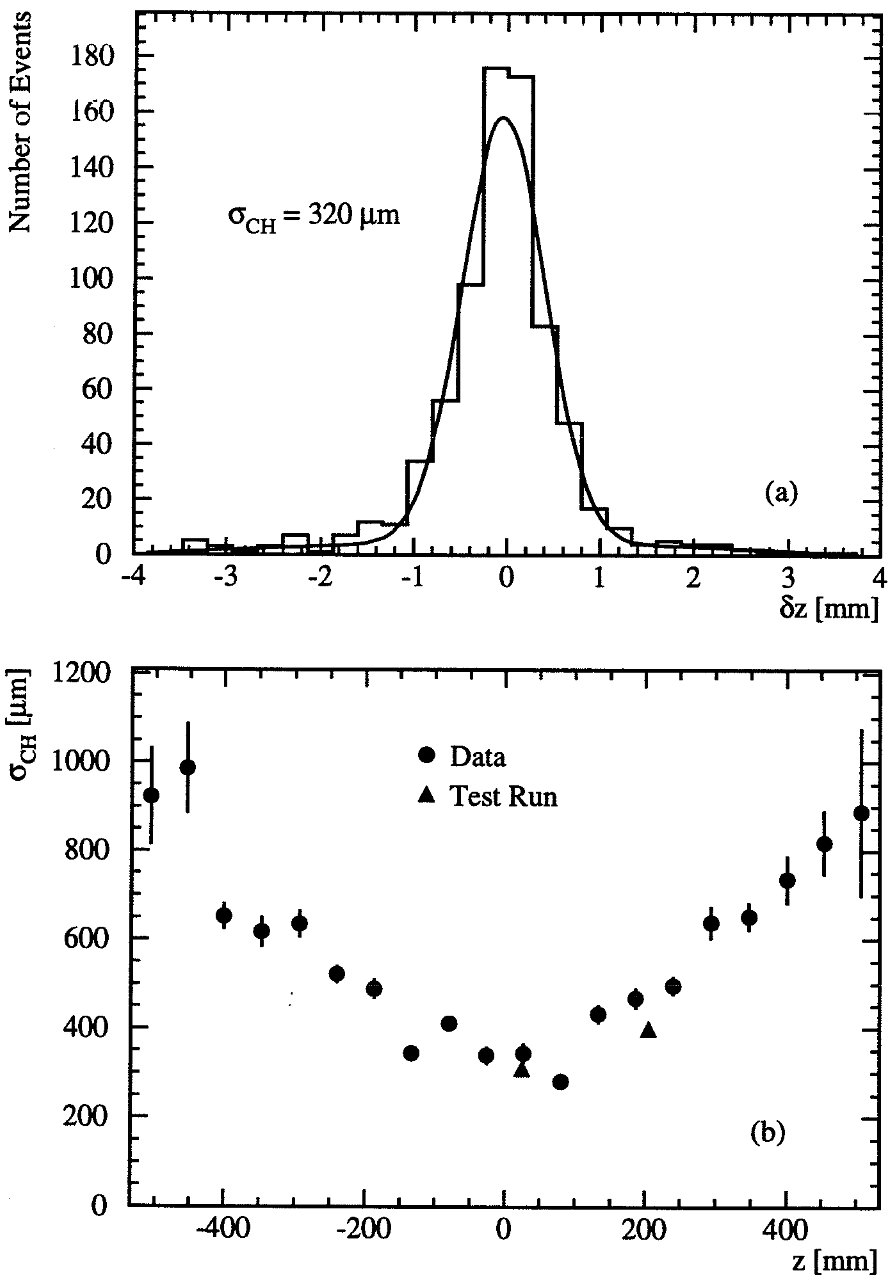

Figure 5.13: (a) $z' - z_{ex}$ for muons crossing the z-detector perpendicular. The width of this distribution results in σ_{CH} = 320 μm. (b) Resolution of one z-chamber as a function of z for data taken 1991 and 1992 and for the test run.

It agrees well with the test beam results. The z dependence of the resolution is a reflection of the fact, that the induced charge avalanche on the anode wire is nearly point-like only for perpendicular incidence. If the track crosses the z-detector at a different angle than $90°(z = 0$ mm), the avalanche is smeared along the anode wire. Therefore, the z-detector hits are wider and the resolution degrades.

5.6.4 Double hit resolution

The double hit resolution is estimated utilizing the back-to-back topology of $e^+e^- \rightarrow e^+e^-$ and $e^+e^- \rightarrow \mu^+\mu^-$ events. Due to the ring like structure of the z-measuring cathode strips, hits produced by either of the two tracks start to overlap in the center of the chamber. Thus, near $\theta = 90°$ in most of the cases the overlapped cluster cannot be separated by the cluster finding algorithm. If one plots the events, with both tracks having the same z-hit assigned, as a function of z, one finds the distribution in Figure 5.14. The width of this distribution is interpreted as double hit resolution, $\sigma_D = 9$ mm.

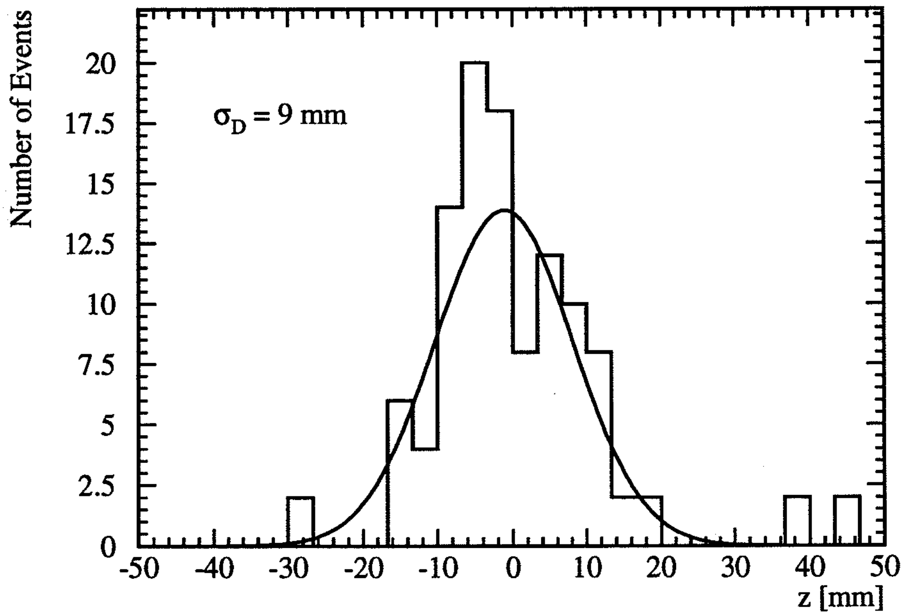

Figure 5.14: The number of $e^+e^- \rightarrow e^+e^-$ and $e^+e^- \rightarrow \mu^+\mu^-$ events with the same z-coordinate assigned to both tracks as a function of z. The width of this distribution is considered as the double hit resolution, σ_D.

5.6.5 Efficiency

The efficiency of the z-detector is studied, using $e^+e^- \rightarrow e^+e^-$ events, with the BGO used as reference. This allows the efficiency to be studied as a function of z and ϕ. In Figure 5.15 and 5.16 the efficiency of the two chambers for 1992 is plotted. The global efficiency for the inner and outer chamber, ε_{ZI} and ε_{ZO}, is determined to be

$$\varepsilon_{ZI} = 93.5\%, \varepsilon_{ZO} = 97.2\%, \tag{5.18}$$

for 1991 and

$$\varepsilon_{ZI} = 92.4\%, \varepsilon_{ZO} = 96.8\%, \tag{5.19}$$

for 1992. The reasons that ε_{ZI} is 4% lower than ε_{ZO} are:

- One high voltage distribution module for the anode wire was not stable during 1991 and 1992. This reduces the efficiency by 2%.
- The inner chamber has eight channels, which do not deliver reliable signals. There are only two such channels in the outer chamber. Due to that the efficiency is reduced by an additional 2% compared to the other chamber.

The combined efficiency to have a hit in at least one chamber, ε_{tot}, is close to 100 % and and the variation with z and ϕ is negligible. If one corrects for the inefficiency caused by hardware problems, the intrinsic efficiency for each chamber is around 97% and fits well to the result derived in the test beam (see Section 5.5).

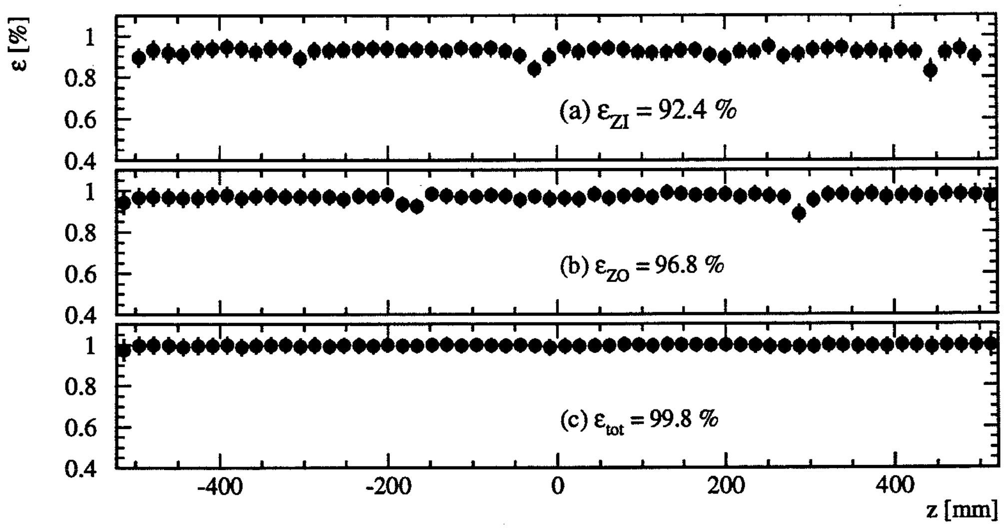

Figure 5.15: Efficiency of the (a) inner and (b) outer z-chamber and (c) their combination as a function of z for 1992.

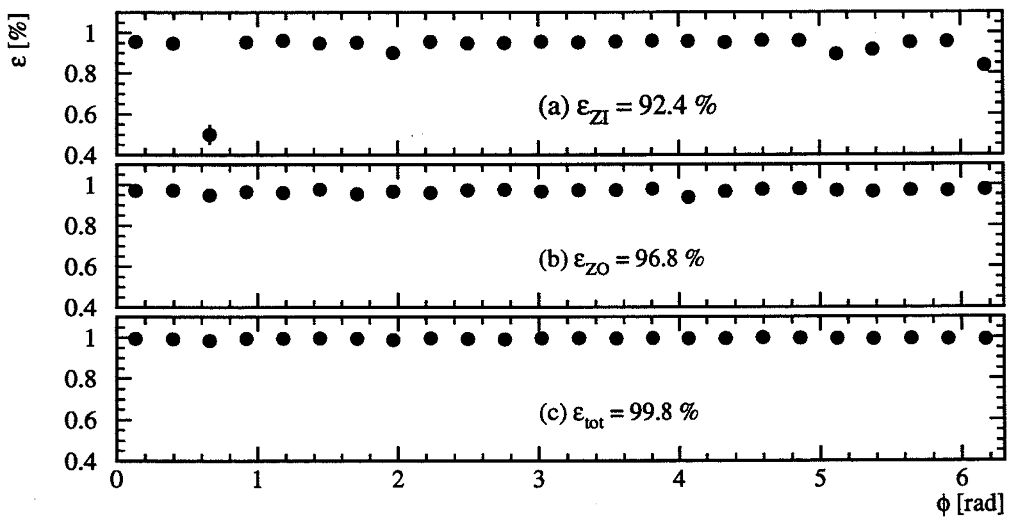

Figure 5.16: Efficiency of the (a) inner and (b) outer z-chamber and (c) their combination as a function of ϕ for 1992.

Chapter 6

Data Analysis

This chapter describes the experimental methods used to analyze the neutral current process $e^+e^- \rightarrow \tau^+\tau^-$ and their results. A complete analysis of the neutral current requires the measurement of the total cross section and of three asymmetries. At LEP the forward-backward, polarization and forward-backward polarization asymmetries are measured. Special emphasis is given to the polarization asymmetries, because they can be determined only in the τ channel.

Since the Monte Carlo technique is an important tool in experimental high energy physics, and in particular for the determination of polarization asymmetries, the basic ideas are introduced in Section 6.1. In Section 6.2 the selection of $e^+e^- \rightarrow \tau^+\tau^-$ events is described, which is especially designed for the measurement of the polarization asymmetries. In Sections 6.4, 6.5 and 6.6 the measurements of the total cross section and the asymmetries are described using the 1990-1992 data taken with the L3 detector. The analysis of the polarization asymmetries is discussed in detail. For the total cross section and the forward-backward asymmetry the general ideas of the measurement are explained and the results are presented.

The conventions used in histograms and figures in this chapter are introduced in Figure 6.1.

6.1 The Monte Carlo Technique

The Monte Carlo (MC) technique is an important tool in high energy physics analysis to describe the performance of detectors. Usually modern detectors are far too complex for an analytical description of their response to a traversing particle. Instead, in the MC technique the interactions of a particle with matter on its path through the detector are modeled locally. The generation of particles and their interactions are treated as a probability process. One has to distinguish three phases.

The process starts with the generation phase. Here events of a certain physical process are generated. Each particle in the event is characterized by its energy and momentum. The distribution function of energy and momentum is defined by the underlying physical model. Event-generators suited for physics at the Z resonance are described in [40] and

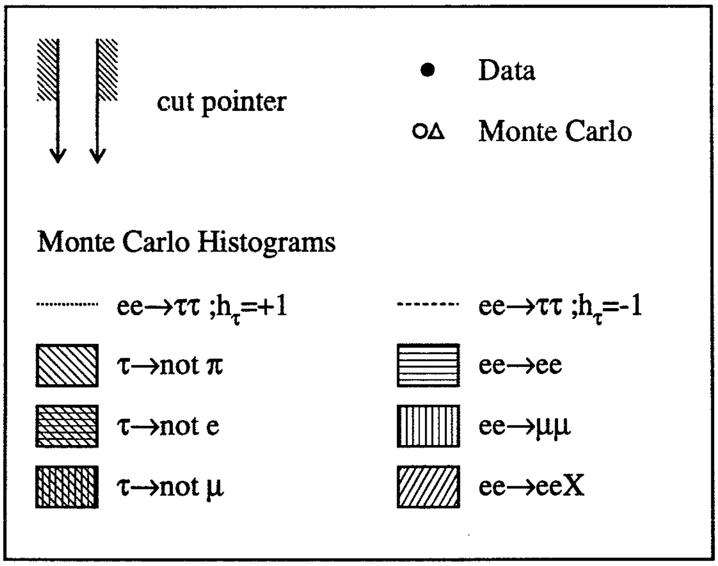

Figure 6.1: Conventions used to label different decay channels and the data in histograms. The arrows indicate the cut on a histogram. The part of the spectrum on the shaded side of the arrow is rejected. The shaded boxes show the contribution of the different decay modes and background. The dashed lines show the expected contributions of the two τ helicity states.

their interface to the L3 software in [41]. In the context of this thesis the most important generators are KORALZ [42], which simulates the process $e^+e^- \to f\bar{f}$, where f can be any fermion except an electron. The decay of the τ lepton is simulated in the package TAUOLA [43].

In the next phase, the simulation phase, the particles are tracked from the generation point through the detector taking the magnetic field into consideration. Interactions of these particles with different detector materials and their subsequent decays are simulated. At this stage empirical information about the behaviour of certain materials is taken into account, which was studied in test beams or earlier experiments. Also non-ideal detector properties, like noisy or broken read-out channels can be introduced. Each particle is followed until it annihilates or its energy falls below a certain cut-off value. Then the remaining energy of the particle is usually deposited in the detector. Phase 2 also simulates the response of the readout electronics. The information at the end of this phase is constructed to be identical to that from the real detector, with additional information that gives the source of each energy deposition. The simulation software is based on the detector-simulation package GEANT [44].

Phase 3, the reconstruction phase is the same for MC and real data events. The information of the readout electronics is analyzed to extract the relevant physical quantities, such as particle tracks, momenta and energy depositions in the different parts of the detector.

If the agreement between the distributions of data and MC for physical observables is satisfactory, one can trust the MC to estimate trigger and detection efficiencies of the detector for certain particle and event classes [1]. If a disagreement appears, one has different possibilities to account for it. The preferred method is to find the subprocess or material, which is not properly simulated and is responsible for the disagreement. A more detailed detector simulation can help to reduce the disagreement. Another possibility is to smear or reweight the variable, which is badly reproduced by the MC according to the corresponding data distribution. Finally, one can consider the disagreement as a contribution to the systematic error of the physics analysis.

6.2 Selection of $e^+e^- \to \tau^+\tau^-$ Events

The overall goal of a selection is the identification of certain events or particles within a data sample containing different types of events and particles. The desired events or particles are selected by applying specific criteria (cuts) to physical observables. The cuts are tuned to find a compromise between maximizing the selection efficiency and minimizing the background contamination.

The selection of $e^+e^- \to \tau^+\tau^-$ events, described in the following, is designed for the measurement of polarization asymmetries. Therefore, one has to avoid selection biases due to explicit cuts on variables which are used to determine the polarization, for example the energy of the final decay products of the τ or the acollinearity of the event. This complicates the selection substantially in comparison with selections aimed at a measurement of total cross sections and forward-backward asymmetries. For an example of this simpler selection see [45,46].

Due to the short lifetime of the τ, one has to select the process $e^+e^- \to \tau^+\tau^-$ by detecting the τ decay products. These decay products are electrons, e, and muons, μ, for leptonic decay modes and charged and neutral pions, π, π^0, for hadronic decay modes of the τ[2]. All decays are accompanied by neutrinos, ν, which escape detection. Therefore, the total energy of all detectable decay particles is distributed over a wide energy range, rather than clustering at the energy of the τ of 45 GeV. Furthermore, a τ decay is characterized by a single charged track or a low multiplicity jet with less than or equal to five charged tracks [3]. Due to the high center-of-mass energy at LEP the jets are highly collimated and the jets or tracks of both τ's are almost back-to-back. An example for such an event seen in the L3 detector is given in Figure 6.2. The τ in the upper hemisphere decays into a ρ, characterized by one charged track in the TEC, which does not point to the center-of-gravity of the BGO shower. The track belongs to the charged π. The π^0 generates the large BGO signal, which does not match with the TEC track. In the lower half of the figure the

[1] This assumes that the number of MC events is normalized to the integrated luminosity.

[2] The main decay modes are listed in Table 2.2

[3] The probability that the τ decays into five charged tracks (5-prong branching ratio) is $(1.11 \pm 0.24) \times 10^{-3}$. The 7-prong branching ratio is less then 1.9×10^{-4} [14].

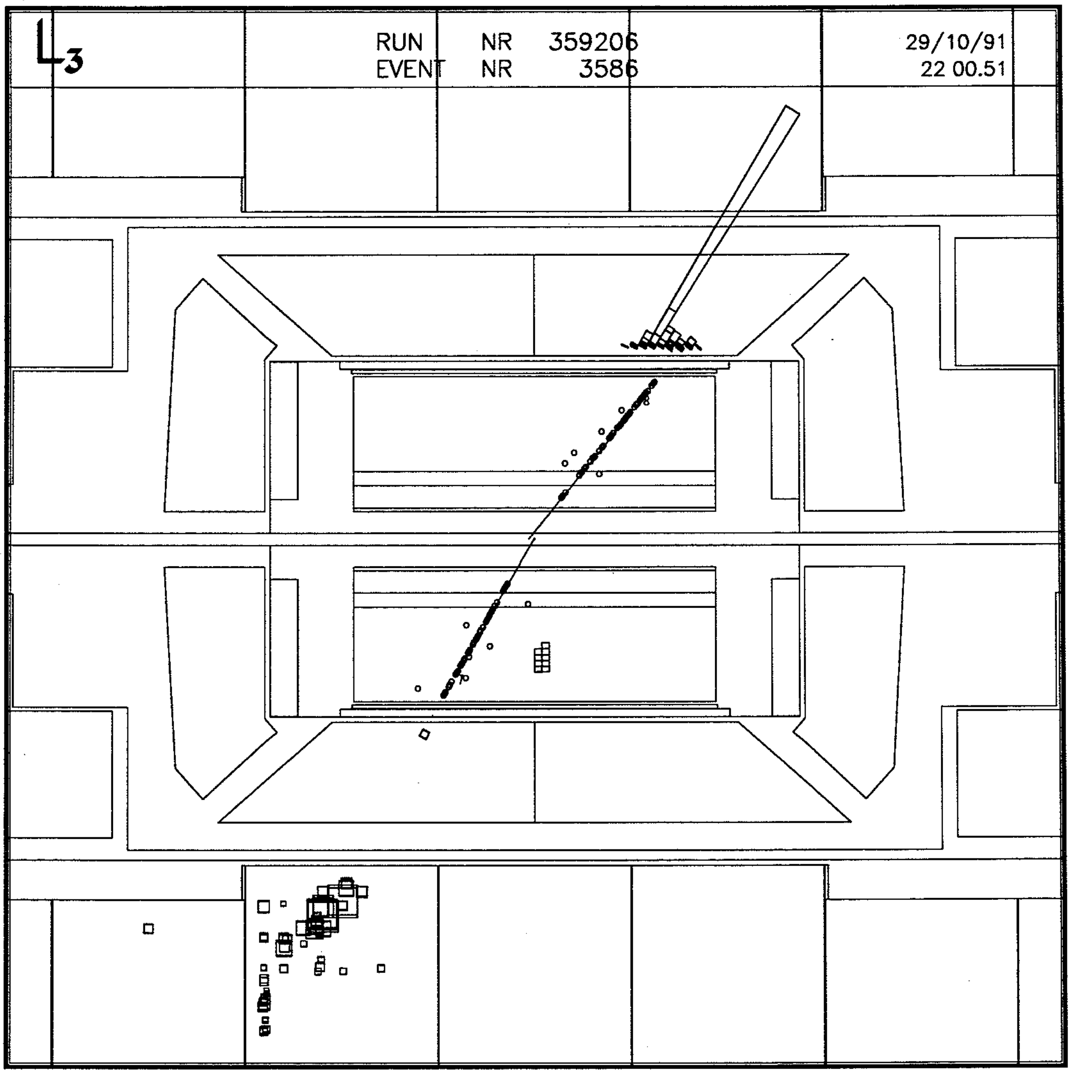

Figure 6.2: A $e^+e^- \to \tau^+\tau^-$ event seen by the L3 detector. The view of the L3 detector in the (r,z) plane parallel to the beam axis is shown. The beam pipe goes from left to right in the middle of the figure. The subdetectors displayed are the TEC, closest to the beam pipe, followed by the BGO and the HCAL at the edge of the figure. The decay in the upper hemisphere is identified as $\tau \to \rho\nu$ and in the lower hemisphere as $\tau \to \pi\nu$.

τ decays into a single π. The π is characterized by the presence of only one charged track lined up with minimal energy deposition in the BGO and an HCAL signal.

The processes, which have to be suppressed by the $e^+e^- \to \tau^+\tau^-$ selection are those with two leptons in the final state, $e^+e^- \to e^+e^-$ and $e^+e^- \to \mu^+\mu^-$, multi hadron production, $e^+e^- \to q\bar{q}$, the two photon process, $e^+e^- \to e^+e^-X$, where the outgoing e^+e^- pair continues in the beam pipe, and cosmic muon events.

The selection is restricted to the central part of the L3 detector (barrel) only, with $|\cos\theta| < 0.72$, which is defined by the acceptance of the z-detector [4]. The polar angle, θ, is determined with the z-detector and each track has to fulfill the requirement above. This reduces the acceptance of $\tau^+\tau^-$ events to 60%. The event is subdivided into two hemispheres, each assigned to one fermion originating from the Z decay. The hemisphere is defined by the plane perpendicular to the thrust axis. The general flowchart of the $e^+e^- \to \tau^+\tau^-$ selection is given in Figure 6.3. One starts from the total data sample recorded with L3. In the *preselection* discussed in Section 6.2.1 the *lepton sample*, $e^+e^- \to \ell^+\ell^-$, is selected. Cosmic muon events, $e^+e^- \to q\bar{q}$ and $e^+e^- \to e^+e^-X$ are rejected. To suppress the remaining background from $e^+e^- \to e^+e^-$ and $e^+e^- \to \mu^+\mu^-$ an *electron* and a *muon identification* is developed, which are discussed in Sections 6.2.2 and 6.2.3 respectively. All events with two identified electrons or muons are rejected. If an electron or muon is detected in only one hemisphere, the particle in the *recoil* hemisphere is tested again. For this additional test, the same criteria as the electron or muon identification are used, but the cuts are less strict. Applying these selection criteria to the 1991 and 1992 data samples selects a $\tau^+\tau^-$ *sample* of 7787 and 16778 candidates respectively. The efficiency within the fiducial volume and the different background sources are given in Table 6.1. The error on the efficiency amounts 0.2%. Since there are small differences

	1991	1992
Efficiency		
$e^+e^- \to \tau^+\tau^-$	86.8 %	86.1 %
Background		
$e^+e^- \to e^+e^-$	0.7 %	0.8 %
$e^+e^- \to \mu^+\mu^-$	0.6 %	0.6 %
$e^+e^- \to e^+e^-X$	0.1 %	0.1 %
$e^+e^- \to q\bar{q}$	2.0 %	2.0 %
cosmic muons	<0.1 %	<0.1 %
Total	3.4 %	3.5 %

Table 6.1: Efficiency and background for the $\tau^+\tau^-$ selection in the fiducial volume $|\cos\theta| < 0.72$.

[4] The measurement of τ polarization with the acollinearity method (see Section 6.6.3) relies on the z-detector.

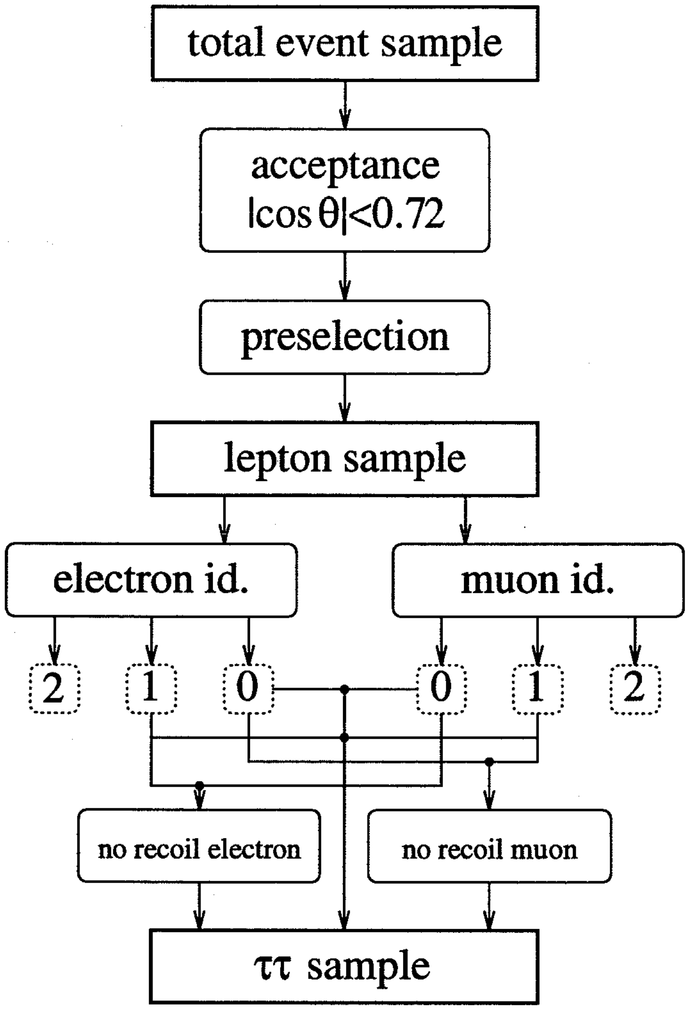

Figure 6.3: The $\tau^+\tau^-$ selection.

in the detector performance and LEP parameters between 1991 and 1992, for simplicity the histograms in the following Sections 6.2.1, 6.2.2, 6.2.3 and 6.3.1 explaining the cut criteria show only 1992 data.

6.2.1 Preselection

The aim of the preselection is to select the leptonic Z decay modes $e^+e^- \rightarrow \ell^+\ell^-$ and to reject $e^+e^- \rightarrow q\bar{q}$, $e^+e^- \rightarrow e^+e^-X$ and cosmic muons.

Cosmic muon events are rejected using the time information of the scintillators and asking for at least one TEC track passing the interaction region within 5 mm in the (r, ϕ) plane. The rejection of $e^+e^- \rightarrow q\bar{q}$ events relies on their high charged track multiplicity at LEP energies due to the fragmentation of quarks. The number of charged particles generated in the fragmentation process depends on the energy of the quark and is typically higher than 10 at LEP. The number of charged tracks in a $\tau^+\tau^-$ event is given by the decay mode and is less or equal to 5 per τ decay [5]. The $e^+e^- \to q\bar{q}$ background is thus reduced requiring not more than five TEC tracks per hemisphere. Furthermore, the maximum angle of a track to the thrust axis should be less than 20° and the number of BGO clusters less than 20. These cuts decrease the $e^+e^- \to q\bar{q}$ background to 2%. The two-photon process $e^+e^- \to e^+e^-X$ is rejected by cutting on the total event energy, $E_{tot} > 8$ GeV, as shown in Figure 6.4. All cuts of the preselection, apart of the cut on E_{tot} are already applied in Figure 6.4.

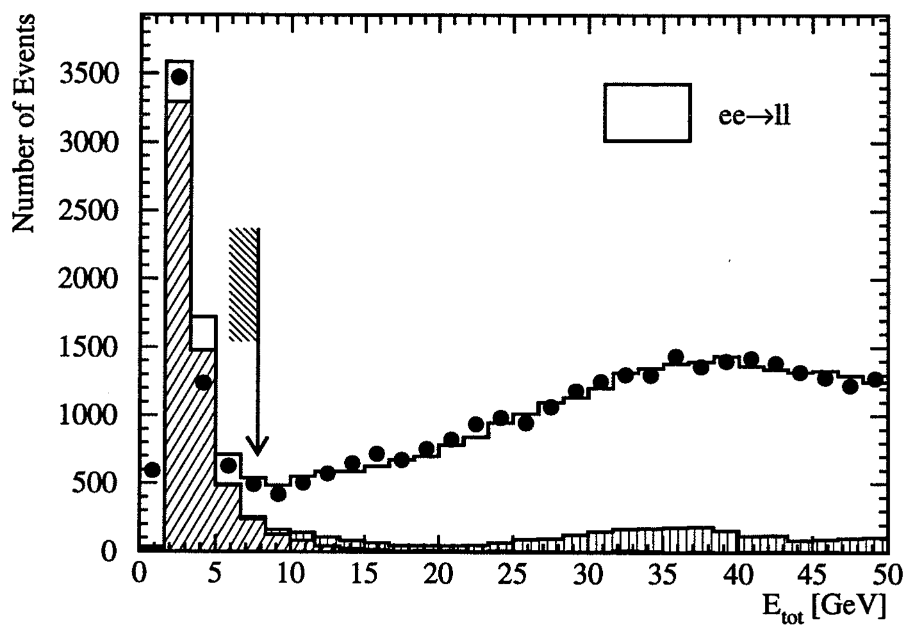

Figure 6.4: The total energy of the event. See Figure 6.1 on Page 62 for the conventions used to label the histograms.

6.2.2 Electron identification

To identify electrons traversing the L3 detector the characteristics of their interaction in the BGO are used. For a few particles which escape detection in the BGO, because they pass through the calorimeter in between the BGO crystals in the carbon fiber support structure, the energy deposition in the HCAL is also considered for identification. Signals in the muon filter and muon chambers are used as an electron veto. An electron candidate is required to have only one charged track per hemisphere in the TEC. The BGO cluster

[5]See Footnote 3 on Page 63.

which the charged track points to, in the following referred to as a charged cluster, is further examined. Following the introduction to this chapter, one tries to avoid a bias of the polarization measurement due to the electron identification by using variables which are almost independent of energy. The flowchart of the electron identification is given in Figure 6.5.

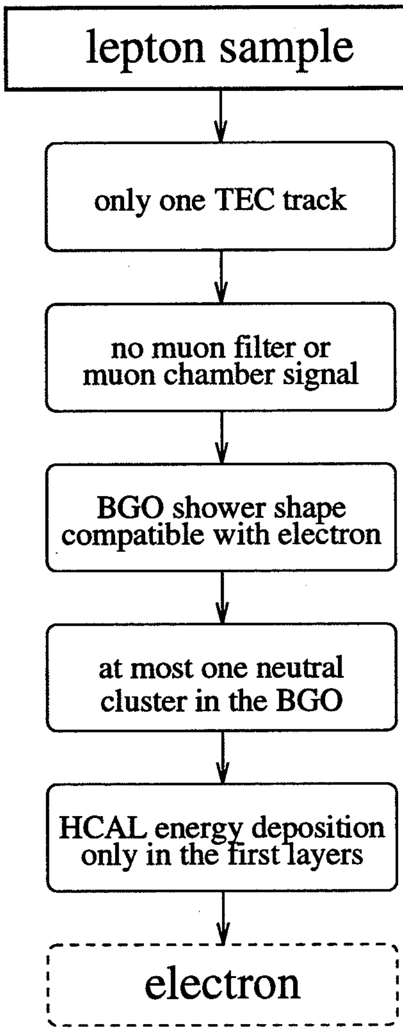

Figure 6.5: The electron identification.

A cluster in the BGO can be characterized, for example, by its lateral shape and the lateral position of its center-of-gravity with respect to the entry point of the particle into the BGO. This entry point is determined with the TEC and the z-detector. One variable describing the lateral shape of a shower is defined as the ratio of the energies deposited in the 3×3 and 5×5 crystal matrix around the shower center :

$$\frac{\sum_9}{\sum_{25}} = \frac{\sum_{i,j=-1}^{+1} E_{i,j}^{Cry}}{\sum_{k,l=-2}^{+2} E_{k,l}^{Cry}}, \tag{6.1}$$

where $E_{i,j}^{Cry}$ is the energy measured in one BGO crystal. The crystal with maximum energy is in the center of the shower, $E_{0,0}^{Cry}$. $\sum_9 / \sum_{25}$ distributions are plotted in Figure 6.6. The top plot, (a), shows the spectrum for data, MC and various background contributions. The MC distributions are normalized to the integrated luminosity. The cut value is marked with an arrow. All electron identification criteria apart from the cut on $\sum_9 / \sum_{25}$ are already applied. The background fraction, β, as a function of the cut value is plotted in (b). β is defined as the fraction of particles, which are selected by the electron identification but do not belong to the processes $e^+e^- \to e^+e^-$ and $\tau \to e\nu\nu$. The efficiency to select electrons, ε, as a function of the cut value is plotted in (c). ε is defined as the fraction of electrons, which are selected out of the total $e^+e^- \to e^+e^-$ and $\tau \to e\nu\nu$ sample which satisfy all other electron identification cuts in the fiducial volume ($|\cos\theta| < 0.72$). The histograms in (b) and (c) illustrate the statement in the beginning of this section, that all cuts are tuned to find a compromise between minimizing β and maximizing ε. All histograms, which explain cut criteria, in this section and in Sections 6.2.3 and 6.3.1 are given in the same manner. For electrons, $\sum_9 / \sum_{25}$ peaks at 0.96. Showers from hadronic particles in the BGO are wider than electromagnetic showers, since the nuclear interaction length is much larger than the radiation length. The tail in Figure 6.6 is mostly populated by pions coming from τ decays. To select electrons, $\sum_9 / \sum_{25}$ is required to be higher than 0.925. The shower shape is characterized also by χ^2_{elm}, which compares the measured energy deposition with the expected one for electrons in the 3×3 crystal matrix . The distribution is shown in Figure 6.7. The cut at 10 is indicated. Furthermore, a cut at 20 mrad on the opening angle between the entry point of the track in the BGO crystal and the center-of-gravity of the shower helps to identify electrons (see Figure 6.8). If the electron hits the BGO only at the carbon fiber support structure between the crystals, it starts to shower deep inside the crystals at the point where it leaves the carbon. In that case the whole shower is not confined in the BGO and a part will reach the HCAL. Such an event can be recognized by its energy deposition restricted to the first HCAL layers. The normalized difference between the total energy in the HCAL, E_{HCAL}, and the energy in the first three HCAL layers, E_{FHCL}, should be less than 0.1, as shown in Figure 6.9. The poor agreement between the data and MC distribution is of secondary importance, because the bulk of electrons deposit no energy in the HCAL. For an electron candidate at most one neutral cluster [6] reconstructed in the BGO is allowed, which is assumed to be a radiative photon.

The efficiency and a breakdown of the different background processes for the electron identification are given in Table 6.2. The error on the efficiency amounts to 0.2%. The agreement of the detection efficiencies for electrons around 45 GeV and electrons with an energy spectrum up to 45 GeV, demonstrates the energy independence of this

[6] A neutral cluster denotes a energy deposition in the BGO, which no TEC track points to. Therefore,

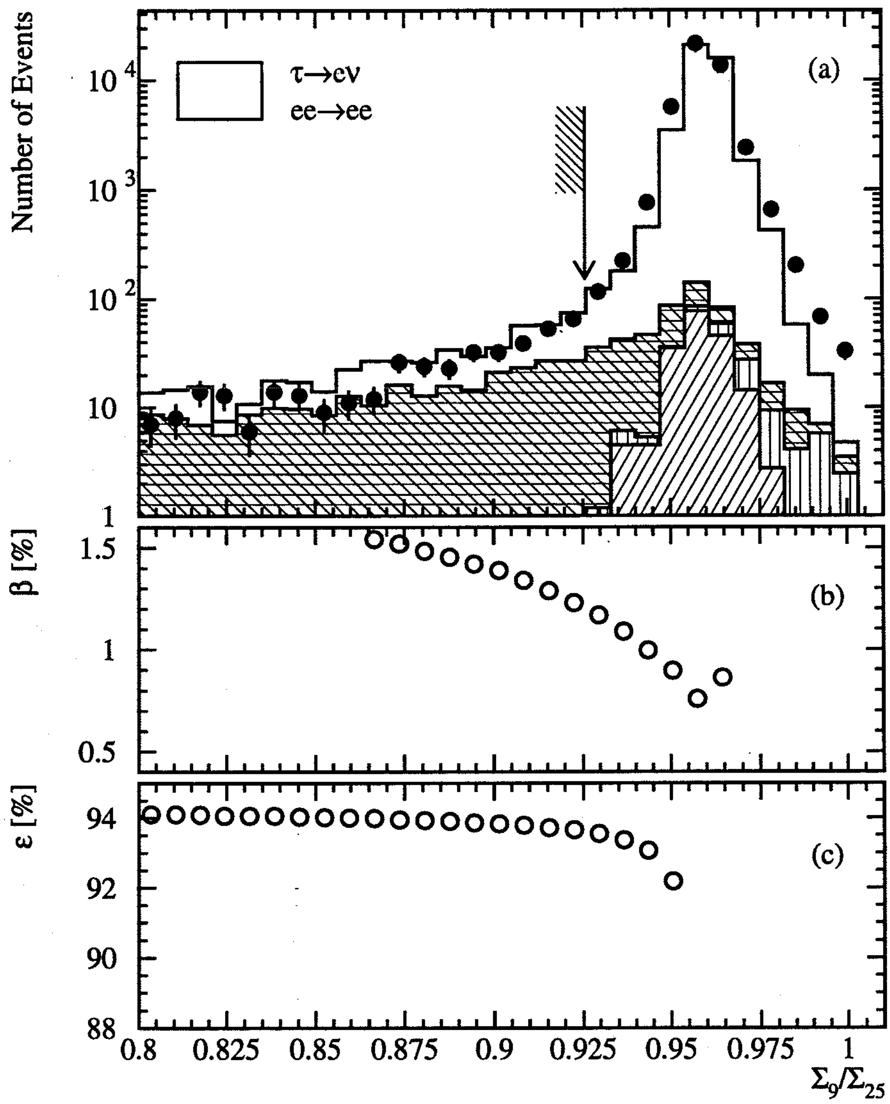

Figure 6.6: The sum of the crystal energy in a 3×3 matrix divided by the sum in a 5×5 matrix around the central crystal. (a) shows the spectrum for data, MC and various background contributions. See Figure 6.1 on Page 62 for the conventions used to label the histograms. In (b) the background ratio, β, is plotted. (c) shows the electron selection efficiency, ε.

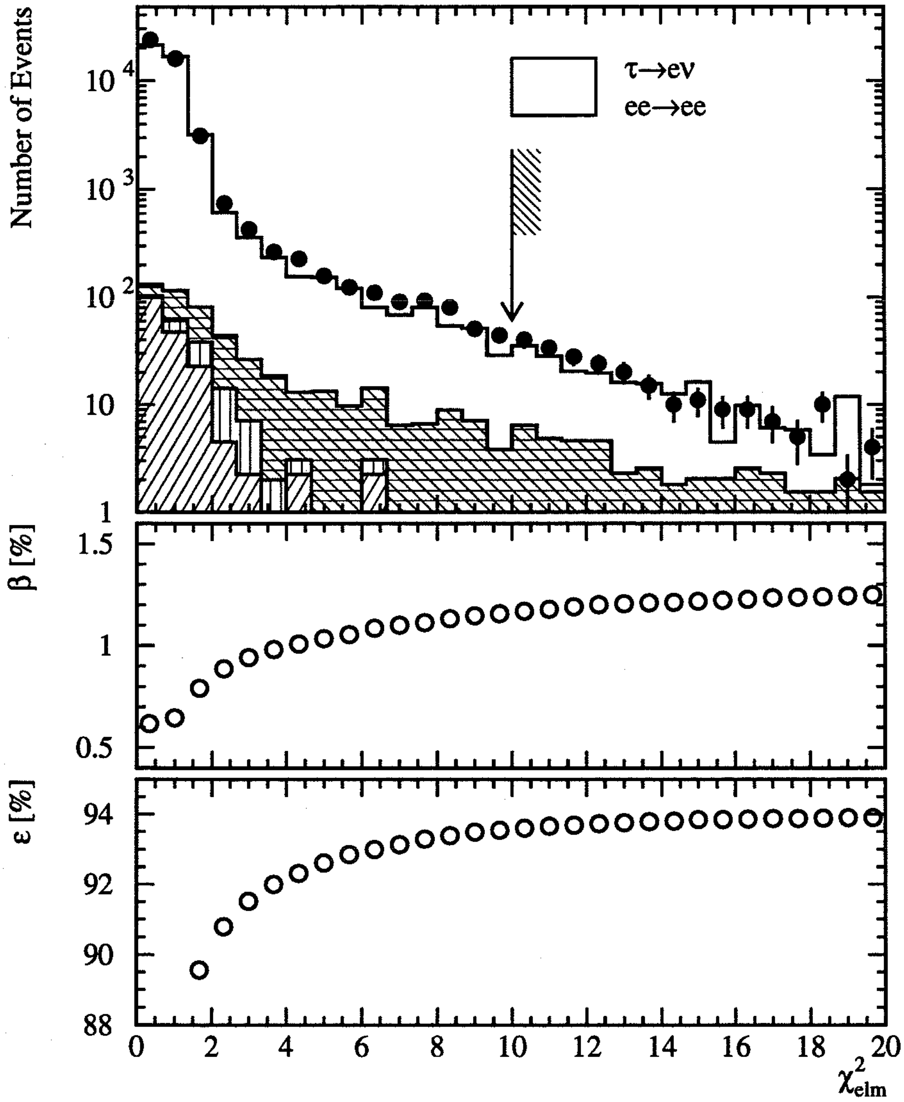

Figure 6.7: The electromagnetic χ^2_{elm} characterizing the shower shape in the BGO.

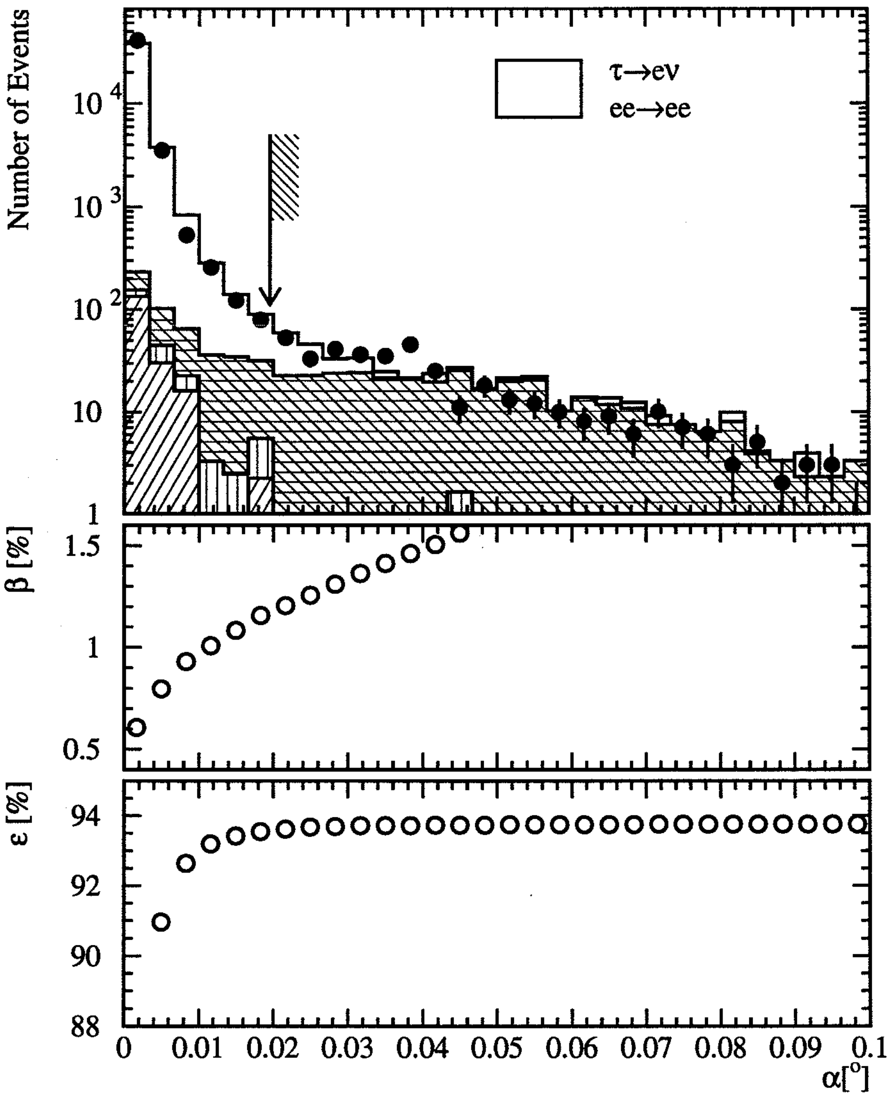

Figure 6.8: The opening angle in ϕ between the TEC track and the charged cluster in the BGO.

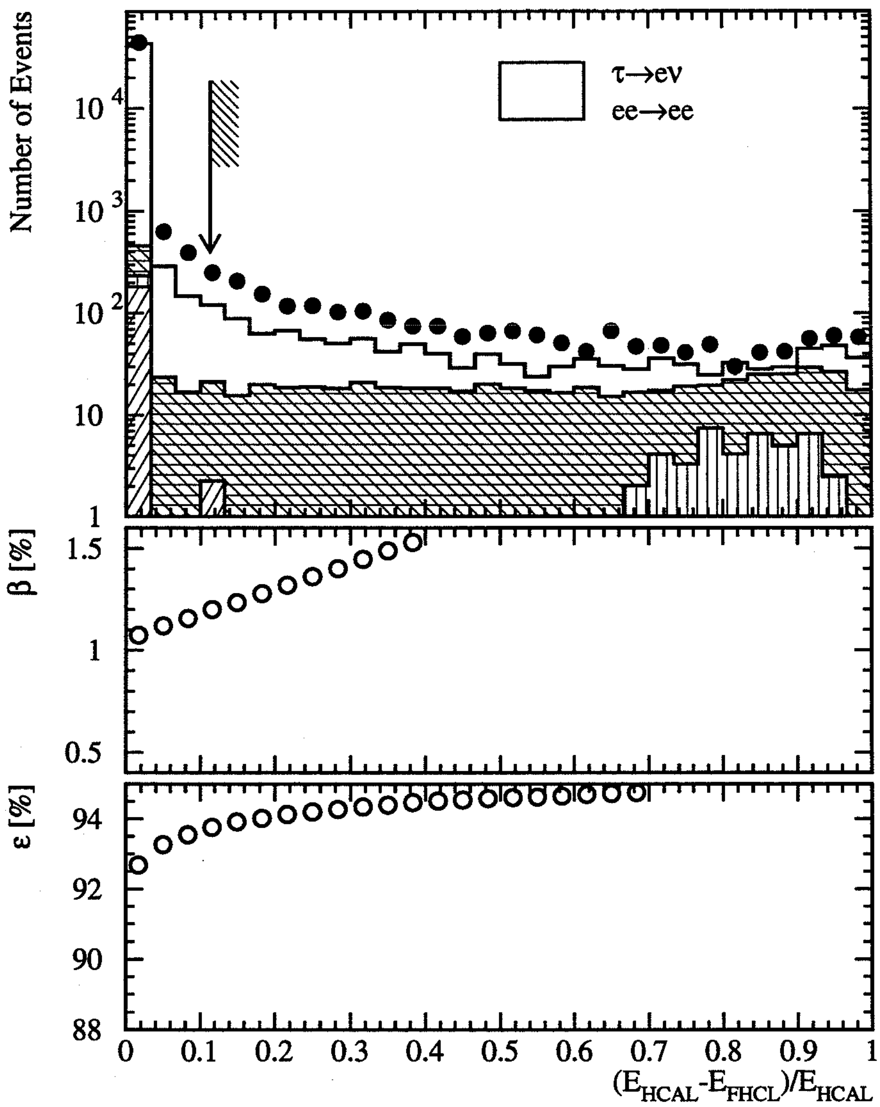

Figure 6.9: The normalized difference, $(E_{\mathrm{HCAL}} - E_{\mathrm{FHCL}})\,/\,E_{\mathrm{HCAL}}$ of the total HCAL energy and the energy in the first three layers of the HCAL.

	1991	1992
Efficiency		
$e^+e^- \to e^+e^-$	93.6 %	93.5 %
$\tau \to e\nu\nu$	94.4 %	93.7 %
Background		
$\tau \to \mu\nu\nu$	negl.	negl.
$\tau \to \pi\nu$	0.3 %	0.3 %
$\tau \to \rho\nu$	0.3 %	0.3 %
$\tau \to a_1\nu$	negl.	negl.
other τ decays	negl.	negl.
$e^+e^- \to \mu^+\mu^-$	0.1 %	0.1 %
$e^+e^- \to e^+e^-X$	0.5 %	0.5 %
Total	1.2 %	1.2 %

Table 6.2: Efficiency and background of the electron identification.

identification. The background consists mainly of $e^+e^- \to e^+e^-X$ and $\tau \to \pi\nu$ decays, where the pion deposits most of its energy in the BGO and $\tau \to \rho\nu$ decays where only one photon coming from a π^0 is reconstructed in the BGO.

6.2.3 Muon identification

To identify muons information from all subdetectors is used, since the muon chambers cover only 85% of the fiducial volume of $|\cos\theta| < 0.72$. Therefore, the muon identification has two streams, each of them sufficient to tag a muon coming from $e^+e^- \to \mu^+\mu^-$ or $\tau \to \mu\nu\nu$. Figure 6.10 shows the flowchart of the muon identification.

The first stream relies only on the muon chambers and accepts all particles, if there is a muon chamber track, detected in at least two out of three layers of the chambers. The tracks has to point to the vertex. Muons from cosmic showers or hadronic punch-through do not usually point to the vertex.

The second stream requires only one track per hemisphere detected by the TEC and then uses the characteristics of the energy deposition of minimum ionizing particles in the calorimeters. Clusters in the BGO from minimum ionizing particles contain a few crystals, where the energy is above the noise threshold (see Figure 6.11). Muon candidates are required to have less than 5 BGO crystals associated with the shower. At most one neutral cluster is allowed in the BGO. In the hadron calorimeter the energy of the tower which was hit by a particle and its direct neighbors, E_{obs}, is added and compared with the expected energy for a minimum ionizing particle, E_{mip}, in these HCAL towers. In Figure

one assumes this energy deposition is caused by a neutral particle. For details about the neutral cluster reconstruction refer to Section 6.3.1.

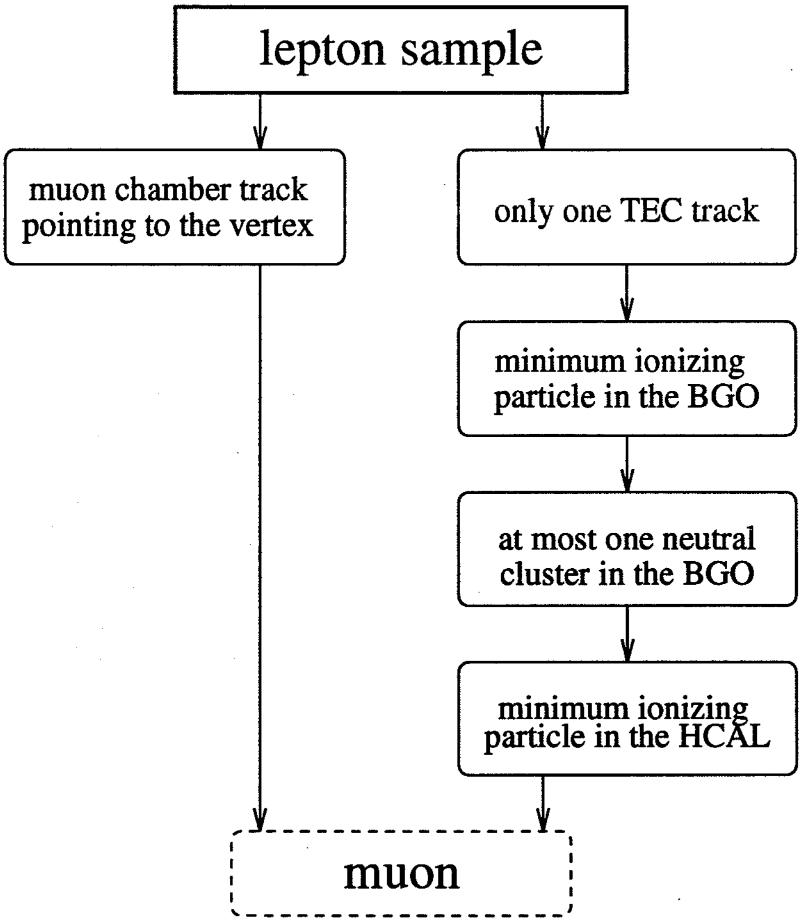

Figure 6.10: The muon identification.

6.12 the difference between E_{mip} and E_{obs} normalized to E_{obs} is plotted. Since one expects almost all energy deposited in the central tower for a muon, this distribution peaks at zero and is cut at -0.4. The reason for the disagreement between the data and MC distributions is, that the HCAL MC simulation is based on an ideal detector, which does not reflect the HCAL resolution properly. Additionally one can cut on the remaining energy of the HCAL cluster, E_{rem}, which is not contained in E_{obs}. This energy must be less than 1 GeV for a muon candidate. Another useful criteria to select muons is the normalized difference between the total energy in both calorimeters and the energy, calculated from the transverse momentum measured in TEC, which should be lower then 0.4.

The combined efficiency and the background for the two streams is given in Table 6.3. The error on the efficiency amounts 0.2%. The main background sources are $e^+e^- \to e^+e^-X$, $\tau \to \pi\nu$, $\tau \to \rho\nu$. The agreement between the selection efficiencies for $e^+e^- \to \mu^+\mu^-$ and $\tau \to \mu\nu\nu$ events demonstrates the weak energy dependence of the muon identification.

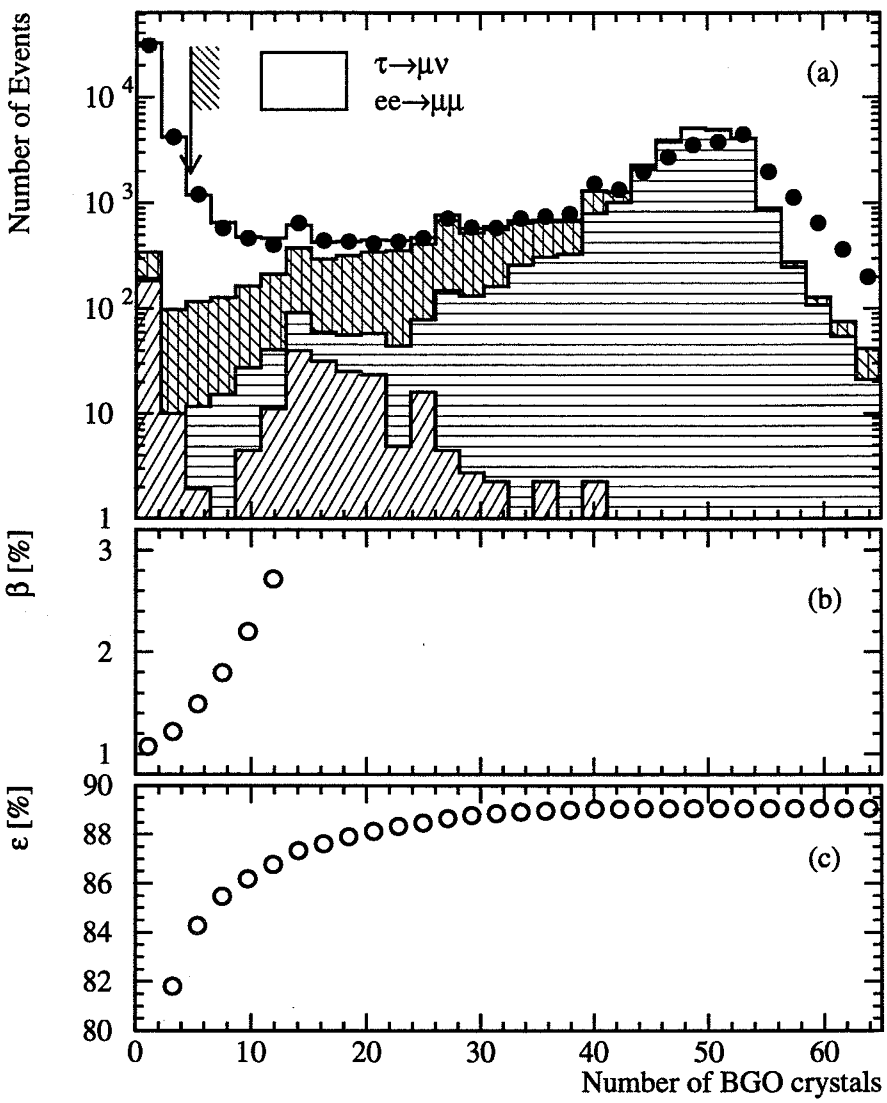

Figure 6.11: The number of crystals belonging to one BGO cluster. (a) shows the spectrum for data, MC and various background contributions. See Figure 6.1 on Page 62 for the conventions used to label the histograms. In (b) the background ratio, β, is plotted. (c) shows the muon selection efficiency, ε.

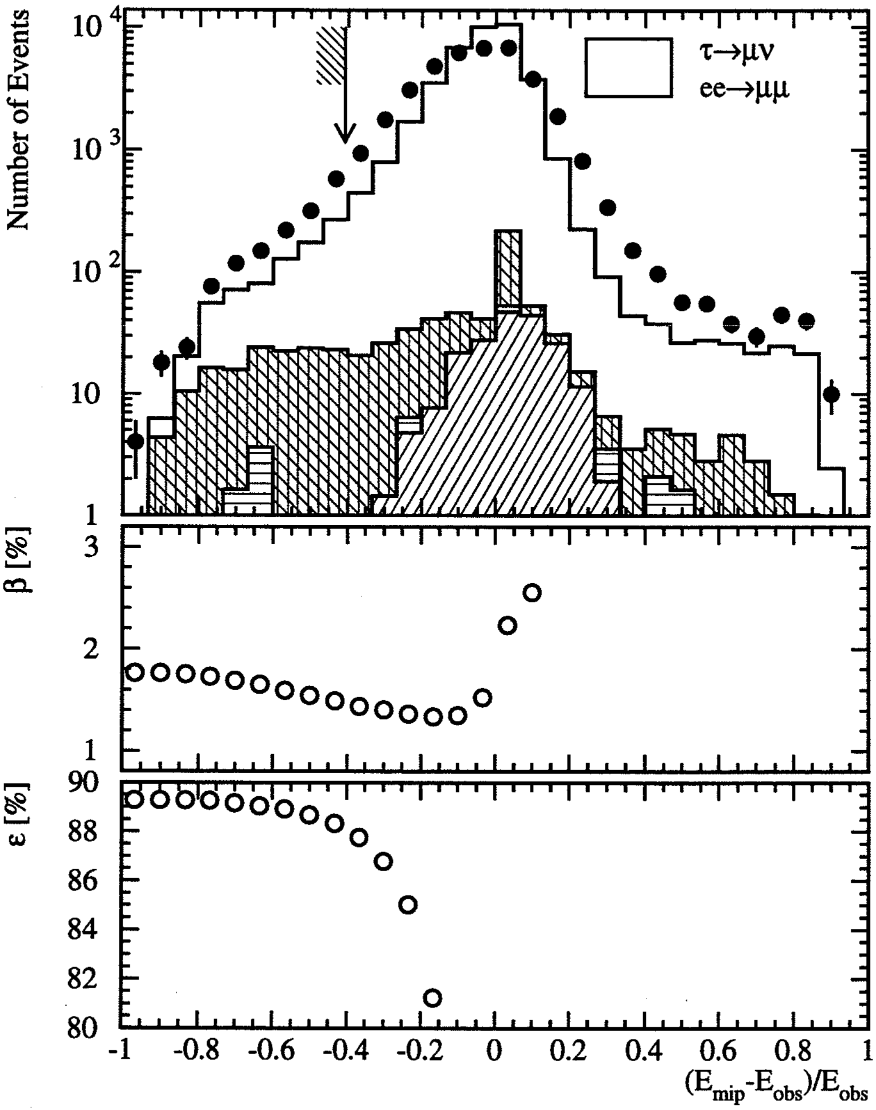

Figure 6.12: The difference between the observed and expected energy of a minimum ionizing particle in the central HCAL towers, $(E_{\text{mip}} - E_{\text{obs}}) \,/\, E_{\text{obs}}$.

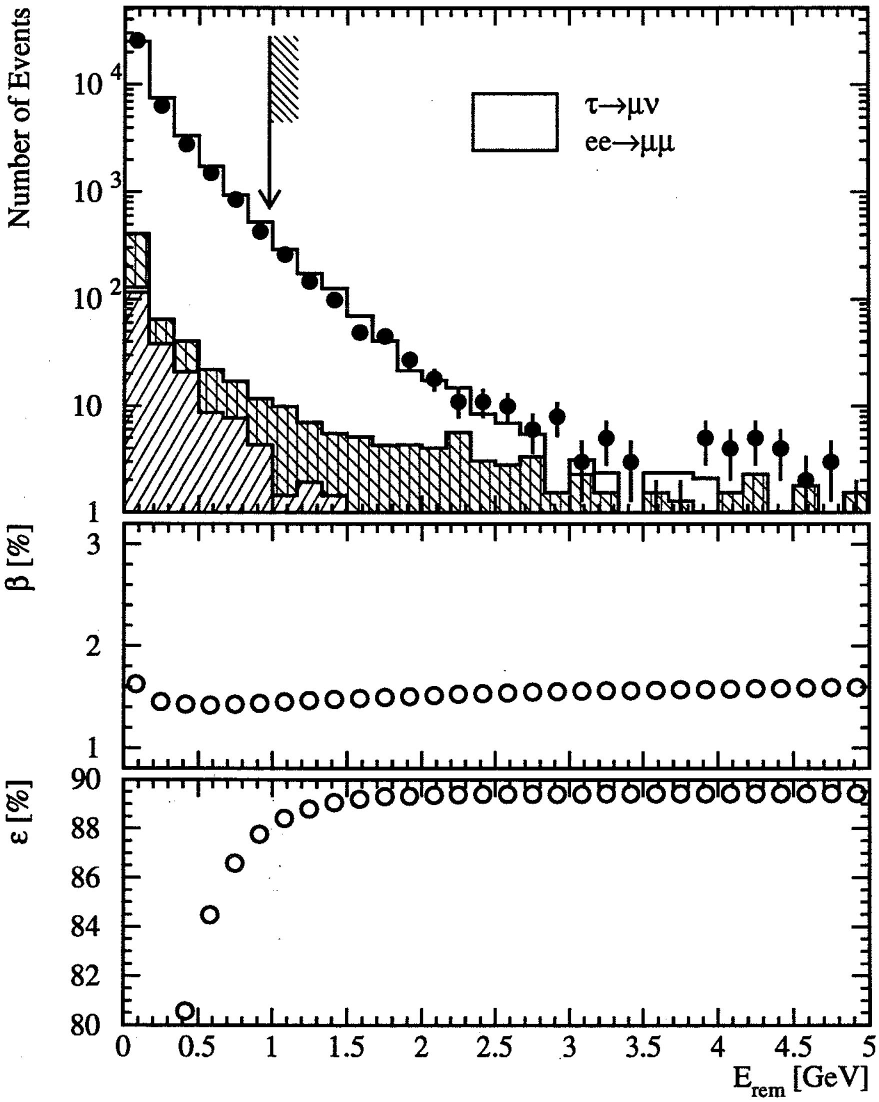

Figure 6.13: The remaining energy, $E_{\rm rem}$, which is not included in $E_{\rm obs}$.

	1991	1992
Efficiency		
$e^+e^- \rightarrow \mu^+\mu^-$	99.0 %	99.0 %
$\tau \rightarrow \mu\nu\nu$	98.7 %	98.9 %
Background		
$\tau \rightarrow e\nu\nu$	0.2 %	0.2 %
$\tau \rightarrow \pi\nu$	0.8 %	0.8 %
$\tau \rightarrow \rho\nu$	0.5 %	0.5 %
$\tau \rightarrow a_1\nu$	0.1 %	0.1 %
other τ decays	0.1 %	0.1 %
$e^+e^- \rightarrow e^+e^-$	negl.	negl.
$e^+e^- \rightarrow e^+e^-X$	0.5 %	0.5 %
Total	2.2 %	2.2 %

Table 6.3: Efficiency and background of the combined muon identification.

6.3 Selection of τ-Decay Modes

The polarization of the τ is measured by analyzing its decay. How one extracts the polarization from the decay depends on the decay mode. The τ polarization has been measured at L3 using the channels $\tau \rightarrow e\nu\nu$, $\tau \rightarrow \mu\nu\nu$, $\tau \rightarrow \pi\nu$, $\tau \rightarrow \rho\nu$ and $\tau \rightarrow a_1\nu$[7]. Since the polarization measurement using the $\tau \rightarrow \pi\nu$ channel is discussed in detail in Section 6.6.3, the selection of this mode is described in Section 6.3.1. The selection for the remaining channels is discussed below in general terms only. The flowchart of the different decay mode selections is given in Figure 6.14.

Beginning from the $\tau^+\tau^-$ sample the $\tau \rightarrow e\nu\nu$ and $\tau \rightarrow \mu\nu\nu$ selection requires only the application of the electron and muon identification. For the hadronic decay modes the electron and muon identification is used as a veto. The selection of $\tau \rightarrow \rho\nu$ and $\tau \rightarrow a_1\nu$ relies on the reconstruction of neutral clusters in the BGO. Two neutral clusters are considered to originate from a π^0 if their invariant mass is within 35 MeV of the π^0 mass. A single neutral cluster is assumed to be a π^0 candidate if its energy exceeds 3 GeV. For $\tau \rightarrow \rho\nu$ decays, one reconstructed π^0 and one charged track identified by the TEC are required. The invariant mass of the charged π and the π^0 should be compatible with the mass of the ρ to reduce the background from non-resonant τ decays. For the $\tau \rightarrow a_1\nu$ 1-prong decays one has to reconstruct two π^0's and one charged track. For the 3-prong mode three charged tracks identified by the TEC are required. The invariant mass of both, the $\pi\pi^0$ pairs or the unlike sign $\pi\pi$ pairs, should fit to the mass of the ρ, which reduces the background from non-resonant τ decays. For the details of these selections refer to [47].

[7]The $\tau \rightarrow a_1\nu$ decay is only analyzed in the three prong mode $a_1 \rightarrow \pi\pi\pi$ with 1990 and 1991 data.

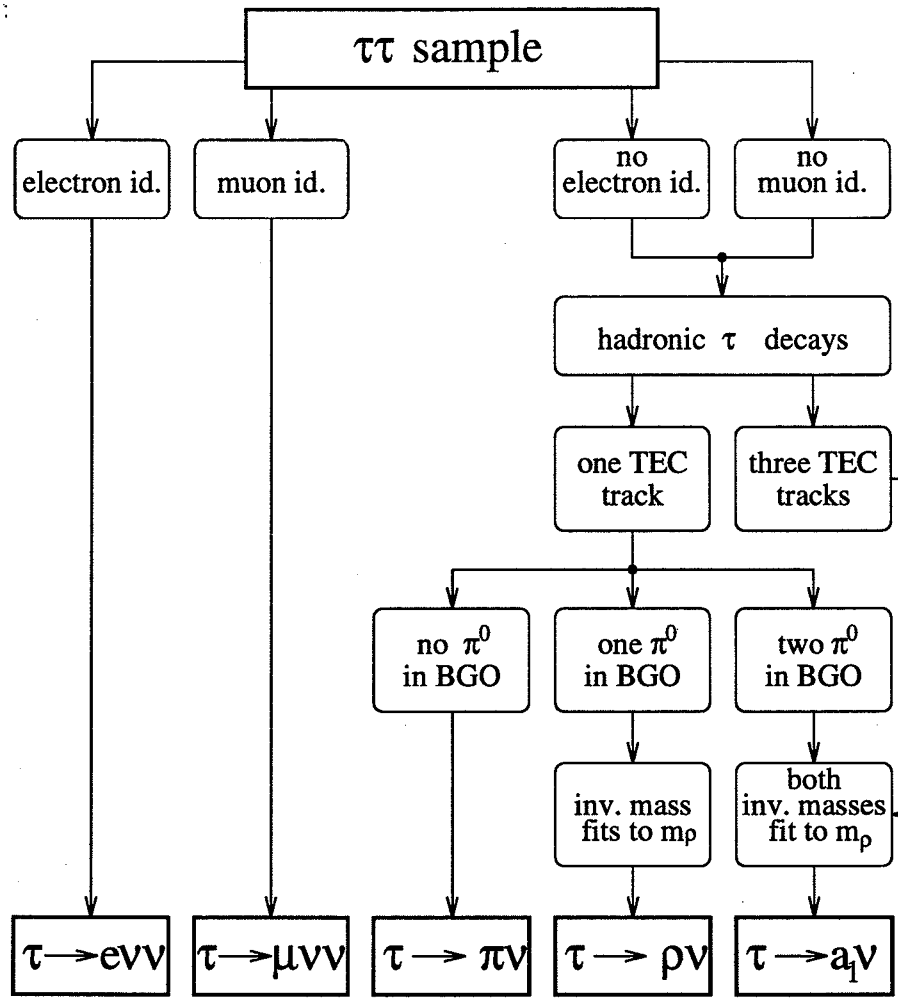

Figure 6.14: The selection of different τ decay modes.

6.3.1 Selection of $\tau \to \pi\nu$ decays

For the $\tau \to \pi\nu$ selection only event hemispheres are considered in which no electron or muon was identified and only one track is reconstructed in the TEC. There are no special cuts to reduce the remaining $\tau \to e\nu\nu$ and $\tau \to \mu\nu\nu$ background. Nevertheless, some of the cuts explained below further suppress the electron and muon contamination. Thus, the remaining background which has to be removed is characterized by the presence of one or more π^0's. Due to the preselection, the $e^+e^- \to e^+e^-$ and $e^+e^- \to \mu^+\mu^-$ rejection and the electron and muon veto the $\tau \to \pi\nu$ sample is already reduced to 84% within the fiducial volume.

To reconstruct the π^0 one has to identify the neutral clusters coming from the decay $\pi^0 \to \gamma\gamma$. Not all photons are well separated from the charged track. Therefore, the neutral cluster may overlap with the cluster to which the TEC track points. To reconstruct also these particles an algorithm is applied which tries to unfold a joint cluster into its neutral and charged components. At first the entry point of the charged particle into the BGO is extrapolated, taking the track coordinates measured with the TEC and the z-detector. For a given entry point in local BGO crystal coordinates the expected average shower shape for a π is known from the test beam analysis of the electromagnetic calorimeter. With an iterative procedure the expected shower shape is subtracted from the measured shower in the BGO within a 30° half-angle cone. Then the remaining cluster energy is assigned to one or more neutral clusters, assuming they originate from π^0's. Clusters inside a 1.4° half-angle cone are ignored, because in that case the charged and neutral particle hit the same crystal. By varying the hypothetical entry points of the neutral particles in the BGO and consequently also the shower shapes, the best solution for these cluster unfolding is extracted (see [47]).

Depending on the number of reconstructed neutral particles one has to consider three cases for the $\tau \rightarrow \pi\nu$ selection. The flowchart of this selection is given in Figure 6.15.

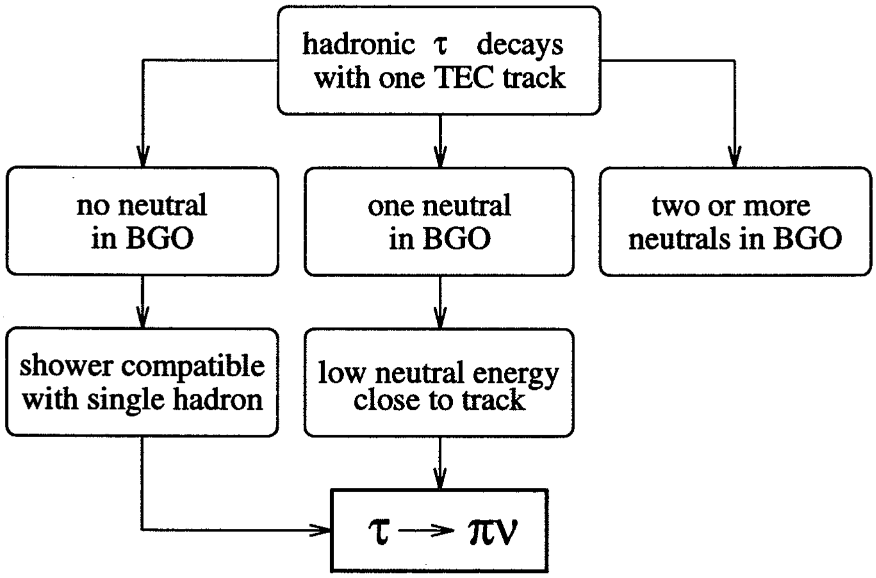

Figure 6.15: The selection of $\tau \rightarrow \pi\nu$.

1. no neutral cluster found in the BGO

- 83 % of the $\tau \rightarrow \pi\nu$ sample [8],
- 19 % contamination from the other hadronic decay modes,
- background is dominated by $\tau \rightarrow \rho\nu$, where the π^0 cannot be reconstructed;

[8]The number is given with respect to the $\tau \rightarrow \pi\nu$ sample after the preselection, $e^+e^- \rightarrow e^+e^-$ and $e^+e^- \rightarrow \mu^+\mu^-$ rejection and the electron and muon veto is applied.

2. one neutral cluster found in the BGO

- 13 % of the $\tau \to \pi\nu$ sample, where the neutral cluster algorithm reconstructs fluctuations in the shower shape as a neutral particle,
- 92 % contamination from the other hadronic decay modes;

3. more than one neutral cluster found in the BGO

- 4 % of the $\tau \to \pi\nu$ sample,
- 98 % contamination from the other hadronic decay modes,
- background is dominated by $\tau \to a_1\nu$ and non-resonant decay modes.

All events of the third class are rejected. For the second class the additional neutral cluster in $\tau \to \pi\nu$ events originates from fluctuations in the shower profile of the charged π which were reconstructed by the neutral cluster algorithm. π^0's give rise to higher energies and can be found also outside the 30° half angle cone. Therefore, requiring an energy of the neutral cluster of less than 1 GeV and the opening angle between the charged and neutral cluster to be less than 20° reduces the background substantially. Figure 6.16 shows the distributions for the opening angle between the charged and neutral cluster,α, for the first and second class. Furthermore, the invariant mass of the neutral bump and the charged bump should be incompatible with the mass of the ρ. The background in the first class are events where the neutral cluster algorithm was not able to separate the neutral particle from the charged one or the neutral particle does not hit the BGO barrel. Nevertheless, at least for the case of unresolved overlapping clusters, the background can be suppressed by looking at the cluster shape. The transverse spread of energy in a cluster, defined as:

$$E_{\text{trans}} = \sum_{i=1}^{N} E_i^{\text{cry}} \sin \alpha_i^{\text{cry}}, \tag{6.2}$$

where α_i^{cry} is the opening angle between the TEC track and the crystal axis, is smaller for clusters without a neutral component. Figure 6.17 shows the distribution for E_{trans}, which is required to be less than 0.4 GeV for $\tau \to \pi\nu$ candidates. An azimuthal opening angle between the TEC track and the center-of-gravity of the cluster of less then 25 mrad is required (see Figure 6.18).

The selection efficiency in the fiducial volume and a breakdown of the background is shown in Table 6.4. The error on the efficiency amounts to 0.7% and 0.4% for 1991 and 1992 respectively. 1582 and 3390 $\tau \to \pi\nu$ decays are selected in the 1991 and 1992 data samples respectively.

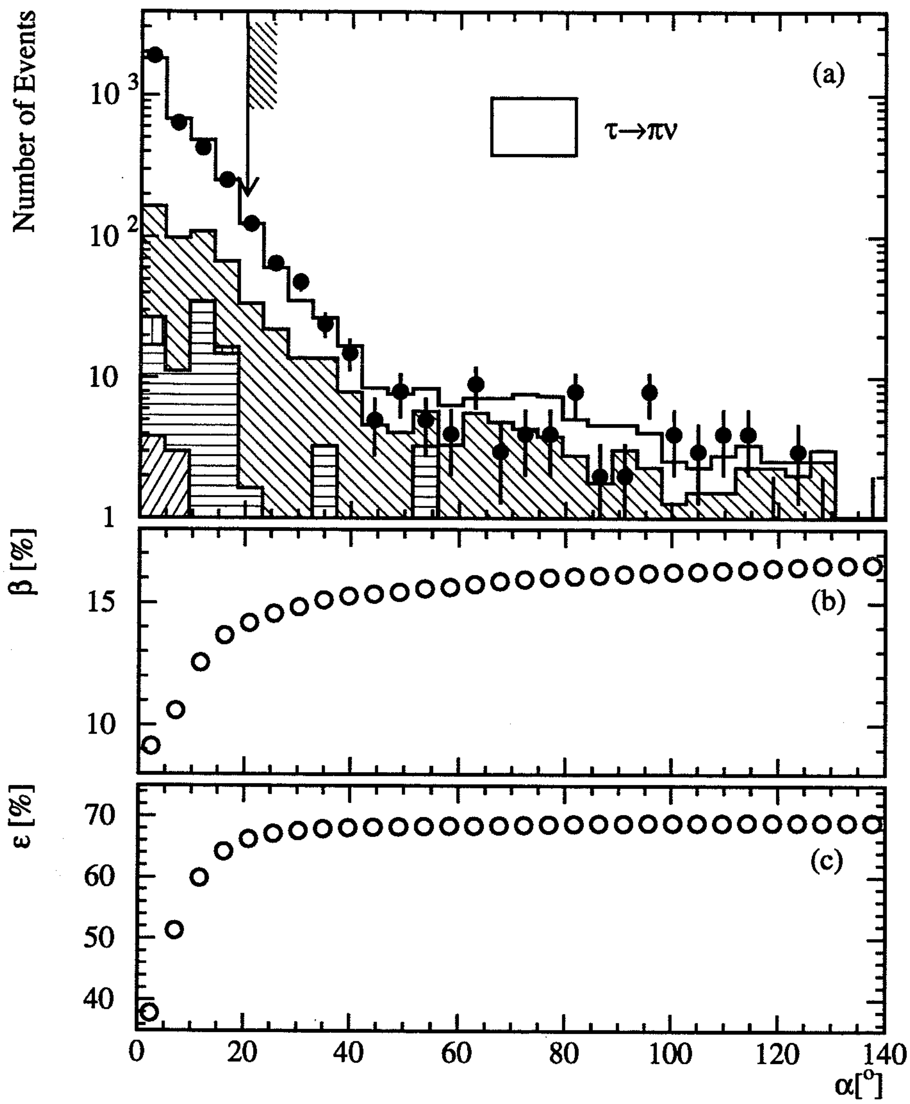

Figure 6.16: The opening angle, α, between the neutral and charged cluster in the BGO. (a) shows the spectrum for data, MC and various background contributions. See Figure 6.1 on Page 62 for the conventions used to label the histograms. In (b) the background ratio, β, is plotted. (c) shows the $\tau \to \pi\nu$ selection efficiency, ε.

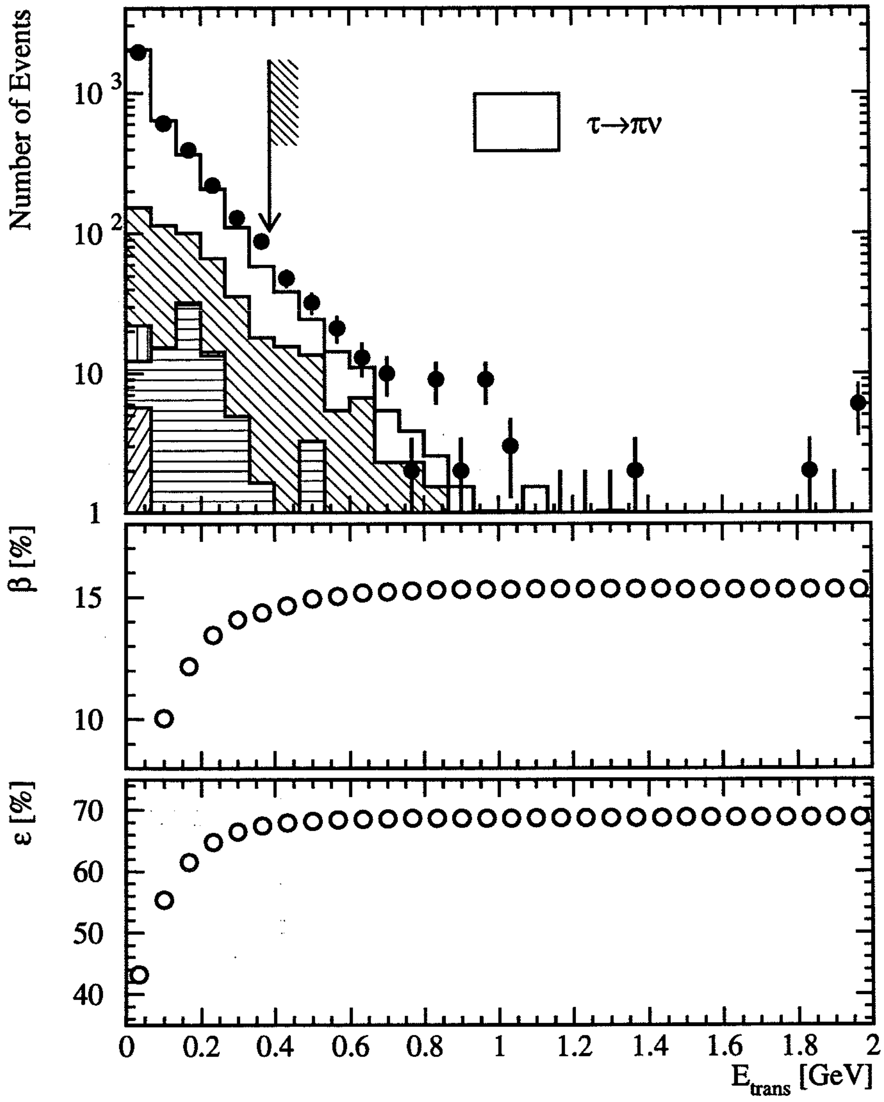

Figure 6.17: The transverse spread of energy for a BGO cluster.

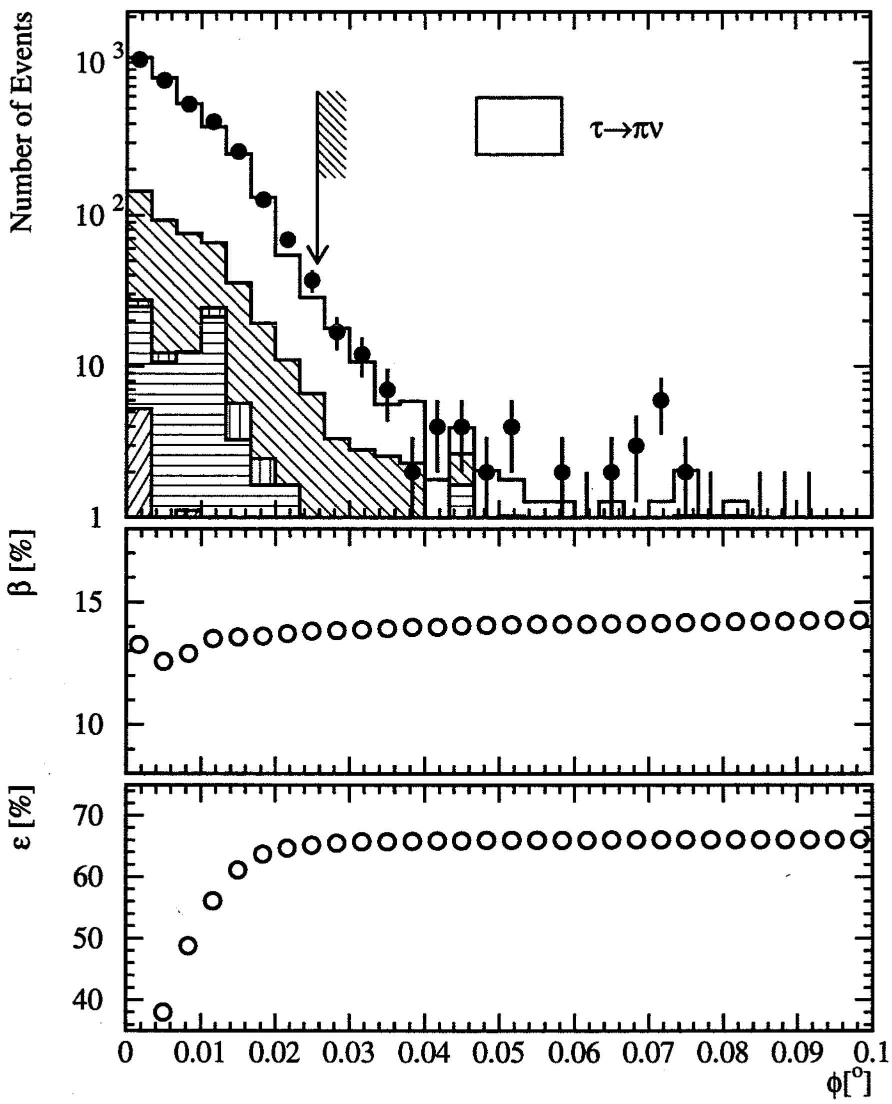

Figure 6.18: The opening angle in ϕ between the TEC track and the charged cluster in the BGO.

	1991	1992
Efficiency		
$\tau \to \pi\nu$	67.9 %	67.4 %
Background		
$\tau \to e\nu\nu$	3.0 %	3.6 %
$\tau \to \mu\nu\nu$	0.4 %	0.3 %
$\tau \to \rho\nu$	4.9 %	5.8 %
$\tau \to a_1\nu$	0.4 %	0.3 %
other τ decays	1.9 %	1.9 %
$e^+e^- \to e^+e^-$	1.8 %	2.1 %
$e^+e^- \to \mu^+\mu^-$	0.5 %	0.3 %
$e^+e^- \to e^+e^-X$	0.3 %	0.2 %
Total	13.2 %	14.5 %

Table 6.4: Efficiency and background of the $\tau \to \pi\nu$ selection.

6.4 Measurement of the Total Cross Section

The measurements of the total cross sections and the forward-backward asymmetries, summarized in the following two sections, have not been performed by the author. As already mentioned in Section 6.2, the selection of $e^+e^- \to \tau^+\tau^-$ events for cross section and forward-backward asymmetry measurements does not requires as much attention to a possible energy bias. Therefore, such a selection is different and in general simpler, than the one described in the previous sections. For details of the selection and the analysis refer to [45,46].

The total cross section is defined as the number of selected $e^+e^- \to \tau^+\tau^-$events, $N_{\tau\tau}^{\mathrm{sel}}$, corrected for the expected number of background events, N_{BG}, and divided by the selection efficiency, $\varepsilon_{\mathrm{sel}}$, the trigger efficiency, $\varepsilon_{\mathrm{tr}}$, the luminosity, $\mathcal{L}$, and the acceptance, A:

$$\sigma_{\mathrm{tot}} = \frac{N_{\tau\tau}^{\mathrm{sel}} - N_{\mathrm{BG}}}{\varepsilon_{\mathrm{sel}}\varepsilon_{\mathrm{tr}}\mathcal{L}A}. \tag{6.3}$$

The $e^+e^- \to \tau^+\tau^-$ events are selected in the fiducial volume defined by the thrust axis of $|\cos\theta| < 0.73$. Since the acceptance depends on the decay modes a systematic error due to the uncertainties of the branching ratios is assigned. The selection efficiency in the fiducial volume using MC $e^+e^- \to \tau^+\tau^-$ events is determined to be $(78.79 \pm 0.11)\%$. The trigger efficiency is found to be $(99.9 \pm 0.05)\%$ by studying the correlation of different trigger types (see Section 4.3.8), which use independent detector information. The background contribution from other Z decay channels is estimated by a MC study to be $(2.75 \pm 0.12)\%$. The contamination of the $e^+e^- \to \tau^+\tau^-$ sample with cosmic muons amounts to $(0.15 \pm 0.05)\%$, which is estimated from the scintillator time distribution assuming the contribution from cosmic muons is flat.

To determine the luminosity delivered to L3 the number of events, N_{ee}, of a well known interaction, the t-channel $e^+e^- \rightarrow e^+e^-$ (Bhabha) scattering at small angles, are counted. The cross section, σ_{ee}, of this reaction is theoretically determined with an accuracy of 0.25%. The dependence of σ_{ee} on the Z exchange and γZ-interference is below 0.05%. The luminosity is given by:

$$\mathcal{L} = \frac{N_{ee}}{\varepsilon_{ee}\sigma_{ee}}. \tag{6.4}$$

ε_{ee} denotes the efficiency to detect Bhabha events which is derived from a MC study. The visible cross section, $\varepsilon_{ee}\sigma_{ee}$, at the Z resonance was determined to be 84.7 nb^{-1} in 1990, 90.7 nb^{-1} in 1991 and 90.3 nb^{-1} in 1992. The systematic error on the luminosity measurement, including the theoretical uncertainty of the Bhabha cross section, amounts to 0.6%.

For 1990 -1992 a total of 25267 $e^+e^- \rightarrow \tau^+\tau^-$ events were selected. The results of the cross section measurements for the different center-of-mass energies, $\sqrt{s}$, are listed in Table 6.5 and plotted in Figure 6.19. The solid line represents the result of a fit to the whole data sample, including the other decay modes of the Z boson and is explained in Section 7.4. The systematic error sources are listed in Table 6.6.

6.5 Measurement of the Forward-Backward Asymmetry

The forward-backward asymmetry is defined as the difference between the forward cross section $\sigma(\cos\theta > 0)$ and the backward cross section $\sigma(\cos\theta < 0)$ divided by the total cross section (see Equations 2.27 and 2.35):

$$\mathcal{A}_{fb} = \frac{\sigma(\cos\theta > 0) - \sigma(\cos\theta < 0)}{\sigma_{tot}}. \tag{6.5}$$

The angular distribution of the cross section is given in the Born approximation by:

$$\frac{d\sigma}{d\cos\theta} = \frac{3}{8}(1 + \cos^2\theta) + \mathcal{A}_{fb}\cos\theta. \tag{6.6}$$

$\mathcal{A}_{fb}$ is the result of a likelihood fit to the differential cross section in $\cos\theta$. Since events with hard initial bremsstrahlung are rejected by cutting on the acollinearity of the event at 250 mrad the Born approximation can be used to determine $\mathcal{A}_{fb}$ directly without introducing a significant bias. All systematic uncertainties related to the total normalization of the cross section cancel for asymmetries if they are symmetric in θ. The measurement of $\mathcal{A}_{fb}$ requires the determination of the charge of the τ to assign the correct sign to $\cos\theta$. Therefore, the observed $\mathcal{A}_{fb}$ has to be corrected for charge confusion, which is discussed in detail for $\mathcal{A}_{fb-pol}$ in Section 6.6.3. For the analysis all events with like sign charge on both hemispheres (15% of the 1992 sample) are excluded. The probability that both tracks are assigned with wrong charge is determined to $(1.20 \pm 0.05)\%$ and used to correct $\mathcal{A}_{fb}$. The background subtraction introduces a systematic bias not larger than 0.003.

1990 Data			
$\sqrt{s}$ [GeV]	N_{events}	$\mathcal{L}$ [nb^{-1}]	σ_{tot} [nb]
88.231	36	337.4	0.219±0.036
89.236	86	404.2	0.445±0.048
90.238	138	319.4	0.912±0.078
91.230	1887	2717.7	1.472±0.034
92.226	190	365.9	1.097±0.080
93.228	133	471.7	0.592±0.051
94.223	94	476.7	0.411±0.042
Total	2564	5093.0	
Systematic Error			±0.9%

1991 Data			
$\sqrt{s}$ [GeV]	N_{events}	$\mathcal{L}$ [nb^{-1}]	σ_{tot} [nb]
91.254	3720	4902.6	1.507±0.025
88.480	95	779.4	0.236±0.024
89.470	229	850.0	0.532±0.035
90.228	359	793.3	0.886±0.047
91.222	2102	2882.3	1.449±0.032
91.967	425	689.3	1.226±0.059
92.966	248	758.2	0.642±0.041
93.716	225	829.9	0.535±0.036
Total	7403	12484.0	
Systematic Error			±0.7%

1992 Data			
$\sqrt{s}$ [GeV]	N_{events}	$\mathcal{L}$ [nb^{-1}]	σ_{tot} [nb]
91.294	15300	20327.4	1.472±0.012
Systematic Error			±0.7%

Table 6.5: Cross sections and their statistical errors for $e^+e^- \to \tau^+\tau^-$, extrapolated to the full solid angle. The quoted systematic error excludes the error of 0. 6% in the luminosity.

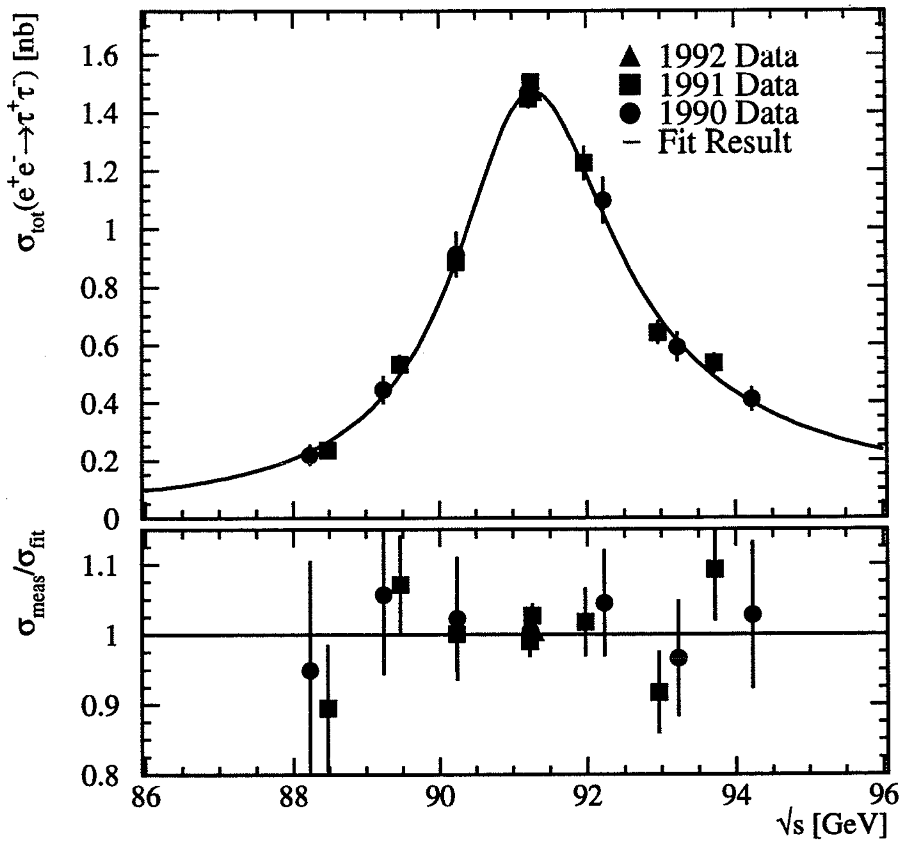

Figure 6.19: The total cross section measurements of the process $e^+e^- \to \tau^+\tau^-$ as a function of $\sqrt{s}$ for 1990-1992. In the bottom plot the ratio of the measured to the fitted cross section is shown.

Error Source	Systematic Error
Selection	0.60%
MC Acceptance and Efficiency	0.21%
Tau-Decay Branching Ratios	0.25%
Background Subtraction	0.14%
Trigger Efficiency	0.05%
Total	0.70%
Luminosity	0.60%

Table 6.6: Systematic errors for the cross section measurement in 1992.

The results of the $\mathcal{A}_{\mathrm{fb}}$ measurements as a function of $\sqrt{s}$ are listed in Table 6.7 and plotted in Figure 6.20. The solid line shows the result of a fit to the whole data sample including other Z decay modes. The breakdown of the systematic errors for the $\mathcal{A}_{\mathrm{fb}}$ measurement is given in Table 6.8.

For further details of the $\mathcal{A}_{\mathrm{fb}}$ measurement see [45,46].

6.6 Measurement of the Polarization Asymmetries

This section describes the measurement of the average polarization asymmetry and the forward-backward polarization asymmetry. Currently there are two methods applied to measure the polarization of the τ. One of them uses the information of the energy spectra of the τ decay particles [7]. The other method measures the polarization using the acollinearity between the charged decay products of both τ's [48].

For the first method the results in the channels $\tau \to e\nu\nu$, $\tau \to \mu\nu\nu$, $\tau \to \pi\nu$, $\tau \to \rho\nu$ and $\tau \to \mathrm{a}_1\nu$ are presented. The measurement in the final state ($\tau \to \pi\nu$; $\tau \to \mathrm{X}n\nu$) is discussed in detail applying the second technique.

6.6.1 Polarization observables

The polarization of the τ as a function of $\cos\theta$, $\mathcal{P}_\tau(\cos\theta)$, is defined as:

$$\mathcal{P}_\tau(\cos\theta) = \frac{\dfrac{d\sigma(h_\tau=+1)}{d\cos\theta} - \dfrac{d\sigma(h_\tau=-1)}{d\cos\theta}}{\dfrac{d\sigma(h_\tau=+1)}{d\cos\theta} + \dfrac{d\sigma(h_\tau=-1)}{d\cos\theta}}. \tag{6.7}$$

h_τ denotes the helicity of the τ. Using the Equations 2.21 and 3.20 $\mathcal{P}_\tau(\cos\theta)$ reads on the Z resonance:

$$\mathcal{P}_\tau(\cos\theta) = -\frac{\mathcal{A}_\tau(1+\cos^2\theta) + 2\mathcal{A}_e\cos\theta}{(1+\cos^2\theta) + 2\mathcal{A}_\tau\mathcal{A}_e\cos\theta}. \tag{6.8}$$

The γ-exchange, the γZ-interference and radiative corrections are neglected. The polarization asymmetries are derived by integration:

$$\begin{aligned} \mathcal{A}_{\mathrm{pol}} &= \int_{-1}^{1} \mathcal{P}_\tau(\cos\theta)d(\cos\theta), \\ \mathcal{A}_{\mathrm{fb-pol}} &= \int_{0}^{1} \mathcal{P}_\tau(\cos\theta)d(\cos\theta) - \int_{-1}^{0} \mathcal{P}_\tau(\cos\theta)d(\cos\theta). \end{aligned} \tag{6.9}$$

The differential decay distribution of the τ in the laboratory frame is given by [49]:

$$\frac{1}{N_i}\frac{dN_i}{dz} = f_i(z) + \mathcal{P}_\tau g_i(z). \tag{6.10}$$

The index i indicates different decay channels and z is an arbitrary polarization dependent observable. The polarization can be extracted experimentally using Equation 6.10. The

1990 Data	
$\sqrt{s}$ [GeV]	$\mathcal{A}_{fb}$
88.231	−0.36±0.20
89.236	0.00±0.15
90.238	−0.13±0.11
91.230	0.077±0.028
92.226	0.09±0.09
93.228	0.07±0.11
94.223	0.04±0.13
Systematic Error	±0.005

1991 Data	
$\sqrt{s}$ [GeV]	$\mathcal{A}_{fb}$
91.254	0.037±0.021
88.480	−0.106±0.128
89.470	−0.152±0.083
90.228	−0.137±0.070
91.222	−0.032±0.029
91.967	0.042±0.063
92.966	0.161±0.080
93.716	0.058±0.082
Systematic Error	±0.005

1992 Data	
$\sqrt{s}$ [GeV]	$\mathcal{A}_{fb}$
91.294	0.015±0.010
Systematic Error	±0.003

Table 6.7: Forward-backward asymmetries, $\mathcal{A}_{fb}$, and their statistical errors, including a cut on the acollinearity angle, $\epsilon < 250$ mrad.

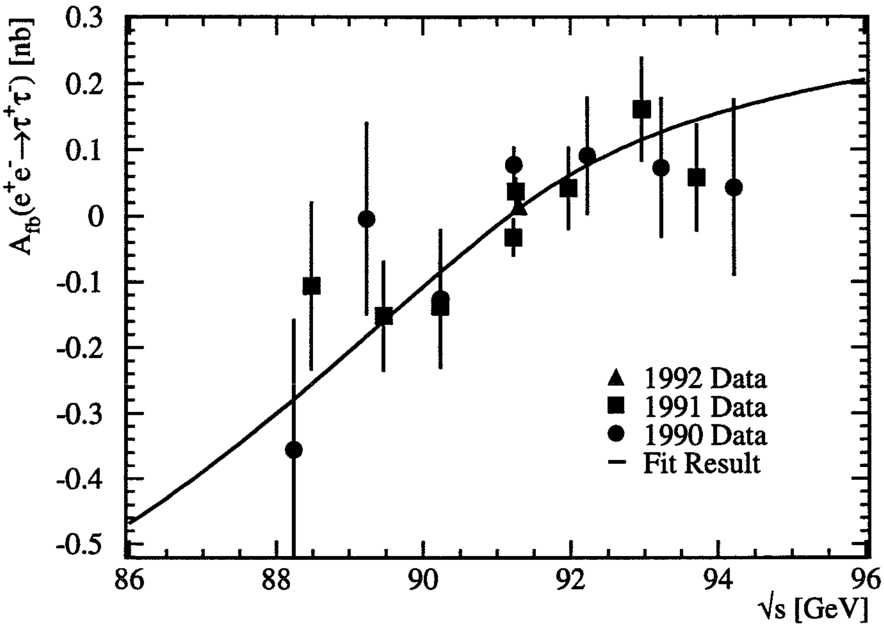

Figure 6.20: The forward-backward asymmetry measurements of the process $e^+e^- \to \tau^+\tau^-$ as a function of $\sqrt{s}$ for 1990-1992.

Error Source	Systematic Error
Background Subtraction	0.003
Charge Confusion	$0.001\mathcal{A}_{fb}$
Total	0.003

Table 6.8: Systematic errors for the $\mathcal{A}_{fb}$ measurement in 1992.

measured spectrum of the observable z is fitted with the functions $f_i(z)$ and $g_i(z)$ leaving $\mathcal{P}_\tau$ as a free parameter. The functions $f_i(z)$ and $g_i(z)$ can either be calculated analytically and then have to be corrected for detector effects such as efficiency and resolution. Alternatively $f_i(z)$ and $g_i(z)$ can be determined by Monte Carlo simulation, where all the detector effects are taken into account. In this paper the measurements are always performed by fitting a linear combination of the Monte Carlo generated distributions for the polarizations $\mathcal{P}_\tau = \pm 1, f_i(z) + g_i(z)$ and $f_i(z) - g_i(z)$, to the data distribution.

In general the functions $f_i(z)$ and $g_i(z)$ depend also on the charged current couplings of the τ to the W boson. In the Standard Model the charged current is described by a V-A interaction. This is experimentally favored by the ARGUS results [50]. Only if these couplings are not regarded as free parameters is it possible to determine $\mathcal{P}_\tau$ by analyzing the decay of *one* τ produced in $e^+e^- \to \tau^+\tau^-$. In the following for the charged current sector V–A coupling is always assumed. However, by analyzing the correlations between *both* τ's it is in principle possible to determine the structure of the charged and the neutral current (see [51,52]).

The energy method

In the rest frame of the τ its decay is governed by its helicity, h_τ. Thus, the angular decay distribution can be written as:

$$\frac{1}{N}\frac{dN}{d\cos\theta^*} = 1 + h_\tau \cos\theta^*, \tag{6.11}$$

where θ^* is the polar angle between the τ direction of flight and the charged decay particle. For hadronic decay modes $\tau \to \pi\nu$, $\tau \to \rho\nu$, $\tau \to a_1\nu$, which are two-body decays, the energy, E^i_{2b}, and momentum, p^i_{2b}, of the charged decay particle, i, are well defined, although the neutrino is not measured. They are given by:

$$\begin{aligned} E^i_{2b} &= \frac{m_\tau^2 + m_i^2}{2m_\tau}, \\ p^i_{2b} &= \frac{m_\tau^2 - m_i^2}{2m_\tau}. \end{aligned} \tag{6.12}$$

For the leptonic decay modes, which are three-body decays, the energy and momentum of the leptons are not fixed. Therefore, Equations 6.12 represent the kinematic limits for the energy and the momentum.

In the laboratory frame the energy of the hadron from the two body decay is no longer fixed. The energy spectrum of the hadron in two-body τ decays reads:

$$\frac{1}{N_i}\frac{dN_i}{du_i} = 1 + \alpha_i \mathcal{P}_\tau (2u_i - 1)\ ;\ \ i = \pi, \rho, a_1, \tag{6.13}$$

where u_i is the energy of the charged τ decay product normalized to the beam energy,

$$u_i = \frac{E_i}{E_{\text{beam}}}. \tag{6.14}$$

The dilution factor,

$$
\begin{aligned}
\alpha_\pi &= 1, \\
\alpha_{\rho,a_1} &= \frac{m_\tau^2 - 2m_{\rho,a_1}^2}{m_\tau^2 + 2m_{\rho,a_1}^2},
\end{aligned}
\tag{6.15}
$$

reduces the $\mathcal{P}_\tau$ sensitivity of the energy spectra for the vector mesons ρ and a_1 and will be discussed later in this section. The energy spectrum for the leptons from three-body τ decays is given by:

$$\frac{1}{N_i}\frac{dN_i}{du_i} = \frac{1}{3}\left[(5 - 9u^2 + 4u^3) + \mathcal{P}_\tau(1 - 9u^2 + 8u^3)\right]; \; i = e, \mu. \tag{6.16}$$

In Figure 6.21 the energy spectra for the helicity states $h_\tau = \pm 1$ are plotted. The sensitivity of the energy spectra to the polarization, $\mathcal{P}_\tau$, is high in the $\tau \to \pi\nu$ channel, because here the difference between the spectra for $h_\tau = \pm 1$ is most significant. It is reduced for $\tau \to \rho\nu$, and $\tau \to \mathrm{a}_1\nu$. The sensitivity for $\tau \to e\nu\nu$ and $\tau \to \mu\nu\nu$ is also lower than $\tau \to \pi\nu$, since the energy of the τ is shared between three particles. In this case it cannot be improved, because the two neutrinos are not detectable.

The dilution factor, α_i, decreases the sensitivity in the channels $\tau \to \rho\nu$ and $\tau \to \mathrm{a}_1\nu$. Since the life time of these vector resonances is very short, one detects only their decay particles, π^0's and π's. The decay distribution of these particles depends on the spin state of the vector resonance itself. To increase the sensitivity of the polarization measurement one has to reconstruct the energy of the vector meson and its spin direction from the decay particles [49,53]. Measuring only the energy of the meson and neglecting the spin state leads to the dilution factor α_i in Equation 6.13. Practically one determines $\mathcal{P}_\tau$ from a 2-dimensional distribution. The variables for the $\tau \to \rho\nu$ channel [53] are usually the angle between the τ and the ρ in the τ rest frame,

$$\cos\theta_\rho^* = \frac{4m_\tau^2}{m_\tau^2 - m_\rho^2}\frac{E_{\pi^0} + E_\pi}{2E_{\mathrm{beam}}} - \frac{m_\tau^2 + m_\rho^2}{m_\tau^2 - m_\rho^2}, \tag{6.17}$$

and the angle between the ρ and the π in the ρ rest frame, which is sensitive to the spin of the ρ:

$$\cos\psi_\rho^* = \frac{m_\rho}{\sqrt{m_\rho^2 - 4m_\pi}}\frac{E_\pi - E_{\pi^0}}{|\vec{p}_\pi + \vec{p}_{\pi^0}|}.$$

In the case of $\tau \to \mathrm{a}_1\nu$ [53] one uses the angle between the τ momentum and the momentum of the 3π system in the τ rest frame,

$$\cos\theta_{a1}^* = \frac{4m_\tau^2}{m_\tau^2 - m_{a1}^2}\frac{E_1 + E_2 + E_3}{2E_{\mathrm{beam}}} - \frac{m_\tau^2 + m_{a1}^2}{m_\tau^2 - m_{a1}^2}, \tag{6.18}$$

and the angle between the normal of the 3π decay plane in its rest frame and the momentum

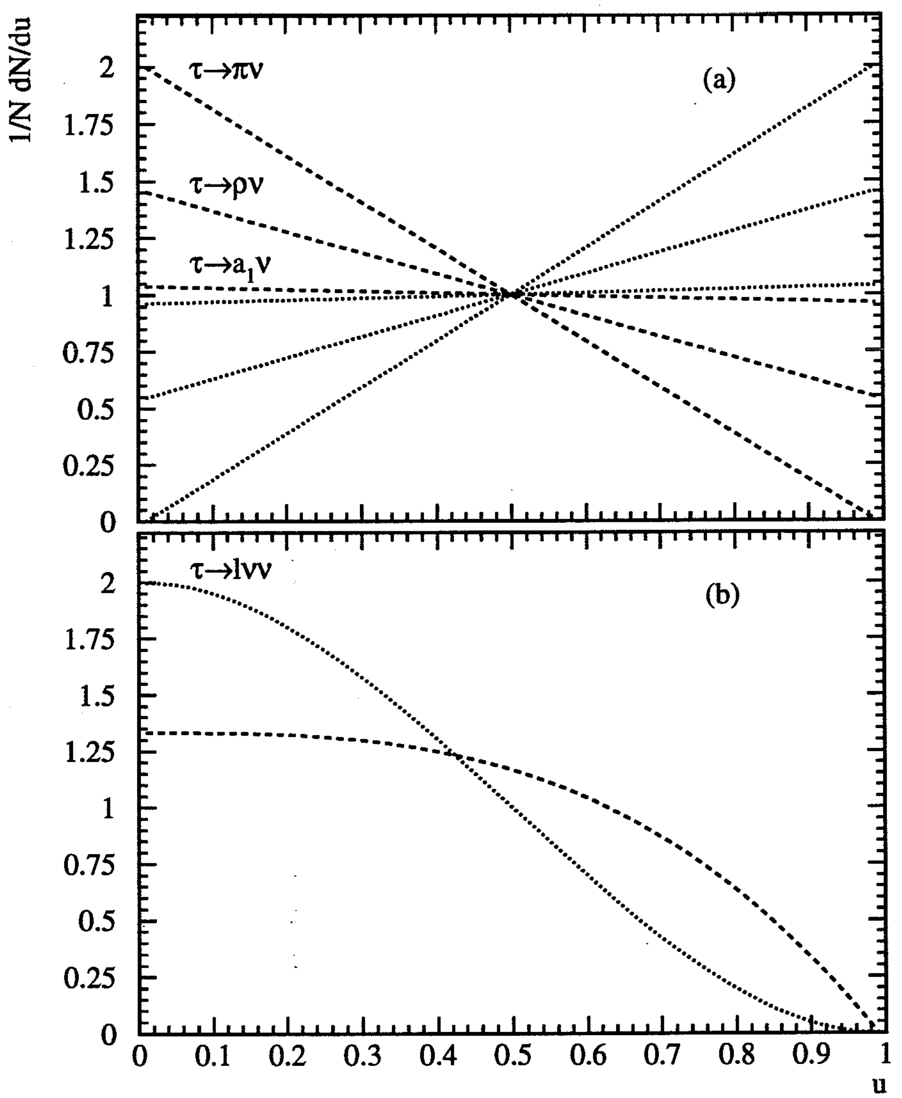

Figure 6.21: The energy spectra of the helicity states $h_\tau = \pm 1$ for (a) the hadronic decay modes $\tau \to \pi\nu$, $\tau \to \rho\nu$, $\tau \to a_1\nu$ and for (b) the leptonic decay modes $\tau \to e\nu\nu$, $\tau \to \mu\nu\nu$. See Figure 6.1 on Page 62 for the conventions used to mark the polarization states.

Channel	Sensitivity	Weight
$\tau \to \pi\nu$	0.58	0.32
$\tau \to \rho\nu$	0.49	0.48
$\tau \to \mathrm{a}_1\nu$	0.23	0.12
$\tau \to \ell\nu\nu$	0.22	0.08

Table 6.9: Sensitivity of different τ decay modes to a $\mathcal{P}_\tau$ measurement for the energy method.

of the 3π system in the laboratory frame:

$$\begin{aligned} \cos\psi^*_{a1} &= \frac{8m_{a1}|\vec{p}_1\cdot(\vec{p}_2\times\vec{p}_3)| \,/\, |\vec{p}_1+\vec{p}_2+\vec{p}_3|}{\sqrt{-\lambda\,[\lambda(m^2_{a1},m^2_{12},m^2_\pi),\lambda(m^2_{a1},m^2_{13},m^2_\pi),\lambda(m^2_{a1},m^2_{23},m^2_\pi)]}}, \\ \lambda(x,y,z) &= x^2+y^2+z^2-2xy-2yz-2xz. \end{aligned} \tag{6.19}$$

m_{ij} is the invariant mass derived from the pions i and j. An optimal method to measure the polarization is proposed in [54], which allows to take into account all relevant information to reconstruct the decay of the τ and subsequent decays. Especially for $\tau \to \mathrm{a}_1\nu$ this method is advantageous, because $\cos\psi^*_{a1}$ is not sufficient to describe the 3π system completely. However, the results presented in this paper are obtained with the technique given by Equation 6.18 and 6.19.

The sensitivity of the different decay channels to the polarization of the τ can be defined as follows [54]:

$$S_i = \frac{1}{\sigma_i(\mathcal{P}_\tau) * \sqrt{N_i}}, \tag{6.20}$$

and is calculated from the analytical expression of the decay distributions for the different channels. $\sigma_i(\mathcal{P}_\tau)$ is the statistical error of the $\mathcal{P}_\tau$measurement in the τ-decay channel i and N_i the number of decays. From the experimental point of view the weight of a certain decay channel to an averaged measurement of $\mathcal{P}_\tau$ is of interest. Thus, one has to fold in the branching ratio, B^i, and normalize the sum of the weights over all investigated decay channels to 1:

$$W_i = \frac{S_i^2 B_i}{\sum_j S_j^2 B_j}. \tag{6.21}$$

In Table 6.9 the sensitivities [54] and weights for a $\mathcal{P}_\tau$ measurement with the energy method are shown.

The acollinearity method

The possibility to measure the polarization of the τ with the acollinearity of the event was proposed in [48]. This method takes advantage of the correlation between both τ's caused by helicity conservation. The spin of the two τ's thus always adds up to one and their helicities are opposite. Assuming we have a $\tau \to \pi\nu$ decay in both hemispheres of the event with polarization $\mathcal{P}_\tau = +1$; then the π's tend to decay in the direction of flight of the mother τ. Thus, in the laboratory frame both π's occur with high energy. This correlation is also present in the acollinearity of the event, which is defined as the angle, ϵ, between the direction of flight of the charged decay products of the τ's:

$$\begin{aligned} \cos\epsilon &= -\vec{n}_\tau^1 \cdot \vec{n}_\tau^2 \\ &= -\sin\theta_1 \sin\theta_2 \cos(\phi_1 - \phi_2) - \cos\theta_1 \cos\theta_2. \end{aligned} \tag{6.22}$$

The acollinearity spectrum $(1\,/\,N)(dN\,/\,d\epsilon)$ can be expressed in the same general form as introduced in Equation 6.10 and is given by:

$$\frac{1}{N}\frac{dN}{d\epsilon} = Q_{11}(\epsilon) + \alpha_1\alpha_2 Q_{22}(\epsilon) + \mathcal{P}_\tau\left[\alpha_1 Q_{21}(\epsilon) + \alpha_2 Q_{12}(\epsilon)\right]. \tag{6.23}$$

The dilution factors α_1 and α_2 are defined in Equation 6.15. The functions Q_{ij} are a fourfold integral of the energies of the τ decay products and their polar angles over the decay distributions of the decay products. For an exact definition see [48] and [55].

To measure the polarization in exclusive decay channels requires the τ decay to be identified in both hemispheres. This reduces the statistics for a given channel substantially. Therefore, it was proposed to use semi-inclusive channels for this analysis. Possible disjoint 1-prong modes are:

- ($\tau \to \pi\nu$; $\tau \to X n\nu$); One τ decays into a π and the other decay mode is any 1-prong mode.
- ($\tau \to \ell\nu\nu$; $\tau \to X n\nu$); One τ decays leptonically and the other is a 1-prong decay, but not $\tau \to \pi\nu$.
- ($\tau \to$ hν; $\tau \to$ hν); Both τ's decay into a ρ or into a a_1.

In Figure 6.22 the acollinearity distributions for these three decay channels are shown. It is clear that the ($\tau \to \pi\nu$; $\tau \to X n\nu$) channel is most sensitive, because the distributions for both polarization states show the largest difference in shape. However, as it was shown in [48], the sensitivity is a factor two smaller than for the energy method in $\tau \to \pi\nu$. Nevertheless, it is worthwhile to measure the polarization using the acollinearity, because from the experimental point of view uncorrelated detector information is used. The acollinearity is determined with the ϕ and θ measurements of the TEC and the z-detector, while the energy method relies on the energy measurement of the calorimeters. Thus, the systematic errors from the measurement of the polarization observable are uncorrelated. The sensitivity for ($\tau \to \ell\nu\nu$; $\tau \to X n\nu$) is reduced due to the two neutrinos in the final state. Since in the acollinearity method the spin of the vector mesons is not analyzed, the sensitivity of the channel ($\tau \to$ hν; $\tau \to$ hν) is much reduced.

A measurement in the most sensitive channel ($\tau \to \pi\nu$; $\tau \to X n\nu$) is discussed in section 6.6.3.

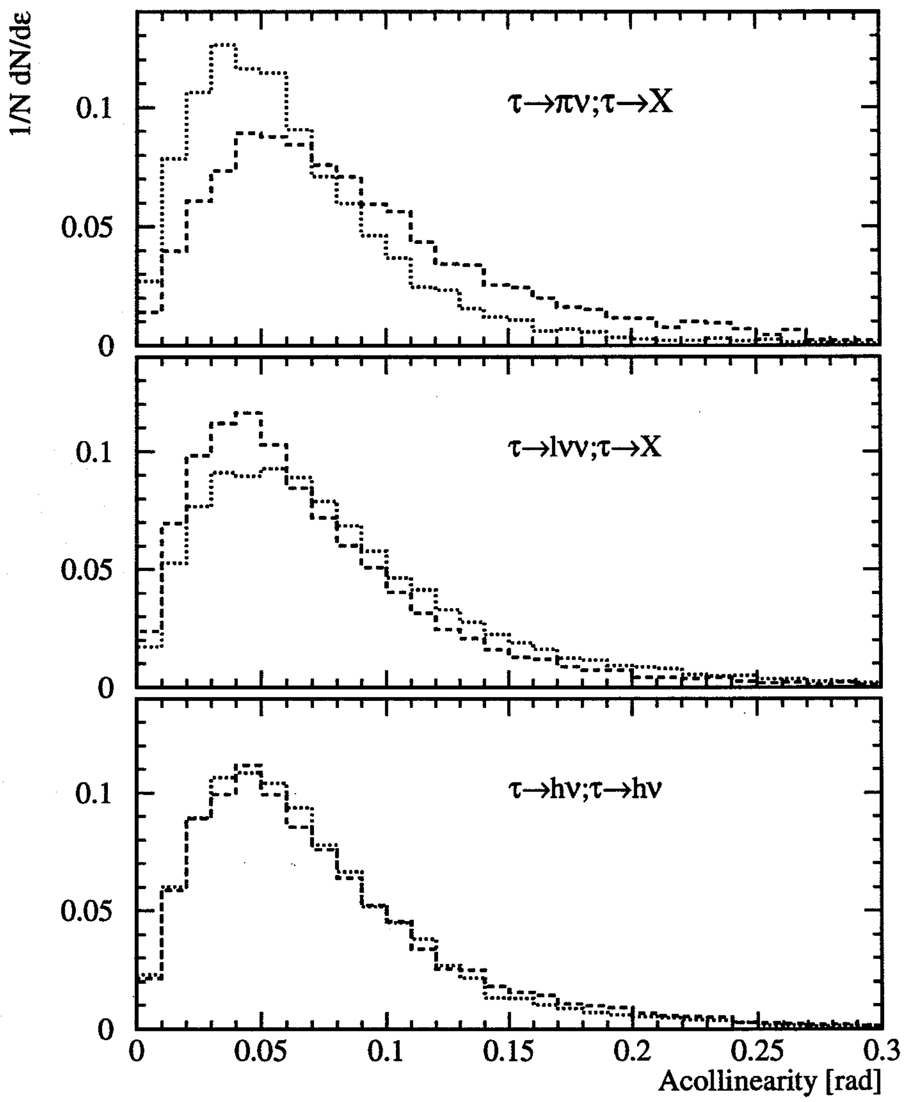

Figure 6.22: Acollinearity distributions for ($\tau \to \pi\nu$; $\tau \to Xn\nu$), ($\tau \to \ell\nu\nu$; $\tau \to Xn\nu$) and ($\tau \to$ hν; $\tau \to$ hν). The plotted MC distributions take into account resolution effects of the L3 detector.

6.6.2 Fitting procedure

For both methods the polarization, $\mathcal{P}_\tau$, is extracted by fitting the distribution of the polarization sensitive variable z for data with thc MC spectra for $\mathcal{P}_\tau = \pm 1$ taking into account the MC predictions for various background processes. The differential decay distribution in z for the MC is expressed by:

$$\frac{dN_{\rm MC}}{dz} = \frac{(1+\mathcal{P}_\tau)}{(1+\hat{\mathcal{P}}_\tau)}\frac{dN^+_{\tau\tau}}{dz} + \frac{(1-\mathcal{P}_\tau)}{(1-\hat{\mathcal{P}}_\tau)}\frac{dN^-_{\tau\tau}}{dz} + r_{\rm BG}\frac{dN_{\rm BG}}{dz}. \tag{6.24}$$

$N^\pm_{\tau\tau}$ is the sum of the signal distribution, $N^\pm_{\tau\to {\rm X}n\nu}$, and background distribution, $N^\pm_{\tau\to noXn\nu}$ for the positive and negative helicity state, taking also into account the polarization of background τ decays. Unpolarized background from $e^+e^- \to e^+e^-$, $e^+e^- \to \mu^+\mu^-$ and $e^+e^- \to e^+e^-X$ is included in $N_{\rm BG}$. $\hat{\mathcal{P}}_\tau$ denotes the generated polarization in the MC sample. The factor $r_{\rm BG}$ normalizes the background and the $e^+e^- \to \tau^+\tau^-$MC sample to the same luminosity.
The distribution in Equation 6.24 is used to fit the data distribution, $N_{\rm D}$, according to a *binned maximum likelihood method.* The likelihood reads as:

$$\mathcal{L} = \prod_i^{\#bins} b_i, \tag{6.25}$$

where b_i is the probability, that the MC and data distribution are compatible with each other for a given bin i of a histogram of observable z. b_i can be calculated from the probability distributions for $N_{MC;i}$ and $N_{D;i}$ assuming Poisson statistics, which is a better approximation than a Gaussian distribution especially for low statistic bins. The probability that $N_{D;i}$ is compatible with an expectation value μ_i is:

$$P(N_{{\rm D};i}|\mu_i) = e^{-\mu_i}\frac{\mu_i^{N_{{\rm D};i}}}{N_{{\rm D};i}!}. \tag{6.26}$$

The expectation value, μ_i, is given by the MC distribution, $N_{{\rm MC};i}$. Since the MC statistics are finite they also follow a Poisson distribution:

$$P(r\mu_i|N_{{\rm MC};i}) = re^{-r\mu_i}\frac{(r\mu_i)^{N_{{\rm MC};i}}}{N_{{\rm MC};i}!}, \tag{6.27}$$

with the normalization factor r given by:

$$r = \frac{\sum_i^{\#bins} N_{{\rm MC};i}}{\sum_i^{\#bins} N_{{\rm D};i}}. \tag{6.28}$$

The probability b_i is the product of the probability that the data distribution agrees with a certain expectation value μ_i and the probability that the MC distribution agrees with the same μ_i integrating over all possible expectation values μ_i:

$$\begin{aligned} b_i &= \int_0^\infty d\mu_i\, P(N_{{\rm D};i}|\mu_i)\, P(r\mu_i|N_{{\rm MC};i}) \\ &= \frac{r^{N_{{\rm MC};i}+1}(N_{{\rm D};i}+N_{{\rm MC};i})!}{(1+r)^{N_{{\rm D};i}+N_{{\rm MC};i}+1}N_{{\rm D};i}!N_{{\rm MC};i}!}. \end{aligned} \tag{6.29}$$

Increasing the MC statistics to infinity, $N_{\rm MC} \to \infty$, reduces Equation 6.29 to Equation 6.26, because the expectation values μ_i are fixed.

The function minimization package MINUIT [56] is used to minimize $-\log \mathcal{L}$.

6.6.3 Measurement with the acollinearity method in ($\tau \to \pi\nu$; $\tau \to Xn\nu$)

The data sample used for this analysis consists of 1582 and 3390 $\tau \to \pi\nu$ decays selected from the 1991 and 1992 data respectively.

The acollinearity, ϵ, is measured with the ϕ information from the TEC and the z coordinate measurement of the z-detector. The azimuthal angle, ϕ, is determined from a fit in the (x, y) plane to the parameters (see Figure 6.23):

- ϕ, the azimuthal angle of the track at the reference point,
- DCA, the distance of closest approach of the track to the reference point,
- ρ, the curvature of the track, defined as the inverse bending radius of the track, $\rho = 1/r$.

The fit is performed using the local ϕ measurements at the anode wires of the TEC, which are associated to a track. As reference point a fill vertex, $V^{fill}_{x,y}$, determined with $e^+e^- \to q\bar{q}$ events [39], is used [9]. The polar angles, θ_1 and θ_2, are derived from a fit to the z coordinates measured in the z-detector at the radius of the anode wires, R_I and R_O, which are associated to both tracks and to the reference point,the fill vertex, $V^{fill}_{x,y,z}$. The free parameters are (see Figure 6.24):

- the polar angles θ_1 and θ_2,
- the impact point in z direction, z_0.

Both tracks are constrained to emerge from the same point in z, the impact point, z_0, because the finite decay length of the τ can be neglected compared to the width of the interaction region in z, $\sigma_z^{\rm int}$ (see Section 5.6.2). Furthermore, the position of z_0 is constrained by $\sigma_z^{\rm int}$.

Before the acollinearity is determined, the following resolution functions, used to constrain the experimental measurements in the fits, have to be analyzed and compared to the respective parameters of the MC simulation:

- the width of the interaction region in z, $\sigma_z^{\rm int}$,
- the z-detector resolution, $\sigma_{\rm CH}$,
- the ϕ resolution of the TEC, $\sigma_\phi^{\rm TEC}$.

[9]For the definition of V^{fill} see Section 5.6.2.

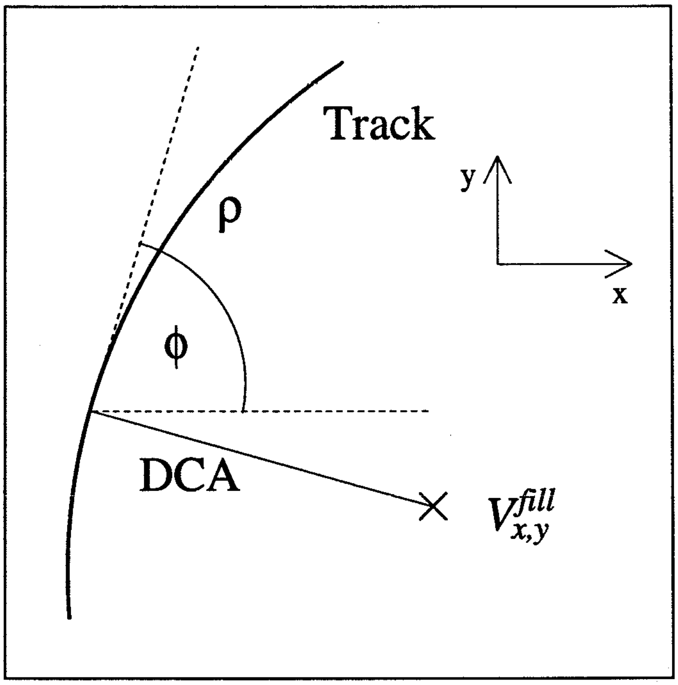

Figure 6.23: Definition of the track parameters in the (x, y) plane.

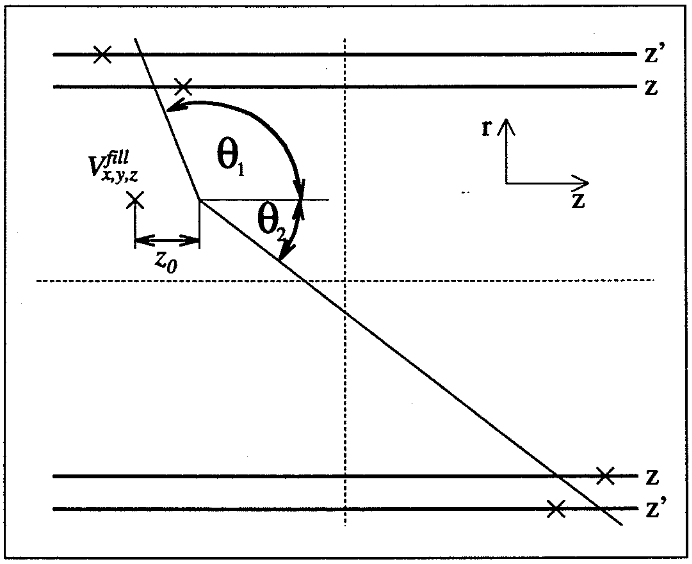

Figure 6.24: Definition of the track parameters in the (r, z) plane.

To avoid a bias of the polarization measurement, the resolutions are determined using MC and data samples from the processes $e^+e^- \to e^+e^-$ and $e^+e^- \to \mu^+\mu^-$. The beam width, σ_z^{int}, is measured as explained in Section 5.6.2. For the $e^+e^- \to \mu^+\mu^-$ MC sample one finds $\sigma_z^{\mathrm{int}} = 10.2$mm. This value is larger than the one measured with data (see Figure 5.12). Therefore, it is not possible to adjust the MC distribution with an additional Gaussian smearing of the reconstructed MC distribution. Agreement must be achieved by using a re-weighting algorithm. The acollinearity resolution is dominated by the beam width, because σ_{CH} and $\sigma_\phi^{\mathrm{TEC}}$ are one order of magnitude smaller. Nevertheless, these resolutions also have to be adjusted in the MC, although it is of less importance than the proper simulation of σ_z^{int}. The measurement of the z-chamber resolution is explained in Section 5.6.3. In the MC the charge avalanche at the anode wires of the z-detector as a result of the ionization process is simulated as point-like, but for inclined tracks these avalanches are scattered along the anode wire. Therefore, the z-detector resolution in the MC is underestimated with rising distance from $z = 0$. Thus, the position of the z-hits has to be smeared according to the measurement of σ_{CH} (see Figure 5.13) as a function of z. Figure 6.25 shows σ_{CH} before and after the smearing, in comparision to the data distribution. The ϕ resolution of TEC is derived from the width of the acoplanarity distribution:

$$\sigma_\phi^{\mathrm{TEC}} = \sigma(\Delta\phi)\,/\,\sqrt{2} = \sigma(\phi_1 - \phi_2)\,/\,\sqrt{2}. \tag{6.30}$$

In Figure 6.26 $\sigma_\phi^{\mathrm{TEC}}$ is plotted as a function of the local ϕ coordinate within one inner TEC sector:

$$\phi_{\mathrm{loc}} = \mathrm{mod}(\phi, 2\pi\,/\,12). \tag{6.31}$$

σ_ϕ^{TEC} is underestimated in the MC. Especially near the anode and cathode the disagreement between data and MC is large. In these regions the electric drift field is not homogeneous and therefore not well simulated in the MC. The smearing of the ϕ coordinate according to this distribution improves the matching of data and MC measurements.

Figure 6.27 shows the acollinearity distribution for ($\tau \to \pi\nu, \tau \to X\pi\nu$) decays with all MC corrections applied for the 1992 data sample. The MC spectrum was fitted to the data distribution according to Section 6.6.2. To measure $\mathcal{A}_\tau$ and $\mathcal{A}_e$ simultaneously according to Equation 6.8, $\mathcal{P}_\tau$ is determined in different $\cos\theta$ bins. In each bin the MC distributions for the helicity states $h_\tau = \pm 1$ are fitted to the data distribution. This fit is performed with two free parameters, the polarization, $\mathcal{P}_\tau$, and the normalization factor, r (see Equation 6.28. The background ratios estimated from MC (see Table 6.4) are fixed. The fit results for r are compatible with 1 in each $\cos\theta$ bin. This is a proof that the determination of the selection efficiencies from the MC sample is correct, since the MC was normalized to the integrated luminosity of the 1991 and 1992 data.

The results for $\mathcal{P}_\tau$ have to be corrected for *charge confusion*. Since θ is defined as the polar angle between the negative charged τ and the z direction, one has to measure the charge of the final charged decay products. The charge is determined by the sign of the curvature, ρ, of the track measured in the TEC. Tracks with higher momentum appear straighter and the reconstruction algorithm can assign the wrong charge to the track.

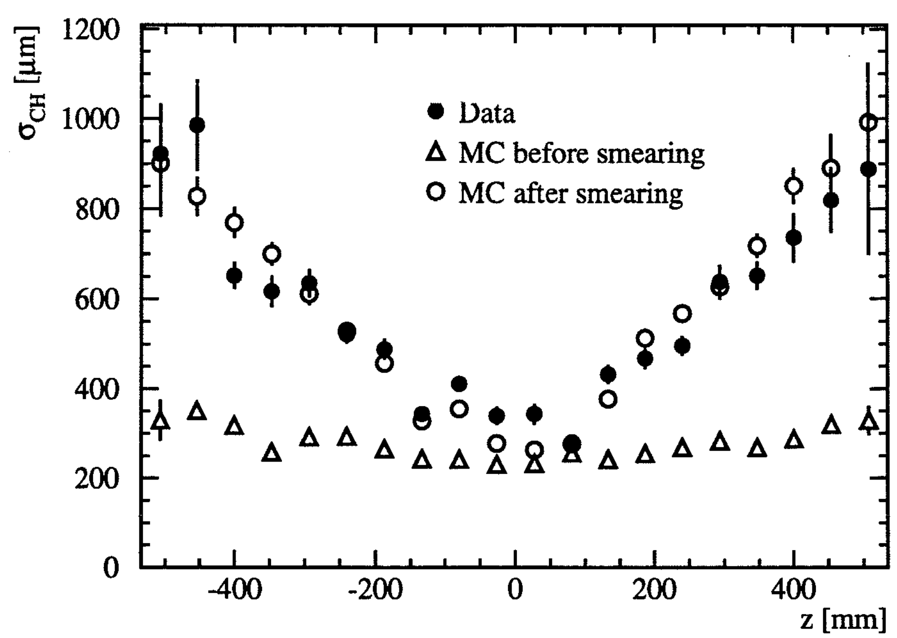

Figure 6.25: Z-chamber resolution for the MC sample before and after smearing in comparison to data.

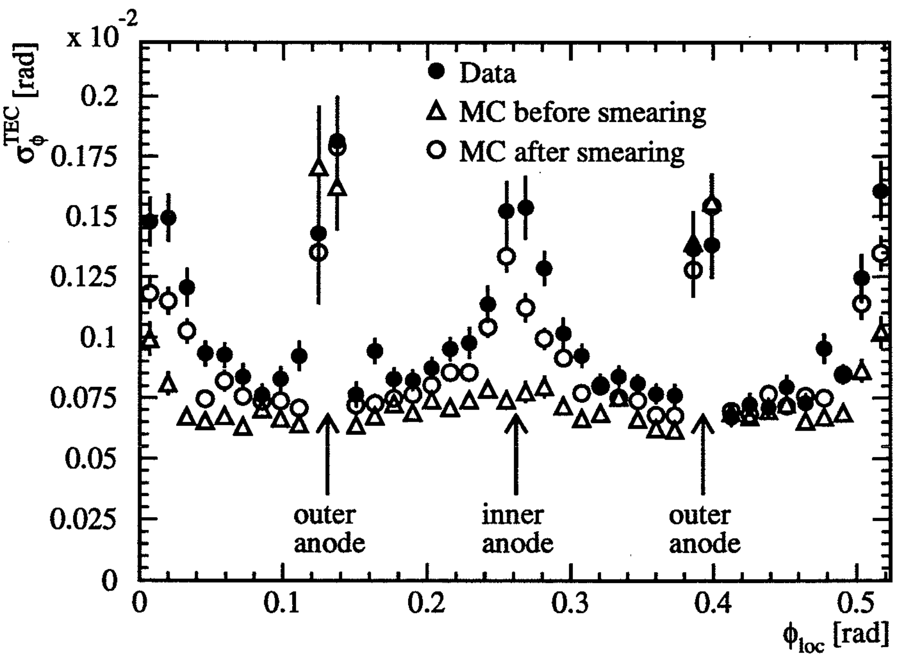

Figure 6.26: TEC ϕ resolution for the MC sample in comparison to data.

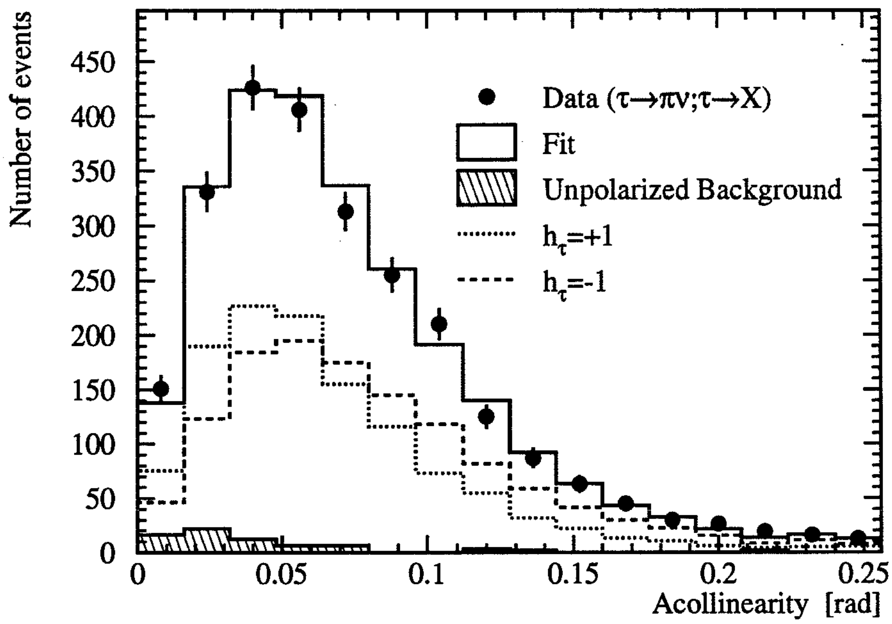

Figure 6.27: Acollinearity distribution for ($\tau \rightarrow \pi\nu$; $\tau \rightarrow Xn\nu$) events. The hatched histogram indicates the unpolarized background. The polarized background is included in the fit.

Therefore, the track with the lower momentum is always used for charge determination. Nevertheless, a possible charge confusion has to be taken into account and is studied using ($\tau \rightarrow \pi\nu$, $\tau \rightarrow \mu\nu\nu$) data events. Due to the high precision momentum measurement in the muon chambers the charge there is well defined and is used as reference for the charge determination with TEC. Using this technique the average charge confusion is measured to be $\zeta = 5 \pm 1\%$. Since the momenta of the tracks and their acollinearity are correlated, the momentum dependence of ζ is also visible in the acollinearity distribution (see Figure 6.28). The fit results of $\mathcal{P}_\tau(\cos\theta)$ have to be corrected for charge confusion. The observed value for the polarization $\mathcal{P}_\tau^{\mathrm{obs}}(\cos\theta)$ is given by (see also Equation 6.7) [10]:

$$\mathcal{P}_\tau^{\mathrm{obs}}(c_\theta) = \frac{N_+^{\mathrm{obs}}(c_\theta) - N_-^{\mathrm{obs}}(c_\theta)}{N_+^{\mathrm{obs}}(c_\theta) + N_-^{\mathrm{obs}}(c_\theta)}, \tag{6.32}$$

where $N_\pm^{\mathrm{obs}}(c_\theta)$ is the number of observed τ decays with helicity $h_f = \pm 1$ in a certain $\cos\theta$ bin. Since the charge confusion $N_\pm^{\mathrm{obs}}(c_\theta)$ is a mixture of the true number of τ decays in the bin $\cos\theta$ and the amount of τ decays, which are flipped from the bin $-c_\theta$ to c_θ:

$$N_\pm^{\mathrm{obs}}(c_\theta) = [1 - \zeta(|c_\theta|)]N_\pm^{\mathrm{true}}(c_\theta) + \zeta(|c_\theta|)N_\mp^{\mathrm{true}}(-c_\theta). \tag{6.33}$$

[10]In the following c_θ denotes $\cos\theta$.

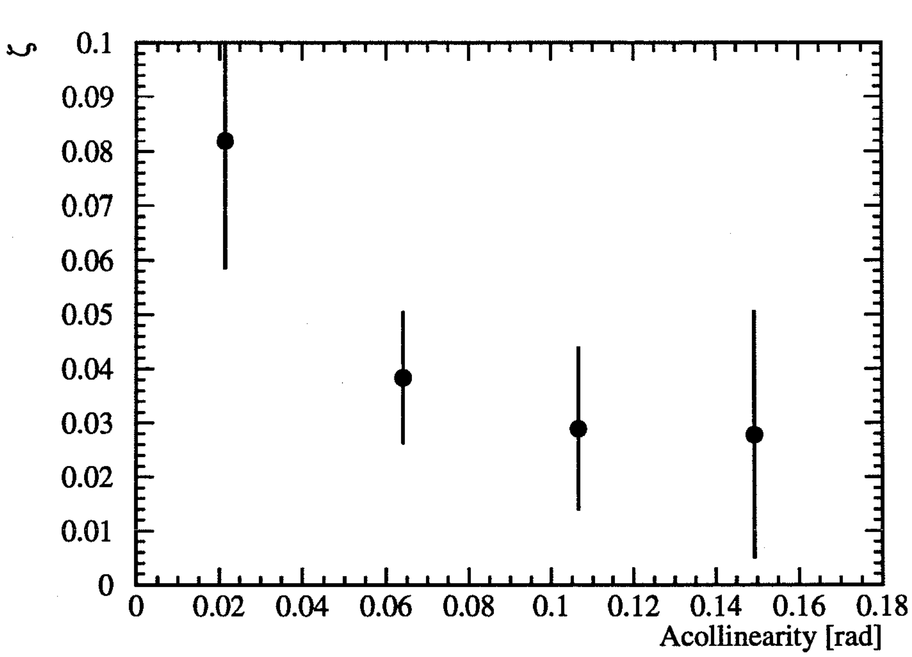

Figure 6.28: The charge confusion,ζ, as a function of the acollinearity.

With Equations 6.32 and 6.33 the true value for the τ polarization, $\mathcal{P}_\tau^{\text{true}}(c_\theta)$ is:

$$\begin{aligned}
&\mathcal{P}_\tau^{\text{true}}(c_\theta) \\
&= \frac{[1+\zeta(|c_\theta|)][N_+^{\text{obs}}(c_\theta)-N_-^{\text{obs}}(c_\theta)]-\zeta(|c_\theta|)[N_+^{\text{obs}}(-c_\theta)-N_-^{\text{obs}}(-c_\theta)]}{[1+\zeta(|c_\theta|)][N_+^{\text{obs}}(c_\theta)+N_-^{\text{obs}}(c_\theta)]-\zeta(|c_\theta|)[N_+^{\text{obs}}(-c_\theta)+N_-^{\text{obs}}(-c_\theta)]} \\
&= \frac{[1+\zeta(|c_\theta|)][A(c_\theta)-1]N_-^{\text{obs}}(c_\theta)-\zeta(|c_\theta|)[A(-c_\theta)-1]N_-^{\text{obs}}(-c_\theta)}{[1+\zeta(|c_\theta|)][A(c_\theta)+1]N_-^{\text{obs}}(c_\theta)-\zeta(|c_\theta|)[A(-c_\theta)+1]N_-^{\text{obs}}(-c_\theta)},
\end{aligned} \tag{6.34}$$

with

$$A(c_\theta) = \frac{1+\mathcal{P}_\tau(c_\theta)}{1-\mathcal{P}_\tau(c_\theta)}. \tag{6.35}$$

If one measures also the forward-backward asymmetry as a function of c_θ:

$$\begin{aligned}
\mathcal{A}_{\text{fb}}^{\text{obs}}(|c_\theta|) &= \frac{N_+^{\text{obs}}(c_\theta)+N_-^{\text{obs}}(c_\theta)-N_+^{\text{obs}}(-c_\theta)-N_-^{\text{obs}}(-c_\theta)}{N_+^{\text{obs}}(c_\theta)+N_-^{\text{obs}}(c_\theta)+N_+^{\text{obs}}(-c_\theta)+N_-^{\text{obs}}(-c_\theta)} \\
&= \frac{[A(c_\theta)+1]N_-^{\text{obs}}(c_\theta)-[A(-c_\theta)+1]N_-^{\text{obs}}(-c_\theta)}{[A(c_\theta)+1]N_-^{\text{obs}}(c_\theta)+[A(-c_\theta)+1]N_-^{\text{obs}}(-c_\theta)},
\end{aligned} \tag{6.36}$$

Equation 6.34 can be expressed as follows:

$\cos\theta$	$\mathcal{P}_\tau^{\text{obs}}$	$\mathcal{P}_\tau^{\text{true}}$	ζ	$\mathcal{A}_{\text{fb}}^{\text{obs}}$
−0.617	0.01±0.14	0.01±0.15	0.045±0.016	0.017±0.011
−0.411	0.08±0.20	0.09±0.20	0.038±0.015	0.012±0.012
−0.206	−0.05±0.18	−0.03±0.19	0.057±0.017	0.012±0.013
0.000	−0.17±0.17	−0.17±0.17	0.089±0.037	0.004±0.018
0.206	−0.40±0.17	−0.42±0.18	0.057±0.017	0.012±0.013
0.411	−0.21±0.16	−0.22±0.16	0.038±0.015	0.012±0.012
0.617	−0.05±0.15	−0.05±0.16	0.045±0.016	0.017±0.011

Table 6.10: The values of $\mathcal{P}_\tau^{\text{obs}}$, $\mathcal{P}_\tau^{\text{true}}$, ζ and $\mathcal{A}_{\text{fb}}^{\text{obs}}$ in the different $\cos\theta$ bins.

$$\mathcal{P}_\tau^{\text{true}}(c_\theta) = \frac{[1+\zeta(|c_\theta|)]\mathcal{P}_\tau^{\text{obs}}(c_\theta)[1+\mathcal{A}_{\text{fb}}^{\text{obs}}(|c_\theta|)] - \zeta(|c_\theta|)\mathcal{P}_\tau^{\text{obs}}(-c_\theta)[1-\mathcal{A}_{\text{fb}}^{\text{obs}}(|c_\theta|)]}{[1+\zeta(|c_\theta|)][1+\mathcal{A}_{\text{fb}}^{\text{obs}}(|c_\theta|)] - \zeta(|c_\theta|)[1-\mathcal{A}_{\text{fb}}^{\text{obs}}(|c_\theta|)]}. \tag{6.37}$$

The error on $\mathcal{P}_\tau^{\text{true}}$ is given by:

$$\Delta\mathcal{P}_\tau^{\text{true}}(c_\theta) = \sqrt{C_1 + C_2}, \tag{6.38}$$

with

$$\begin{aligned} C_1 &= [\Delta\mathcal{P}_\tau^{\text{obs}}(c_\theta)]^2 \frac{1+2\mathcal{A}_{\text{fb}}^{\text{obs}}(|c_\theta|)+2\zeta(|c_\theta|)}{1+2\mathcal{A}_{\text{fb}}^{\text{obs}}(|c_\theta|)}, \\ C_2 &= [\Delta\zeta(|c_\theta|)]^2[\mathcal{P}_\tau^{\text{obs}}(c_\theta) - \mathcal{P}_\tau^{\text{obs}}(-c_\theta)]^2 \frac{1-6\mathcal{A}_{\text{fb}}^{\text{obs}}(|c_\theta|)}{1-2\mathcal{A}_{\text{fb}}^{\text{obs}}(|c_\theta|)}. \end{aligned}$$

Terms proportional to ζ^2, $\mathcal{A}_{\text{fb}}^2$ and $\zeta\mathcal{A}_{\text{fb}}$ are neglected in Equation 6.38. In Table 6.6.3 the numerical values for $\mathcal{P}_\tau^{\text{obs}}$, $\mathcal{P}_\tau^{\text{true}}$, ζ and $\mathcal{A}_{\text{fb}}^{\text{obs}}$ are listed. $\mathcal{A}_{\text{fb}}^{\text{obs}}$ was measured using the whole $e^+e^- \rightarrow \tau^+\tau^-$ sample by counting forward and backward scattered events. The variation of ζ with the energy of the pion and therefore also with the acollinearity is neglected.

In Figure 6.29 the result of the polarization measurement corrected for charge confusion, $\mathcal{P}_\tau^{\text{true}}(\cos\theta)$, is plotted. The errors on the points are statistical only, taking into account the data and MC statistics. The solid and dashed line correspond to the fit of $\mathcal{P}_\tau(\cos\theta)$ using Equation 6.8 with and without the assumption of lepton universality respectively. The results, not assuming universality are:

$$\begin{aligned} \mathcal{A}_e &= 0.132 \pm 0.087(\textit{stat.}) \pm 0.049(\textit{sys.}), \\ \mathcal{A}_\tau &= 0.111 \pm 0.058(\textit{stat.}) \pm 0.038(\textit{sys.}). \end{aligned} \tag{6.39}$$

with a χ^2 / DOF = 3.6 / 5. The following systematic error sources are considered:

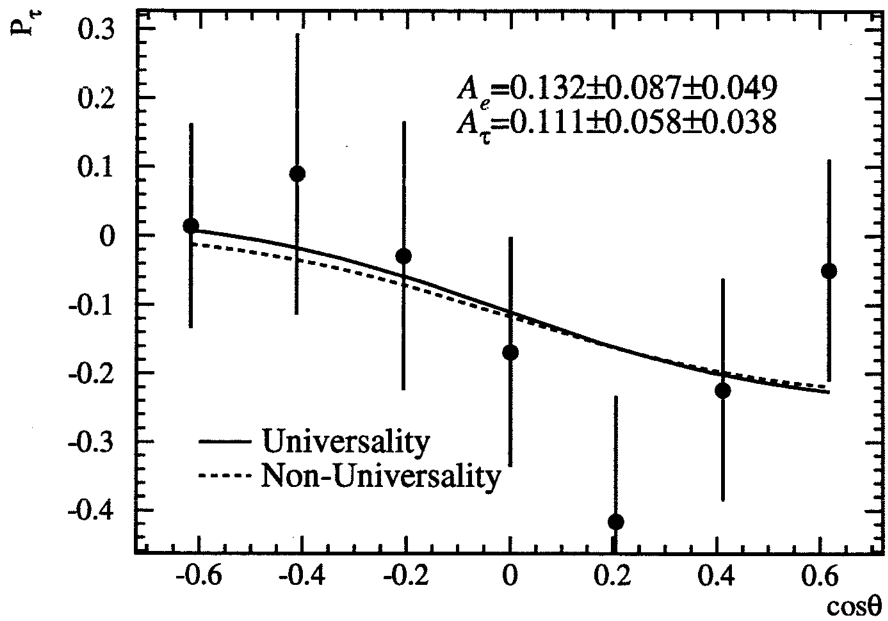

Figure 6.29: The τ polarization, $\mathcal{P}_\tau^{\mathrm{true}}$, as a function of $\cos\theta$. The fit results with and without lepton universality are indicated by the solid and dashed line respectively.

1. **Bias due to the $e^+e^- \to \tau^+\tau^-$ and $\tau \to \pi\nu$ selection:** To estimate the systematic contribution of the selection criteria to the final results of $\mathcal{A}_\tau$ and $\mathcal{A}_e$ important cuts of the electron and muon identification and of the $\tau \to \pi\nu$ selection are changed within reasonable limits. The change in $\mathcal{A}_\tau$ and $\mathcal{A}_e$ is attributed as the systematic error.

2. **Uncertainty in the beam width:** For the θ determination the intersection point with the beam line, z_0, is constrained by the beam width, σ_z^{int}. The value for σ_z^{int} was changed within its error, quoted in Equation 5.11.

3. **Uncertainty in the vertex measurement:** The position of the reference point in z is given by the fill vertex, V_z^{fill}. As an upper limit for a possible bias all fill vertices are shifted in the same direction by $\pm$ 0.15mm and $\pm$ 0.10mm, which correspond to the accuracy of the average vertex measurements for the whole 1991 and 1992 data samples respectively.

5. **Error from branching ratios:** Since $\mathcal{A}_e$ and $\mathcal{A}_\tau$ are determined in a semi-inclusive channel, the results also depend on the branching ratios of the different τ decay modes. For the branching ratios the latest world averages [14] shown in Table 2.2 are used. These branching ratios are varied independently within their errors. The sum of the branching ratios is always normalized to 1.

Error Source	Systematic Error	
	$\mathcal{A}_e$	$\mathcal{A}_\tau$
Selection	0.003	0.016
Beam Width	negl.	0.013
Vertex	0.016	0.009
Branching Ratios	0.003	0.005
Background	0.003	0.009
Charge Confusion	0.010	negl.
MC statistics	0.045	0.030
Total	0.049	0.038

Table 6.11: Systematic errors for the measurement of polarization asymmetries with the acollinearity method.

6. **Background estimation:** The background contamination in the data sample is estimated using the MC and is fixed in the fit to determine $\mathcal{P}_\tau(\cos\theta)$. The influence of the fixed background ratio is studied by varying it by 20%.

7. **Correction of charge confusion:** The acollinearity dependence of the charge confusion, ζ, is neglected in the correction of $\mathcal{A}_e$. The systematic error introduced is estimated by changing ζ within the maximum and minimum value, plotted in Figure 6.28.

The breakdown of the different systematic error sources for the $\mathcal{A}_e$ and $\mathcal{A}_\tau$ measurement is shown in Table 6.11.

6.6.4 Measurements with the energy method

In this section the results of the measurements of polarization asymmetries in the channels $\tau \to e\nu\nu$, $\tau \to \mu\nu\nu$, $\tau \to \pi\nu$, $\tau \to \rho\nu$ and $\tau \to a_1\nu$ with the energy method are summarized [47]. No details are presented, since this analysis has not been performed by the author. The values for $\mathcal{A}_e$ and $\mathcal{A}_\tau$ are presented in Table 6.12. The breakdown of the systematic errors for $\mathcal{A}_\tau$ is given in Table 6.13. For $\mathcal{A}_e$ the systematic error is attributed to charge confusion and the finite MC statistics. The error from charge confusion is estimated to be 0.01 for all channels, except for $\tau \to \mu\nu\nu$. Here it is is negligible, because of the excellent momentum resolution of the muon chambers. Only the average polarization was determined in the channel $\tau \to a_1\nu$ using 1991 data.

$\tau \to e\nu\nu$

In the leptonic decay mode $\tau \to e\nu\nu$ the polarization is measured with the normalized energy, u_e, (see Equation 6.16) of the electron. The energy is estimated by the sum of the

Decay Mode	$\mathcal{A}_e$	$\Delta\mathcal{A}_e$		$\mathcal{A}_\tau$	$\Delta\mathcal{A}_\tau$	
		stat.	syst.		stat.	syst.
$\tau \to c\nu\nu$	0.274	0.085	0.031	0.111	0.058	0.035
$\tau \to \mu\nu\nu$	0.226	0.078	0.028	0.180	0.056	0.034
$\tau \to \pi\nu$	0.158	0.044	0.021	0.168	0.030	0.055
$\tau \to \rho\nu$	0.084	0.028	0.015	0.195	0.020	0.019
$\tau \to a_1\nu$	–	–	–	-0.105	0.164	0.093

Table 6.12: Results of the polarization measurement with the energy method including the 1991 and 1992 data sample (for $\tau \to a_1\nu$ 1991 only).

Error Source	Decay Mode				
	$\tau \to e\nu\nu$	$\tau \to \mu\nu\nu$	$\tau \to \pi\nu$	$\tau \to \rho\nu$	$\tau \to a_1\nu$
Selection	0.015	0.010	0.017	0.008	0.045
Energy Calibration	0.014	0.017	0.050	0.013	0.033
Background	0.020	0.019	0.009	0.008	0.010
MC statistics	0.020	0.020	0.014	0.007	0.073
Total	0.035	0.034	0.055	0.019	0.093

Table 6.13: Breakdown of systematic errors for $\mathcal{A}_\tau$.

three most energetic clusters in the BGO, assuming they originated from electrons and photons. The spectrum of u_E is shown in Figure 6.30.

$\tau \to \mu\nu\nu$

As for electrons the polarization of the τ is measured with the normalized energy of the muon, u_μ. The energy is determined from the momentum measured in the muon chambers, p_μ, combined with the most probable energy loss of the muon in the calorimeters. The distribution of u_μ is shown in Figure 6.31.

$\tau \to \pi\nu$

The polarization of the τ in the $\tau \to \pi\nu$ mode is measured with the normalized energy of the π, u_π, which is estimated by the energy deposition in both calorimeters combined with the TEC momentum. The energy spectrum is shown in Figure 6.32.

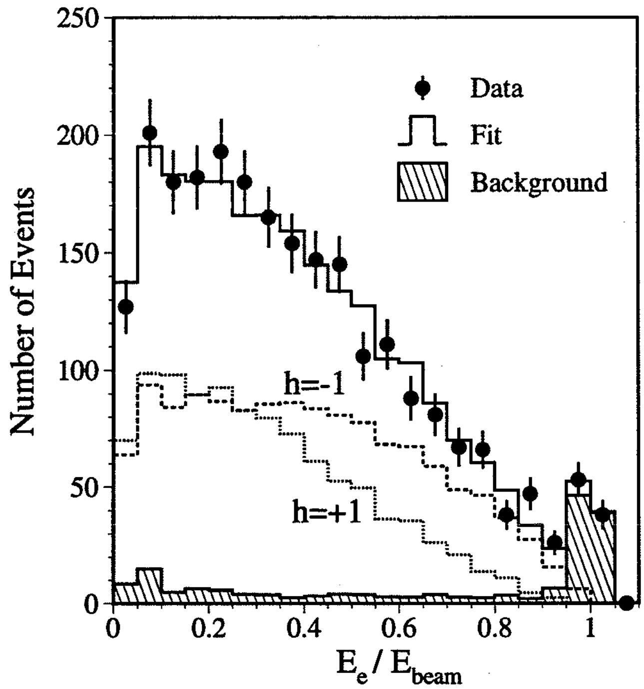

Figure 6.30: The normalized electron energy, $u_e = E_e / E_{\text{beam}}$.

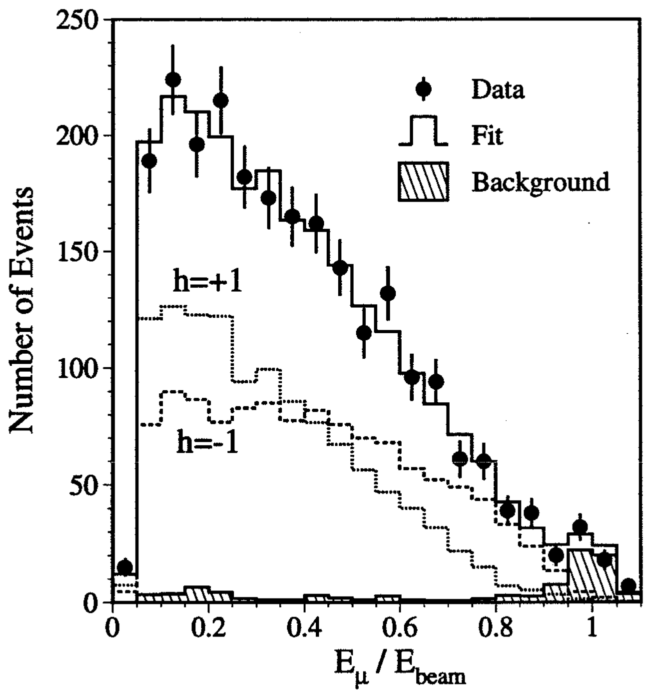

Figure 6.31: The normalized muon energy, $u_\mu = E_\mu / E_{\text{beam}}$.

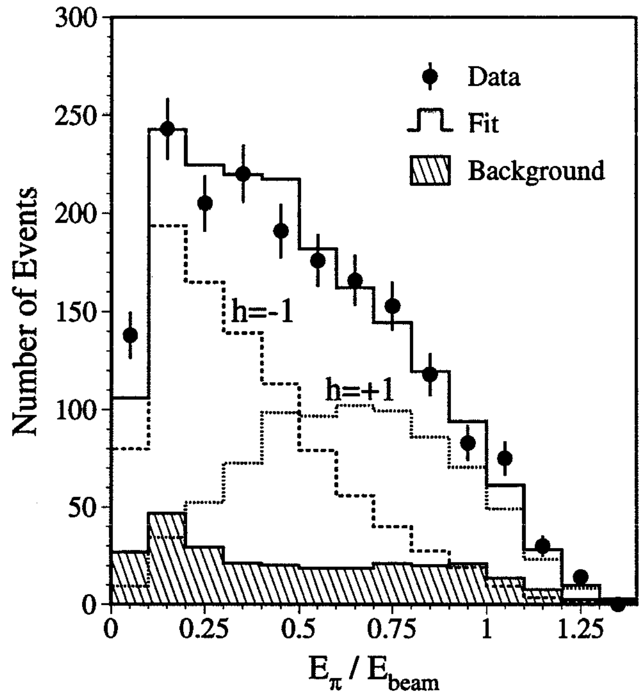

Figure 6.32: The normalized π energy, $u_\pi = E_\pi / E_{\mathrm{beam}}$.

$\tau \rightarrow \rho\nu$

$\mathcal{P}_\tau$ is determined from a fit to $\cos\theta^*_\rho$ and $\cos\psi^*_\rho$ (see Equation 6.17). The distribution of $\cos\psi^*$ in four different bins of $\cos\theta^*$ is shown in Figure 6.33.

$\tau \rightarrow a_1\nu$

The polarization is determined from a fit to $\cos\theta^*_{a1}$ and $\cos\psi^*_{a1}$ (see Equation 6.18).

6.6.5 Combination of the polarization results

In this section the procedure to combine the measurements of the polarization asymmetries for the different decay modes is explained. Special attention is given to the problem of how to combine the results of the energy and acollinearity methods for the same decay mode.

Combining the energy and acollinearity results in the channel $\tau \rightarrow \pi\nu$

The determination of the polarization for the energy method relies on the energy measurement in both calorimeters and the momentum measurement in TEC. For the acollinearity method, the ϕ and θ information from TEC and z-detector is used. The systematic errors

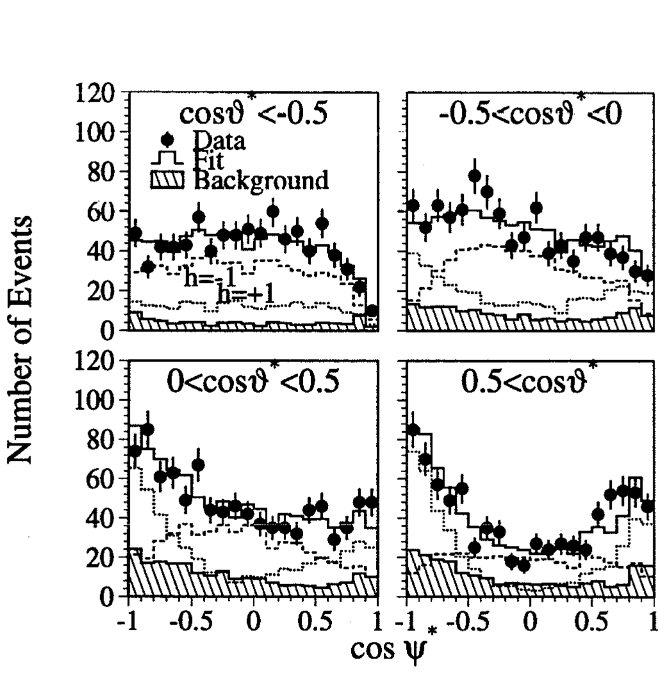

Figure 6.33: Distribution of $\cos\psi^*$ for ρ's in four different $\cos\theta^*$ bins.

of these measurements are thus uncorrelated. On the other hand one uses the same data and MC samples. Therefore, the statistical errors are correlated. The combination of the results is done using the BLUE's method described in [57].

Assuming we have measurements of the asymmetries with the energy method, $\mathcal{A}_\ell^{\mathrm{E}}$ and with the acollinearity method, $\mathcal{A}_\ell^{\varepsilon}$, then the common mean of both measurements is a linear combination of the single results multiplied with weight factors, α_ℓ^{E} and $\alpha_\ell^{\varepsilon}$:

$$\hat{\mathcal{A}}_\ell = \alpha_\ell^{\mathrm{E}}\mathcal{A}_\ell^{\mathrm{E}} + \alpha_\ell^{\varepsilon}\mathcal{A}_\ell^{\varepsilon}. \tag{6.40}$$

The weight factors are normalized:

$$\alpha_\ell^{\mathrm{E}} + \alpha_\ell^{\varepsilon} = 1. \tag{6.41}$$

The common error is then given by:

$$(\Delta\hat{\mathcal{A}}_\ell)^2 = (\alpha_\ell^{\mathrm{E}}, \alpha_\ell^{\varepsilon})E\begin{pmatrix} \alpha_\ell^{\mathrm{E}} \\ \alpha_\ell^{\varepsilon} \end{pmatrix}. \tag{6.42}$$

The error matrix, E, is defined as:

$$E = \begin{pmatrix} (\Delta\mathcal{A}_\ell^{\mathrm{E}})^2 & r_\ell\Delta\mathcal{A}_\ell^{\mathrm{E}}\Delta\mathcal{A}_\ell^{\varepsilon} \\ r_\ell\Delta\mathcal{A}_\ell^{\mathrm{E}}\Delta\mathcal{A}_\ell^{\varepsilon} & (\Delta\mathcal{A}_\ell^{\varepsilon})^2 \end{pmatrix}, \tag{6.43}$$

where r_ℓ is the correlation coefficient between both methods. To get the best possible error, $\Delta\hat{\mathcal{A}}_\ell$, one has to minimize the right-hand side of Equation 6.42 using α_ℓ^{E} or $\alpha_\ell^{\varepsilon}$ as a free parameter. The other weight factor is then fixed by Equation 6.41. The result is:

$$\alpha_\ell^{\mathrm{E}} = \frac{(\Delta\mathcal{A}_\ell^{\varepsilon})^2 - r_\ell \Delta\mathcal{A}_\ell^{\mathrm{E}} \Delta\mathcal{A}_\ell^{\varepsilon}}{(\Delta\mathcal{A}_\ell^{\varepsilon})^2 - r_\ell \Delta\mathcal{A}_\ell^{\mathrm{E}} \Delta\mathcal{A}_\ell^{\varepsilon} + (\Delta\mathcal{A}_\ell^{\mathrm{E}})^2}. \tag{6.44}$$

In order to estimate r_ℓ the error, $\Delta\mathcal{A}_\ell^m$, $m = \mathrm{E}, \epsilon$, is split up into three contributions:

$$(\Delta\mathcal{A}_\ell^m)^2 = (\Delta\mathcal{A}_\ell^{m,cor})^2 + (\Delta\mathcal{A}_\ell^{m,no})^2 + (\Delta\mathcal{A}_\ell^{m,full})^2. \tag{6.45}$$

$\Delta\mathcal{A}_\ell^{m,\mathrm{cor}}$: Here the statistical errors of the data and MC sample are combined. The correlation factor of these errors is denoted with r'_ℓ.

$\Delta\mathcal{A}_\ell^{m,\mathrm{no}}$: The uncorrelated part of the systematic error for both methods is summed here. For $\mathcal{A}_e^E$ no uncorrelated systematic error exists. For $\mathcal{A}_e^\epsilon$ the error due to the vertex and the branching ratios is considered. The uncorrelated part of $\mathcal{A}_\tau^E$ is the error of the energy calibration and for $\mathcal{A}_\tau^\epsilon$ it is the errors due to beam width, vertex and branching ratios.

$\Delta\mathcal{A}_\ell^{m,\mathrm{full}}$: The fully correlated part of the systematic error is given by the selection criteria and the background for both methods.

The error matrix, E, can also be expressed as a sum of matrices, each corresponding to one of the three contributions, with their correlation coefficients, r'_ℓ, 0 and 1 respectively. Then the overall correlation coefficient, r_ℓ, is given by:

$$r_\ell = \frac{r'_\ell \Delta\mathcal{A}_\ell^{E,\mathrm{cor}} \Delta\mathcal{A}_\ell^{\epsilon,\mathrm{cor}} + \Delta\mathcal{A}_\ell^{E,\mathrm{full}} \Delta\mathcal{A}_\ell^{\epsilon,\mathrm{full}}}{\Delta\mathcal{A}_\ell^{\mathrm{E}} \Delta\mathcal{A}_\ell^{\varepsilon}}. \tag{6.46}$$

The unknown parameter r'_ℓ can be estimated by a MC study. The idea is to perform a certain number of MC experiments, N_{exp}, and use the results of these experiments on $\mathcal{A}_e$ and $\mathcal{A}_\tau$ to estimate the correlation of the statistical errors between both methods. MC distributions for the energy of the pion and its acollinearity are generated, folding in detector effects such as efficiencies and resolutions. These distributions contain the same statistics of the data and MC sample used in the fits of the real experiment. The elements of the error matrix can then be calculated by:

$$E_\ell^{ij} = \frac{1}{N_{\mathrm{exp}}} \sum_{k=1}^{N_{\mathrm{exp}}} \left(\mathcal{A}_{\ell,k}^i - \bar{\mathcal{A}}_\ell^i\right) \left(\mathcal{A}_{\ell,k}^j - \bar{\mathcal{A}}_\ell^j\right); \quad i,j = E, \epsilon, \tag{6.47}$$

where $\mathcal{A}_{\ell,k}^i$ is the result of the kth MC polarization experiment with method i. The mean value $\bar{\mathcal{A}}_\ell$ is given by:

$$\bar{\mathcal{A}}_\ell^i = \frac{\sum_{k=1}^{N_{\mathrm{exp}}} \mathcal{A}_{\ell,k}^i}{N_{\mathrm{exp}}}. \tag{6.48}$$

The correlation coefficient, r'_ℓ, is calculable from the elements of E_ℓ^{ij}:

$$r'_\ell = \frac{E_\ell^{E,\epsilon}}{\sqrt{E_\ell^{E,E} E_\ell^{\epsilon,\epsilon}}}. \tag{6.49}$$

r'_E and r'_ϵ are found to be 0.3. The numerical values for the total correlation coefficients for $\mathcal{A}_e$ and $\mathcal{A}_\tau$, r_e and r_τ, defined in Equation 6.46 are 0.31 and 0.23 respectively. The combined results for $\mathcal{A}_e$ and $\mathcal{A}_\tau$ in the channel $\tau \to \pi\nu$ for the acollinearity and energy method are:

$$\begin{aligned} \hat{\mathcal{A}}_e &= 0.152 \pm 0.044(stat.) \pm 0.022(sys.), \\ \hat{\mathcal{A}}_\tau &= 0.139 \pm 0.037(stat.) \pm 0.037(sys.). \end{aligned} \tag{6.50}$$

Combining the results on $\mathcal{A}_e$ and $\mathcal{A}_\tau$ for the different decay modes

The results on $\mathcal{A}_e$ and $\mathcal{A}_\tau$ in the different decay channels using the energy method (see Table 6.12, except for $\tau \to \pi\nu$) and the result for the energy and acollinearity method in the channel $\tau \to \pi\nu$ (see Equation 6.50) are combined to a weighted average and error. For the calculation of the mean value and error of the polarization asymmetries, the statistical and systematic errors are treated as uncorrelated, except for the error assigned to charge confusion for $\mathcal{A}_e$. The charge and the polar angle are measured with the same method for all decay channels considered. Only for the channel $\tau \to \mu\nu\nu$ the charge confusion can be neglected. The results are:

$$\begin{aligned} \mathcal{A}_e &= 0.126 \pm 0.022(stat.) \pm 0.013(sys.), \\ \mathcal{A}_\tau &= 0.172 \pm 0.016(stat.) \pm 0.014(sys.). \end{aligned} \tag{6.51}$$

In Equation 6.8, which is used to determine $\mathcal{A}_e$ and $\mathcal{A}_\tau$, the contribution of the γ-exchange and the γZ-interference is neglected, as well as radiative corrections. The package ZFITTER [9] calculates the polarization asymmetries with all these effects taken into account as a function of the center-of-mass energy, $\sqrt{s}$, and the mass, m_Z, and width, Γ_Z, of the Z boson. In Figure 6.34 the differences between the polarization asymmetries, taking into account the γ-exchange, the γZ-interference and radiative corrections and the polarization asymmetries, where certain corrections are neglected, $\Delta_{pol} = \mathcal{A}_{pol}^{cor} - \mathcal{A}_{pol}^{nocor}$ and $\Delta_{fb-pol} = \mathcal{A}_{fb-pol}^{cor} - \mathcal{A}_{fb-pol}^{nocor}$ are plotted. For m_Z and Γ_Z the L3 measurements are used (see Chapter 7 and Table 7.3). The effect of neglecting each of the three corrections is shown separately, while the solid line shows the effect on neglecting them all. The corrections show qualitatively the same behavior for $\mathcal{A}_{pol}$ and $\mathcal{A}_{fb-pol}$. Neglecting the γZ-interference leads to a $\sqrt{s}$ dependence of Δ_{pol} and Δ_{fb-pol}. The size of the effect due to neglecting the γ-exchange and radiative corrections is almost constant in the displayed $\sqrt{s}$ region. The vertical lines show the Z mass measurement of L3 and the $\sqrt{s}$ points with highest luminosity, where LEP ran in 1991 ($\sqrt{s}$ = 91.254 GeV) and 1992 ($\sqrt{s}$ = 91.294, see Table 6.5). The combined correction for the γ-exchange, the γZ-interference and radiative corrections at these energy points amounts to:

$$\begin{aligned} \Delta_{pol} &\simeq 0.0006, \\ \Delta_{fb-pol} &\simeq 0.0004. \end{aligned} \tag{6.52}$$

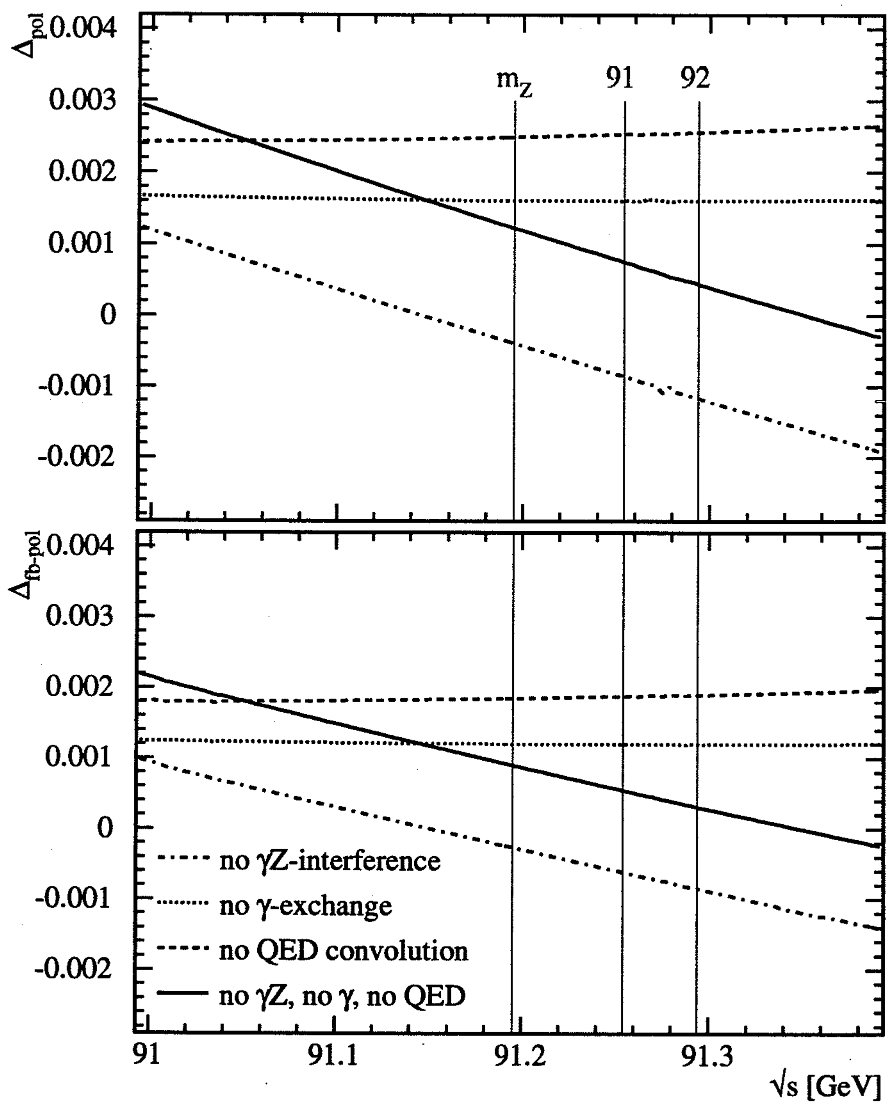

Figure 6.34: The difference of the polarization asymmetries with and without the γ-exchange, γZ-interference and radiative corrections (QED convolution), Δ_{pol} and Δ_{fb-pol} as a function of $\sqrt{s}$. The solid line represents the case where all three corrections are neglected, while the dashed lines show their individual contributions. The vertical lines denotes the m_Z measurement of L3 and the $\sqrt{s}$ points with the highest luminosity, where LEP ran in 1991 and 1992.

The difference for $\mathcal{A}_{pol}$ is lower than the value $\Delta_{pol} \simeq 0.0025$ given in [58], since the effects of the γ-exchange and γZ-interference were not considered in that investigation. But $\Delta_{pol} \simeq 0.0025$ is in good agreement with the line in Figure 6.34 if only radiative corrections are neglected. The corrections Δ_{pol} and Δ_{fb-pol} are not significant in comparison to the errors on $\mathcal{A}_e$ and $\mathcal{A}_\tau$[11]. However, the final result for $\mathcal{A}_e$ and $\mathcal{A}_\tau$ is corrected with Δ_{pol} and Δ_{fb-pol}:

$$\boxed{\begin{aligned} \mathcal{A}_e &= 0.125 \pm 0.022(stat.) \pm 0.013(sys.), \\ \mathcal{A}_\tau &= 0.171 \pm 0.016(stat.) \pm 0.014(sys.). \end{aligned}} \tag{6.53}$$

The $\sqrt{s}$ points where LEP was not running on the Z peak in 1991 are neglected in the corrections in Equation 6.52, since the luminosity is much reduced. Nevertheless, for future analyzes the corrections Δ_{pol} and Δ_{fb-pol} can become significant and have to be taken into account properly [12]

The results on $\mathcal{A}_e$ and $\mathcal{A}_\tau$ can be treated as independent, since their correlation in the combined fit to the $\mathcal{P}_\tau(\cos\theta)$ spectrum is 0.03. The ratio of $\mathcal{A}_e$ and $\mathcal{A}_\tau$ is compatible with 1 and thus confirms the e-τ universality:

$$\frac{\mathcal{A}_e}{\mathcal{A}_\tau} = 0.73 \pm 0.18. \tag{6.54}$$

6.6.6 Comparision of polarization results between the LEP experiments

All LEP experiments performed a measurement of the polarization asymmetries and published their results using the 1990-1991 data samples [13] [47,59–61]. The numbers for $\mathcal{A}_e$ and $\mathcal{A}_\tau$, listed in Table 6.14, represent preliminary results using the 1990-1992 statistics (see [62] and references therein). For the L3 collaboration the results in Equation 6.53 are used. The LEP mean value is derived by combining the single measurements. The common systematic error due to the LEP energy uncertainty is small and is neglected. In Figure 6.35 the results are plotted. All experimental results agree within the errors.

The LEP average for the ratio of $\mathcal{A}_e$ and $\mathcal{A}_\tau$ is determined to be:

$$\frac{\mathcal{A}_e}{\mathcal{A}_\tau} = 0.799 \pm 0.097. \tag{6.55}$$

The mean value is 2σ away from 1, but is still compatible with the assumption of lepton universality.

[11] $\mathcal{A}_e$ and $\mathcal{A}_\tau$ are related to $\mathcal{A}_{fb-pol}$ and $\mathcal{A}_{pol}$ by Equation 3.19.

[12] In 1993 the LEP experiments collected 25% of the annual integrated luminosity at two energy points at $\pm$ 1.8 GeV from the Z resonance. At these points the absolute values for Δ_{pol} and Δ_{fb-pol} are one order of magnitude higher than those in Equation 6.52.

[13] The OPAL collaboration published results using only the 1990 data.

Experiment	$\mathcal{A}_e$	$\mathcal{A}_\tau$
ALEPH	0.127±0.017	0.137±0.014
DELPHI	0.081±0.033	0.154±0.023
L3	0.125±0.026	0.171±0.021
OPAL	0.117±0.033	0.150±0.025
LEP average	0.119±0.012	0.149±0.010

Table 6.14: The measurements of $\mathcal{A}_e$ and $\mathcal{A}_\tau$ for the LEP experiments and their average using the 1990-1992 data samples.

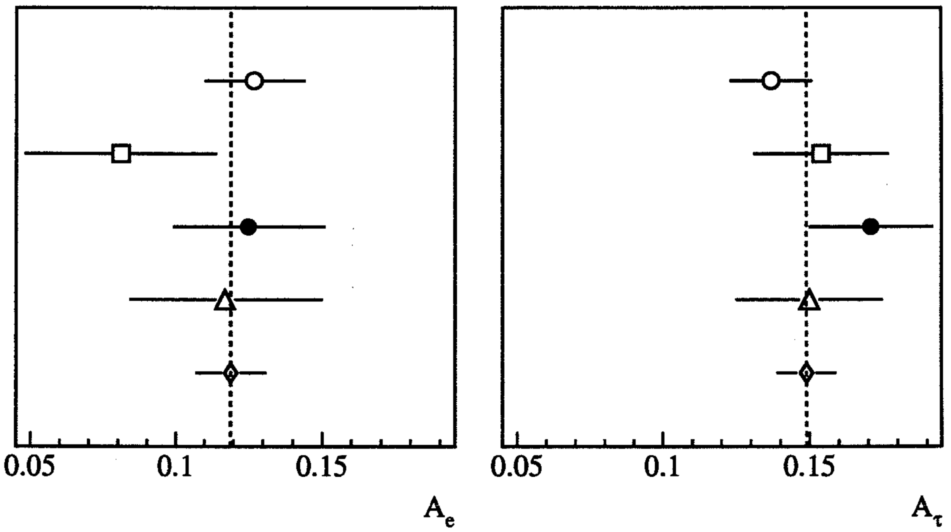

Figure 6.35: The measurements of $\mathcal{A}_e$ and $\mathcal{A}_\tau$ for the LEP experiments, ALEPH(○), DELPHI(□), L3(•) and OPAL(△), and their average(◇) using the 1990-1992 data samples. The dashed line indicate the LEP average.

Chapter 7

Determination of Neutral Current Parameters

Neutral current parameters of the process $e^+e^- \rightarrow \tau^+\tau^-$ for the S-matrix (see Section 3.1), effective coupling (see Section 3.2) and partial width approaches (see Section 3.3) are determined in a χ^2 fit to the experimental results for the total cross section (see Table 6.5), the forward-backward asymmetry (see Table 6.7) and the polarization asymmetries (see Equation 6.53). To compare the obtained results with the other decay channels, the measurements of total cross sections and forward-backward asymmetries published in [46] are used.

Conventions for labeling the fit results for the different final states are introduced in Figure 7.1.

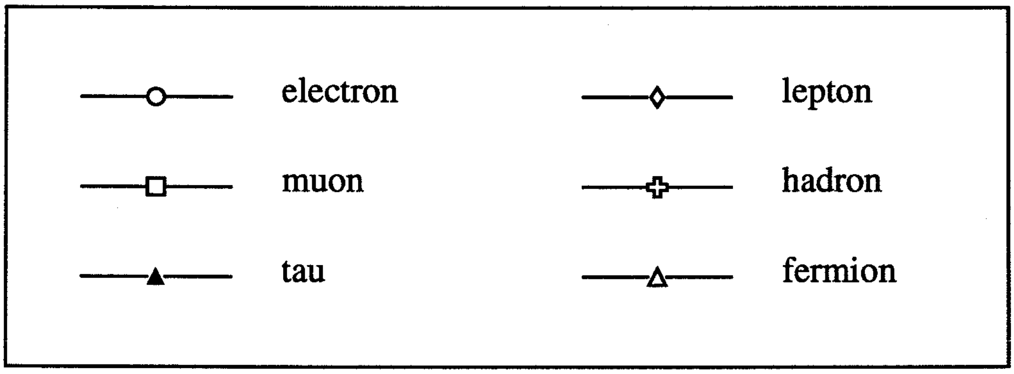

Figure 7.1: Conventions for labeling the fit results for the different final states. With *electron, muon* and *tau* fit parameters of the corresponding lepton are denoted. *Lepton* marks leptonic fit parameters assuming lepton universality. Fit parameters for hadronic final states are signed with *hadron.* In a simultaneous fit to hadron and all lepton channels the parameters common to all channels are denoted with *fermion.*

7.1 Fitting Procedure

The neutral current parameters are determined in a χ^2 fit using the function minimization package MINUIT [56]. The χ^2 is defined as the matrix product of the difference vector, $\Delta^i = y^i_{ex} - y^i_{th}$ between the experimental measurements and the theoretical predictions and the inverse covariance matrix E^{ij} [63]:

$$\chi^2 = \Delta\, E^{-1} \Delta^T. \tag{7.1}$$

To obtain theoretical predictions for cross sections and asymmetries the analytical program ZFITTER 4.53 [9] is used for the effective coupling and partial width approaches. For the S-matrix ansatz the package SMATASY [64] was developed. SMATASY is a ZFITTER extension based on the interface ZUSMAT. ZUSMAT realizes the S-matrix ansatz for total cross sections and SMATASY extends it for asymmetries. Since SMATASY is implemented in ZFITTER, it relies on the same treatment of radiative corrections. ZFITTER includes electroweak radiative corrections to $O(\alpha)$ and a common exponentiation of initial and final state bremsstrahlung [65,66]. The corrections to $O(\alpha^2)$ are taken into account in the leading-log approximation and include the production of photon and fermion pairs in the initial state. Furthermore, the $O(\alpha)$ and $O(\alpha^2)$ corrections are supplemented with the $O(\alpha\alpha_s m_t^2 \,/\, m_W^2)$ and the $O(\alpha^2 m_t^4 \,/\, m_W^4)$ corrections from t quark insertions in the gauge-boson self energies and in the $Zb\bar{b}$ vertex [67,68]. QCD corrections in the final state with quarks are considered up to $O(\alpha_s{}^3)$ [69,70].

The covariance matrix E^{ij} contains the statistical and systematic errors of the individual measurements as well as the uncertainties in the luminosity determination and the LEP beam energy. The error on the determination of the LEP beam energy is taken into account according to Equation 4.3 and Table 4.2. Systematic errors for the cross section and asymmetry measurement are treated as uncorrelated between different Z decay channels. For each final state the systematic errors are fully correlated between different energy points and between the data sets from different years. The systematic uncertainty in the luminosity (see Table 6.6) is correlated for all cross sections in all channels and all years. Statistical errors, $\delta\sigma^{\rm st}_{\rm tot}$ and $\delta\mathcal{A}^{\rm st}_{\rm A}$, are uncorrelated. These errors are corrected by a factor, which accounts for deviations of the measurement from the theoretical prediction, $\sigma^{\rm th}_{\rm tot}$ and $\mathcal{A}^{\rm th}_{\rm A}$:

$$\begin{aligned} \delta\bar{\sigma}^{\rm st}_{\rm tot}(s) &= \delta\sigma^{\rm st}_{\rm tot}(s)\sqrt{\frac{\sigma^{\rm th}_{\rm tot}(s)}{\sigma_{\rm tot}(s)}}, \\ \delta\bar{\mathcal{A}}^{\rm st}_{\rm A}(s) &= \delta\mathcal{A}^{\rm st}_{\rm A}(s)\sqrt{\frac{1-\mathcal{A}^{\rm th}_{\rm A}(s)^2}{1-\mathcal{A}_{\rm A}(s)^2}}\sqrt{\frac{\sigma_{\rm tot}(s)}{\sigma^{\rm th}_{\rm tot}(s)}}. \end{aligned} \tag{7.2}$$

For the process $e^+e^- \to e^+e^-$ one has also to take into account the t-channel exchange of the photon and Z boson. Since ZFITTER computes only the s-channel one has to use other programs, such as ALIBABA [71]. ALIBABA is not suited for fitting purposes, because the calculations are very time consuming. Therefore, ALIBABA is used only in the beginning of the fit procedure to calculate the t-channel and s/t-interference contribution. This contribution is then subtracted from the measured $e^+e^- \to e^+e^-$ cross sections and forward-backward asymmetries. The remaining s-channel part is fitted using ZFITTER (SMATASY). For this method an additional systematic error of 0.3% for the cross section and 0.003 for the forward-backward asymmetry is assigned.

The measurements for σ_{tot} are corrected for the LEP beam spread of 51 MeV(see Section 4.2.3).

7.2 Results in the S-Matrix Approach

The free parameters of the S-matrix approach are the mass and width of the Z boson, $\overline{m}_Z$ and $\overline{\Gamma}_Z$ (see Equation 3.2 and 3.3) and the four complex helicity amplitudes R_Z^{fi} (see Equation 3.6 and 3.8). Instead of R_Z^{fi}, one can choose the Z-exchange and γZ-interference term for each cross section, $\sigma_A(s)$ (see Equation 3.7), r_A^f and j_A^f, which represent 8 free parameters in addition to $\overline{m}_Z$ and $\overline{\Gamma}_Z$. The use of R_Z^{fi} introduces correlations between the different cross sections, while fitting r_A^f and j_A^f treats every $\sigma_A(s)$ as independent. In the following it is always assumed that the imaginary parts of R_Z^{fi} are zero. Thus, the number of free parameters is reduced by four. This is a reasonable assumption, since the imaginary parts are caused by electroweak corrections, which are very small in the vicinity of the Z resonance. The process $e^+e^- \to \tau^+\tau^-$ is the only process at LEP, where all the real parts of R_Z^{fi} can be determined, because the short lifetime of the τ allows the polarization asymmetries to be measured in addition to the total cross section and the forward-backward asymmetry. These measurements correspond to a complete set of σ_A. To fit r_A^f and j_A^f directly one needs a measurement of σ_A or $\mathcal{A}_A$ as a function of the center-of-mass energy, $\sqrt{s}$. Since the statistics for events taken off the Z peak are very limited, the polarization asymmetries are not yet measured as a function of $\sqrt{s}$.

A unique feature of the S-matrix approach is the possibility to determine all parameters in one decay channel, exclusively. The S-matrix ansatz has no specific parameters attributed to the initial and final state only. There is thus no correlation between different decay channels, because of identical initial state particles.

The results of the fit to $\overline{m}_Z$, $\overline{\Gamma}_Z$ and the $R_Z^{\tau i}$ are shown in the second column of Table 7.1 using the neutral current measurements in the τ channel only. For comparison the measurements in the remaining lepton channels, $e^+e^- \to e^+e^-$ and $e^+e^- \to \mu^+\mu^-$ are also interpreted within the S-matrix approach. The only observables which can then be measured are the total cross section and the forward-backward asymmetry. Therefore, besides $\overline{m}_Z$ and $\overline{\Gamma}_Z$ the free parameters are the Z-exchange and γZ-interference terms r_{tot}^f, r_{fb}^f, j_{tot}^f and j_{fb}^f. To compare the fit results with the numbers from the $e^+e^- \to \tau^+\tau^-$ channel, the $R_Z^{\tau i}$ are converted into these parameters. The results are compared in Figure 7.2. The upper three points in each plot correspond to the fit results in the lepton channels. The numbers for the three lepton channels show good agreement for all six parameters. The errors on the interference terms in the τ channel are much smaller, since they are not free parameters. j_A^τ are determined by $R_Z^{\tau i}$ and profit from the accurate measurements of polarization

Parameter	$e^+e^- \rightarrow \tau^+\tau^-$	$e^+e^- \rightarrow \ell^+\ell^-$	$e^+e^- \rightarrow q\bar{q}$	$e^+e^- \rightarrow f\bar{f}$	Standard Model
$\overline{m}_Z$ [GeV]	91.155±0.036	91.167±0.021	91.153±0.015	91.160±0.013	–
$\overline{\Gamma}_Z$ [GeV]	2.501±0.061	2.477±0.033	2.498±0.011	2.496±0.011	2.499±0.009
R_Z^{f0}	0.437±0.012	0.431±0.008	–	0.434±0.006	0.434±0.005
R_Z^{f1}	-0.363±0.011	-0.361±0.008	–	-0.364±0.007	-0.374±0.010
R_Z^{f2}	0.321±0.011	0.315±0.009	–	0.317±0.008	0.323±0.002
R_Z^{f3}	-0.381±0.011	-0.379±0.008	–	-0.381±0.007	-0.374±0.010
r_{tot}^{had}	–	–	2.865±0.031	2.861±0.030	2.866±0.020
j_{tot}^{had}	–	–	0.66±0.73	0.47±0.63	0.212±0.015
χ^2/DOF	25/28	79/92	6/12	86/106	–

Table 7.1: Fit results in the S-matrix approach. In the second column the results in $e^+e^- \rightarrow \tau^+\tau^-$ channel only are shown. Assuming universality all lepton channels are combined for the results in the third column. In the fourth column the results for the $e^+e^- \rightarrow q\bar{q}$ channel are shown. All data assuming lepton universality are considered in the fifth column. In the last column the Standard Model predictions are listed. For the free parameters m_Z and m_t the results of the fit in Section 7.6 are taken. The Higgs mass is varied between 60 [72] and 1000 GeV and α_s is constrained to $\alpha_s = 0.123 \pm 0.006$ [28].

asymmetries. Since $\overline{m}_Z$ and the interference term are correlated ($\sigma_A^{\gamma Z,f}(s = \overline{m}_Z) = 0$) [1] the error on $\overline{m}_Z$ is also minimal for τ leptons. The results in the lepton channels confirm lepton universality. Therefore, all measurements of the lepton channels are fitted simultaneously assuming lepton universality. The parameter set with helicity amplitudes $R_Z^{\ell i}$ is used. The results are shown in the third column of Table 7.1. For comparison these numbers are converted to r_{tot}^f, r_{fb}^f, j_{tot}^f and j_{fb}^f and plotted in in Figure 7.2. Additionally, a four parameter fit to the hadron cross section was performed to determine $\overline{m}_Z$, $\overline{\Gamma}_Z$, r_{tot}^{had} and j_{tot}^{had}. The results are shown in column 3 of Table 7.1. The numbers for $\overline{m}_Z$ and $\overline{\Gamma}_Z$ are plotted in Figure 7.2. Note that the error on $\overline{m}_Z$ is only a factor 2.4 larger for the process $e^+e^- \rightarrow \tau^+\tau^-$ than for $e^+e^- \rightarrow q\bar{q}$. Using all leptonic results reduces the factor to 1.4. Without a measurement of the polarization asymmetries the error on $\overline{m}_Z$ for all lepton channels would be 2.7 times larger than in the $e^+e^- \rightarrow q\bar{q}$ channel. Finally, a simultaneous fit to all data assuming lepton universality was performed (see last column in Table 7.1 and Figure 7.2). The results of these analyzes have been published for the 1991 data [73–75].

In the last column of Table 7.1 the Standard Model predictions for the S-matrix parameters are listed. In Figure 7.2 the solid vertical lines denotes the Standard Model predictions and the hatched band their errors. For the predictions the results of the fit in the framework of the Standard Model in Section 7.6 are used. For the Z and t-quark mass, $m_Z = (91.198 \pm 0.009)$ GeV and $m_t = (188^{+28+17}_{-33-18})$ GeV are obtained. m_H is varied

[1] $\sigma_A^{\gamma Z,f}$ denotes the part of the cross section which is proportional to j_A^f.

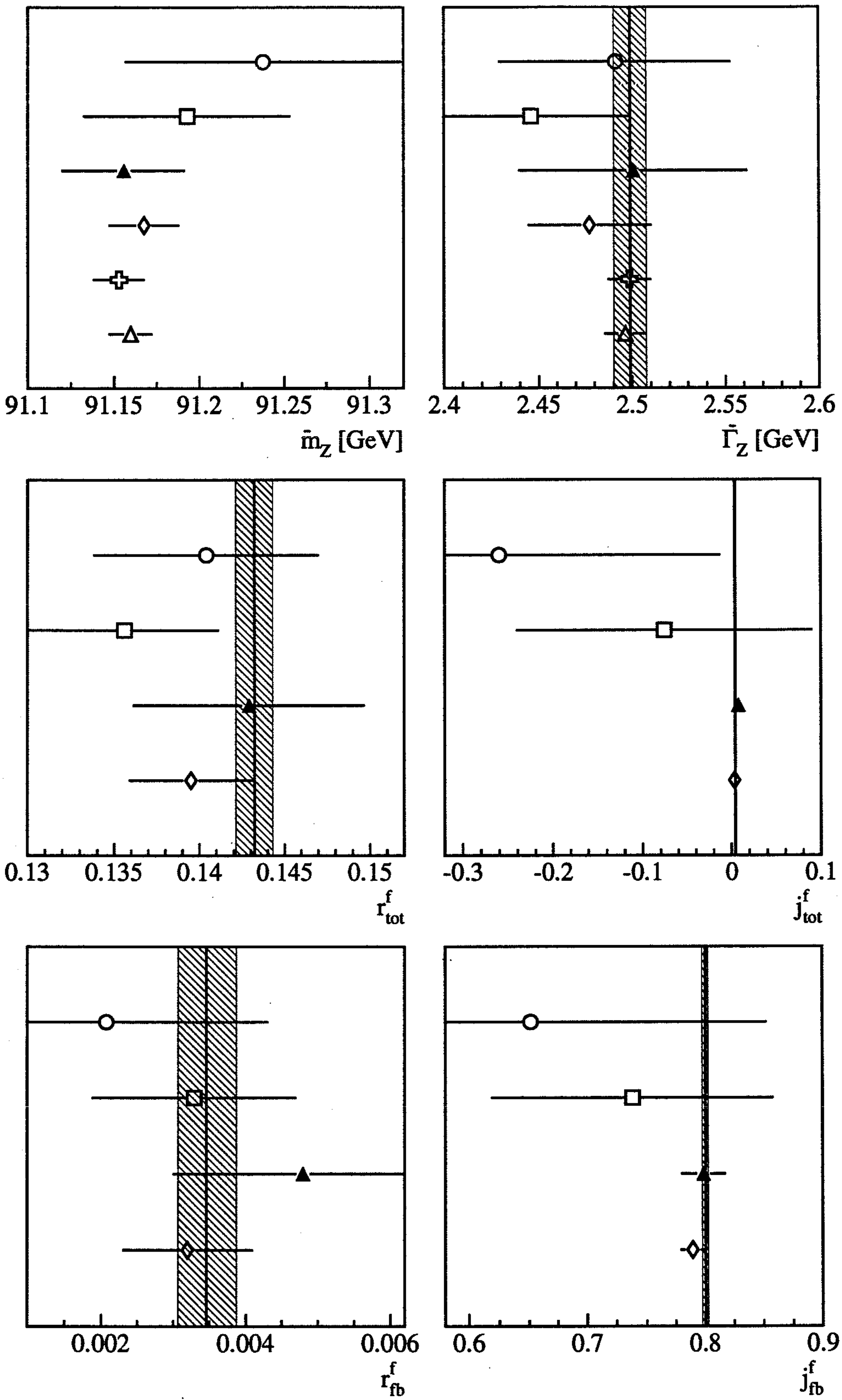

Figure 7.2: Fit results in the S-matrix approach are compared for the six parameters $\overline{m}_Z$, $\overline{\Gamma}_Z$, r^f_{tot}, j^f_{tot}, r^f_{fb} and j^f_{fb} in different fermion channels. The solid vertical lines denote the Standard Model predictions and the hatched regions their error range.

between 60 [72] and 1000 GeV and α_s is constrained by $\alpha_s = 0.123 \pm 0.006$ [28]. All parameters agree well with the Standard Model prediction [2]. The predictions of the Standard Model shown in the next sections are derived in the same manner.

7.3 Results in the Effective Coupling Approach

The free parameters in the effective coupling approach are the mass and width of the Z boson, m_Z and Γ_Z (see Equation 3.1 and the effective vector and axial-vector couplings for electrons and the final state fermions, $\hat{g}_V^e$, $\hat{g}_A^e$, $\hat{g}_V^f$ and $\hat{g}_A^f$. In the effective Born approximation the total width of the Z boson is $\sqrt{s}$ dependent due to self-energy insertions in the Z propagator. Therefore, the different definitions of m_Z, Γ_Z in the effective coupling and partial width approaches and $\overline{m}_Z$, $\overline{\Gamma}_Z$ used in the S-matrix approach lead to a shift as given in Equation 3.3. The effective coupling approach can only be applied to the lepton channels. For hadronic decay modes it is not possible, since the determination of the Z couplings to $q\bar{q}$ pairs requires the measurement of the total cross section and at least one asymmetry for each quark channel [3].

The effective couplings are parameters related to the initial or final state of the scattering process. In general one cannot determine the couplings to the electron and the final state lepton separately using only measurements of the corresponding scattering process. It is possible for $e^+e^- \to e^+e^-$ scattering, because initial and final state fermions are identical. Due to the measurement of the polarization asymmetries in the process $e^+e^- \to \tau^+\tau^-$ one can also determine the electron and τ couplings, without adding any information from other channels. But for $e^+e^- \to \mu^+\mu^-$ scattering one has also to take into account information from the electron channel to determine the electron and muon couplings separately.

A simultaneous fit to all leptonic measurements is performed with and without the assumption of lepton universality. The results are listed in Table 7.2 and the couplings are plotted in Figure 7.3. The vector and axial-vector couplings are in good agreement between the lepton channels, which confirms the hypothesis of lepton universality. The polarization asymmetries are very sensitive to the vector couplings, which is reflected in the small uncertainties for $\hat{g}_V^e$ and $\hat{g}_V^\tau$ compared to $\hat{g}_V^\mu$. A fit without the polarization asymmetries yields an error for $\hat{g}_V^\ell$ of 0.0052, while the error on the axial-vector coupling remains unaffected. The error of $\hat{g}_A^\ell$ is mostly determined by the measurement of the total cross section. Furthermore, the polarization asymmetries determine the relative sign of the couplings, since they are linear in the couplings (see Equation 3.19). The mean value of $\overline{m}_Z$, $\overline{\Gamma}_Z$ and m_Z, Γ_Z differ by the amount calculated in Equation 3.3 for fits using the same data set and the identical lepton treatment, i.e. third column in Table 7.1 and in Table 7.2.

The fit results in the effective coupling approach are in good agreement with the Standard Model predictions.

[2] In Section 7.6 it is explained, how the Standard Model predictions are derived from m_Z, m_t and m_H.

[3] L3 has performed a measurement of the forward-backward asymmetry for c and b quarks [76].

Parameter	Treatment of Charged Leptons		Standard Model
	Non-Universality	Universality	
m_Z[GeV]	91.197±0.020	91.201±0.020	–
Γ_Z[GeV]	2.479±0.033	2.478±0.033	2.500±0.009
$\hat{g}_V^e$	-0.0333±0.0055	–	–
$\hat{g}_V^\mu$	-0.0428±0.0174	–	–
$\hat{g}_V^\tau$	-0.0454±0.0053	–	–
$\hat{g}_V^\ell$	–	-0.0391±0.0033	-0.0369±0.0023
$\hat{g}_A^e$	-0.4986±0.0033	–	–
$\hat{g}_A^\mu$	-0.4966±0.0040	–	–
$\hat{g}_A^\tau$	-0.4993±0.0042	–	–
$\hat{g}_A^\ell$	–	-0.4981±0.0032	-0.5016±0.0008
χ^2/DOF	78/106	82/110	–

Table 7.2: Fit results in the effective coupling approach with and without lepton universality. The Standard Model predictions are given in the third column.

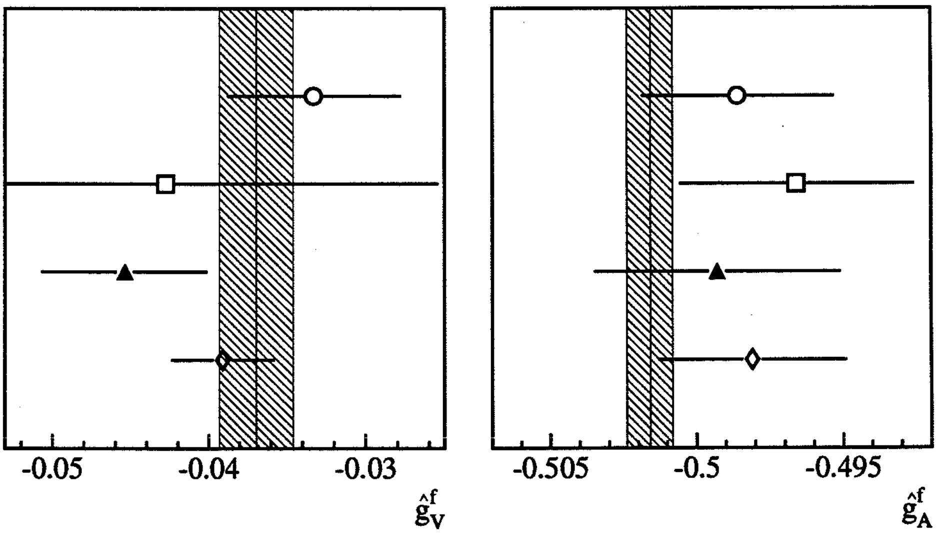

Figure 7.3: Fit results for the effective couplings, $\hat{g}_V^f$ and $\hat{g}_A^f$ of different lepton channels. The solid vertical lines denote the Standard Model predictions and the hatched regions their error range.

7.4 Results in the Partial Width Approach

The free parameters of the partial width approach are the mass and width of the Z boson, m_Z and Γ_Z, and the partial decay widths for electrons, Γ_e, and the final state fermions, Γ_f.

As explained in the effective coupling approach, it is not possible to determine the parameters of the partial width approach using only the cross section from one 3Z decay mode. Therefore, all fermion channels, including hadrons are fit simultaneously with and without lepton universality. The results are listed in Table 7.3. The partial decay widths for the leptons are plotted in Figure 7.4. The results for the three lepton flavors confirm

Parameter	Treatment of Charged Leptons		Standard
	Non-Universality	Universality	Model
m_Z[GeV]	91.195±0.009	91.195±0.009	–
Γ_Z[GeV]	2.494±0.011	2.494±0.011	2.500±0.009
Γ_e[MeV]	83.48±0.57	–	–
Γ_μ[MeV]	83.12±0.83	–	–
Γ_τ[MeV]	83.97±0.99	–	–
Γ_ℓ[MeV]	–	83.48±0.47	84.14±0.32
Γ_{had}[GeV]	1.747±0.012	1.747±0.010	1.745±0.007
χ^2/DOF	52/58	52/60	–

Table 7.3: Fit results in the partial width approach with and without lepton universality. In the third column the Standard Model predictions are listed.

lepton universality and are in good agreement with the Standard Model predictions.

The error on the Z mass is 9 MeV (added in quadrature) larger in the S-matrix approach than in the partial width approach (compare the fifth column in Table 7.1 and the third column in Table 7.3). According to Section 3.3 the interference term, j^f_{tot}, is fixed in the implementation of the partial width approach in ZFITTER. This leads to an underestimation of the error on m_Z. The effect can be reproduced in the S-matrix approach by fixing the γZ-interference terms for the total cross section. The results of an equivalent fit in the S-matrix approach using only the total cross sections for leptons and hadrons are shown in Table 7.4. One fit is performed with free interference terms and in a second step the interference terms are fixed to the value expected by the Standard Model (see Equation 3.23). Lepton universality is assumed. In the fit with fixed j^f_{tot} the error of $\overline{m}_Z$ is the same as in the partial width approach. The shift between $\overline{m}_Z$ and m_Z is equal to the expected -34 MeV (see Equation 3.3) only in the case of fixed j^f_{tot}(compare the third column of Table 7.3 and Table 7.4. The correlation between $\overline{m}_Z$ and $j^{\text{had}}_{\text{tot}}$ is plotted in Figure 7.5. The γZ-interference term is restricted within the Standard Model to (see Table 7.1):

$$j^{\text{had}}_{\text{tot}}(SM) = 0.212 \pm 0.015. \tag{7.3}$$

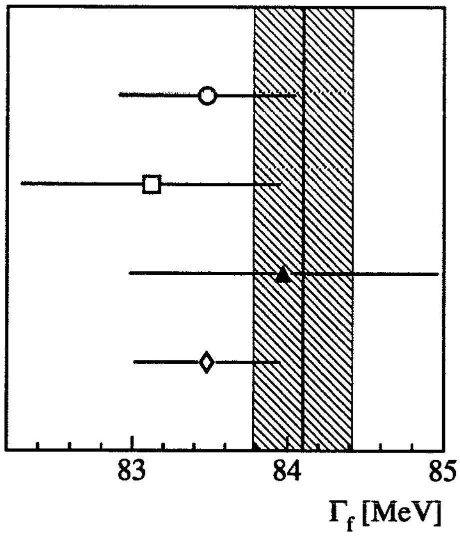

Figure 7.4: The fit results for the partial widths, Γ_f, for different lepton channels. The solid vertical lines denote the Standard Model predictions and the hatched regions their error range.

The allowed range of $j_{tot}^{had}(SM)$ is shown in Figure 7.5. It is clear, that a restriction of j_{tot}^{had} to $j_{tot}^{had}(SM)$ underestimates the error of the Z mass and introduces a bias on the Z mass measurement. Thus, it is not valid to use the term *model independent* for the partial width ansatz with fixed interference term.

7.5 Results in the Combined Partial Width and Effective Coupling Approach

For leptons one can avoid the Standard Model dependence due to the fixed γZ-interference term in the partial width approach by using the effective coupling ansatz. Here the interference terms are defined as a function of the axial-vector and vector couplings. This is not possible for hadrons [4]. Therefore, the preferred model-independent fit, alternatively to the fit in the S-matrix approach, should be a fit using the effective coupling approach for the lepton channels and the partial width approach for the hadrons, simultaneously. Furthermore, one can modify the standard partial width approach implemented in ZFITTER to allow for a fit of j_{tot}^{f}. This was done in [77]. The results of these fits with standard ZFITTER and the modified ZFITTER are listed in Table 7.5. The same effect on the determination of the Z mass as in Table 7.4 can be observed if j_{tot}^{had} is treated as a free parameter in the partial width approach. The effective couplings are not significantly

[4]This is discussed in Section 7.3

Parameter	free j^f_{tot}	fixed j^f_{tot}
$\overline{m}_Z$[GeV]	91.156±0.014	91.161±0.009
$\overline{\Gamma}_Z$[GeV]	2.497±0.011	2.496±0.011
r^{ℓ}_{tot}	0.1416±0.0016	0.1415±0.0016
j^{ℓ}_{tot}	0.008±0.065	fixed to 0.006
r^{had}_{tot}	2.863±0.030	2.861±0.029
j^{had}_{tot}	0.52±0.71	fixed to 0.22
χ^2/DOF	52/58	52/60

Table 7.4: Fit results in the S-matrix approach with released and fixed interference terms j^f_{tot}. Only cross sections are used in the fit.

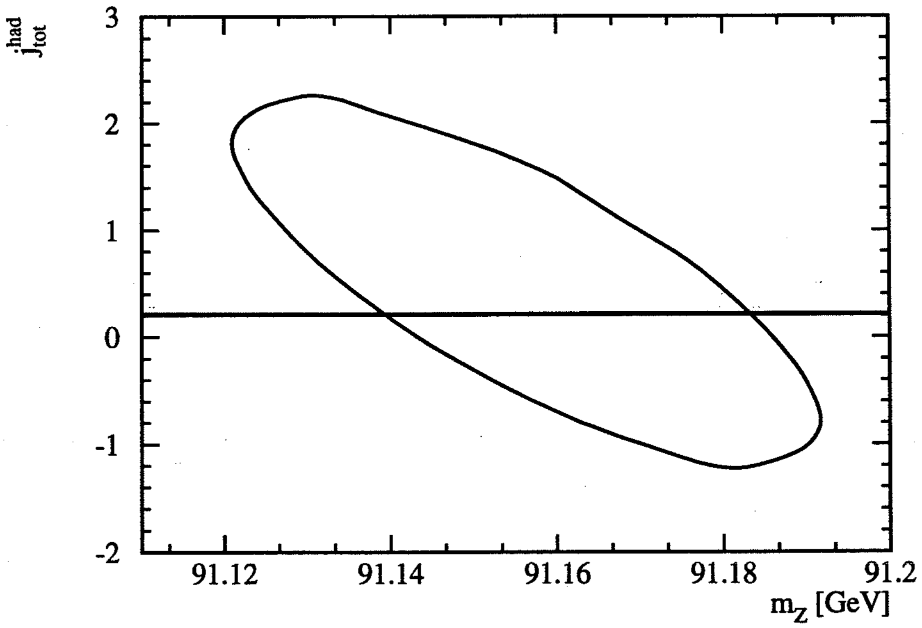

Figure 7.5: Correlation between the mass of the Z, $\overline{m}_Z$, and the hadronic interference term, j^{had}_{tot}. The 95% confidence level contour for $\overline{m}_Z$ and j^{had}_{tot} is shown. The band corresponds to the Standard Model prediction for j^{had}_{tot}.

Parameter	Standard ZFITTER [9] Treatment of Charged Leptons Non-Universality	Standard ZFITTER [9] Treatment of Charged Leptons Universality	Modified ZFITTER [77] Treatment of Charged Leptons Non-Universality	Modified ZFITTER [77] Treatment of Charged Leptons Universality
m_Z [GeV]	91.197±0.009	91.198±0.009	91.192±0.013	91.193±0.013
Γ_Z [GeV]	2.494±0.011	2.494±0.011	2.495±0.011	2.495±0.011
$\hat{g}_V^e$	-0.0334±0.0055	–	-0.0332±0.0055	–
$\hat{g}_V^\mu$	-0.043±0.017	–	-0.042±0.017	–
$\hat{g}_V^\tau$	-0.0456±0.0053	–	-0.0456±0.0053	–
$\hat{g}_V^\ell$	–	-0.0391±0.0032	–	-0.0390±0.0032
$\hat{g}_A^e$	-0.5000±0.0017	–	-0.5001±0.0017	–
$\hat{g}_A^\mu$	-0.4980±0.0028	–	-0.4982±0.0028	–
$\hat{g}_A^\tau$	-0.5008±0.0030	–	-0.5010±0.0030	–
$\hat{g}_A^\ell$	–	-0.4996±0.0014	–	-0.4997±0.0014
Γ_{had}[GeV]	1.746±0.012	1.746±0.010	1.747±0.012	1.747±0.010
j_{tot}^{had}	–	–	0.81±0.87	0.75±0.87
χ^2/DOF	85/105	88/109	85/104	88/108

Table 7.5: Combined fit results in the effective coupling approach for leptons and the partial width approach for hadrons.

affected by the different treatment of the interference term. Note that the uncertainty of the axial-vector couplings is considerably smaller than in the pure effective couplings fit without the hadron cross sections. The results for the effective couplings in the fit with released interference term are plotted in Figure 7.6. From the vector and axial-vector couplings and their correlations the effective weak mixing angle, $\sin^2\hat{\theta}_W$ and the $\hat{\rho}$ parameter can be derived (see Equations 3.12 and 3.13). The results for $\sin^2\hat{\theta}_W$ and $\hat{\rho}$ for the fits with released hadronic interference term are plotted in Figure 7.7. All results are in agreement with the Standard Model and confirm lepton universality. The ratios of the couplings between different lepton channels are determined to be:

$$\begin{aligned} \hat{g}_A^\mu / \hat{g}_A^e &= 0.9962 \pm 0.0068, & \hat{g}_A^\tau / \hat{g}_A^e &= 1.0018 \pm 0.0072, \\ \hat{g}_V^\mu / \hat{g}_V^e &= 1.27 \pm 0.47, & \hat{g}_V^\tau / \hat{g}_V^e &= 1.37 \pm 0.27. \end{aligned} \tag{7.4}$$

From the τ couplings the following values for $\sin^2\hat{\theta}_W$ and $\hat{\rho}$ are determined:

$$\begin{aligned} \sin^2\hat{\theta}_W^\tau &= 0.2273 \pm 0.0027, \\ \hat{\rho}^\tau &= 1.004 \pm 0.012. \end{aligned} \tag{7.5}$$

Assuming lepton universality the results are:

$$\begin{aligned} \sin^2\hat{\theta}_W^\ell &= 0.2305 \pm 0.0016, \\ \hat{\rho}^\ell &= 0.9988 \pm 0.0058. \end{aligned} \tag{7.6}$$

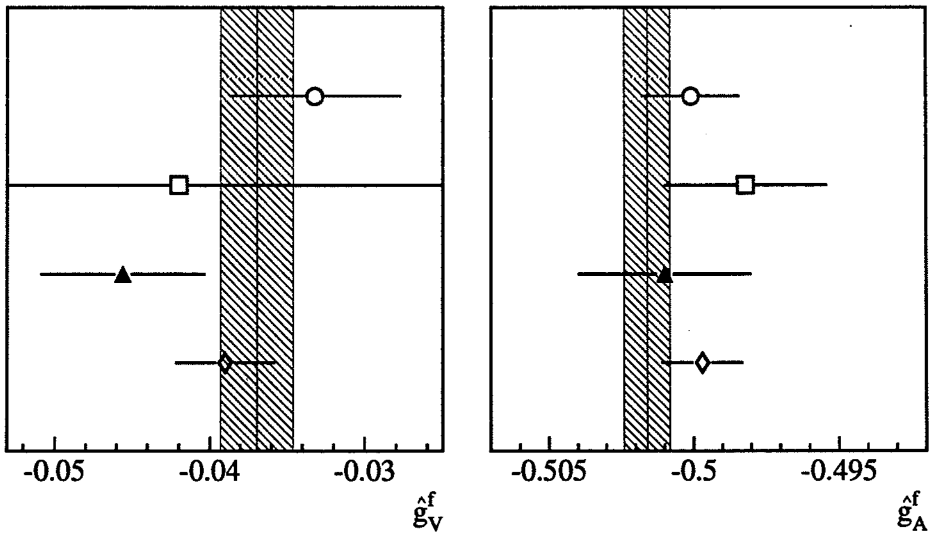

Figure 7.6: Fit results for the effective couplings, $\hat{g}_V^f$ and $\hat{g}_A^f$, of different lepton channels in the combined partial width and effective coupling approach. The solid vertical lines denote the Standard Model predictions and the hatched regions their error range.

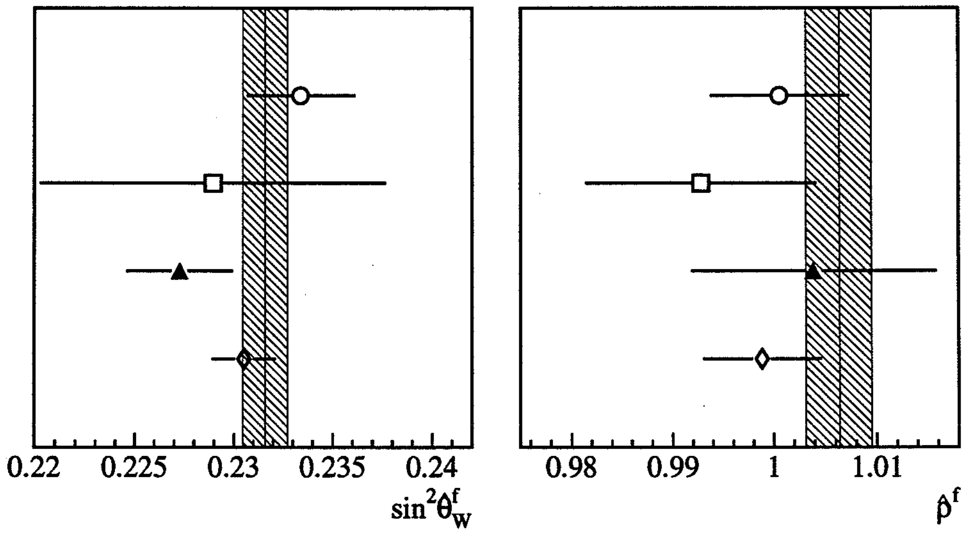

Figure 7.7: $\sin^2\hat{\theta}_W$ and $\hat{\rho}$ derived from the vector and axial-vector couplings of the fit with released hadronic interference term. The solid vertical lines denote the Standard Model predictions and the hatched regions their error range.

In a truly model independent fit with released total hadronic interference term, j_{tot}^{had}, the main uncertainty on the Z mass of $\delta m_Z(j_{tot}^{had}) = 9$ MeV originates from the poor measurement of j_{tot}^{had} at LEP. Therefore, a more realistic number for δm_Z including the uncertainty on j_{tot}^{had} is:

$$\delta m_Z = \pm\, 6\,\mathrm{MeV}(Exp.) \pm 7\,\mathrm{MeV}(LEP) \pm 9\,\mathrm{MeV}(j_{tot}^{had}). \qquad (7.7)$$

The first contribution to δm_Z arises from statistical and systematic uncertainties of the experimental measurements excluding contributions from j_{tot}^{had}. The second error is given by the precision of the LEP energy. One possibility to improve the determination of j_{tot}^{f} is to measure cross sections far from the Z peak. This is discussed in Appendix B and in more detail in [78,79].

7.6 Results in the Framework of the Standard Model

The measurements of cross sections and asymmetries for the processes $e^+e^- \to e^+e^-$, $e^+e^- \to \mu^+\mu^-$, $e^+e^- \to \tau^+\tau^-$ and $e^+e^- \to q\bar{q}$ are used to estimate the mass of the t quark within the Standard Model. To fit the data the Standard Model branch of ZFITTER is used. The free parameters are the mass of the Z boson, m_Z, and the mass of the t quark, m_t. α_s is constrained by our independent measurement using hadronic event topologies and τ decays, $\alpha_s = 0.123 \pm 0.006$ [28]. Since the sensitivity to the Higgs mass is weak at LEP, m_H is fixed at 300 GeV. The mass of the t quark is determined to be:

$$m_t = 188^{+28+17}_{-33-18}\ \mathrm{GeV}. \qquad (7.8)$$

The second error correspond to a variation of the Higgs mass, m_H, between 60 and 1000 GeV. The lower value, $m_H = 60$ GeV, is motivated by our present limit on the Higgs mass from direct searches [72], while the upper bound is chosen, because the Higgs should not be heavier than 1000 GeV for unitarity reasons. The value of m_t is consistent with $m_t = 174 \pm 10^{+13}_{-12}$ GeV, published by the CDF collaboration [6], which reported first evidence for t-quark production. The result for the Z mass is the same as derived in the combined effective coupling and partial width approach, if the hadronic interference term is fixed (see Table 7.5):

$$m_Z = 91.198 \pm 0.009\ \mathrm{GeV}. \qquad (7.9)$$

Using the value of Equation 7.8 for m_t, the leading parts of the electroweak corrections are fixed. With the equations 2.42, 2.43 and 2.44 and $G_\mu = 1.16639 \times 10^{-5}\ \mathrm{GeV}^{-2}$ [14] Δr and $\sin^2\theta_W$ are determined to be:

$$\begin{aligned} \Delta r &= 0.034 \pm 0.012, & (7.10)\\ \sin^2\theta_W &= 0.2223 \pm 0.0040. & (7.11) \end{aligned}$$

The mass of the W boson is then given by Equation 2.10 using the measurement for m_Z and the value for $\sin^2\theta_W$ from Equation 7.11:

$$m_W = 80.42 \pm 0.21\ \mathrm{GeV}, \qquad (7.12)$$

which is consistent with the measurements of the CDF [80] and UA2 [81] experiments. Since the electroweak corrections are fixed, the form factors κ^f and ρ^f are known and the effective weak mixing angle and the effective vector and axial-vector couplings can be determined. The effective weak mixing angle is:

$$\sin^2 \hat{\theta}_W = 0.2316 \pm 0.0011. \tag{7.13}$$

The Standard Model values for the couplings are given in Table 7.2. The total and partial widths of the Z boson can be derived from the Equations 2.24 and 2.25 and their values are listed in Table 7.3. The Standard Model predictions for the S-matrix parameters are derived from the Equations 3.14 and 3.10 using the Standard Model values for the vector and axial-vector couplings. The numbers for R_Z^{fi} are listed in Table 7.1.

7.7 Comparison of the Neutral Current Results between the LEP experiments

The S-matrix analysis has only been performed by the L3 collaboration. Therefore, in the following the results of the combined fit using the partial width and effective coupling approaches are compared between the LEP experiments and an average is presented. The results are based on the 1990-1992 data sample for all experiments and some preliminary measurements for 1993. They are presented in [62]. The LEP collaborations agreed on a common parameter set for their model independent fits, where the correlations among the parameters are minimal. Using the mean values, errors and the full correlation matrix of these parameters, the numbers for the parameters of the combined partial width and effective coupling fits of Section 7.5 are derived for each experiment.

The results of the τ couplings for each experiment and their average are listed in Table 7.6 and plotted in Figure 7.8. The measurements from all experiments are in good

	$\hat{g}_V^\tau$	$\hat{g}_A^\tau$
ALEPH	-0.0372±0.0033	-0.5025±0.0017
DELPHI	-0.0404±0.0056	-0.5016±0.0025
L3	-0.0453±0.0052	-0.5023±0.0027
OPAL	-0.0403±0.0057	-0.5006±0.0019
LEP	-0.0399±0.0024	-0.5020±0.0011
Standard Model	-0.0356±0.0010	-0.5012±0.0004

Table 7.6: The vector and axial-vector couplings for $e^+e^- \to \tau^+\tau^-$ for the LEP experiments,ALEPH, DELPHI, L3 and OPAL, their average and the prediction of the Standard Model.

agreement with each other. The largest deviation from the LEP average of 2σ is the measurement of $\hat{g}_V^\tau$ from the L3 collaboration [5]. The LEP averages for the couplings in the remaining lepton channels, $e^+e^- \rightarrow e^+e^-$ and $e^+e^- \rightarrow \mu^+\mu^-$, are compatible with the $e^+e^- \rightarrow \tau^+\tau^-$ results and thus confirm lepton universality (see Table 7.7 and Figure 7.9).

The ratios of the vector and axial-vector coupling between the lepton channels are

	$\hat{g}_V^f$	$\hat{g}_A^f$
$e^+e^- \rightarrow e^+e^-$	-0.0347±0.0023	-0.50141±0.00066
$e^+e^- \rightarrow \mu^+\mu^-$	-0.0341±0.0057	-0.5013±0.0010
$e^+e^- \rightarrow \tau^+\tau^-$	-0.0399±0.0024	-0.5020±0.0011
$e^+e^- \rightarrow \ell^+\ell^-$	-0.0364±0.0014	-0.50135±0.00055
Standard Model	-0.03564±0.00099	-0.50124±0.00038

Table 7.7: The LEP average for the vector and axial-vector couplings for the lepton channels and the Standard Model Predictions.

determined to be:

$$\begin{aligned} \hat{g}_A^\mu / \hat{g}_A^e &= 0.9997 \pm 0.0023, & \hat{g}_A^\tau / \hat{g}_A^e &= 1.0011 \pm 0.0024, \\ \hat{g}_V^\mu / \hat{g}_V^e &= 0.99 \pm 0.20, & \hat{g}_V^\tau / \hat{g}_V^e &= 1.15 \pm 0.11. \end{aligned} \tag{7.14}$$

The LEP average for the effective weak mixing angle is derived to:

$$\sin^2 \hat{\theta}_W = 0.2322 \pm 0.0005, \tag{7.15}$$

taking into account in addition to the leptonic asymmetries also hadronic forward-backward asymmetries (see the references in [62]).

The Standard Model predictions given in the tables and figures of this section are determined from the results of a fit within the framework of the Standard Model. The results of this fit to the combined LEP data are:

$$\begin{aligned} m_Z &= 91.1899 \pm 0.0044 \text{ GeV}, \\ m_t &= 172^{+13+18}_{-14-20} \text{ GeV}. \end{aligned} \tag{7.16}$$

Derived quantities are:

$$\sin^2 \theta_W = 0.2251 \pm 0.0015^{+0.0003}_{-0.0003}, \tag{7.17}$$

$$\sin^2 \hat{\theta}_W = 0.2323 \pm 0.0002^{+0.0002}_{-0.0002}, \tag{7.18}$$

$$m_W = 80.28 \pm 0.08^{+0.01}_{-0.02} \text{ GeV}. \tag{7.19}$$

The second error corresponds to a variation of the Higgs mass between 60 and 1000 GeV. The measurements of the τ couplings from the LEP experiments as well as the averages of the couplings for the lepton channels are in agreement with the Standard Model predictions.

[5] The values for $\hat{g}_V^\tau$ and $\hat{g}_A^\tau$ in Table 7.6 are different from the values presented in Section 7.5, because the data set used for the fits in [62] includes a preliminary measurement for the hadron cross section using 1993 data. This influences also the values for the couplings, since the fit parameters are correlated.

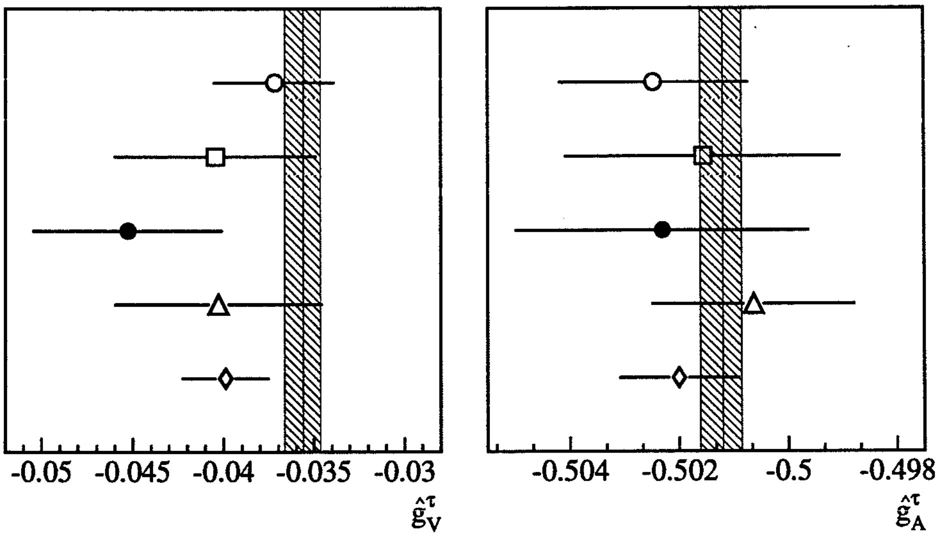

Figure 7.8: The vector and axial-vector couplings for $e^+e^- \rightarrow \tau^+\tau^-$ for the LEP experiments,ALEPH(○), DELPHI(□), L3(•) and OPAL(△), and their average(◇). The solid vertical lines denote the Standard Model predictions and the hatched regions their error range.

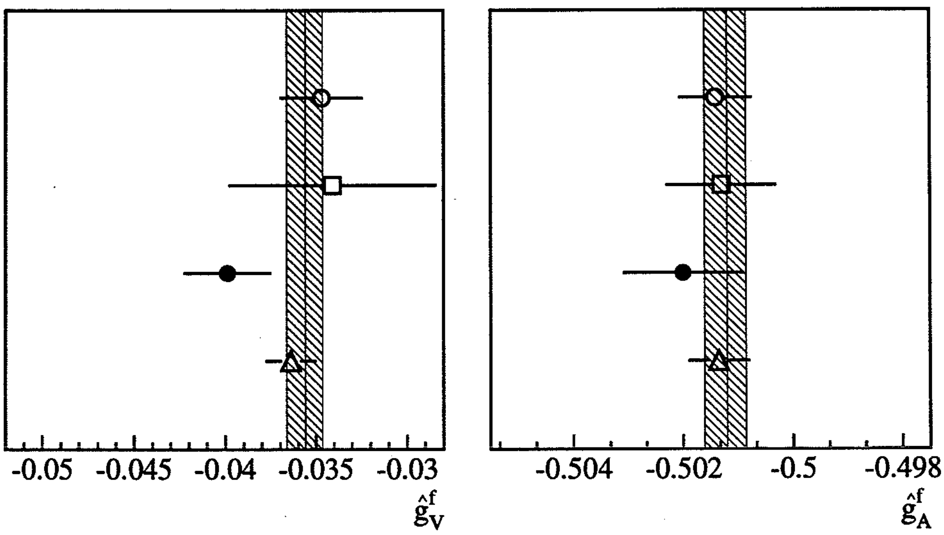

Figure 7.9: The LEP average for the vector and axial-vector couplings for the lepton channels, $e^+e^- \rightarrow e^+e^-$ (○), $e^+e^- \rightarrow \mu^+\mu^-$ (□), $e^+e^- \rightarrow \tau^+\tau^-$ (•) and $e^+e^- \rightarrow \ell^+\ell^-$ (△). The solid vertical lines denote the Standard Model predictions and the hatched regions their error range.

The most precise determination of $\sin^2 \hat{\theta}_W$ from a single measurement is performed by the SLD collaboration [82] at SLAC. Their measurement of the left-right asymmetry gives:

$$\sin^2 \hat{\theta}_W = 0.2294 \pm 0.0010. \tag{7.20}$$

This result differs from the LEP average by 2.3σ. The neutrino experiments, CDHS [83], CHARM [84] and CCFR [85] measure the weak mixing angle to:

$$\sin^2 \theta_W = 0.2256 \pm 0.0047, \tag{7.21}$$

which is in good agreement with the LEP value in Equation 7.17.

Chapter 8

Summary

In this thesis the analysis of the neutral current process $e^+e^- \rightarrow \tau^+\tau^-$ has been discussed. Results on measurements of the total cross section, the forward-backward asymmetry, the polarization asymmetry and the forward-backward polarization asymmetry have been presented using the data which were collected with the L3 detector from 1990 to 1992. Special emphasis was given to the measurement of the polarization asymmetry and forward-backward polarization asymmetry. Combining these two measurements $\mathcal{A}_e$ and $\mathcal{A}_\tau$ can be extracted. The results are:

$$\begin{aligned} \mathcal{A}_e &= 0.125 \pm 0.022(stat.) \pm 0.013(sys.), \\ \mathcal{A}_\tau &= 0.171 \pm 0.016(stat.) \pm 0.014(sys.). \end{aligned}$$

These numbers are in good agreement with each other which supports the assumption of lepton universality. The polarization asymmetries are not compatible with zero. This proofs that the neutral current must be described by a mixture of vector and axial-vector couplings. The results of the other LEP collaborations agree with the L3 measurements on $\mathcal{A}_e$ and $\mathcal{A}_\tau$. The total cross section and forward-backward asymmetry have been measured at different center-of-mass energies. The results can be found in Table 6.5 and Table 6.7.

The measurements are interpreted in the context of different model independent approaches. In the S-matrix approach the helicity amplitudes are determined to be:

$$\begin{aligned} R_Z^{\tau 0} &= 0.437 \pm 0.012, \\ R_Z^{\tau 1} &= -0.363 \pm 0.011, \\ R_Z^{\tau 2} &= 0.321 \pm 0.012, \\ R_Z^{\tau 3} &= -0.381 \pm 0.012. \end{aligned}$$

Using exclusively measurements from the channel $e^+e^- \rightarrow \tau^+\tau^-$, the mass and width of the Z boson are measured in the S-matrix approach to be:

$$\begin{aligned} \overline{m}_Z &= 91.155 \pm 0.036 \text{ GeV}, \\ \overline{\Gamma}_Z &= 2.501 \pm 0.061 \text{ GeV}. \end{aligned}$$

These results correspond to following numbers for m_Z and Γ_Z:

$$\begin{aligned} m_Z &= 91.189 \pm 0.036 \text{ GeV}, \\ \Gamma_Z &= 2.502 \pm 0.061 \text{ GeV}. \end{aligned}$$

In the effective coupling approach the couplings of τ to the Z boson are determined to be:

$$\begin{aligned} \hat{g}_V^\tau &= -0.0454 \pm 0.0053, \\ \hat{g}_A^\tau &= -0.4993 \pm 0.0042. \end{aligned}$$

The effective weak mixing angle, defined by $\hat{g}_V^\tau$ and $\hat{g}_A^\tau$, is derived:

$$\sin^2 \hat{\theta}_W = 0.2273 \pm 0.0027.$$

The partial decay width of the Z boson into $\tau^+\tau^-$ pairs is a parameter in the partial width approach. It is measured to be:

$$\Gamma_\tau = 83.97 \pm 0.99 \text{ MeV}.$$

All the measurements are in good agreement with the results in the other lepton channels, $e^+e^- \rightarrow e^+e^-$ and $e^+e^- \rightarrow \mu^+\mu^-$ and thus confirm the hypothesis of lepton universality. All measurements are compatible with the Standard Model. The precise measurements of cross sections and asymmetries show significant deviations from the Born level expectations, which are caused by higher order corrections. These corrections are sensitive to the mass of the t quark, which is therefore obtained to:

$$m_t = 188^{+28+17}_{-33-18} \text{ GeV}.$$

The lepton universality and the compatibility with the Standard Model is also confirmed for the combined data of the LEP experiments, ALEPH, DELPHI, L3 and OPAL. The SLD collaboration performed a precise measurement of the effective weak mixing angle, which deviates by 2.3σ from the LEP average. The less precise results on the weak mixing angle from the neutrino experiments, CDHS, CHARM and CCFR are in agreement with the LEP result.

In 1993 the L3 detector collected a data sample with improved LEP energy uncertainty. Therefore, the errors on mass and width of the Z boson will decrease significantly. It is foreseen to operate LEP at a center-of-mass energy in the vicinity of the Z resonance at least until end of 1996. Therefore, it is expected that the number of recorded Z decays will increase by a factor of five in comparison with the dataset used in this thesis.

The use of larger data samples reduces the statistical error and also allows a better understanding of systematic detector effects. This can lead to reduced systematic errors. A preliminary measurement of the τ polarization with the energy method using the 1993 data sample shows that the systematic uncertainty due to the energy calibration can be reduced in the $\tau \rightarrow \pi\nu$ channel to $\approx 2.6\%$. For the other decay modes it remains the same and no major improvement is expected. Also the systematic errors of the acollinearity method will not improve significantly in 1993. Here a major improvement can be achieved by using the new silicon micro-vertex detector (SMD) of L3, which has been fully operational since the beginning of 1994. This device allows a vertex determination on an event by event basis. Therefore, one of the main contributions to the systematic error of the acollinearity method, the uncertainty in the beam width, will disappear and the vertex uncertainty will improve. Thus, the systematic error related to pure detector uncertainties might be reduced to $\approx 1\%$. The question as to whether the acollinearity method can challenge the energy method depends on a variety of factors, such as the actual performance of the SMD, the precision of the alignment of the SMD with the other L3 subdetectors and last but not least on the final data statistics which will be collected at LEP in the vicinity of the Z resonance.

Appendix A

Z-Detector Geometry Constants

The origin of the coordinate system for the z-detector is placed in the center of the L3 detector. The z axis corresponds to the detector axis. The four cathode layers are named from inside to outside, u, z, v, z'. The first two belong to the inner z-chamber, Z_I, and the remaining two to the outer chamber, Z_O. The number of strips for each layer is

$$N_{Strip} = 240,$$

with a pitch of

$$\omega = 4.45 \text{ mm}.$$

Therefore, the active length of the cathode layers amounts to

$$L_{eff} = N_{Strip}\ \omega = 1068 \text{ mm}.$$

The radii of the cathode layers are:

$$\begin{aligned} R_u &= 471.0 \text{ mm}, \\ R_z &= 478.0 \text{ mm}, \\ R_v &= 480.0 \text{ mm}, \\ R_{z'} &= 487.0 \text{ mm}. \end{aligned}$$

The radii of the inner and outer anode layer are:

$$\begin{aligned} R_I &= 474.5 \text{ mm}, \\ R_O &= 483.5 \text{ mm}. \end{aligned}$$

The anode-cathode distance amounts to:

$$L = |R_{u,z} - R_I| = |R_{v,z'} - R_O| = 3.5 \text{ mm}.$$

The angle of the cathode strips with respect to the chamber axis are:

$$\begin{aligned} \alpha_u &= -\ 69^\circ, \\ \alpha_z &= +\ 90^\circ, \\ \alpha_v &= +\ 69^\circ, \\ \alpha_{z'} &= +\ 90^\circ. \end{aligned}$$

Appendix B

A Possibility to Improve the Measurement of γZ-Interference Terms at LEP

It is shown in Section 7.4 that the uncertainty of the hadronic γZ-interference term, $j_{\mathrm{tot}}^{\mathrm{had}}$, results in an additional error on m_Z of 9 MeV(see Equation 7.7). The situation remains the same, if one includes the 1993 data into the analysis. The error on m_Z is then given by:

$$\delta m_Z = \pm\, 3\ \mathrm{MeV}(Exp.) \pm 3\ \mathrm{MeV}(LEP) \pm 8\ \mathrm{MeV}(j_{\mathrm{tot}}^{\mathrm{had}}). \tag{B.1}$$

LEP was running 1993 at three energy points, one on the Z pole and two off the pole at ± 2 GeV, with an energy calibration for each point using the method of resonant depolarization (see Section 4.2). Therefore, the uncertainty of the Z mass caused by the LEP energy measurement decreases to 3 MeV compared to the previous years (see Equation 7.7). Hence, the error on $j_{\mathrm{tot}}^{\mathrm{had}}$ is still the dominant contribution to the error on the mass of the Z boson. Therefore, it is highly desirable to improve the measurement of $j_{\mathrm{tot}}^{\mathrm{had}}$.

γZ-interference terms can be measured by analyzing the process $e^+e^- \rightarrow f\bar{f}$ at energies off the Z pole [86], because j_{tot}^{f} is scaled by a factor $(s - \overline{m}_Z^2)\,/\,s$ (see Equation 3.8). In Figure B.1 the relative contribution of the hadronic γZ-interference to the total hadronic cross section, $|\sigma_{\mathrm{tot}}^{\gamma Z,f}\,/\,\sigma_{\mathrm{tot}}|$ [1] is plotted. The plot implies that such a measurement should be performed below the Z resonance.

In [78] it is investigated, at which energy one should operate LEP to improve the measurement of $j_{\mathrm{tot}}^{\mathrm{had}}$, while keeping the loss in event statistics as small as possible. For this study the L3 hadron cross sections of 1990-1993 are used and extrapolated for a further LEP run, assuming an integrated luminosity of $\mathcal{L} = 40\ \mathrm{pb}^{-1}$. A scanning scenario with three energy points is considered. Two points are fixed at the Z pole and above the pole at 94.25 GeVrespectively. The energy for the third point varies between 60 and 89 GeV. The luminosity is distributed as follows. The luminosity for the two off-peak points is chosen in such a way, that the number of events collected at these energies is equal. The

[1] For the definition of $\sigma_{\mathrm{tot}}^{\gamma Z,f}$ see the footnote on Page 122.

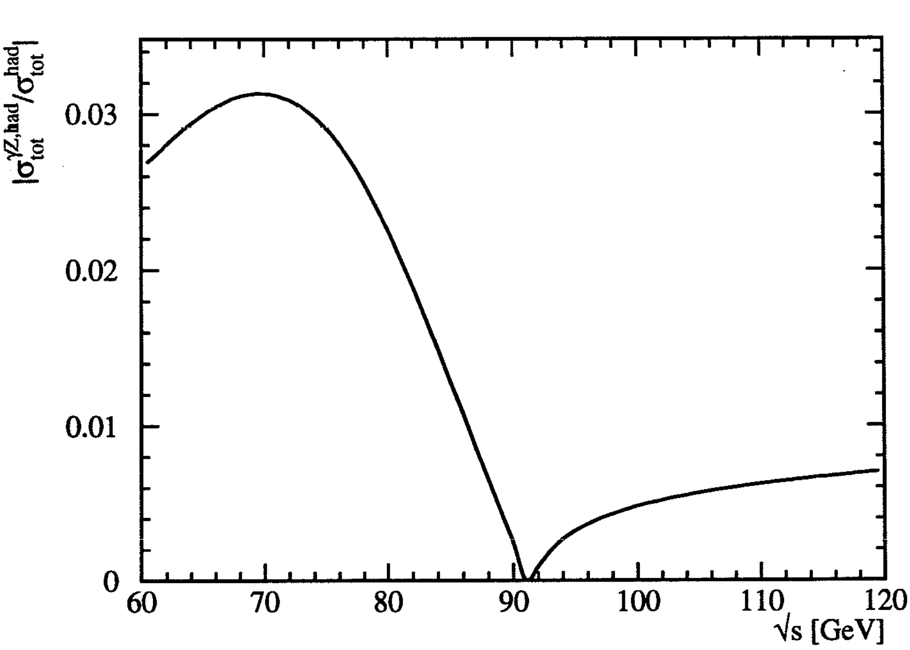

Figure B.1: The relative contribution of the hadronic γZ-interference to the total hadronic cross section around the Z resonance.

remaining luminosity is spent at the peak to conserve the total luminosity to $\mathcal{L} = 40\,\text{pb}^{-1}$. No energy calibration using the method of resonant depolarization is assumed. Therefore, the same errors as 1990-1991a for the LEP energy measurement are assumed (see Table 4.2). The systematic uncertainty of the luminosity measurement is taken to 0.3%, since L3 installed a new precise silicon luminosity monitor [87] in 1993.

With no energy points off the Z pole, e.g. taking the $40\,\text{pb}^{-1}$ exclusivly on the peak, the error on the Z mass in a fit to the total hadron cross sections, leaving the hadronic γZ-interference term free, will be 14 MeV. Therefore, further data taken on the peak, will not improve the measurement of m_Z. Now we add the two additional energy points as described above, and evaluate the error on the Z mass, δm_Z, and the hadronic γZ-interference term, δj_{tot}^{had}. Figure B.2 show the contour lines of constant errors δm_Z and δj_{tot}^{had} as function of the energy, E_{add}, and luminosity, $\mathcal{L}_{add}$, of an additional point below the peak. The most sensitive energy region lies in the vicinity of 80 GeV center-of-mass energy. The evolution of δm_Z with the luminosity for the additional points at $E_{add} = 80$ GeV is shown in Figure B.3. It suggests to spend at least $\mathcal{L}_{add} = 2\,\text{pb}^{-1}$ at 80 GeV. This will improve the error on the Z mass to 7 MeV. On the other hand it is not justified to take more than $\mathcal{L}_{add} = 4\,\text{pb}^{-1}$, as further improvements on δm_Z beyond $4\,\text{pb}^{-1}$ are marginal. A scenario with an energy point below the peak at 80 GeV and a luminosity between $2-4\,\text{pb}^{-1}$ reduces the event statistics by $5-10\%$, compared to a run exclusivly on the peak. Figure B.3 also shows the δm_Z evolution for an energy point above the peak at $E_{add} = 140$ GeV. Even a scenario with

$\mathcal{L}_{add} = 20\ pb^{-1}$ taken at 140 GeV would only reduce the error to 8 MeV [79]. The arrow indicates the underestimated error on m_Z for the case of a fixed hadronic γZ-interference term and the total luminosity is spent on the peak.

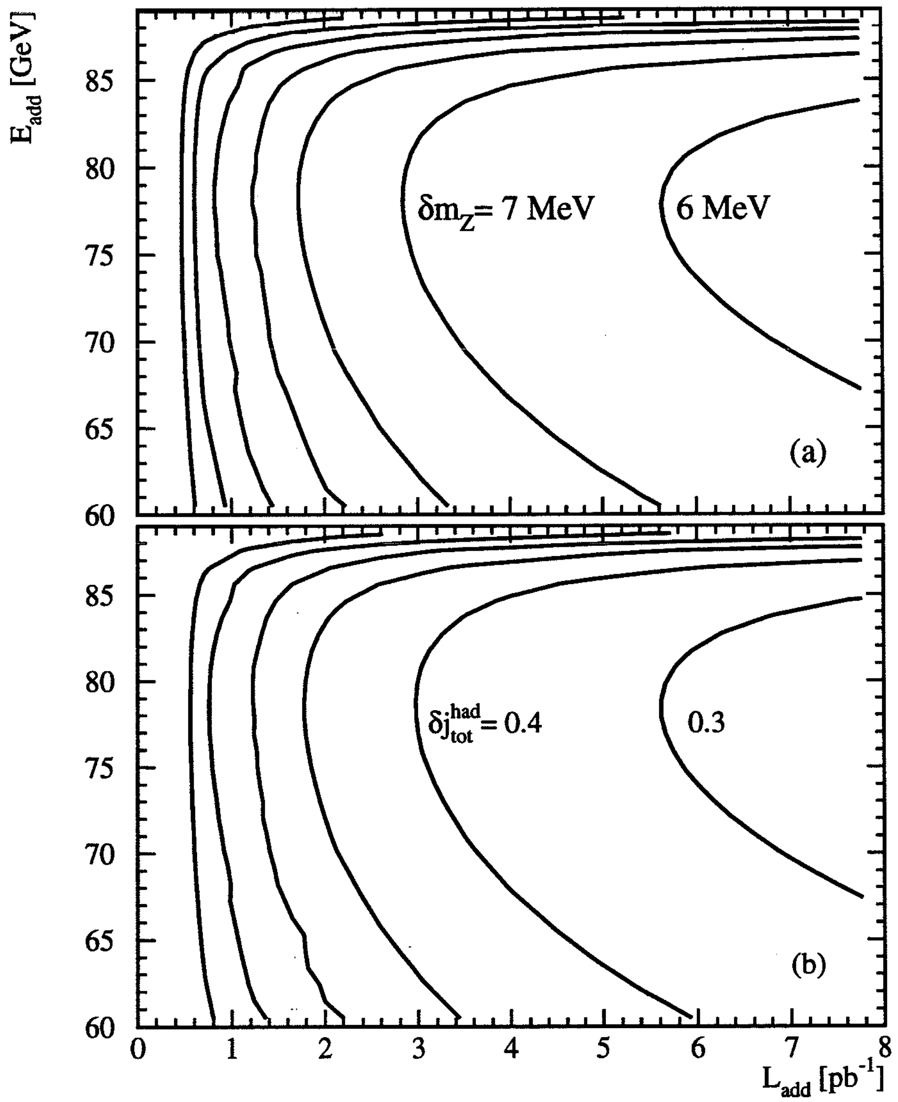

Figure B.2: The error on (a) the Z mass and (b) the hadronic γZ-interference term as a function of E_{add} and $\mathcal{L}_{add}$. Shown are the contour lines of constant error in steps of (a) 1 MeVand (b) 0.1.

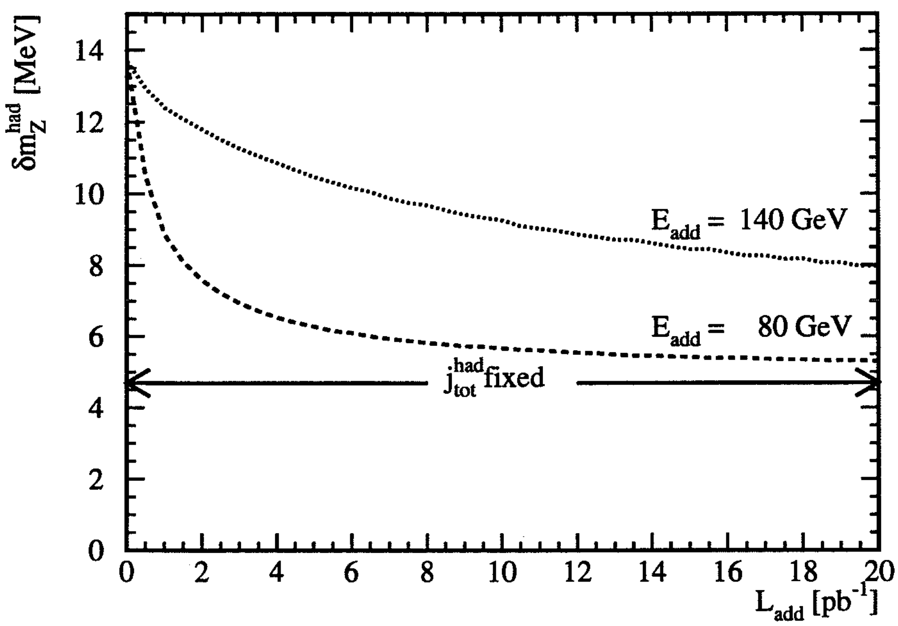

Figure B.3: Evolution of δm_Z with the luminosity, $\mathcal{L}_{add}$, spent at an additional energy point, $E_{add} = 80$ GeV and 140 GeV. The arrow indicates the error on m_Z, if the hadronic γZ-interference term is fixed and the total luminosity is spend on the peak.

Bibliography

[1] S.L. Glashow, Nucl. Phys. **22** (1961) 579;
S. Weinberg, Phys. Rev. Lett. **19** (1967) 1264;
A. Salam, *"Elementary Particle Theory"*, Ed. N. Svartholm, Stockholm, "Almquist and Wiksell" (1968) 367.

[2] for the Standard Model Lagrangian see for example: K. Grotz, H.V. Klapdor, *" Die schwache Wechselwirkung in Kern-, Teilchen- und Astrophysik"*, B.G. Teubner Stuttgart 1989.

[3] P. W. Higgs, Phys. Lett. **12** (1964) 132, Phys. Rev. Lett. **13** (1964) 508 and Phys. Rev. **145** (1966) 1156;
F. Englert and R. Brout, Phys. Rev. Lett. **13** (1964) 321.

[4] Gargamelle Collab., F.J. Hasert *et al.*, Phys. Lett. **B46** (1973) 121.

[5] E. Fermi, *" Versuch einer Theorie der β-Strahlen"*, Z. Phys. **88** (1934) 161.

[6] CDF Collab., F. Abe *et al.*, *"Evidence for Top Quark Production in* $p\bar{p}$ *Collisions at* $\sqrt{s} = 1.8$ *TeV"*, FERMILAB-PUB-94/097-E (1994).

[7] S. Jadach, Z. Was *et al.*, in *"Z Physics at LEP 1"*, CERN Report CERN 89-08, eds G. Altarelli,R. Kleiss and C. Verzegnassi (CERN, Geneva, 1989) Vol. 1, p. 235.

[8] M. Consoli, W. Hollik and F. Jegerlehner, in *"Z Physics at LEP 1"*, CERN Report CERN 89-08, eds G. Altarelli,R. Kleiss and C. Verzegnassi, Vol. 1, p. 7.

[9] D. Bardin *et al.*, FORTRAN package ZFITTER; CERN-TH 6443/92; Z. Phys. **C44** (1989) 493; Nucl. Phys. **B351** (1991) 1; Phys. Lett. **B255** (1991) 290.

[10] M. L. Perl *et al.*, Phys. Rev. Lett. **35** (1975) 1489.

[11] R. Brandelik *et al.*, Phys. Lett. **73B** (1978) 109.

[12] BES Collab., J. Z. Bai *et al.*, Phys. Rev. Lett. **69** (1992) 3021.

[13] A. Kounine, *"Tau Physics at LEP"*, talk given at the XXIXth Rencontres de Moriond "Electroweak Interactions and Unified Theories", to be published by Edition Frontiers, 1994.

[14] Particle Data Group, Phys. Rev. **D45** (1992) III.54.

[15] G. Altarelli *et al.*(eds.), *"Z Physics at LEP 1"*, CERN 89-08 (1989).

[16] A. Leike, T. Riemann, J. Rose, Phys. Lett. **B273** (1991) 513;
T. Riemann, Phys. Lett. **B293** (1992) 451.

[17] D. Bardin, A. Leike, T. Riemann, M. Sachwitz, Phys. Lett. **B206** (1988) 539;
S. Willenbrock, G. Valencia, Phys. Lett. **B259** (1991) 373.

[18] R. Stuart, *"Gauge-Invariant Perturbation Theory near a Gauge Resonance"*, CERN-TH 6261-91 (1991).

[19] R. Stuart, Phys. Lett. **B262** (1991) 113;
R. Stuart, Phys. Lett. **B272** (1991) 353.

[20] LEP Design report vol. I, *"The LEP injector chain"*, CERN-LEP/TH/83-29 (1983).
LEP Design report vol. II, *"The LEP main ring"*, CERN-LEP/TH/84-01 (1984).

[21] ALEPH Collab., D. Decamp *et al.*, Nucl. Inst. Meth. **A 294** (1990) 121.

[22] DELPHI Collab., P. Aarnio *et al.*, Nucl. Inst. Meth. **A 303** (1991) 233.

[23] L3 Collab., B. Adeva *et al.*, Nucl. Inst. Meth. **A 289** (1990) 35.

[24] OPAL Collab, K. Ahmet *et al.*, Nucl. Inst. Meth. **A 305** (1991) 275.

[25] The Working Group on LEP Energy: L. Arnaudon *et al.*, *"The Energy Calibration of LEP in 1991"*, CERN-PPE/92-125 and CERN-SL/92-37(DI) (1992).

[26] The Working Group on LEP Energy and the LEP Collaborations, Phys. Lett. **B307** (1993) 187.

[27] The Working Group on LEP Energy: L. Arnaudon *et al.*, *"Effects of Terrestrial Tides on the LEP Beam Energy"*, CERN-SL/94-07(BI) (1994).

[28] L3 Collab., O. Adriani *et al.*, Physics Reports **236** (1993) 1.

[29] Y. Peng, *"The Muon Spectrometer of the L3 Detector at LEP"*, PhD Thesis, NIKHEF-H, Amsterdam (1988).

[30] The L3 BGO Collab., J.A. Bakken *et al.*, *" Results on the calibration of the L3 BGO calorimeter with cosmic rays"*, Preprint CERN-PPE/93-184 (1993), submitted to Nucl. Instr. and Meth.

[31] F. Beissel *et al.*, Nucl. Inst. Meth. **A332** (1993) 33.

[32] K. Deiters *et al.*, Nucl. Inst. Meth. **A323** (1992) 162.

[33] G. Charpak, G. Petersen, A. Policarpo, F. Sauli, Nucl. Inst. Meth. **148** (1978) 471.

[34] G. Fischer, J. Plch, Nucl. Inst. Meth. **100** (1972) 515.

[35] D.E. Lee, S.E. Sobottka, H.A. Thiessen, Nucl. Inst. Meth. **104** (1972) 179.

[36] I. Endo *et al.*, Nucl. Inst. Meth. **188** (1981) 51.

[37] A. Breskin *et al.*, Nucl. Inst. Meth. **143** (1977) 29.

[38] J. Chiba *et al.*, Nucl. Inst. Meth. **206** (1983) 451.

[39] J. C. Sens, P. Vikas, *"Reconstruction of the L3 fill vertices"*, L3 Note 1027 (1991).

[40] *"Z Physics at LEP 1, Vol. 3: Event Generators and Software"*, CERN Report CERN 89-08, eds G. Altarelli,R. Kleiss and C. Verzegnassi.

[41] M. W. Grünewald, *"Event Generators and L3 Software"*, L3 Note 1264.

[42] S. Jadach, B. Ward, Z. Was, Comp. Phys. Comm. **66** (1991) 276.

[43] S. Jadach, J. Kühn, Z. Was, Comp. Phys. Comm. **64** (1991) 275.

[44] R. Brun *et al.*, *GEANT 3 Users Guide*, CERN DD/EE84-1.

[45] M. W. Grünewald, *"Measurement of the Tau-Pair Cross Section and Charge Asymmetry at the* Z^0 *Resonance"*, PhD Thesis, CalTech, 1993.

[46] L3 Collab., M. Acciarri *et al.*, *"Measurement of Cross Sections and Leptonic Forward-Backward Asymmetries at the Z Pole and Determination of Electroweak Parameters"*, Preprint CERN-PPE/94-45, CERN, 1994, submitted to Z. Phy. C.

[47] L3 Collab., O. Adriani *et al.*, Phys. Lett. **B 294** (1992) 466.

[48] R. Alemany *et al.*, Nucl. Phys. **B379** (1992) 3.

[49] K. Hagiwara, A.D. Martin, D. Zeppenfeld, Phys. Lett. **B235** (1990) 198.

[50] ARGUS Collab., H. Albrecht *et al.*, Phys. Lett. **B250** (1990) 164.

[51] Y. Tsai, Phys. Rev. **D4** (1971) 2821.

[52] ALEPH Collab., D. Buskulic *et al.*, Phys. Lett. **B321** (1994) 168.

[53] A. Rougé, Z. Phys. **C48** (1990) 75.

[54] M. Davier, L. Duflot, F. Le Diberder, A. Rougé, Phys. Lett. **B306** (1993) 411.

[55] W. Fetscher, Phys. Rev. **D42** (1990) 1544.

[56] F. James, *"MINUIT Function Minimization and Error Analysis"*, CERN Program Library Entry and Long Writeup D506 MINUIT.

[57] L. Lyons, D. Gibaut, P. Clifford, Nucl. Inst. Meth. **A270** (1988) 110.

[58] S. N. Ganguli, *"On Electroweak Mixing Angle* $\sin\theta^2_{\mathrm{eff}}$ *from Forward-Backward Asymmetry of charged Lepton and* $\mathrm{b\bar{b}}$*, and* τ*-Polarization"*, L3 Note 1042 (1991).

[59] ALEPH Collab., D. Buskulic *et al.*, Z. Phys. **C59** (1993) 369.

[60] DELPHI Collab., P. Abreu *et al.*, Z. Phys. **C55** (1992) 555.

[61] OPAL Collab., G. Alexander *et al.*, Phys. Lett. **B266** (1991) 201.

[62] The LEP Electroweak Working Group, A. Blondel *et al.*, *"Updated Parameters of the* Z^0 *Resonance from Combined Preliminary Data of the LEP Experiments"*, LEPEWWG/94-01 (1994).

[63] H.J. Behrend *et al.*, Phys. Lett. **B183** (1987) 400.
W. de Boer, Nucl. Inst. Meth. **A278** (1989) 687.

[64] S. Kirsch, T. Riemann, *" SMATASY - A Program for the Model Independent Description of the Z Resonance "*, DESY 94-125 (1994), to be published in Comp. Phys. Comm. .

[65] A. Akhundov, D. Bardin, T. Riemann, Nucl. Phys. **B276** (1986) 1.

[66] D. Bardin, P. Christova, O. Fedorenko, Nucl. Phys. **B197** (1982) 1.

[67] M. Consoli, W. Hollik, F. Jegerlehner, Phys. Lett. **B227** (1989) 167.

[68] J. van der Bij, F. Hoogeveen, Nucl. Phys. **B283** (1987) 477.

[69] S. Gorishny, A. Kataev, S. Larin, Phys. Lett. **B259** (1991) 144.

[70] K. Chetyrkin, J. Kühn, Phys. Lett. **B248** (1990) 359.

[71] W. Beenakker, F.B. Berends, S.C. van der Marck, Nucl. Phys. **B349** (1991) 323.

[72] L3 Collab., O. Adriani *et al.*, Phys. Lett. **B 303** (1993) 391.

[73] S. Kirsch, S. Riemann, *"A Combined Fit to the L3 Data Using the S-Matrix Approach"*, L3-Note 1233 (1992).

[74] L3 Collab., O. Adriani *et al.*, Phys. Lett. **B 315** (1993) 494.

[75] S. Kirsch, *"Neutral Current Physics with the* τ *Lepton at LEP"*, plenary talk given at the XVI Kazimierz Meeting on Elementary Particle Physics, DESY 93-157 (1993).

[76] L3 Collab., O. Adriani *et al.*, Phys. Lett. **B 292** (1992) 454.

[77] S. Riemann, *private communication.*

[78] M. Grünewald, S. Kirsch, *" A Possible Modification of a LEP Energy Scan for an Improved Determination of Z-Boson Parameters "* Preprint CERN-PPE/93-188, CERN, 1993.
M. Grünewald, S. Kirsch, *"A Proposal For Additional Center-of-Mass Energy Points in the 1994 LEP Run "* L3-Note 1564, CERN, 1994.

[79] S. Kirsch, *"A Model Independent Analysis of the Z Lineshape"*, talk given at the XXIXth Rencontres de Moriond "Electroweak Interactions and Unified Theories", DESY 94-101 (1994).

[80] CDF Collab., F. Abe *et al.*, Phys. Rev. Lett. **65** (1990) 2243,
CDF Collab., F. Abe *et al.*, Phys. Rev. **D43** (1991) 2070.

[81] UA2 Collab., J. Alitti *et al.*, Phys. Lett. **B276** (1992) 354.

[82] SLD Collab., K. Abe *et al.*, Phys. Rev. Lett. **73** (1994) 25.

[83] CDHS Collab., H. Abramowitcz *et al.*, Phys. Rev. Lett. **57** (1986) 298;
CDHS Collab., A. Blondel *et al.*, Z. Phys. **C45** (1990) 361.

[84] CHARM Collab., J. V. Allaby *et al.*, Phys. Lett. **B177** (1986) 446;
CHARM Collab., J. V. Allaby *et al.*, Z. Phys. **C36** (1987) 611.

[85] CCFR Collab., *" A Precise Measurement of the Weak Mixing Angle in Neutrino Nucleon Scattering "*, NEVIS-R 1498, submitted to Phys. Rev. Lett..

[86] G. Isidori, Phys. Lett. **B314** (1993) 139.

[87] M. Merk, *"The New Luminosity Monitor of L3"*, talk given at the XXIXth Rencontres de Moriond "Electroweak Interactions and Unified Theories", to be published by Edition Frontiers, 1994.